UNIVERSITY OF COPENHAGEN
FACULTY OF SCIENCE

PhD Thesis

Parameterizing Southern Ocean eddy-induced circulation in coarse resolution ocean models

Author
Mads Bruun Poulsen

Academic advisor
Markus Jochum

Department
Niels Bohr Institute,
Centre for Ice and Climate

This thesis has been submitted on November 30th 2018 to the PhD School of The Faculty of Science, University of Copenhagen.

Abstract

Baroclinic mesoscale eddies in the Southern Ocean induce a circulation which modulates wind-driven ventilation of the interior ocean, with implication for exchanges of heat and carbon dioxide with the atmosphere. In coarse resolution ocean general circulation models which do not explicitly resolve mesoscale eddies, eddy-induced circulation is typically parameterized with a skew-diffusive tracer flux that depends on an eddy transfer coefficient, κ. Several plausible closures for κ exist, yet consensus on a specific expression for κ remains largely absent in the ocean modeling community and results in uncertain Southern Ocean ventilation rate estimates. With the use of two ocean general circulation models of coarse and eddy-resolving horizontal resolution, this thesis assesses the properties of two recently proposed expressions for κ with the aim to provide guidance towards the optimal closure.

First an expression for κ which solely depends on local stratification is examined in a suite of model simulations with varying intensity of the zonal wind stress in the Southern Ocean. The simulations suggest that implementation of a dynamic κ alleviates coarse models from an overly sensitive overturning circulation although the parameterized eddy-induced circulation does not completely match that found in the eddy-resolving model. The latter shortcoming is associated with an overly strong poleward eddy heat transport in the coarse model, which is largely compensated by mean-flow heat transports. In addition, the coarse model demonstrates a centennial equilibration time scale to wind stress change that, if representative of the dynamics, has implication for evaluation of eddy compensation in eddying models.

Second, an expression for κ which additionally depends on eddy geometry and energy is investigated. It is shown that this closure derives from a correspondence between horizontal eddy buoyancy fluxes and variance ellipses, which offers a concise geometric interpretation of baroclinic mean-flow stability and vertical momentum transfers. The eddy geometry is examined in the eddy-resolving model to assess its potential to form basis for parameterization. The geometry obeys simple probability distributions and is insensitive to external forcing change, but also possesses vertical structure which relates to the orientation of horizontal eddy buoyancy fluxes with respect to the large-scale buoyancy gradient. This structure is not explained by rotational fluxes and hence represents a possible parameterization challenge.

The thesis also presents estimates of κ extracted directly from the eddy-resolving model and provides a discussion on the assumption of horizontally down-gradient eddy fluxes upon which the skew-diffusive tracer flux relies. In particular, this discussion reiterates a previous finding that a dynamically important component of the horizontal eddy buoyancy flux appears unaccounted for in coarse models.

Resumé

Barokline mesoskala “eddies” i det Sydlige Hav inducerer en cirkulation som modulerer vinddreven ventilation af dybhavet og påvirker derigennem udvekslingen af varme og kuldioxid med atmosfæren. I numeriske cirkulationsmodeller af havet hvor den horisontale modelopløsning er for grov til at repræsentere eddies, er den eddy-inducerede cirkulation typisk parameteriseret via en diffusiv flux som afhænger af en eddykoefficient, κ. Der findes flere plausible modeller for κ, men konsensus om en specifik model for κ har ikke indfundet sig blandt havmodellører og resulterer derfor i en usikkerhed omkring ventilationsraten for det Sydlige Hav. Denne afhandling benytter sig af en havmodel, konfigureret i både en grov og i en fin horisontal modelopløsning, for at undersøge egenskaberne ved to nyligt foreslåede udtryk for κ med henblik på at danne et mere informeret grundlag for fremtidige implementeringer.

Først undersøges et udtryk for κ som funktion af den vertikale stabilitet i vandsøjlen gennem en række modeleksperimenter hvor den zonale vindstyrke i det Sydlige Hav varieres i intensitet. Simuleringerne indikerer at en dynamisk model for κ i groftopløste cirkulationsmodeller er i stand til at reducere ventilationratens følsomhed over for vindstyrken på trods af at den parameteriserede eddy-inducerede cirkulation ikke helt stemmer overens med den diagnostiserede cirkulation i den fintopløste model. Denne uoverensstemmelse falder sammen med en for kraftig meridional eddy-induceret varmetransport i den groftopløste model som i høj grad bliver kompenseret af varmetransporten drevet af storskala-cirkulationen. Derudover indikerer den groftopløste model også at tidsskalaen for at det Sydlige Hav indfinder sig i en ny ligevægt efter en ændring i vindstyrken er århundrede, hvilket har implikationer for diagnosticering af eddykompensation i højopløste havmodeller.

Desuden undersøges et udtryk for κ som afhænger af energien og geometrien i eddyfeltet. Der bliver i denne afhandling vist at denne model for κ kan udledes gennem en sammenhæng mellem eddyfluxe og geometrien af variansellipser, og at denne sammenhæng muliggør en geometrisk fortolkning af stabiliteten af storskala-cirkulationen og de vertikale udvekslinger af momentum. Geometrien af eddyfeltet undersøges i den højopløste havmodel som led i en vurdering af hvorvidt denne model for κ kan implementeres i groftopløste modeller. Sandsynlighedsfordelingerne for de geometriske parametre er relativt simple og geometrien udviser derudover også ufølsomhed over for ændringer i forceringen af havmodellen. Dog har geometrien en vertikal afhængighed som ikke kan forklares ud fra tilstedeværelsen af rotationelle eddyfluxe og udgør derfor en parameteriseringsudfordring.

Afhandlingen præsenterer også estimater af κ diagnostiseret direkte fra den højopløste model og diskuterer den grundlæggende antagelse hvorpå parameteriseringen af den eddy-inducerede cirkulation bygger. Denne diskussion fremhæver især et tidligere publiseret resultat som konkluderer at et dynamisk vigtigt bidrag til de horisontale eddyfluxe mangler parameterisering i groftopløste havmodeller.

Foreword

It has been nothing less but a privilege to be granted three years of time to dive into the world of physical oceanography and acquire a better understanding of why the Southern Ocean circulates the way that it does. Being a student in a paleoclimate research group means that I have also had the fortunate opportunity to learn about our planet's fascinating climate history as interpreted from various proxy records and I have been forced to think about my own research from different perspectives. I believe this has been healthy for my scientific education, although I must admit that it has not always been easy to convince ice core scientists that eddies in the Southern Ocean do matter. As a perfectionist and idealist, writing a PhD thesis has also been a life learning experience which has been rather demoralizing on occasions. Science, in practice, does involve compromise, opinion, impatience and conjecture, and scientific literature also has the habit of elevating your confusion to a higher level. And then there exist such concepts as rotational eddy fluxes which make you sleepless at night.

I am certain that my time as a PhD student would not have been half as good without my office mate, Søren. From a manager's point of view, a lot of time has definitely been wasted in the office on discussions about politics, existentialism, tedious university bureaucracy and science as an institution, but in the long run I do believe that you are more productive as a human being if you have a true friend by your side. I am also immensely grateful to my girlfriend, Christine, for respecting that a small fraction of my brain has been constantly thinking about the ocean for the last three years, and for always providing me with support when my spirit was low.

I am indebted to Roman for making sure that the computational infrastructure has been as close as possible to the inviscid limit throughout my studies, and to the e-science department for providing the computational resources that made this thesis work possible. I am also very grateful to my supervisor, Markus, for guiding me in the right directions and especially for acting as a necessary counter pole to my perfectionism. Many thanks also to David Marshall for hosting me in his welcoming group in Oxford during the spring of 2017, and to James Maddison for invaluable help with mathematical details. Martin, my friend, also deserves acknowledgement for reading an early version of my thesis. Lastly I would also like to express my gratitude towards the Centre for Ice and Climate, the Ice2Ice family, and TeamOcean - it makes the difference to be working in a friendly, supporting, and inspiring environment.

Contents

1 The role of the Southern Ocean in past and present climate change **1**
- 1.1 Southern Ocean eddies and contemporary climate change 3
- 1.2 Interhemispheric climate change during the last glacial 5
- 1.3 Aim and structure of the thesis 8

2 Theoretical background **11**
- 2.1 Mathematical preliminaries and notation 11
  - 2.1.1 Governing equations 12
  - 2.1.2 Averaging operators and Reynolds decomposition 13
- 2.2 Residual-mean theory 14
  - 2.2.1 Transformed Eulerian mean 15
  - 2.2.2 Thickness-weighted mean velocity 19
  - 2.2.3 Temporal residual-mean velocity 21
  - 2.2.4 Eliassen-Palm flux tensor 22
  - 2.2.5 Geometry of the Eliassen-Palm flux tensor 24
- 2.3 Parameterizing the effect of baroclinic mesoscale eddies 26
  - 2.3.1 Gent-McWilliams parameterization 29
  - 2.3.2 Gent-McWilliams and the quasi-stokes velocity 31
  - 2.3.3 Eddy transfer coefficient 32
  - 2.3.4 Rotational eddy buoyancy fluxes 34
- 2.4 Scientific challenges 35
  - 2.4.1 Eddy saturation 37
  - 2.4.2 Eddy compensation 38

3 The Parallel Ocean Program **41**
- 3.1 Model setup 41
  - 3.1.1 Coarse resolution model 41
  - 3.1.2 Eddy-resolving model 42
  - 3.1.3 Surface boundary conditions 43
- 3.2 Simulations 44
  - 3.2.1 Control integration 44
  - 3.2.2 Wind stress perturbation experiments 45
  - 3.2.3 A note on high performance computing, output frequency and data amounts 47

4 Parameterized and resolved Southern Ocean eddy compensation **49**
4.1 Introduction . . . 52
4.2 Model description, experimental setup and spin-up assessment . . . 54
4.3 Decomposition of the meridional overturning circulation . . . 59
4.3.1 Choice of temporal resolution . . . 60
4.4 Results . . . 61
4.4.1 Background state overturning . . . 61
4.4.2 Wind stress perturbation experiments . . . 64
4.4.2.1 Circulation response . . . 64
4.4.2.2 Changes in the $1036.5\,\mathrm{kg/m^3}$ density surface . . . 67
4.4.2.3 Northward heat transport response . . . 68
4.4.2.4 Buoyancy forcing response . . . 72
4.5 Discussion . . . 73
4.6 Summary . . . 76
4.7 Supplementary results . . . 77
4.7.1 Weddell Sea polynya . . . 78
4.7.1.1 Circulation changes associated with deep convection . . . 78
4.7.1.2 What causes the onset of deep convection? . . . 80
4.7.2 The influence of the seasonal cycle on the isopycnal streamfunction . . . 84
4.7.3 The time scale of eddy compensation . . . 84

5 A geometric interpretation of Southern Ocean eddy form stress **87**
5.1 Introduction . . . 90
5.2 Geometric framework . . . 92
5.2.1 Eddy stress tensor . . . 92
5.2.2 Reynolds stress ellipse . . . 94
5.2.3 Eddy form stress ellipse . . . 94
5.2.4 Eddy efficiency . . . 98
5.3 Rotational eddy buoyancy fluxes . . . 99
5.4 Model setup and output post-processing . . . 101
5.5 Results . . . 102
5.5.1 Geometric decomposition . . . 102
5.5.2 Eddy efficiency α . . . 106
5.5.3 Response to change in wind stress forcing . . . 108
5.6 Discussion . . . 111
5.7 Summary . . . 112
5.8 Supplementary results . . . 113
5.8.1 Eddy transfer coefficient estimates . . . 113

6 Acquired insight and outlook **119**
6.1 Conclusions from this thesis work . . . 119
6.2 Looking ahead . . . 121
6.2.1 A divergent eddy buoyancy flux along mean buoyancy contours . . . 121
6.2.2 Eddy forcing of the residual circulation . . . 122

6.2.3 The Vertical structure in eddy energy 124
6.2.4 Non-local response to Southern Ocean wind stress change 126

Abbreviations **128**

Bibliography **129**

Chapter 1

The role of the Southern Ocean in past and present climate change

The network of currents in the world's ocean, termed the global overturning circulation, plays a vital role in shaping the climate on Earth. The circulation is responsible for a substantial fraction of the integrated poleward heat transport which compensates the radiative imbalance at the top of the atmosphere and results in a milder climate at mid- and high latitudes. The ocean exchanges properties with the atmosphere, such as heat and carbon dioxide, and property anomalies in the oceanic mixed layer subduct into and resurface from the interior ocean via the ocean circulation. The relatively long advective time scale of the ocean, in combination with the quasi-adiabatic nature of the ocean interior, implies that the ocean has a long memory and is able to record anomalous property exchanges for centuries. This characteristic of the ocean is especially important in the light of contemporary anthropogenic climate change where ocean uptake of excess heat attenuates atmospheric warming. Obtaining a complete account of the driving processes of the global overturning circulation is thus paramount to understand the present climate on Earth as well as numerical model simulations of past climate where the oceanic circulation was likely different.

The discussion on the driving processes of the global overturning circulation mainly focuses on how water masses in the interior ocean are brought back to the surface mixed layer (e.g. Kuhlbrodt et al., 2007). In the paradigm which prevailed during most of the last century, widespread upwelling through the pycnocline via diapycnal mixing was hypothesized to entirely balance the production of deep and abyssal water masses at high latitudes (Stommel and Arons, 1959; Munk, 1966, and schematically shown for the Atlantic Ocean in Figure 1.1 by the yellow, black and blue arrows). With the emergence of realistic numerical ocean simulations by the end of the last century it was understood that wind-driven upwelling along outcropping isopycnals in the Southern Ocean provides an additional pathway to resurface deep water masses (Döös and Webb, 1994; Gnanadesikan, 1999; Marshall and Speer, 2012, green arrows in Figure 1.1). Essential to upwelling in the Southern Ocean is the dynamical constraint imposed by the existence of the Drake Passage latitude band (62°S-56°S) which is unblocked by topography in the upper part of the water column; within this latitude band, no geostrophically-balanced meridional volume transport is permitted in the zonal average. Notably, Toggweiler and

Samuels (1995) demonstrated that this unique basin geometry enables upwelling of deep water of North Atlantic origin which enters the Southern Ocean at a depth where it is possible to sustain a net poleward geostrophic flow, thus connecting the circulation in the northern and southern hemisphere.

The generation of turbulent kinetic energy by breaking internal waves is recognized as the main energy source for diapycnal mixing (Wunsch and Ferrari, 2004). The energy required to raise deep water to the surface in the Southern Ocean, on the other hand, is provided by the strong atmospheric westerly winds in the southern hemisphere mid latitudes (black ⊙ symbols in Figure 1.1). Global estimates of the work done by the surface wind stress on the ocean's circulation show that the majority of the energy enters the world ocean south of 40°S (Wunsch, 1998). Physically, the zonal wind stress drives a northward surface Ekman current whose divergence provides a mechanical lift of the interior ocean water column below, equivalent to a gain of gravitational potential energy, and gives rise to the poleward sloping isopycnals (Toggweiler and Samuels, 1998; Storch et al., 2012). The subset of isopycnals which outcrop provides an adiabatic connection between the surface equatorward Ekman transport and deep poleward geostrophic flow, and an exchange of heat and freshwater with the atmosphere and the sea ice in the Southern Ocean mixed layer drives the transformation of water upon upwelling (Abernathey et al., 2016).

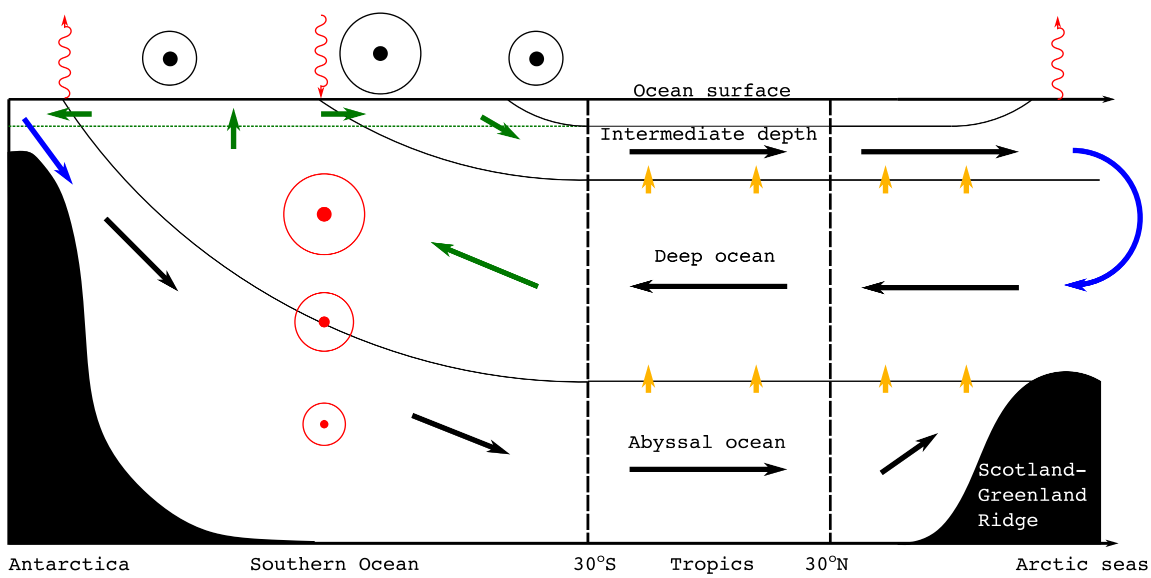

Figure 1.1: Schematic of the meridional overturning circulation in the Atlantic Ocean. Solid black lines are isopycnal surfaces and solid black arrows indicate the direction of volume transport in the interior ocean. Deep and bottom water formation is indicated by blue arrows and takes place at high latitudes via a loss of buoyancy (indicated by the wavy red arrows) due to interaction with the atmosphere and/or the sea ice. Bottom water fills the abyss and upwells via diapycnal mixing (yellow arrows) at lower latitudes. Deep water either upwells due to diapycnal mixing or via adiabatic upwelling to the mixed layer in the Southern Ocean as a function of the zonal wind stress (black arrows pointing out of the page, visualized by the ⊙ symbols). In the Southern Ocean mixed-layer (green dashed line), upwelled water transforms to a lighter or a denser water class (green arrows) depending on the surface buoyancy forcing and ocean mixing. The red ⊙ symbols indicate the presence of the vertically-sheared Antarctic Circumpolar Current.

As described in Talley (2013), both interior ocean diapycnal mixing and Southern Ocean adiabatic upwelling play important roles in the modern view of the global ocean circulation. Diapycnal mixing provides the means for Antarctic Bottom Water, formed along the margin of the Antarctic continent, to upwell diffusively at low latitudes, but it is mainly the Southern Ocean which ventilates the deep water masses in the three major ocean basins, including the northern-sourced North Atlantic Deep Water. Water which upwells to the surface Southern Ocean along relatively shallow isopycnals transforms to lighter water in the mixed layer, flows northward with the Ekman drift and subducts further to the north. In the Atlantic Ocean, as depicted schematically in Figure 1.1, this water flows toward the northern hemisphere and completes the so-called upper overturning cell. Conversely, water which upwells further to the south in the Southern Ocean densifies and contributes to the formation of Antarctic Bottom Water, which spreads northward in the abyssal ocean and upwells diffusively, thereby completing the lower overturning cell.

In addition to the meridional circulation thus described, the basin geometry of the Southern Ocean also permits the existence of the eastward-flowing Antarctic Circumpolar Current and hence an exchange of water masses between the ocean basins (red $\odot$ symbols in Figure 1.1). The vertical shear of the circumpolar current is dynamically linked to the poleward sloping isopycnals via thermal wind balance, and its volume transport through Drake Passage is the largest observed in the ocean (Cunningham et al., 2003; Koenig et al., 2014; Donohue et al., 2016). The large-scale circulation in the Southern Ocean is therefore fundamentally three-dimensional, with a double-cell meridional overturning circulation superposed on the strong zonal flow of the Antarctic Circumpolar Current. The Southern Ocean thus functions in analogy to a crossroads where most of the water masses found in the interior of the global ocean upwell, transform, subduct, and redistribute, emphasizing its central role in shaping the structure of the world's ocean.

1.1 Southern Ocean eddies and contemporary climate change

The Southern Ocean plays a primary role in the global ocean heat uptake because of the relatively low temperature of water which here upwells to the surface, and because of the intense water mass subduction associated with the northward Ekman transport (Marshall and Zanna, 2014). This property of the Southern Ocean is important from a perspective of contemporary climate change where anthropogenic emission of carbon dioxide and other greenhouse gasses to the atmosphere have led to a global-scale warming since the Industrial Revolution. Based on the Coupled Model Intercomparison Project (CMIP5) model ensemble mean, Frölicher et al. (2015) estimate that $75\% \pm 22\%$ of the ocean uptake of excess anthropogenic heat generated in the period 1861-2005 takes place south of 30°S. Substantial subsurface warming in the Southern Ocean is also recorded by the extensive network of autonomous floats released to the ocean (Gille, 2002; Böning et al., 2008). In addition to the warming, a southward displacement of the Southern Ocean isopycnals has been reported (Böning et al., 2008). This hydrographic change has been related to the poleward migration and intensification of the southern hemisphere westerlies, which is mainly attributed to the loss of Antarctic stratospheric ozone due to human activities (Thompson and Solomon, 2002; Marshall, 2003; Ferreira et al., 2015).

Perhaps most important to global climate change, the stronger atmospheric winds have been hypothesized to drive a stronger overturning circulation in the Southern Ocean (see review by Rintoul and Garabato, 2013). Since the Southern Ocean presently contributes substantially to the oceanic drawdown of atmospheric anthropogenic CO_2 (Frölicher et al., 2015), it has been suggested that increased upwelling of deep water masses rich in natural carbon leads to a stronger outgassing of CO_2 to the atmosphere and hence weakens the Southern Ocean as a net sink of atmospheric carbon dioxide (Le Quéré et al., 2007; Lovenduski et al., 2007).

The question on the response of the Southern Ocean meridional overturning circulation to increased zonal wind stress has however proved complicated to answer due to the dynamical coupling between oceanic mesoscale eddies and the large-scale circulation. Since the commence of the satellite era, satellite altimetry has provided observations of sea surface height anomalies which have revealed the presence of oceanic fronts and a rich eddy field in the Southern Ocean (Gille, 1994; Morrow et al., 1994; Orsi et al., 1995; Chelton et al., 1998; Sallée et al., 2008; Mazloff et al., 2010; Thompson and Garabato, 2014; Frenger et al., 2015; Stewart et al., 2015). The fronts are associated with relatively strong horizontal density gradients and strong horizontal flow, and are steered by bottom topography through potential vorticity conservation which gives rise to stationary meanders in the Antarctic Circumpolar Current (see e.g. review by Rintoul, 2018). Transient eddies mainly emanate from the fronts via baroclinic instability, typically downstream from complex topography, and are associated with an elevated level of eddy kinetic energy (Bischoff and Thompson, 2014; Thompson and Garabato, 2014; Barthel et al., 2017). Fundamentally, this eddy energy is extracted from the reservoir of energy which resides in the mean background density structure and circulation (Lorenz, 1955; Vallis, 2006). Eddies flux momentum, heat, and other tracers, with important implication for, for example, the poleward oceanic heat transport Gille (2003); Griesel et al. (2009); Mazloff et al. (2010); Treguier et al. (2010); Bryan et al. (2014).

In particular, baroclinic mesoscale eddies in the Southern Ocean induce a circulation which opposes the equatorward surface Ekman transport and the poleward geostrophic flow at depth (see Thompson, 2008, for an informal introduction to the concept of eddy-induced circulation). Thus, the effective meridional overturning circulation in the Southern Ocean is the residual of the sum of a mean wind-driven circulation and an eddy-induced circulation (Marshall, 1997; Marshall and Radko, 2003; Olbers and Visbeck, 2005; Vallis, 2006), and it is the residual circulation which is relevant in advection of tracers, such as dissolved carbon. The sensitivity of the residual circulation to wind stress change therefore relies on the response of the eddy-induced circulation and its ability to balance changes in the northward Ekman transport. No complete theory presently exists to predict the overturning response and most of the recent literature on the topic builds upon experiments with eddy-resolving models (Hallberg and Gnanadesikan, 2006; Viebahn and Eden, 2010; Dufour et al., 2012; Munday et al., 2013; Morrison and Hogg, 2013; Bishop et al., 2016). These models agree that eddy-induced circulation compensates change in wind-driven overturning, but the degree of compensation varies between the different model setups and experimental designs.

Projections of contemporary climate change are typically conducted with coarse resolution ocean general circulation models which do not explicitly resolve motion on the mesoscale. Instead these models introduce the effects of eddies on oceanic tracers through parameterizations which rely on assumptions on the nature of eddy tracer fluxes. The widely used eddy parameterization by Gent and McWilliams (1990) introduces the main effect of baroclinic instability, a reduction of available potential energy, via an eddy-induced circulation which acts to flatten isopycnals. In this eddy closure, the magnitude of the parameterized eddy-induced circulation depends on the isopycnal slope and an eddy transfer coefficient, κ. Both Hallberg and Gnanadesikan (2006) and Munday et al. (2013) show that the modeled Southern Ocean residual meridional overturning circulation is overly sensitive to zonal wind stress change when κ is implemented as a constant, equivalent to an insufficient degree of eddy compensation. Research into the structure and physics of κ has led to several closures which allow for spatiotemporal variations (Visbeck et al., 1997; Ferreira et al., 2005; Eden and Greatbatch, 2008; Eden et al., 2009; Marshall et al., 2012). Farneti et al. (2015) generally find that model implementations of such dynamic transfer coefficients decrease the parameterized sensitivity of the residual circulation, but also demonstrate that the sensitivity varies considerably between models. With no clear eddy compensation benchmark provided by the eddy-resolving models, it is presently difficult to differentiate between the different closures for κ. Thus, the future role of the Southern Ocean as a net sink of atmospheric carbon dioxide will likely remain a topic of dispute, unless targeted comparison studies, involving both coarse and eddy-resolving models, are carried out to evaluate the efficacy of the different proposed eddy transfer coefficients.

1.2 Interhemispheric climate change during the last glacial

As seen from temperature proxy records obtained from deep ice cores drilled on the Greenland ice sheet, the climate in the region of the North Atlantic has been remarkably variable during the last glacial (Dansgaard et al., 1993; Grootes et al., 1993). This variability is mainly characterized by several so-called Dansgaard-Oeschger events (upper panel of Figure 1.2 and Johnsen et al., 1992). Each such event follows a canonical pattern which consists of abrupt warming from cold to milder glacial conditions (interstadials), followed by a return to cold glacial conditions (stadials) through gradual cooling (Steffensen et al., 2008). The events occur irregularly through the last glacial and vary considerably in duration from a few centuries to millennia, and with an estimated amplitude between 5 and 16°C (Rasmussen et al., 2014). The imprint of Dansgaard-Oeschger climate variability in the North Atlantic has also been documented in several paleoclimate archives which express regional climate variability in other parts of the world (see e.g. Dokken et al., 2013, for a brief summary). In particular, Antarctic ice core proxy records reveal gradual temperature variations, characterized by so-called Antarctic Isotope Maximum events, which share an anti-phase relationship with Dansgaard-Oeschger events (lower panel of Figure 1.2 and EPICA Community Members, 2006). Modulated by an estimated phase shift of a couple of centuries (WAIS Divide Project Members, 2015), this relationship suggests that regional climate change in the northern hemisphere was able to play the role as a precursor for climate change in the southern hemisphere. Hence, as inferred from ice cores, interhemispheric climate change was an inherent part of the last glacial period.

The physical mechanism which controls the interhemispheric teleconnection is still debated. Many studies advocate a role for the ocean circulation in the Atlantic basin in explaining the

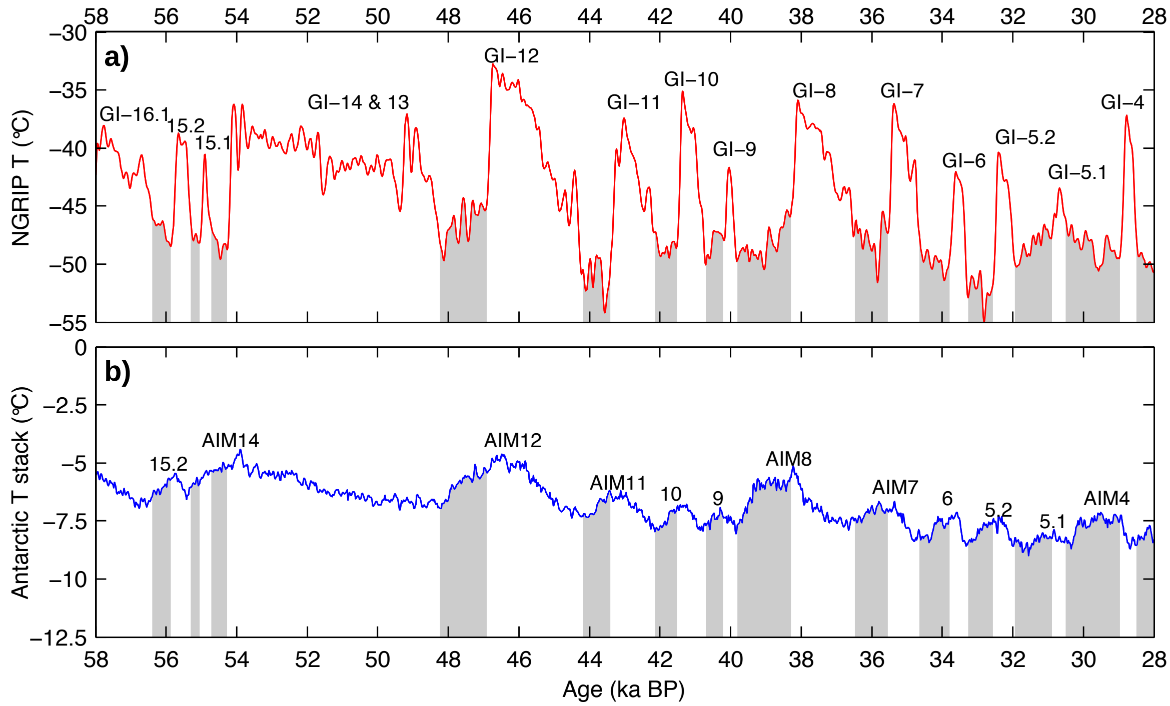

Figure 1.2: Temperature reconstructions based on isotopic composition of ice cores drilled on the Greenland ice sheet (upper panel) and Antarctic ice sheet (lower panel). Please see Pedro et al. (2018), from whom the figure is borrowed (with consent), for more details. Greenland interstadials are highlighted with the "GI" labels and follow the numbering in Rasmussen et al. (2014), and the Antarctic Isotopic Maximum events with the label "AIM" and follow the numbering in EPICA Community Members (2006). Note the anti-phase relationship between the Dansgaard-Oeschger events and the Antarctic Isotopic Maximum events: Antarctica begins to cool a couple of centuries after the abrupt warming in the North Atlantic.

interhemispheric coupling given the characteristic centennial time scale inferred from the ice core proxy records, and the ocean's ability to store and release the amount of heat necessary to sustain interstadial conditions for centuries (see e.g. the recent review by Pedro et al., 2018). The possible involvement of the Atlantic Ocean has gained additional support by the observation that the heat transport associated with the Atlantic meridional overturning circulation is northward at all latitudes. This property has led to the concept of the bipolar seesaw, in which a weakening of the overturning circulation is hypothesized to weaken the cross-equatorial heat transport, resulting in a cooling and a warming of the North and South Atlantic, respectively. An influential derivative of this simple concept was presented by Stocker and Johnson (2003) who were able to model the major features of the anti-phase ice core signal relationship, thus highlighting the relevance of the bipolar seesaw.

The conceptual model by Stocker and Johnson (2003), however, does not specify how the climate signal is conveyed from the North Atlantic to the Antarctic Continent. It is commonly thought that a change in the state of the meridional overturning circulation, emanating in the North Atlantic, is communicated to the South Atlantic via a combination of Kelvin and Rossby waves (Figure 1.3 and Kawase, 1987; Goodman, 2001; Stocker and Johnson, 2003; Marshall and Johnson, 2013). Such wave propagation displaces the Atlantic pycnocline and thereby changes the advective cross-equatorial heat transports, leading to the build-up of a heat anomaly in the South Atlantic. The further signal propagation into the Southern Ocean via waves, on the other hand, is not possible because of the absence of meridional boundaries to guide Kelvin waves beyond the South Atlantic. The propagation of the South Atlantic heat anomaly to the Antarctic continent is thus limited to oceanic advective heat transports across the Southern Ocean and to atmospheric processes.

The relative importance of the individual contributions are unknown, but as noted in the preceding section, a substantial part of the poleward heat transport in the Southern Ocean is by the means of mesoscale eddies. Pedro et al. (2018) simulate the build-up of a heat anomaly in the South Atlantic by hosing freshwater in the North Atlantic, and find that increased eddy fluxes are responsible for bringing the South Atlantic heat anomaly across the Southern Ocean to the Antarctic sea ice edge (visualized in the lower part of Figure 1.3). The subsequent sea ice retreat leads to a surface warming and enhanced atmospheric poleward advection of heat, and hence results in a warming on the Antarctic continent while the North Atlantic cools.

The coarse resolution ocean model used by Pedro et al. (2018) employs the Gent and McWilliams (1990) parameterization with a constant value for κ. As discussed in the preceding section, previous studies have shown that this parameterization choice leads to an overly

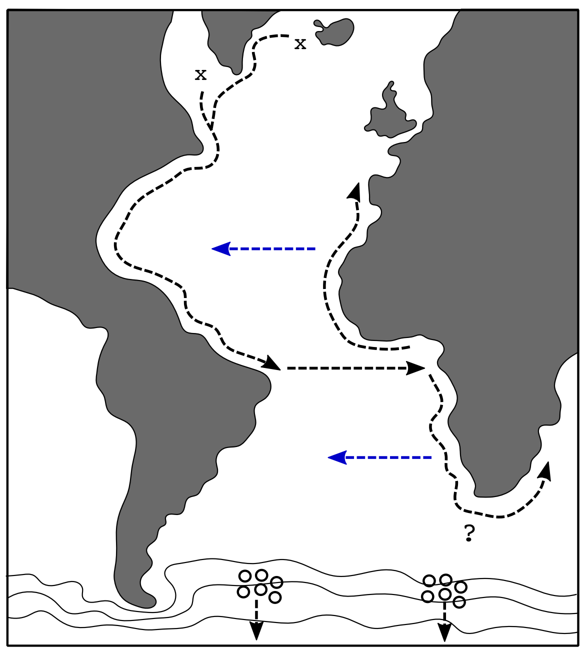

Figure 1.3: Schematic illustrating signal propagation in the Atlantic Ocean and across the Southern Ocean. A climate anomaly, such as a freshwater anomaly, is introduced in the North Atlantic regions marked with "X". This anomaly spreads into the Atlantic Basin via coastal and equatorial Kelvin waves (black dashed arrows) and westward propagating Rossby waves (blue dashed arrows). These waves deform the interior ocean density surfaces and result in changed cross-equatorial heat flux. The Kelvin wave veers off at the southern tip of Africa and the southward propagation of the climate anomaly in the South Atlantic is restricted to advective processes. One possible option, poleward heat flux by mesoscale eddies in the Antarctic Circumpolar Current (streamlines in black solid thin lines), is drawn by circular rings and arrows in the Southern Ocean. This schematic is drawn with inspiration from Marshall and Johnson (2013).

sensitive circulation in the Southern Ocean with respect to wind stress forcing. Therefore, while the sequence of processes in their coarse resolution model offers a compelling explanation for the interhemispheric ice core signal anti-phase relationship, a natural next step appears to check whether the modeled oceanic signal transmission also emerges with a more physical closure for κ. As discussed in detail in the preceding section, the optimal choice for κ is not presently clear and ultimately requires guidance from targeted model comparison studies.

1.3 Aim and structure of the thesis

The preceding sections describe two examples of how parameterization of Southern Ocean eddy-induced circulation in coarse resolution ocean models impacts the interpretation of simulations of past and present climate change. While most ocean models employ the parameterization scheme of Gent and McWilliams (1990), insufficient confidence in the details of the implementation, such as the correct expression for κ, results in a wide spectrum of approaches adopted by the different ocean modeling groups around the world's universities (see Table 1 of Farneti et al., 2015, for an example). Ultimately, these different approaches contribute to the spread in model simulations documented by large international model comparison efforts (Flato et al., 2013). The fact that ocean modeling groups are faced with these decisions on model implementation details emanates from an incomplete understanding of the physics of the large-scale turbulence in the ocean, in spite of that the topic has received a considerable amount of attention during the last several decades. Motivated by the remaining challenges within the field, the present thesis examines the properties of two recently proposed expressions for κ with the aim to provide guidance towards the optimal closure.

Firstly, this thesis aims to address the hypothesis that implementing a dynamic κ in a coarse ocean model provides the correct sensitivity of the Southern Ocean residual overturning circulation to the zonal wind stress. This is assessed with a series of realistic model simulations at coarse and eddy resolving horizontal resolution where the zonal wind stress in the Southern Ocean is varied in magnitude. The coarse model employs the Gent and McWilliams (1990) parameterization in combination with the closure for κ proposed by Ferreira et al. (2005),

$$\kappa = \kappa_0 \frac{\mathcal{N}^2}{\mathcal{N}_{\text{ref}}^2},$$

where $\mathcal{N}$ is the buoyancy frequency, and κ_0 and $\mathcal{N}_{\text{ref}}$ are reference values. Similar model comparison studies have been conducted in the past, but with κ set equal to a globally constant value (e.g. Hallberg and Gnanadesikan, 2006). Furthermore, this part of the thesis distinguishes itself from prior efforts (e.g. Bitz and Polvani, 2012; Bryan et al., 2014) by considering forced simulations (no atmosphere-ocean feedbacks) on a global grid domain (no open boundaries) to facilitate a more mechanistic approach to the model comparison. The results from this study are presented in Chapter 4 and are published in *Ocean Modelling* with the following reference:

Poulsen, M. B., M. Jochum, and R. Nuterman, 2018: Parameterized and resolved southern ocean eddy compensation. *Ocean Modelling*, **124**, 1–15, doi:10.1016/j.ocemod.2018.01.008

Secondly, this thesis is concerned with the interpretation of the recently proposed eddy transfer coefficient by Marshall et al. (2012),

$$\kappa = \alpha E \frac{\mathcal{N}_0}{\mathcal{M}^2},$$

which derives from a quasi-geostrophic context. Besides its dependence on the vertical and horizontal ocean stratification, $\mathcal{N}_0$ and $\mathcal{M}$ respectively, this expression is formulated in terms of the geometry of the Eliassen-Palm flux tensor, captured by α, as well as the eddy energy, E. The motivation for studying this particular closure for κ is that its recent implementation into different idealized models have shown a promising representation of various eddy effects (Bachman et al., 2017; Mak et al., 2017, 2018) that no other formulation for κ has been able to achieve. This thesis specifically provides an interpretation of α and relates it to the stability of vertically-sheared mean-flow. In addition, this thesis investigates α in an eddy-resolving general circulation model of 0.1° horizontal grid resolution and discusses the possibility to parameterize α in coarse resolution models. The results from this study are presented in Chapter 5 and have been submitted to *Journal of Physical Oceanography* for publication with the following reference:

Poulsen, M. B., M. Jochum, J. R. Maddison, D. P. Marshall, and R. Nuterman, Submitted: A geometric interpretation of southern ocean eddy form stress. *Journal of Physical Oceanography*.

The structure of the thesis is the following: Chapter 2 provides a review of the theoretical foundation of the subsequent chapters with a particular focus on residual-mean theory, eddy-mean flow interaction, and common eddy parameterizations. Chapter 3 describes the numerical ocean model used in this thesis work, The Parallel Ocean Program Version 2, and details its configuration on the two different horizontal grids as well as the chosen forcing. Chapter 4 and 5 present the manuscripts of Poulsen et al. (2018) and Poulsen et al. (Submitted), respectively, as well as supplementary results which did not enter the manuscripts themselves. Chapter 6 draws together the key conclusions from Chapter 4 and 5, and discusses the open questions which have appeared during the thesis work and which the author thinks deserve an answer in the future.

Chapter 2

Theoretical background

The present chapter reviews the theoretical background and scientific results upon which the subsequent chapters are based, with the intention to make the thesis available to a wider audience than the small community of scientists which are familiar with the physics of the Southern Ocean. A particular hope is that, by reading the present chapter, the remainder of the thesis is accessible to any person with an education in the physical sciences which to some extent covers geophysical fluid dynamics.

Section 2.1 outlines and defines the equations, operators, variable decompositions and notation used in the remainder of the thesis. Section 2.2 discusses so-called residual-mean theory and its application to the Southern Ocean as an attempt to rationalize the observations from the Southern Ocean that were described in Chapter 1. Section 2.2 also outlines the forcing of the Southern Ocean large-scale circulation by mesoscale eddies, whose presence is an expression of the instability of the circulation itself. Section 2.3 reviews common eddy parameterizations for use in coarse resolution ocean models which are unable to resolve motion on the mesoscale. Specifically, the connection between the popular Gent-McWilliams eddy parameterization scheme and residual-mean theory is discussed. Lastly, Section 2.4 touches upon contemporary scientific challenges for the Southern Ocean community, namely the concepts of eddy saturation and eddy compensation, which motivate much of the work presented in the following chapters of this dissertation.

2.1 Mathematical preliminaries and notation

This thesis discusses the physics of the Southern Ocean with the aid from the averaged Boussinesq and quasi-geostrophic equations. These equations, and the applied averaging operators and variable decompositions, are outlined below. The reader is referred to Pedlosky (1987) or Vallis (2006) for a derivation of the equations and for a more exhaustive description than what is presented in the following.

2.1.1 Governing equations

The Boussinesq-approximated primitive equations are

$$\frac{\partial \mathbf{u}}{\partial t} + (\mathbf{v} \cdot \nabla)\,\mathbf{u} + f\mathbf{k} \times \mathbf{u} = -\,\frac{\nabla_h p}{\rho_0} + \boldsymbol{\mathcal{F}} \tag{2.1a}$$

$$\frac{\partial p}{\partial z} = -\,\rho g \tag{2.1b}$$

$$\nabla \cdot \mathbf{v} = 0 \tag{2.1c}$$

$$\frac{\partial b}{\partial t} + \mathbf{v} \cdot \nabla b = \mathcal{B}, \tag{2.1d}$$

which are, from top to bottom, the horizontal momentum equation, the vertical momentum balance (hydrostatic balance), mass conservation and the thermodynamic equation. $\mathbf{u} = (u, v, 0)$ is the horizontal velocity, $\mathbf{v} = (u, v, w)$ is the three-dimensional velocity, f is the Coriolis parameter, $\mathbf{k} = (0, 0, 1)$ is the vertical unit vector, p is the pressure field, $\boldsymbol{\mathcal{F}}$ denotes frictional forces, g is the gravitational acceleration, b is buoyancy (definition follows later) and $\mathcal{B}$ is buoyancy forcing. ∇ and ∇_h are the three-dimensional and horizontal divergence operator, respectively. The density variable, ρ, is here decomposed according to $\rho(x, y, z, t) = \rho_0(z) + \delta\rho(x, y, z, t)$, and the central part in the Boussinesq approximation is the assumption that density variations are relatively small compared to the background state, $\delta\rho \ll \rho_0$, which is a good approximation in the ocean. If pressure is decomposed according to $p(x, y, z, t) = p_0(z) + \delta p(x, y, z, t)$, and $p_0(z)$ is defined such that

$$\frac{\partial p_0}{\partial z} \equiv -\rho_0 g, \tag{2.2}$$

then the validity of eq. (2.1b) relies on the assumption that pressure deviations are in hydrostatic balance with density fluctuations,

$$\frac{\partial \delta p}{\partial z} = -\delta\rho g = \rho_0 b, \tag{2.3}$$

as well. Here buoyancy b is defined as $b \equiv -g\delta\rho/\rho_0$.

The second set of equations is the quasi-geostrophic equations, which derives from a truncated asymptotic expansion of the primitive equations, eq. 2.1a-(2.1d), in the Rossby number, Ro, which is required to be small, Ro $\ll 1$. The circulation is geostrophically balanced to lowest order in the expansion, and at order Ro the deviation from geostrophic balance is described by,

$$\frac{\partial \mathbf{u}_g}{\partial t} + (\mathbf{u}_g \cdot \nabla)\,\mathbf{u}_g + f_0\mathbf{k} \times \mathbf{u}_{\mathrm{ag}} + \beta y\mathbf{k} \times \mathbf{u}_g = -\,\frac{\nabla_h p_{\mathrm{ag}}}{\rho_0} + \boldsymbol{\mathcal{F}} \tag{2.4a}$$

$$\nabla \cdot \mathbf{u}_g = \nabla \cdot \mathbf{u}_{\mathrm{ag}} = 0 \tag{2.4b}$$

$$\frac{\partial b}{\partial t} + \mathbf{u}_g \cdot \nabla b + \mathcal{N}_0^2 w_{\mathrm{ag}} = \mathcal{B}, \tag{2.4c}$$

which are known as the quasi-geostrophic equations. From top to bottom, these equations are the horizontal momentum equation, continuity equation and the thermodynamic equation. Here $\mathbf{u}_g = (u_g, v_g, 0)$ is the horizontal geostrophic velocity, $\mathbf{u}_{\mathrm{ag}} = (u_{\mathrm{ag}}, v_{\mathrm{ag}}, w_{\mathrm{ag}})$ is the ageostrophic velocity and p_{ag} is the part of the pressure field which is not associated with geostrophic balance. The β-plane approximation has been used, $f = f_0 + \beta y$, where $\beta y \ll f_0$, and the vertical stratification is given by

$$\mathcal{N}_0^2 = \frac{\partial b_0}{\partial z}, \tag{2.5}$$

where $b_0(z)$ is the background buoyancy profile which b varies about. The main advantage of the quasi-geostrophic assumptions is that it is possible to reduce the governing set of equations to one prognostic equation, namely the quasi-geostrophic potential vorticity equation, in terms of a single variable. The main disadvantage of the quasi-geostrophic equations are their limited applicability: they apply to a fluid of low Rossby number, Ro $\ll 1$, with horizontal length scale of the motion close to the baroclinic deformation radius, and with small meridional excursions to satisfy $\beta y \ll f_0$. These limitations imply that deviations from the background stratification, b_0, must be small.

2.1.2 Averaging operators and Reynolds decomposition

Define $\langle q \rangle$ to denote an average of the variable q along a closed zonal path of length L,

$$\langle q \rangle = \frac{1}{L} \oint_x q \, \mathrm{d}x, \tag{2.6}$$

and define $\overline{q}$ to denote a temporal average of q between t_1 and t_2,

$$\overline{q} = \frac{1}{T} \int_{t_1}^{t_2} q \, \mathrm{d}t, \tag{2.7}$$

where $T = t_2 - t_1$.

Any variable q may then be written as the sum of its mean and the fluctuation about the mean, a so-called Reynolds decomposition,

$$q = \langle q \rangle + q^+ \tag{2.8}$$
$$q = \overline{q} + q'. \tag{2.9}$$

We assume that this variable decomposition satisfy

$$\overline{\overline{q}} = \overline{q}, \quad \overline{q'} = 0, \quad \overline{\overline{q_1} q_2'} = 0, \tag{2.10}$$

but that $\overline{q_1' q_2'}$ is not necessarily zero (see e.g. Bachman et al., 2015, for a discussion on the assumptions of the Reynolds decomposition). A similar set of axioms is assumed to apply to the zonal decomposition (2.8). Importantly, the decompositions (2.8)-(2.9) combine to yield

$$q = \overline{q} + q' + \overline{\langle q \rangle} - \overline{\langle q \rangle} = \overline{\langle q \rangle} + \overline{q - \langle q \rangle} + q' = \overline{\langle q \rangle} + \overline{q^+} + q', \tag{2.11}$$

such that q is expressed as the sum of its zonal- and time-mean, the time-mean of its fluctuation along the zonal direction and lastly its transient fluctuation. The decomposition (2.11) will prove useful in the following as it exposes the part of q which is related to stationary meanders (standing waves) and transient eddies/waves in the ocean circulation.

2.2 Residual-mean theory

Scaling and averaging are often invoked tools to reduce the complexity of the governing equations for fluid motion on Earth. The zonal flow of the Antarctic Circumpolar Current, although modulated by standing meanders due to bottom topography, have led to the idea that a theory based on the zonally-averaged equations of motion is meaningful and may provide insight into the dynamics of the Southern Ocean stratification and meridional circulation. As discussed in the preceding chapter, dynamical and thermodynamical processes are coupled in the Southern Ocean and hence the momentum- and thermodynamic equations must necessarily be treated in unison for any such theory to be useful. Finally, the presence of baroclinic mesoscale eddies suggest that it is relevant to separate the large-scale circulation from the motion on the mesoscale, in order to understand their mutual interaction. These requirements to a potentially useful theory have resulted in the adoption of the residual-mean framework by the oceanographic community, which today constitutes a cornerstone in the present understanding of the meridional overturning circulation in the Southern Ocean.

Residual-mean theory was first discussed in the context of the zonally-averaged circulation in the atmosphere (Andrews and McIntyre, 1976), and was later applied to the case of the ocean (Gent et al., 1995; Cronin, 1996; Treguier et al., 1997; Marshall, 1997; Marshall and Radko, 2003; Olbers and Visbeck, 2005; Ferreira et al., 2005; McDougall and McIntosh, 1996, 2001). The term *residual-mean* refers to the fact that the averaged governing equations are transformed such that tracers and momentum are advected by a residual velocity, and not only by the averaged velocity. The residual velocity takes into account the motion induced due to the presence of mesoscale eddies or standing waves in the ocean, and the transformation provides a simplification to the system of equations when the residual velocity is appropriately defined (see e.g. Vallis, 2006). The residual velocity is often chosen such that eddy fluxes of momentum and buoyancy solely appear in the horizontal momentum equation for adiabatic motion, and hence no eddy flux of buoyancy is present in the thermodynamic equation.

The relevance of the residual velocity in advection of tracers became obvious in past studies which diagnosed the time-mean oceanic meridional overturning circulation streamfunction, $\overline{\psi}(y, z)$, via zonal integration at fixed height (Eulerian integration) of the meridional velocity field,

$$\overline{\psi}(y, z) = -\overline{\oint_x \int_{\eta_B}^{z} v \, \mathrm{d}z' \, \mathrm{d}x} = -\int_{\eta_B}^{z} L \left\langle \overline{v} \right\rangle \, \mathrm{d}z'. \tag{2.12}$$

This Eulerian streamfunction expresses the southward transport of fluid at latitude y between a given surface of constant depth, z, and the ocean bottom, η_B, and $\overline{\psi}$ has on the rightmost side of eq. (2.12) been expressed in terms of the averaging operators defined by eq. (2.6)-(2.7). As seen from eq. (2.12), $\overline{\psi}$ depends on vertical integration of the Eulerian zonal-mean and time-mean meridional velocity field, $\langle \overline{v} \rangle$, which according to eq. (2.11) excludes the contributions from standing meanders and transient eddies in the circulation. As seen in e.g. Döös and Webb (1994); McIntosh and McDougall (1996); Viebahn and Eden (2012), this streamfunction gives an impression of a substantial diabatic component to the meridional circulation in the Southern Ocean, an artifact which is the result of the chosen type of zonal integration, and contrasts with the often emphasized adiabatic nature of the world's ocean interior. Perhaps the most well-known circulation artifact which appears in $\overline{\psi}$ is the Deacon cell, which suggests strong diabatic downwelling in the northern part of the Southern Ocean (Döös and Webb, 1994). Thus it is not the Eulerian zonal- and time-mean velocity field which advects tracers in the time-mean zonally-averaged ocean, but, as will become evident in the following, the residual velocity.

The usefulness of transforming the averaged equations such that the eddy buoyancy flux appears in the momentum equation instead of the buoyancy equation also becomes apparent when one realizes that the horizontal eddy buoyancy flux in reality is an eddy form stress in disguise. This stress is responsible for vertical transfers of horizontal momentum and has been discussed in the context of the Antarctic Circumpolar Current by Johnson and Bryden (1989); Wolff et al. (1991); Olbers (1998); Masich et al. (2018) among others. The zonally- and vertically-integrated zonal momentum balance in the open Drake Passage latitude band reveals that the momentum input by the zonal wind stress must be balanced by a combination of meridional fluxes of zonal momentum, bottom friction and bottom form drag. The latter force was hypothesized by Munk and Palmén (1951) to balance the vast majority of the surface wind stress in the Southern Ocean, and this approximate force balance has been confirmed in several ocean model studies in the past (Wolff et al., 1991; Ivchenko et al., 1996; Hogg and Blundell, 2006; Howard et al., 2014; Masich et al., 2015). The eddy form stress thus constitutes an important connection between the surface and bottom Southern Ocean, and ensures the necessary downward transfer of horizontal momentum in the water column to close the zonal momentum budget.

In the case where the governing equations are averaged in the zonal direction at fixed latitude and depth, the transformation of the equations using the residual velocity (the transformed Eulerian mean equations) allows the total eddy force in the horizontal momentum equation to be expressed as the divergence of a flux, the so-called Eliassen-Palm flux (Andrews and McIntyre, 1976). In quasi-geostrophy, when the equations are averaged in time instead of in the zonal direction, it has been shown by Plumb (1986) and Cronin (1996) that the eddy force can be expressed as the divergence of a rank-two eddy stress tensor. More generally, when more physically meaningful averaging is applied, such as thickness-weighted averaging, the primitive equations may undergo a similar transformation where the eddy force in the horizontal momentum equation appears as the divergence of the Eliassen-Palm flux tensor (Young, 2012; Maddison and Marshall, 2013). Residual-mean theory thus allows for a rearrangement of eddy fluxes and exposure of the combined eddy force on the residual circulation.

2.2.1 Transformed Eulerian mean

To introduce the concept of the residual velocity, this section considers the transformed Eulerian mean equations from the perspective of the Boussinesq system of equations. The equations are here averaged in the zonal direction at fixed height and latitude by applying the operator (2.6) to eq. (2.1a)-(2.1d),

$$\frac{\partial \langle \mathbf{u} \rangle}{\partial t} + (\langle \mathbf{v} \rangle \cdot \nabla) \langle \mathbf{u} \rangle + f\mathbf{k} \times \langle \mathbf{u} \rangle = - \frac{\nabla_h \langle p \rangle}{\rho_0} - \nabla \cdot \mathsf{R} + \langle \boldsymbol{\mathcal{F}} \rangle \tag{2.13a}$$

$$\frac{\partial \langle p \rangle}{\partial z} = \langle b \rangle \rho_0 \tag{2.13b}$$

$$\nabla \cdot \langle \mathbf{v} \rangle = 0 \tag{2.13c}$$

$$\frac{\partial \langle b \rangle}{\partial t} + \langle \mathbf{v} \rangle \cdot \nabla \langle b \rangle = - \nabla \cdot \left\langle \mathbf{v}^+ b^+ \right\rangle + \langle \mathcal{B} \rangle , \tag{2.13d}$$

and the variables have been decomposed according to (2.8). Here R is a rank-two tensor which holds the eddy Reynolds stresses. Note that some of the terms in the above equations are zero by performing zonal averaging, but are retained for now to allow for a more general treatment of the transformation.

From eq. (2.13d) it is visible that the zonally-averaged velocity, $\langle \mathbf{v} \rangle$, has a component through zonally-averaged buoyancy surfaces, $\langle b \rangle$, in steady and adiabatic conditions when $\nabla \cdot \langle \mathbf{v}^+ b^+ \rangle \neq 0$. To overcome this apparent inconsistency with the adiabatic nature of the ocean, the idea is to express the averaged equations in term of the residual velocity $\mathbf{v}_{\text{res}}$,

$$\mathbf{v}_{\text{res}} = \langle \mathbf{v} \rangle + \mathbf{v}^* = \langle \mathbf{v} \rangle + \nabla \times \boldsymbol{\psi}^*, \tag{2.14}$$

where $\boldsymbol{\psi}^*$ is the vector streamfunction associated with the eddy-induced velocity $\mathbf{v}^*$, and $\nabla \cdot \mathbf{v}_{\text{res}} = 0$ since the eddy-induced velocity is non-divergent by construction. The residual-mean form of the averaged thermodynamic equation is,

$$\frac{\partial \langle b \rangle}{\partial t} + \mathbf{v}_{\text{res}} \cdot \nabla \langle b \rangle = -\nabla \cdot \mathbf{F}_{\text{res}} + \mathcal{B}, \tag{2.15}$$

where the divergence of the residual eddy flux of buoyancy, $\mathbf{F}_{\text{res}}$, is

$$\nabla \cdot \mathbf{F}_{\text{res}} = \nabla \cdot \left(\left\langle \mathbf{v}^+ b^+ \right\rangle + \nabla \langle b \rangle \times \boldsymbol{\psi}^* \right). \tag{2.16}$$

A common choice for $\boldsymbol{\psi}^*$ is (see e.g. Ferreira et al., 2005)

$$\boldsymbol{\psi}^* = \frac{\mathbf{k} \times \langle \mathbf{v}^+ b^+ \rangle}{\langle b \rangle_z}, \tag{2.17}$$

where the subscript z on $\langle b \rangle$ is short-hand notation for the partial vertical derivative. This particular choice for the streamfunction results in the eddy-induced velocity $\mathbf{v}^*$,

$$\mathbf{u}^* = -\frac{\partial}{\partial z} \left(\frac{\langle \mathbf{u}^+ b^+ \rangle}{\langle b \rangle_z} \right), \quad w^* = \nabla_h \cdot \left(\frac{\langle \mathbf{u}^+ b^+ \rangle}{\langle b \rangle_z} \right). \tag{2.18}$$

The residual flux, $\mathbf{F}_{\text{res}}$, which arises by inserting eq. (2.17) in (2.16) is

$$\mathbf{F}_{\text{res}} = \frac{\nabla \langle b \rangle \cdot \langle \mathbf{v}^+ b^+ \rangle}{\langle b \rangle_z} \mathbf{k}. \tag{2.19}$$

It is often assumed that the eddy buoyancy flux behaves adiabatically in the interior ocean, such that eddy fluxes align with surfaces of constant buoyancy, $\nabla \langle b \rangle \cdot \langle \mathbf{v}^+ b^+ \rangle = 0$ (see Treguier et al., 1997, for a discussion on this assumption). In that case one finds that $\mathbf{F}_{\text{res}} = \mathbf{0}$ and the residual-mean thermodynamic equation, eq. (2.15), is free from explicit eddy fluxes,

$$\frac{\partial \langle b \rangle}{\partial t} + \mathbf{v}_{\text{res}} \cdot \nabla \langle b \rangle = \mathcal{B}. \tag{2.20}$$

For steady flow in the interior ocean where it is assumed that $\mathcal{B}$ vanishes, $\mathbf{v}_{\text{res}} \cdot \nabla \langle b \rangle = 0$ and the streamlines of the residual circulation are aligned with buoyancy surfaces. Hence tracers are advected along zonally-averaged buoyancy surfaces by the residual velocity under steady and adiabatic conditions.

An illuminating use of the transformed Eulerian mean equations with respect to the Southern Ocean meridional circulation is provided by Marshall (1997); Marshall and Radko (2003); Olbers and Visbeck (2005). The two latter studies consider a steady-state zonal- and time mean model for the Southern Ocean on a f-plane with an adiabatic interior. According to decomposition (2.11),

$$\left\langle \overline{\mathbf{v}b} \right\rangle = \langle \overline{\mathbf{v}} \rangle \left\langle \overline{b} \right\rangle + \left\langle \overline{\mathbf{v}^+}\, \overline{b^+} \right\rangle + \left\langle \overline{\mathbf{v}'b'} \right\rangle, \tag{2.21}$$

but if the zonal integration path is taken to follow time-mean streamlines of the zonal flow, such that $\left\langle \overline{\mathbf{v}^+}\, \overline{b^+} \right\rangle = 0$, the remaining eddy correlation term is due to transient eddies only. In this framework, the steady-state zonal- and time mean zonal momentum equation expressed with the residual velocity, assuming negligible momentum fluxes as in Marshall and Radko (2003), is

$$- f_0 v_{\text{res}} = \left\langle \overline{\mathcal{F}_x} \right\rangle - f_0 v^*. \tag{2.22}$$

From the defined eddy-induced streamfunction, eq. (2.17), it is seen that

$$v^* = -\frac{\partial}{\partial z}\left(\frac{\left\langle \overline{v'b'} \right\rangle}{\left\langle \overline{b} \right\rangle_z} \right) \quad \text{and} \quad w^* = \frac{\partial}{\partial y}\left(\frac{\left\langle \overline{v'b'} \right\rangle}{\left\langle \overline{b} \right\rangle_z} \right), \tag{2.23}$$

and one may define the eddy-induced velocity streamfunction in the meridional plane as

$$\psi^* = \frac{\left\langle \overline{v'b'} \right\rangle}{\left\langle \overline{b} \right\rangle_z}. \tag{2.24}$$

Equating the frictional force term, $\left\langle \overline{\mathcal{F}_x} \right\rangle$, to the vertical divergence of the turbulent stress present in the surface boundary layer due to the surface wind stress, and replacing v_{res} and v^* with their respective streamfunctions, one obtains

$$\frac{\partial \psi_{\text{res}}}{\partial z} = \frac{1}{f_0} \frac{\partial \left\langle \overline{\tau^x} \right\rangle}{\partial z} + \frac{\partial \psi^*}{\partial z}. \tag{2.25}$$

Integrating vertically from some point in the interior ocean, where the influence from the wind stress has vanished, to the surface where $\langle\overline{\tau^x}\rangle = \langle\overline{\tau_s^x}\rangle$, the zonal momentum balance reads

$$\psi_{\text{res}} = -\frac{\langle\overline{\tau_s^x}\rangle}{f_0} + \psi^* = \overline{\psi} + \psi^*. \tag{2.26}$$

This balance outlines that the residual meridional circulation, which in the interior ocean is along surfaces of constant buoyancy under steady adiabatic conditions, is set by two contributions: an overturning due to the northward surface Ekman current, $-\langle\overline{\tau_s^x}\rangle/f_0$, and an overturning circulation induced by the eddies, ψ^*. The former contribution is positive since $f_0 < 0$ in the southern hemisphere and the latter contribution is negative because $\overline{b'v'}$ is poleward in the zonal mean, and hence the eddy-induced circulation counteracts the directly wind-driven circulation. The physics implied by the simple residual-mean model is that the northward surface Ekman current steepens the isopycnals and the eddies flatten them via baroclinic instability. It is the balance between these two physical processes, in this particular model, which determines the zonally-averaged time mean stratification in the Southern Ocean (see Figure 2.1 for a conceptual schematic of the residual circulation).

An interesting limit of the model is for $\psi_{\text{res}} = 0$ where the zonal momentum balance, eq. (2.26), is

$$\langle\overline{\tau_s^x}\rangle = f_0 \frac{\langle\overline{b'v'}\rangle}{\langle\overline{b}\rangle_z} \approx \frac{f_0}{\mathcal{N}_0^2}\langle\overline{b'v'}\rangle = -\frac{1}{\rho_0}\left\langle\overline{\eta'\frac{\partial p'}{\partial x}}\right\rangle, \tag{2.27}$$

where the mesoscale eddies are assumed to be geostrophically-balanced and it is used that $\eta' = -b'/\mathcal{N}_0^2$, where η' is the interior ocean neutral surface displacement. The right hand side of eq. (2.27) is a zonal interfacial form stress and gives rise to vertical transfers of zonal momentum (Vallis, 2006). Hence the limiting case expressed by eq. (2.27) implies that all

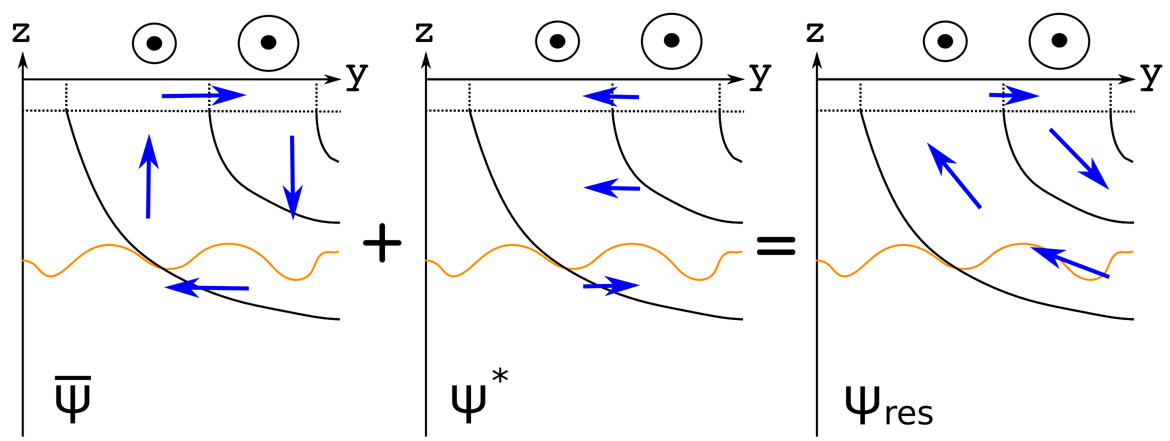

Figure 2.1: Conceptual schematic of the streamfunction contributions to the residual circulation in the zonally-averaged model by Marshall and Radko (2003). Black solid lines are surfaces of constant zonally-averaged buoyancy, the solid orange line marks the height of bottom topography and dotted black lines denote the surface mixed-layer. Blue arrows visualize the nature of the meridional circulation and ⊙ symbols denote the eastward wind stress. The left panel displays the overturning circulation due to the surface wind stress, the middle panel the eddy-induced circulation and the right panel the residual circulation, where the residual circulation is aligned with surfaces of constant buoyancy.

zonal momentum input at the surface ocean is fluxed downward via eddy form stress and is eventually balanced by bottom form drag (see Johnson and Bryden, 1989, for a detailed discussion of this limiting momentum balance).

2.2.2 Thickness-weighted mean velocity

As shown in McIntosh and McDougall (1996), the meridional residual velocity defined in the preceding section by eq. (2.14) and (2.17),

$$v_{\mathrm{res}} = \langle v \rangle + v^* = \langle v \rangle - \frac{\partial}{\partial z}\left(\frac{\langle b^+ v^+ \rangle}{\langle b \rangle_z}\right), \tag{2.28}$$

is an approximation to the so-called *thickness-weighted mean velocity* which arises from isopycnal averaging of the meridional velocity field. This velocity is the theme of the present section and will outline an equivalent way of looking at the residual-mean circulation in the zonal average. It also constitutes a natural starting point for the discussion of the time-averaged ocean circulation and the temporal residual-mean velocity.

Consider the vertically-integrated meridional velocity between two isopycnal surfaces of height $\eta_1(x, y, t)$ and $\eta_2(x, y, t)$,

$$T = \int_{\eta_1}^{\eta_2} v(x, y, z, t)\, \mathrm{d}z. \tag{2.29}$$

If the height of the isopycnal surfaces are decomposed according to (2.8), one may write T as

$$T = \int_{\langle \eta_1 \rangle + \eta_1^+}^{\langle \eta_2 \rangle + \eta_2^+} v\, \mathrm{d}z = \int_{\langle \eta_1 \rangle}^{\langle \eta_2 \rangle} v\, \mathrm{d}z + \int_{\langle \eta_2 \rangle}^{\langle \eta_2 \rangle + \eta_2^+} v\, \mathrm{d}z + \int_{\langle \eta_1 \rangle + \eta_1^+}^{\langle \eta_1 \rangle} v\, \mathrm{d}z, \tag{2.30}$$

where $\langle \eta_1 \rangle$ is the zonally-averaged height of the lower isopycnal and η_1^+ is the fluctuation of the isopycnal height in the zonal direction, and similarly for η_2 (see left panel of Figure 2.2 for a schematic of the isopycnal layer in consideration). By using a Taylor expansion of the meridional velocity about the zonally-averaged height of the isopycnals, McIntosh and McDougall (1996) show that the zonal average of T becomes

$$\langle T \rangle = \left\langle \int_{\langle \eta_1 \rangle + \eta_1^+}^{\langle \eta_2 \rangle + \eta_2^+} v\, \mathrm{d}z \right\rangle = \left\langle \int_{\langle \eta_1 \rangle}^{\langle \eta_2 \rangle} v\, \mathrm{d}z \right\rangle - \frac{\left\langle v^+|_{z=\langle \eta_2 \rangle} b_2^+|_{z=\langle \eta_2 \rangle} \right\rangle}{\langle b \rangle_z|_{z=\langle \eta_2 \rangle}} + \frac{\left\langle v^+|_{z=\langle \eta_1 \rangle} b_1^+|_{z=\langle \eta_1 \rangle} \right\rangle}{\langle b \rangle_z|_{z=\langle \eta_1 \rangle}}. \tag{2.31}$$

An important point is to note that all terms on the right hand side are evaluated at fixed depth, and hence the zonal average is performed at fixed depth, whereas the zonal integration on the left hand side follows the vertical excursions of the isopycnal layer. Now examining the limit where $\eta_1 \to \eta_2$, one finds that, term by term,

$$\left\langle \int_{\langle \eta_1 \rangle + \eta_1^+}^{\langle \eta_2 \rangle + \eta_2^+} v\, \mathrm{d}z \right\rangle = \left\langle v \int_{\langle \eta_1 \rangle + \eta_1^+}^{\langle \eta_2 \rangle + \eta_2^+} \mathrm{d}z \right\rangle = \langle vh \rangle\,, \tag{2.32}$$

where $h = \eta_2 - \eta_1$ is the isopycnal thickness, and

$$\left\langle \int_{\langle \eta_1 \rangle}^{\langle \eta_2 \rangle} v \,\mathrm{d}z \right\rangle = \left\langle v \int_{\langle \eta_1 \rangle}^{\langle \eta_2 \rangle} \mathrm{d}z \right\rangle = \langle v \langle h \rangle \rangle = \langle h \rangle \langle v \rangle \,, \tag{2.33}$$

where $\langle h \rangle = \langle \eta_2 \rangle - \langle \eta_1 \rangle$ is the zonally-averaged layer thickness, and lastly

$$-\frac{\left\langle v^+|_{z=\langle \eta_2 \rangle} b_2^+|_{z=\langle \eta_2 \rangle} \right\rangle}{\langle b \rangle_z|_{z=\langle \eta_2 \rangle}} + \frac{\left\langle v^+|_{z=\langle \eta_1 \rangle} b_1^+|_{z=\langle \eta_1 \rangle} \right\rangle}{\langle b \rangle_z|_{z=\langle \eta_1 \rangle}} = -\langle h \rangle \frac{\partial}{\partial z}\left(\frac{\langle v^+ b^+ \rangle}{\langle b \rangle_z} \right). \tag{2.34}$$

Combining these results, the thickness weighted zonally-averaged meridional velocity is

$$\frac{\langle T \rangle}{\langle h \rangle} = \frac{\langle vh \rangle}{\langle h \rangle} = \langle v \rangle - \frac{\partial}{\partial z}\left(\frac{\langle b^+ v^+ \rangle}{\langle b \rangle_z} \right), \tag{2.35}$$

where it is understood that the zonal integral on the left hand side follows the isopycnal with mean height $\langle \eta \rangle$ and on the right hand side the zonal average is taken at fixed height $\langle \eta \rangle$. The right hand side is the meridional residual velocity that was obtained in the preceding section, and hence the above equation shows that an ocean modeler may diagnose the relevant zonally-averaged meridional overturning circulation in two ways: either by calculating the eddy-induced meridional velocity and add it to the Eulerian mean velocity field to form the residual velocity field, which may then be integrated in the vertical direction to obtain the streamfunction for the residual circulation. Or alternative, by integrating the meridional velocity field in density space to obtain the isopycnal streamfunction, ψ_I,

$$\psi_I(y, b, t) = -\oint_x \int_{\eta_B}^{\eta} v \,\mathrm{d}z \,\mathrm{d}x, \tag{2.36}$$

and subsequently interpolate the isopycnal streamfunction back to height coordinates. Here η_B denotes the ocean bottom, and ψ_I expresses the instantaneous southward transport of fluid

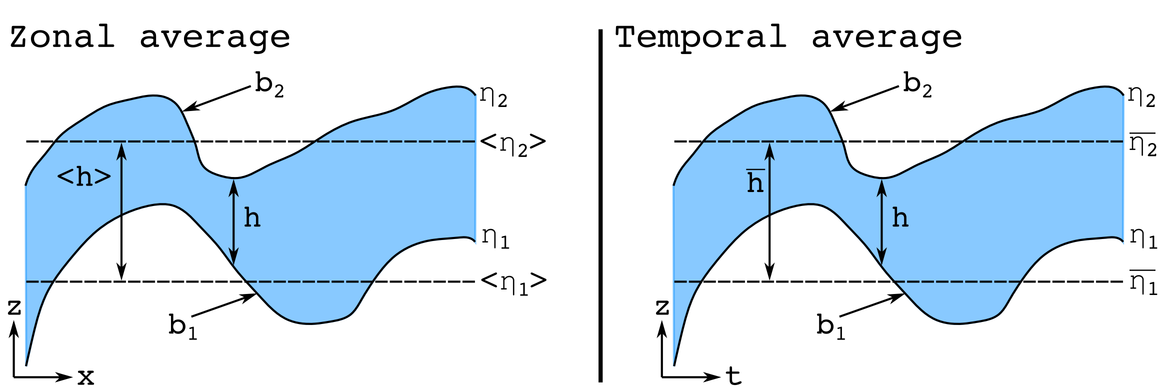

Figure 2.2: Schematic of isopycnal averaging for the zonal average case (left) and temporal average case (right). The height of the two isopycnals, η_1 and η_2, with value b_1 and b_2, are depicted by the solid black wavy lines. Their average height is indicated by the dashed black lines. This schematic is a combination of the schematics shown in McIntosh and McDougall (1996); McDougall and McIntosh (2001); Vallis (2006).

at latitude y below an isopycnal of value b with height $\eta(x, y, t)$. A good example of the latter case for the overturning in the Southern Ocean is shown in Döös and Webb (1994).

2.2.3 Temporal residual-mean velocity

While the transformed Eulerian mean provides a theory for the zonally-averaged circulation, it is desirable to construct a theory for the time-averaged three-dimensional flow to guide parameterization of the time-averaged eddy effect on the mean circulation. This problem was addressed by McDougall and McIntosh (1996, 2001) who developed the temporal residual-mean velocity, which is analog to the residual-mean velocity appropriate to the zonally-averaged ocean but here developed for the time-averaged ocean circulation instead. Starting in a similar manner as before, McDougall and McIntosh (2001) consider the horizontal transport between two density surfaces, η_1 and η_2,

$$\mathbf{T} = \int_{\overline{\eta_1}+\eta_1'}^{\overline{\eta_2}+\eta_2'} \mathbf{u}(x, y, z, t)\,\mathrm{d}z, \tag{2.37}$$

where the instantaneous surfaces of constant density have been split into its time-mean position, $\overline{\eta}$, and its temporal fluctuation about it, η' (See right panel of Figure 2.2 for a schematic of the two isopycnals). Following the same procedure as before, McDougall and McIntosh (2001) find that the time-averaged thickness-weighted velocity between the two isopycnal surfaces is

$$\frac{\overline{\mathbf{u}h}}{\overline{h}} = \overline{\mathbf{u}} + \frac{\partial \boldsymbol{\psi}_{\mathrm{qs}}}{\partial z}, \tag{2.38}$$

in the limit where $\eta_1 \to \eta_2$. As before, the time-average on the left hand side is evaluated following the vertical excursions of the isopycnal with time-mean height $\overline{\eta}$, whereas the time-average on the right hand side is evaluated at the fixed depth $\overline{\eta}$. The sum of the two terms on the right hand side is the horizontal component of the *temporal residual-mean velocity*,

$$\mathbf{u}_{\mathrm{trm}} = \overline{\mathbf{u}} + \frac{\partial \boldsymbol{\psi}_{\mathrm{qs}}}{\partial z}, \tag{2.39}$$

and $\boldsymbol{\psi}_{\mathrm{qs}}$ is the quasi-stokes streamfunction,

$$\boldsymbol{\psi}_{\mathrm{qs}} \equiv \overline{\int_{\overline{\eta}}^{\overline{\eta}+\eta'} \mathbf{u}\,\mathrm{d}z} \approx -\frac{\overline{\mathbf{u}'b'}}{\overline{b}_z} + \frac{\overline{\mathbf{u}}_z}{\overline{b}_z}\left(\frac{\overline{\Phi}}{\overline{b}_z}\right), \tag{2.40}$$

where $\overline{\Phi} = \overline{b'b'}/2$ is the eddy buoyancy variance. The first term in eq. (2.40) also appears in the streamfunction for the eddy-induced circulation in the zonally-averaged case, eq. (2.17), and hence it is seen that the quasi-stokes streamfunction advocates for an additional term in the eddy-induced circulation in the time-averaged case. Similar to the residual-mean velocity in the zonally-averaged case, the temporal residual-mean velocity is equivalent to the thickness-weighted time-mean velocity in density space. Importantly, McDougall and McIntosh (2001) show that the buoyancy of the isopycnal with time-mean height $\overline{\eta}$ relates to the time-mean buoyancy at fixed depth via

$$\tilde{b} = \overline{b} - \frac{\partial}{\partial z}\left(\frac{\overline{\Phi}}{\overline{b}_z}\right), \tag{2.41}$$

and that the three-dimensional temporal residual mean velocity, $\mathbf{v}_{\mathrm{trm}}$, has no component through $\tilde{b}$ surfaces,

$$\frac{\partial \tilde{b}}{\partial t} + \nabla \cdot \left(\mathbf{v}_{\mathrm{trm}} \tilde{b}\right) = 0, \tag{2.42}$$

when the flow is adiabatic. This property of the temporal residual-mean velocity is similar to the residual-mean velocity in the zonally-averaged case, eq. (2.20), when $\mathcal{B} = 0$.

In general the time-averaged transport of fluid below a density surface $\eta = \overline{\eta} + \eta'$ is

$$\overline{\int_{\eta_B}^{\eta} \mathbf{u}\,\mathrm{d}z} = \int_{\eta_B}^{\overline{\eta}} \overline{\mathbf{u}}\,\mathrm{d}z + \overline{\int_{\overline{\eta}}^{\overline{\eta}+\eta'} \mathbf{u}\,\mathrm{d}z}, \tag{2.43}$$

where the last term is the quasi-stokes streamfunction. This expression for the transport can be used together with the isopycnal streamfunction, eq. (2.36), to express the time-averaged isopycnal streamfunction for the meridional circulation as (Viebahn and Eden, 2012),

$$\overline{\psi_I}(y,b) = -\overline{\oint_x \int_{\eta_B}^{\eta} v\,\mathrm{d}z\,\mathrm{d}x} = -\oint_x \overline{\int_{\eta_B}^{\eta} v\,\mathrm{d}z}\,\mathrm{d}x = -\oint_x \int_{\eta_B}^{\overline{\eta}} \overline{v}\,\mathrm{d}z\,\mathrm{d}x - \overline{\oint_x \int_{\overline{\eta}}^{\overline{\eta}+\eta'} v\,\mathrm{d}z\,\mathrm{d}x} = \Psi_I + \psi_I^*. \tag{2.44}$$

Here

$$\Psi_I(y,b) = -\oint_x \int_{\eta_B}^{\overline{\eta}} \overline{v}\,\mathrm{d}z\,\mathrm{d}x \tag{2.45}$$

expresses the southward transport associated with the time-mean velocity field below the time-mean density surface $\overline{\eta}$ of value b, which according to eq. (2.36) also includes the transport due to stationary excursions in the flow-field in the zonal direction, and

$$\psi_I^*(y,b) = -\overline{\oint_x \int_{\overline{\eta}}^{\overline{\eta}+\eta'} v\,\mathrm{d}z\,\mathrm{d}x} \tag{2.46}$$

is the time-mean southward transport below the density surface b of time-mean height $\overline{\eta}$ due to temporal fluctuations of the density surface, η', because of the presence of transient eddies. The time-averaged isopycnal streamfunction, $\overline{\psi_I}$, and its decomposition into Ψ_I and ψ_I^*, is explored in Chapter 4 where the representation of transient eddies in coarse resolution ocean models is discussed.

2.2.4 Eliassen-Palm flux tensor

In the zonal- and time-mean residual-mean framework by Marshall and Radko (2003), the zonal momentum balance, eq. (2.26), was subject to an eddy force in the form of a vertical divergence of an eddy form stress,

$$\frac{\partial}{\partial z}\left(\frac{f_0}{\mathcal{N}_0^2}\left\langle\overline{b'v'}\right\rangle\right), \tag{2.47}$$

and eddy forcing due to eddy Reynolds stresses was neglected on the basis of observational estimates, such as those presented in Gille (2003). To better appreciate the full eddy force in the residual-mean framework, this section provides a more general view based on the divergence of the so-called Eliassen-Palm flux tensor. The discussion of this forcing tensor is based on the time-averaged quasi-geostrophic equations to favor a more simple mathematical framework.

Following Maddison and Marshall (2013), combining the quasi-geostrophic momentum and thermodynamic equations, eq. (2.4a) and (2.4c), into one single vector equation yields the quasi-geostrophic induction equation,

$$\frac{\partial \mathbf{D}}{\partial t} + (\mathbf{u}_g \cdot \nabla)\,\mathbf{D} + f_0 \mathbf{u}_{ag} + \beta y \mathbf{u}_g = \frac{\mathbf{k} \times \nabla p_{ag}}{\rho_0} + \mathbf{G}, \tag{2.48}$$

where $\mathbf{D}$ is the induction vector,

$$\mathbf{D} = \begin{bmatrix} v_g, & -u_g, & \frac{f_0}{\mathcal{N}_0^2} b \end{bmatrix}^T, \tag{2.49}$$

and $\mathbf{G}$ is the combined external forcing vector. The quasi-geostrophic induction equation is a compact representation of the quasi-geostrophic set of equations; the momentum equation is retrieved via $\mathbf{k} \times$ (2.48), the thermodynamic equation via $\mathcal{N}_0^2/f_0 \mathbf{k} \cdot$ (2.48), and the quasi-geostrophic potential vorticity equation follows from $\nabla \cdot$ (2.48). The latter equation, in the limit of vanishing forcing, is

$$\frac{\partial q}{\partial t} + \mathbf{u}_g \cdot \nabla q = 0, \tag{2.50}$$

where q is the quasi-geostrophic potential vorticity,

$$q = \zeta + \beta y + \frac{\partial}{\partial z}\left(\frac{f_0}{\mathcal{N}_0^2} b\right), \tag{2.51}$$

and $\zeta = \partial v_g/\partial x - \partial u_g/\partial y$.

The time-averaged induction equation is

$$\frac{\partial \overline{\mathbf{D}}}{\partial t} + (\overline{\mathbf{u}_g} \cdot \nabla)\,\overline{\mathbf{D}} + f_0 \overline{\mathbf{u}_{ag}} + \beta y \overline{\mathbf{u}_g} = \frac{\mathbf{k} \times \nabla \overline{p_{ag}}}{\rho_0} + \overline{\mathbf{G}} - \nabla \cdot \mathsf{T} \tag{2.52}$$

where

$$\mathsf{T} = \begin{bmatrix} N & M-K & R \\ M+K & -N & S \\ 0 & 0 & 0 \end{bmatrix} \tag{2.53}$$

is the eddy induction tensor and holds the eddy correlation terms. Specifically, M and N are the Reynolds stresses,

$$M = \frac{\overline{v_g' v_g'} - \overline{u_g' u_g'}}{2}, \quad N = \overline{u_g' v_g'}, \tag{2.54}$$

R and S are the eddy interfacial form stresses,

$$R = \frac{f_0}{\mathcal{N}_0^2}\overline{b' u_g'}, \quad S = \frac{f_0}{\mathcal{N}_0^2}\overline{b' v_g'}, \tag{2.55}$$

and K is the eddy kinetic energy,

$$K = \frac{\overline{u_g' u_g'} + \overline{v_g' v_g'}}{2}. \tag{2.56}$$

Since the potential vorticity equation is reached through the divergence of the induction equation, the eddy forcing in the time-averaged quasi-geostrophic potential vorticity equation is expressed by the double divergence of $\mathbf{T}$. As $\nabla \cdot (\nabla \cdot \mathbf{A}) = 0$, where $\mathbf{A}$ is any anti-symmetric tensor, the eddy forcing is equivalently expressed by $\nabla \cdot [\nabla \cdot (\mathbf{T} + \mathbf{A})]$, and hence $\mathbf{A}$ constitutes a gauge freedom. Specifically, as shown in Maddison and Marshall (2013), one may choose $\mathbf{A}$ such that

$$\mathbf{T}_R = \mathbf{T} + \mathbf{A} = \begin{bmatrix} N & M - K & 0 \\ M + K & -N & 0 \\ R & S & 0 \end{bmatrix}, \tag{2.57}$$

where the eddy form stresses, R and S, have been moved to the momentum equation. This gauge choice then takes the quasi-geostrophic equations to their residual-mean form in which the thermodynamic equation is devoid from eddy buoyancy fluxes. The eddy force in the momentum equation is $\mathbf{k} \times (\nabla \cdot \mathbf{T}_R) = \nabla \cdot \mathbf{E}$, where $\mathbf{E}$ is the residual-mean form of the quasi-geostrophic Eliassen-Palm flux tensor,

$$\mathbf{E} = \begin{bmatrix} -M + K & N & 0 \\ N & M + K & 0 \\ -S & R & 0 \end{bmatrix}. \tag{2.58}$$

A related form of this tensor has previously been derived and discussed in Cronin (1996). In the zonal average, the zonal eddy force in the residual-mean formulation is

$$\langle -\mathbf{i} \cdot (\nabla \cdot \mathbf{E}) \rangle = -\frac{\partial \langle N \rangle}{\partial y} + \frac{\partial \langle S \rangle}{\partial z} = -\frac{\partial}{\partial y} \left(\langle \overline{u_g' v_g'} \rangle \right) + \frac{\partial}{\partial z} \left(\frac{f_0}{\mathcal{N}_0^2} \langle \overline{b' v_g'} \rangle \right). \tag{2.59}$$

This expression states that the zonally-averaged zonal flow accelerates if there exists a meridional convergence of the meridional eddy flux of zonal momentum and/or if there exists a vertical convergence in the zonal eddy form stress. A conceptual schematic of the implied eddy-mean flow interaction is shown in Figure 5.1, and the eddy form stress holds particular focus in Chapter 5.

2.2.5 Geometry of the Eliassen-Palm flux tensor

In Marshall et al. (2012) it is shown that the magnitudes of the eddy Reynolds stress and eddy form stress are bounded in terms of the available eddy energy according to

$$M^2 + N^2 \leq K^2 \tag{2.60a}$$

$$R^2 + S^2 \leq 4\frac{f_0^2}{\mathcal{N}_0^2} K P, \tag{2.60b}$$

where P is the quasi-geostrophic eddy potential energy,

$$P = \frac{\overline{b'b'}}{2\mathcal{N}_0^2}. \tag{2.61}$$

These energetic bounds combine to form a norm of the eddy stress tensor, (2.58), which shows that the overall stress magnitude is bounded by an expression for the total energy,

$$2(M^2 + N^2 + K^2) + R^2 + S^2 \leq 4L^2, \tag{2.62}$$

where L is a weighted expression for the total eddy energy,

$$L = K + \frac{f_0^2}{\mathcal{N}_0^2}P. \tag{2.63}$$

In particular, the eddy stress bounds, (2.60a) and (2.60b), can be used to express the stress magnitude in terms of L,

$$\sqrt{M^2 + N^2} = \gamma_m K = \gamma_m L \cos^2(\lambda^*) \tag{2.64a}$$

$$\sqrt{R^2 + S^2} = \gamma_b 2\frac{f_0}{\mathcal{N}_0}\sqrt{KP} = \gamma_b L \sin(2\lambda^*), \tag{2.64b}$$

where

$$\gamma_m = \frac{\sqrt{M^2 + N^2}}{K}, \quad \gamma_b = \frac{\mathcal{N}_0}{2f_0}\sqrt{\frac{R^2 + S^2}{KP}} \tag{2.65}$$

are the momentum and buoyancy anisotropies, which follow from the energetic stress bounds and are bounded between zero and unity. λ^* is an angle bounded according to $0 \leq \lambda^* \leq \pi/2$ and determines the partitioning of energy between eddy kinetic energy and scaled eddy potential energy,

$$\frac{K}{L} = \cos^2(\lambda^*), \quad \frac{f_0^2}{\mathcal{N}_0^2}\frac{P}{L} = \sin^2(\lambda^*). \tag{2.66}$$

Furthermore, one may define two angles, ϕ_m and ϕ_b, which determine the horizontal orientation of the Reynolds stress,

$$\cos(2\phi_m) = -\frac{M}{\sqrt{M^2 + N^2}}, \quad \sin(2\phi_m) = \frac{N}{\sqrt{M^2 + N^2}} \tag{2.67}$$

and the form stress,

$$\cos(\phi_b) = \frac{R}{\sqrt{R^2 + S^2}}, \quad \sin(\phi_b) = \frac{S}{\sqrt{R^2 + S^2}}, \tag{2.68}$$

with respect to the zonal direction. The factor of two which appears in the expression for the eddy momentum flux angle, ϕ_m, is motivated by the π symmetry between M and N. That is, N transforms to M when the eddy momentum flux is examined in a coordinate system rotated by $\pi/4$ (see Fig. 2 in Tamarin et al., 2016, for an illustration of this property).

The virtue of deriving the energetic bounds and defining the eddy angles is that one may express the eddy stresses, M, N, R and S, in terms of L and five bounded dimensionless geometric parameters, namely the two anisotropies, γ_m and γ_b, and the three angles, λ^*, ϕ_m and ϕ_b. While the definitions of the angles may seem arbitrary, as will be shown in Chapter 5, the geometry thus defined is related to the geometry of variance ellipses. Notably, the size, shape and orientation of these ellipses with respect to the mean-flow circulation constitute a tool to diagnose its stability. The idea of exploiting the eddy geometry to understand eddy-mean flow interaction has already been used in the past for eddy momentum fluxes (e.g. Hoskins et al., 1983; Morrow et al., 1994; Waterman and Lilly, 2015), but the eddy form stress geometry has not previously been explored. The potential to gain insight into eddy buoyancy fluxes via the geometry is discussed in Chapter 5.

2.3 Parameterizing the effect of baroclinic mesoscale eddies

In the context of geophysical fluid dynamics, a parameterization is a representation of a small-scale process in a physical system, for example the ocean, in terms of the large-scale physical properties of the system itself. A useful parameterization thus relies on the assumption that it is possible to relate the physics which unfold on the different spatial scales of the system. A particular demand for parameterizations is found in the ocean modeling community, which is forced to settle on some finite model grid resolution which matches their available computing resources. Most numerical ocean models are therefore unable to explicitly resolve all relevant physical processes which ideally should be present in the model, and hence, from the perspective of an ocean modeler, "small-scale" typically refers to the unresolved subgrid-scale in the model. Since the common horizontal grid resolution of ocean general circulation models is about $1^\circ \times 1^\circ$, the subgrid-scale includes processes which operate on a characteristic length scale of about a couple of hundreds of kilometers and smaller. Examples of such unresolved processes are internal wave breaking, various types of fluid instabilities (convective, barotropic, baroclinic) and the effect on tracers of the presence of turbulence on the mesoscale.

From a practical perspective, scientists are interested in developing parameterizations for use in coarse resolution ocean general circulation models in order to improve simulations of the present-day ocean mean-state, as well as increase the fidelity in projections of future ocean states. The advance of available computer power allows ocean models of increasingly fine resolution to be used (see e.g. Arbic et al., 2012; Bryan et al., 2014; Bishop et al., 2016; Hogg et al., 2017) and arguably eliminates the need for parameterizations at some point in the future. Paleoclimate model studies, on the other hand, especially those targeted at modeling Dansgaard-Oeschger events or glacial-interglacial transitions (see e.g. Jochum et al., 2012; Peltier and Vettoretti, 2014; Kleppin et al., 2015), require that it is possible to integrate coupled general circulation models forward for thousands of model years on a reasonable human time scale. Hence where finer model resolution supersedes the need for parameterizations due to increased computer power, the emergent possibility to forward integrate coarse resolution models for unprecedented time pushes the need for accurate representations of the subgrid-scale physics.

From a theoretical perspective, parameterizations also constitute a key element in formulating closed problems. In the transformed Eulerian mean framework previously discussed, as an example, one is often faced with more unknowns than equations and is forced to parameterize unknowns in terms of the other system variables to enable further progress. In Marshall and Radko (2003), for example, a closure for the meridional eddy buoyancy flux, $\langle \overline{b'v'} \rangle$, was required to close the governing set of equations and seek solutions. The ability of simple analytical models of the ocean circulation to represent the main features of more complex models, such as general circulation models, thus constitute a measure of the quality of the employed parameterizations and the physical assumptions upon which they rest.

The present dissertation is concerned with processes related to the presence of baroclinic mesoscale eddies in the interior ocean, which themselves arise due to baroclinic instability. Fundamentally, this fluid instability is associated with a transfer of available potential energy to eddy kinetic energy (Lorenz, 1955; Pedlosky, 1987; Vallis, 2006; Storch et al., 2012). Baroclinic instability is normally treated within the framework of the linearized quasi-geostrophic equations, and probably the most simple physical account of the instability is provided by the analytical model of Eady (1949). A necessary criterion for baroclinic instability is the presence of a vertical velocity shear, which through thermal wind balance is associated with tilted isopycnals. If a stably stratified ocean with zero horizontal density gradient defines a reference state of minimum potential energy, then regions of tilted isopycnals are characterized by an upward vertical displacement of the local center of mass and hence available potential energy. Since baroclinic instability constitutes a sink of potential energy, the presence of this type of fluid instability reduces the isopycnal slope and the vertical shear in the horizontal velocity. In the model by Eady, which among other simplifications assumes a constant vertical velocity shear of magnitude Λ, a characteristic measure of the instability growth rate,

$$\sigma = \frac{\Lambda H}{L_d}, \tag{2.69}$$

appears in the analytical solution. Here H is the characteristic depth of the system, hence $\Lambda H = U$ where U is the characteristic zonal velocity, and L_d is the baroclinic deformation radius. The most unstable configuration of the Eady model is for an initial perturbation of characteristic wavelength $3.9L_d$, hence for an appropriate choice of L_d and U one finds that the strongest instability occurs on a characteristic length scale of $\sim 100\,\mathrm{km}$ and on a time scale of about a month. Although a crude approximation to the real ocean, this simple analytical model suggests that numerical ocean models of coarse resolution are unable to explicitly represent the full extent of this natural sink of available potential energy, with implication for the ocean stratification and circulation.

Motivated by mixing length theory (Prandtl, 1925), the fundamental assumption which underlies most parameterizations of processes related to mesoscale eddies is that the averaged eddy effect behaves similarly to molecular diffusion i.e. that an averaged eddy flux of a tracer τ, $\mathbf{F} = \overline{\tau'\mathbf{v}'}$, can be parameterized according to

$$\mathbf{F} = -\mathsf{K}\nabla\overline{\tau}, \tag{2.70}$$

where K is a diffusivity tensor of rank two. In terms of the prognostic equation for $\overline{\tau}$, this parameterization implies

$$\frac{\partial \overline{\tau}}{\partial t} + \overline{\mathbf{v}} \cdot \nabla \overline{\tau} = -\nabla \cdot \overline{\tau' \mathbf{v}'} = \nabla \cdot (\mathsf{K} \nabla \overline{\tau}) \,. \tag{2.71}$$

For the following discussion it is instructive to divide K into a symmetric contribution, S, and an anti-symmetric, A,

$$\mathsf{K} = \mathsf{S} + \mathsf{A}, \tag{2.72}$$

where

$$\mathsf{S} = \frac{1}{2} \left(\mathsf{K} + \mathsf{K}^T \right) \tag{2.73}$$

$$\mathsf{A} = \frac{1}{2} \left(\mathsf{K} - \mathsf{K}^T \right), \tag{2.74}$$

because S and A describe two different types of diffusion. The diffusive flux of any tracer τ associated with A, which we henceforth denote $\mathbf{F}_A$, is perpendicular to its large-scale gradient $\nabla \overline{\tau}$,

$$\mathbf{F}_A \cdot \nabla \overline{\tau} = - \left(\mathsf{A} \nabla \overline{\tau} \right) \cdot \nabla \overline{\tau} = 0. \tag{2.75}$$

That is, $\mathbf{F}_A$ is skew with respect to $\nabla \overline{\tau}$. The same is generally not true for the symmetric tensor S,

$$\mathbf{F}_S \cdot \nabla \overline{\tau} = - \left(\mathsf{S} \nabla \overline{\tau} \right) \cdot \nabla \overline{\tau}, \tag{2.76}$$

where $\mathbf{F}_S = - \left(\mathsf{S} \nabla \overline{\tau} \right)$. Isotropic diffusion, for example, described by S with some diffusivity magnitude K on the diagonal, has $\mathbf{F}_S \cdot \nabla \overline{\tau} = -K |\nabla \overline{\tau}|^2 < 0$ i.e. the diffusion is directed down the mean tracer gradient as long as $K > 0$.

One effect related to the presence of mesoscale eddies which requires parameterization is eddy mixing of tracers. Given the adiabatic nature of the interior ocean, it is commonly assumed that this process takes place along neutral surfaces, which often are approximated by potential density surfaces. Thus, in the context of the discussion above, this suggests that one may parameterize this process by a down-gradient diffusion of tracers along isopycnal surfaces through an appropriate formulation of S (see left panel of Figure 2.3 for a visualization). A mixing parameterization of this type was first discussed by Redi (1982), who suggested a symmetric diffusion tensor on a similar form as

$$\mathsf{S}_{\mathrm{Redi}} = \mu \begin{bmatrix} 1 & 0 & s_x \\ 0 & 1 & s_y \\ s_x & s_y & |\mathbf{s}|^2 \end{bmatrix}. \tag{2.77}$$

Here $\mathbf{s} = (s_x, s_y)$ is the isopycnal slope vector,

$$\mathbf{s} = -\nabla_h \overline{b} / \frac{\partial \overline{b}}{\partial z}, \tag{2.78}$$

μ is the tracer diffusivity, and $\mathsf{S}_{\mathrm{Redi}}$ is here presented in the weak isopycnal slope limit with no cross-isopycnal diffusion. Diffusion of tracers associated with $\mathsf{S}_{\mathrm{Redi}}$ is often referred to as isopycnal diffusion, or Redi-diffusion, and reduces to simple horizontal diffusion when $\mathbf{s} = \mathbf{0}$.

Like mixing, down-gradient diffusion of this type is inherently variance-dissipating and will evolve towards an alignment of iso-surfaces of a given tracer with interior ocean isopycnals. The implementation of isopycnal diffusion in a numerical ocean model requires the specification of the tracer diffusivity, μ, and will be discussed in section 2.3.3.

Another important eddy effect is the sink of available potential energy due to baroclinic instability. An influential study which addressed this problem was that by Gent and McWilliams (1990), which introduces what today is known as the Gent-McWilliams parameterization. In combination with the follow-up paper by Gent et al. (1995), they show that a parameterization of baroclinic instability via down-gradient diffusion of isopycnal thickness results in several desirable properties. This parameterization is explained in detail in the following subsection, but with the alternative approach taken in Griffies (1998), which offers a more transparent derivation in terms of a skew-diffusive flux.

2.3.1 Gent-McWilliams parameterization

Gent and McWilliams (1990) draws on the earlier result by Redi (1982) and hence provide a more complete description on how ocean mesoscale eddies should be represented in coarse resolution ocean models. In addition to the properties already provided by isopycnal diffusion via $\mathbf{S}_{\text{Redi}}$, Gent and McWilliams (1990) identify that eddy tracer fluxes, especially those of salt and temperature, must be implemented in a way to ensure a sink of available potential energy while the domain-averaged moments of buoyancy are conserved. The latter constraint follows

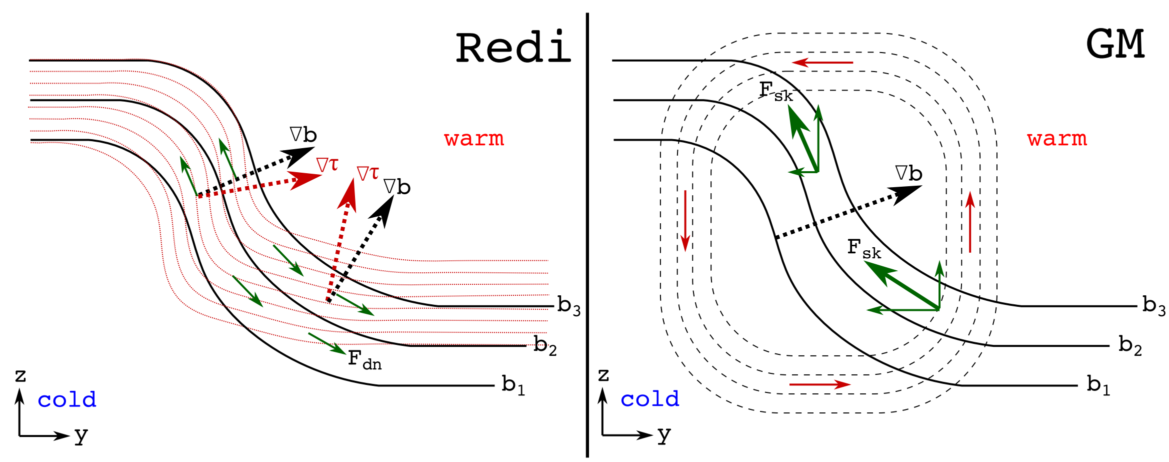

Figure 2.3: Conceptual visualization of isopycnal/Redi diffusion (left) and Gent-McWilliams eddy stirring (right) for an idealized two-dimensional ocean front in the meridional y-z plane. The solid black lines, b_1, b_2 and b_3, are buoyancy contours and the dashed black arrows indicate the buoyancy gradient, ∇b. The red dotted lines in the left panel are concentration contours of an arbitrary passive tracer, τ, and the red arrows indicate the direction of the tracer gradient, $\nabla \tau$. The green arrows in the left panel indicate the direction of the diffusive tracer flux, F_{dn}, which is down the tracer gradient along neutral surfaces. The thick green arrow in the right panel is the diffusive flux of buoyancy, F_{sk}, which is skew with respect to the buoyancy gradient and is constructed such that the meridional component is down-gradient and the vertical component is up-gradient (thin green arrows). The black dashed lines are the contours of the streamfunction associated with the eddy-induced velocity (red arrows), which, equivalent to the skew flux, flattens the buoyancy surfaces. This figure is drawn with inspiration from Gent et al. (1995), Griffies (1998) and Vallis (2006).

from the adiabatic property of the ocean and is naturally achieved through skew-diffusion as this type of diffusion preserves the system-integrated variance of the tracer in consideration. Moreover, since the tracer flux is perpendicular to its gradient, the volume of water of each density class is also preserved.

In order to construct a skew tracer-diffusion which provides a sink of available potential energy, Griffies (1998) notes that one may exploit a simplifying gauge freedom in the specification of A. This gauge freedom emerges because it is the flux divergence which is dynamically relevant for the tracer equation (2.71) and not the flux itself. That is,

$$-\nabla \cdot \mathbf{F}_A = \nabla \cdot (\mathsf{A}\nabla\overline{\tau}) = \nabla \cdot ([\mathsf{A} + \mathsf{B}]\, \nabla\overline{\tau})\,, \tag{2.79}$$

where $\nabla \cdot (\mathsf{B}\nabla\overline{\tau}) = 0$, which is satisfied as long as B is anti-symmetric and $\nabla \cdot \mathsf{B} = \mathbf{0}$. Griffies (1998) exploits this degree of freedom to express

$$\mathsf{A}' = \mathsf{A} + \mathsf{B} = \begin{bmatrix} 0 & 0 & -K_x \\ 0 & 0 & -K_y \\ K_x & K_y & 0 \end{bmatrix}. \tag{2.80}$$

The key step in the Gent-McWilliams parameterization is to let the diffusivity depend on the isopycnal slope,

$$\begin{bmatrix} K_x \\ K_y \end{bmatrix} = \kappa \begin{bmatrix} s_x \\ s_y \end{bmatrix} = \kappa \mathbf{s}, \tag{2.81}$$

which imply that

$$\mathsf{A}' = \mathsf{A}_{\mathrm{GM}} = \kappa \begin{bmatrix} 0 & 0 & -s_x \\ 0 & 0 & -s_y \\ s_x & s_y & 0 \end{bmatrix}. \tag{2.82}$$

Here κ is an eddy transfer coefficient to be determined (see the discussion in Section 2.3.3). The consequence of this scheme on the eddy buoyancy flux, $F = -\mathsf{A}_{\mathrm{GM}}\nabla\overline{b}$, is

$$\overline{b'\mathbf{u}'} = -\kappa\nabla_h\overline{b} \quad \text{and} \quad \overline{b'w'} = \kappa|\mathbf{s}|^2\frac{\partial\overline{b}}{\partial z}, \tag{2.83}$$

i.e. a down-gradient flux in the horizontal direction and an up-gradient flux in the vertical direction if $\kappa > 0$, which in combination is skewed with respect to the isopycnal slope (see right panel of Figure 2.3). This specific orientation of the skew flux ensures that potential energy is lost from the system via a flattening of the isopycnals and hence mimics the desired property of baroclinic instability (Gent et al., 1995). Equivalently, provided that the circulation is in thermal wind balance, Greatbatch and Lamb (1990) show that one can arrive at the same property by adding vertical mixing of horizontal momentum to the horizontal momentum equation.

The Gent-McWilliams parameterization is often discussed in terms of its alternative interpretation as an eddy-induced velocity, and this is also the case in the present dissertation. Therefore, consider a tracer advection by the divergence-free velocity field $\mathbf{v}^*$,

$$\mathbf{v}^* \cdot \nabla\overline{\tau} = \nabla \cdot (\mathbf{v}^*\overline{\tau}) \tag{2.84}$$

where $\mathbf{v}^*\overline{\tau}$ is an advective flux. Since $\nabla \cdot \mathbf{v}^* = 0$ by definition, $\mathbf{v}^*$ can be represented by a vector streamfunction $\boldsymbol{\psi}^*$,

$$\mathbf{v}^* = \nabla \times \boldsymbol{\psi}^*. \tag{2.85}$$

Because the flux may be expanded in terms of the streamfunction,

$$\mathbf{v}^*\overline{\tau} = (\nabla \times \boldsymbol{\psi}^*)\,\overline{\tau} = \boldsymbol{\psi}^* \times \nabla\overline{\tau} + \nabla \times (\boldsymbol{\psi}^*\overline{\tau})\,, \tag{2.86}$$

it is seen that the advective flux consists of a component perpendicular to $\nabla\overline{\tau}$, similar to the skew diffusion given by A_{GM}, and a purely rotational component with no divergence. The advective flux by the divergence-free velocity $\mathbf{v}^*$ and the skew-diffusive flux provided by A_{GM} are thus related via the divergence,

$$\nabla \cdot (\mathbf{v}^*\overline{\tau}) = \nabla \cdot (\boldsymbol{\psi}^* \times \nabla\overline{\tau}) = -\nabla \cdot (\mathsf{A}_{\mathrm{GM}}\nabla\overline{\tau})\,. \tag{2.87}$$

Griffies (1998) demonstrates that

$$\mathbf{v}^* = -\nabla \cdot \mathsf{A}_{\mathrm{GM}} \tag{2.88}$$

which results in

$$\mathbf{u}^* = -\frac{\partial \boldsymbol{\psi}^*_{\mathrm{GM}}}{\partial z} \quad \text{and} \quad w^* = \nabla_h \cdot \boldsymbol{\psi}^*_{\mathrm{GM}}, \tag{2.89}$$

where $\boldsymbol{\psi}^*_{\mathrm{GM}} = \kappa\mathbf{s}$ is the two-dimensional streamfunction of the circulation induced by the parameterized eddies. Hence the eddy-induced velocity provides an alternative view to the skew flux; the eddy-induced advection of tracers is oriented such that it weakens the isopycnal slope and removes potential energy from the system (see right panel of Figure 2.3). The eddy-induced velocity also constitutes an alternative way to implement the Gent-McWilliams parameterization in ocean models; either one substitutes the eddy correlation term in the tracer equation with the skew-diffusive flux (together with the Redi-diffusion),

$$\frac{\partial\overline{\tau}}{\partial t} + \overline{\mathbf{v}} \cdot \nabla\overline{\tau} = -\nabla \cdot \overline{\tau'\mathbf{v}'} = \nabla \cdot \left([\mathsf{S}_{\mathrm{Redi}} + \mathsf{A}_{\mathrm{GM}}]\,\nabla\overline{\tau}\right), \tag{2.90}$$

or one adds the eddy-induced velocity to the Eulerian velocity field in the advective term in the tracer equation,

$$\frac{\partial\overline{\tau}}{\partial t} + (\overline{\mathbf{v}} + \mathbf{v}^*) \cdot \nabla\overline{\tau} = \nabla \cdot (\mathsf{S}_{\mathrm{Redi}}\nabla\overline{\tau})\,. \tag{2.91}$$

It is important to note that the Gent-McWilliams scheme solely applies to the tracer equation and hence does not provide a resolution to the closure for eddy momentum fluxes. In terms of the eddy-induced velocity, this expresses an inconsistency as tracers are advected by the residual velocity, $\mathbf{v}_{\mathrm{res}} = \mathbf{v} + \mathbf{v}^*$, but momentum only by the Eulerian velocity field, $\mathbf{v}$. A discussion on this issue can be found in, for example, Ringler and Gent (2011).

2.3.2 Gent-McWilliams and the quasi-stokes velocity

Since coarse resolution models do no resolve mesoscale eddies, one may interpret the coarse model's resolved velocity field in the tracer equation as the Eulerian time-mean velocity, $\overline{\mathbf{v}}$, i.e. a low-pass filtered velocity field. Moreover, as seen from the preceding section, the Gent-

McWilliams scheme can be interpreted as a parameterization of the eddy-induced circulation in the context of the residual-mean velocity. Thus, one can view $\boldsymbol{\psi}^*_{\mathrm{GM}} = \kappa \mathbf{s}$ as a parameterization of the quasi-stokes streamfunction, eq. (2.40), by McDougall and McIntosh (2001),

$$\boldsymbol{\psi}_{\mathrm{qs}} \approx \kappa \tilde{\mathbf{s}}, \tag{2.92}$$

where $\tilde{\mathbf{s}}$ is the isopycnal slope vector but expressed in the modified buoyancy variable $\tilde{b}$, eq. (2.41) (McDougall et al., 2007). Both $\boldsymbol{\psi}_{\mathrm{qs}}$ and $\boldsymbol{\psi}^*_{\mathrm{GM}}$ share the same property that they describe a velocity field which generally has a component across buoyancy surfaces, but, when combined with the Eulerian time-mean velocity field, provides a residual circulation which is along buoyancy surfaces. In order to evaluate the skill of parameterizing eddies with $\boldsymbol{\psi}^*_{\mathrm{GM}}$ in coarse ocean models, one may compare the parameterized circulation to the isopycnal streamfunction of the quasi-stokes circulation in an eddying model, ψ^*_I, given by eq. (2.46). Following Hirst and McDougall (1998) and Spence et al. (2009), one may obtain the isopycnal streamfunction of the parameterized eddy-induced circulation via

$$\psi^*_{I,\mathrm{GM}}(y,b) = -\overline{\oint_x \int_{\eta_B}^{\eta} v_{\mathrm{GM}}\, \mathrm{d}z\, \mathrm{d}x}, \tag{2.93}$$

where v_{GM} is the meridional velocity of the Gent-McWilliams parameterization. Here time-averaging is applied as the last operation, and hence this version of $\psi^*_{I,\mathrm{GM}}$ also contains circulation contributions due to temporal fluctuations of the eddy-induced velocity and density fields as function of, for example, the seasonal cycle and other low-frequency variability. Alternatively, to avoid these extra contributions which are not due to mesoscale eddy activity, one could apply the time-mean operator first.

In this thesis, no attempt is made to remove the seasonal cycle from the eddy-induced circulation and the isopycnal streamfunction for the residual circulation in a coarse model is computed and decomposed according to

$$\overline{\psi_I} = -\overline{\oint_x \int_{\eta_B}^{\eta} v + v_{\mathrm{GM}}\, \mathrm{d}z\mathrm{d}x} = \underbrace{-\overline{\oint_x \int_{\eta_B}^{\eta} v\, \mathrm{d}z\mathrm{d}x}}_{\Psi_I} \underbrace{-\overline{\oint_x \int_{\eta_B}^{\eta} v_{\mathrm{GM}}\, \mathrm{d}z\mathrm{d}x}}_{\psi^*_{I,\mathrm{GM}}}, \tag{2.94}$$

where $v + v_{\mathrm{GM}}$ is effective transport velocity in the coarse model and v is the resolved velocity field. The decision not to remove the seasonal cycle is motivated by the fact that those studies we desire to compare to in Chapter 4 also do not remove the seasonal cycle (e.g. Bishop et al., 2016), and also because it is difficult to make a clean separation between temporal variability due to mesoscale eddies and that due to the seasonal cycle. A discussion on the influence of the seasonal cycle on the eddy-induced overturning circulation is provided in Section 4.7.2.

2.3.3 Eddy transfer coefficient

The use of $\mathsf{S}_{\mathrm{Redi}}$ and A_{GM} in ocean general circulation models require a specification of μ and κ, respectively. Based on numerical float dispersion experiments, linear stability theory and inversions using eddying ocean models, it is today recognized that neither of these are constant

(Roberts and Marshall, 2000; Eden et al., 2007b; Griesel et al., 2010; Abernathey et al., 2010; Griesel et al., 2015). Moreover, a theory for κ should ideally include the possibility of a local negative diffusivity in order to support sharpening of ocean fronts. Several theories for κ have been proposed in the past, and those presented in Ferreira et al. (2005) and Marshall et al. (2012) are of special interest to the work presented in this dissertation.

In the study by Ferreira et al. (2005), an ocean model formulated in terms of the residual-mean velocity is used in combination with an adjoint optimization process to obtain the eddy buoyancy flux field which minimizes the model-observation discrepancy. The optimized eddy stress field was used to infer κ, which in the horizontal mean correlates with vertical variations in the stratification, $\mathcal{N}^2$, and prompted the authors to suggest that

$$\kappa_{\mathrm{FMH}} = \kappa_0 \frac{\mathcal{N}^2}{\mathcal{N}^2_{\mathrm{ref}}} \tag{2.95}$$

may constitute a useful parameterization for κ. Here κ_0 and $\mathcal{N}^2_{\mathrm{ref}}$ are reference values for the transfer coefficient and the vertical stratification, respectively. Some physical justification for κ_{FMH} is provided by mixing length theory if the mixing length is set equal to the baroclinic deformation radius, which scales with $\mathcal{N}$. An implementation of κ_{FMH}, as well as choices for κ_0 and $\mathcal{N}^2_{\mathrm{ref}}$, is discussed in Danabasoglu and Marshall (2007), which also report several model improvements when compared to the same model using a spatiotemporal constant value for κ.

Based on the geometry and energy of the eddy field, obtained through a reformulation of the Eliassen-Palm flux tensor (see Section 2.2.5), Marshall et al. (2012) suggest

$$\kappa_{\mathrm{MMB}} = \alpha E \frac{\mathcal{N}_0}{\mathcal{M}^2} \tag{2.96}$$

as an estimate for κ. Here α holds information on the eddy field geometry, E is the eddy energy and $\mathcal{M}^2 = |\nabla_h \overline{b}|$ is the horizontal stratification. α is theoretically bounded according to $|\alpha| \leq 1$, in contrast to the parameters involved in e.g. κ_{FMH}, and is the result of an energetic bound on the eddy flux. Hence κ_{MMB} is energetically consistent by construction, but requires a parameterization for both α and E. κ_{MMB} has recently been studied and implemented in idealized ocean models, which have shown promising representations of eddy saturation (Mak et al., 2017, 2018), a concept discussed in Section 2.4, and inferred diffusivity (Bachman et al., 2017). The idea of phrasing the problem of κ in terms of eddy energetics is not new and was already discussed by Eden and Greatbatch (2008), where mixing length theory was used to suggest

$$\kappa_{\mathrm{EG}} = L_e V_e = L_e \sqrt{K}. \tag{2.97}$$

Here L_e and V_e are the characteristic length and velocity associated with mesoscale eddies, and K is the eddy kinetic energy. Notably, a prognostic equation for K is provided in Eden and Greatbatch (2008).

A theory for the tracer diffusivity, μ, has received less attention in the scientific community. Often this parameter is set equal to κ or it is assigned a constant value (see e.g. Table 1 in Farneti et al., 2015). However, as discussed above, μ and κ are related to two different physical processes associated with mesoscale turbulence in the ocean, and hence it is not self-evident that $\mu = \kappa$. Assuming so, however, provides a computational simplification in numerical ocean models and a faster forward model integration (Griffies, 1998) which may explain the common use of $\mu = \kappa$ in the modeling community.

2.3.4 Rotational eddy buoyancy fluxes

As seen in equation (2.83), parameterizing the effect of baroclinic instability through skew-diffusion, together with the assumption presented in eq. (2.81), results in horizontally down-gradient eddy buoyancy fluxes if $\kappa > 0$. In general, however, we may write the horizontal eddy buoyancy flux as

$$\overline{b'\mathbf{u}'} = -\kappa\nabla_h\overline{b} - \nu\mathbf{k}\times\nabla_h\overline{b} + \mathbf{k}\times\nabla_h\chi_{\mathrm{rot}}, \tag{2.98}$$

which consists of, from left to right, a component along $\nabla\overline{b}$ which scales with κ, a component along $\overline{b}$-contours which scales with ν, and a horizontally divergence-free rotational component associated with the scalar potential χ_{rot}. The Gent-McWilliams scheme offers a parameterization for the along-gradient flux, but not for the along-contour component proportional to ν. Insight into the meaning of ν may be obtained by using the flux decomposition, eq. (2.98), in the averaged quasi-geostrophic buoyancy budget,

$$\frac{\partial\overline{b}}{\partial t} + \overline{\mathbf{u}}_g\cdot\nabla_h\overline{b} + \mathcal{N}_0^2\overline{w}_{\mathrm{ag}} = \overline{\mathcal{B}} - \nabla_h\cdot\overline{b'\mathbf{u}_g'}, \tag{2.99}$$

where one finds that

$$\frac{\partial\overline{b}}{\partial t} + \left(\overline{\mathbf{u}}_g + \mathbf{k}\times\nabla_h\nu\right)\cdot\nabla_h\overline{b} + \mathcal{N}_0^2\overline{w}_{\mathrm{ag}} = \overline{\mathcal{B}} + \nabla_h\cdot\left(\kappa\nabla_h\overline{b}\right). \tag{2.100}$$

The term related to κ here appears as horizontal diffusion of $\overline{b}$, as expected, whereas the term related to ν appears as horizontal advection of $\overline{b}$ by $\mathbf{k}\times\nabla_h\nu$, and hence ν can be interpreted as a streamfunction (Eden et al., 2007b). If advection by ν is important to the buoyancy budget, a complete parameterization for the horizontal eddy buoyancy flux must include the along-contour component of the flux. It is therefore natural to ask: to what extent are horizontal eddy buoyancy fluxes down-gradient, and is it appropriate to ignore the dynamical effect from along-contour fluxes?

One may therefore attempt to diagnose κ and ν in eddying ocean models to answer these questions, which has, for example, been the focus in the past studies by Roberts and Marshall (2000); Eden (2006); Eden et al. (2007b,a). Solving for κ and ν in eq. (2.98),

$$\kappa = -\left|\nabla_h\overline{b}\right|^{-2}\left(\overline{b'\mathbf{u}'} - \mathbf{k}\times\nabla_h\chi_{\mathrm{rot}}\right)\cdot\nabla_h\overline{b} \tag{2.101}$$

$$\nu = -\left|\nabla_h\overline{b}\right|^{-2}\left(\overline{b'\mathbf{u}'} - \mathbf{k}\times\nabla_h\chi_{\mathrm{rot}}\right)\cdot\left(\mathbf{k}\times\nabla_h\overline{b}\right), \tag{2.102}$$

however shows that this may be complicated by the presence of purely rotational horizontal fluxes, $\mathbf{k}\times\nabla_h\chi_{\mathrm{rot}}$, which do not influence the dynamics. Two approaches to estimate χ_{rot} and remove rotational fluxes are discussed in Chapter 5 of the present dissertation, but it is here appropriate to briefly discuss the physical interpretation of rotational fluxes by Marshall and Shutts (1981), which has influenced much of the succeeding literature on the topic. Specifically, Marshall and Shutts (1981) study the budget of eddy variance, $\overline{\Phi} = \overline{b'b'}/2$,

$$\frac{\partial \overline{\Phi}}{\partial t} + \nabla_h \cdot \overline{\mathbf{u}_g \Phi} + \overline{b'\mathbf{u}'_g} \cdot \nabla_h \bar{b} + \mathcal{N}^2 \overline{b' w'_{\mathrm{ag}}} = \overline{b'B'}, \tag{2.103}$$

which, in quasi-geostrophy, is the eddy potential energy budget. This budget is obtained by multiplying the Reynolds-decomposed buoyancy budget with b' and subsequently apply the averaging operator (2.7). The terms in eq. (2.103) are, from left to right, eddy variance tendency, horizontal advection of eddy variance, production of eddy variance, baroclinic conversion of eddy potential energy to eddy kinetic energy, and diabatic forcing. In the steady and adiabatic limit ($\overline{b'B'} = 0$), and using the flux decomposition (2.98), we have

$$\nabla_h \cdot \overline{\mathbf{u}_g \Phi} + (\mathbf{k} \times \nabla_h \chi_{\mathrm{rot}}) \cdot \nabla_h \bar{b} + \mathcal{N}^2 \overline{b' w'_{\mathrm{ag}}} = \kappa |\nabla_h \bar{b}|^2. \tag{2.104}$$

The key assumptions in Marshall and Shutts (1981) is that $\overline{\mathbf{u}_g \Phi} = \overline{\mathbf{u}}_g \overline{\Phi}$ and $\overline{\mathbf{u}}_g \cdot \nabla_h \bar{b} = J(\psi, \bar{b}) = 0$ i.e. the streamlines of the horizontal mean-flow coincides with contours of mean buoyancy, $\psi = \psi(\bar{b})$, where $\overline{\mathbf{u}}_g = \mathbf{k} \times \nabla_h \psi$. Therefore, $\overline{\mathbf{u}}_g = \frac{\partial \psi}{\partial \bar{b}} \mathbf{k} \times \nabla_h \bar{b}$ and

$$(\mathbf{k} \times \nabla_h [\chi_{\mathrm{rot}} - \chi]) \cdot \nabla_h \bar{b} + \mathcal{N}^2 \overline{b' w'_{\mathrm{ag}}} = \kappa |\nabla_h \bar{b}|^2 \tag{2.105}$$

where $\chi = \overline{\Phi} \frac{\partial \psi}{\partial \bar{b}}$ is a scalar potential. If one decides to set $\chi_{\mathrm{rot}} = \chi$ we have that

$$\mathcal{N}^2 \overline{b' w'_{\mathrm{ag}}} = \kappa |\nabla_h \bar{b}|^2, \tag{2.106}$$

which directly connects horizontal down-gradient diffusion of buoyancy with baroclinic instability, consistent with the Gent-McWilliams parameterization discussed in Section 2.3.1.

Is it physically meaningful to set $\chi_{\mathrm{rot}} = \chi$? Starting with the definition of the horizontal rotational eddy buoyancy flux, $\overline{b'\mathbf{u}'_g}_{\mathrm{rot}} = \mathbf{k} \times \nabla_h \chi_{\mathrm{rot}}$, we see that $\chi = \chi_{\mathrm{rot}}$ implies $\overline{b'\mathbf{u}'_g}_{\mathrm{rot}} \propto \mathbf{k} \times \nabla_h \overline{\Phi}$ i.e. the horizontal rotational eddy buoyancy flux is along contours of $\overline{\Phi}$. Following Griesel et al. (2010), a similar result is obtained if we imagine that horizontal eddy motion is along contours of b', $\mathbf{u}'_g \propto \mathbf{k} \times \nabla_h b'$, such that $\overline{b'\mathbf{u}'_g} \propto \mathbf{k} \times \nabla_h \overline{\Phi}$. Hence the part of the horizontal eddy motion which is along eddy buoyancy contours give rise to a rotational eddy buoyancy flux which follows contours of $\overline{\Phi}$.

2.4 Scientific challenges

The majority of the variability in the southern hemisphere westerlies is captured by the Southern Annular Mode, which has, as the name suggests, an approximate zonally-constant doughnut-like structure (Thompson and Wallace, 2000). This mode of variability is related to fluctuations in the atmospheric meridional pressure gradient, and its configuration is often quantified by an index based upon a normalized difference in zonally-averaged sea level pressure between mid and high southern hemisphere latitudes (see for example Marshall, 2003). The index is commonly interpreted as an indicator for the strength and meridional offset of the westerlies (Sallée et al., 2008; Treguier et al., 2010; Morrow et al., 2010; Bitz and Polvani, 2012; Dufour et al., 2012; Cheon et al., 2014; Ferreira et al., 2015).

Recent anthropogenic emission of carbon dioxide to the atmosphere and loss of ozone in the lower part of the southern hemisphere polar stratosphere have led to a positive trend in this index since the 1960s, particularly during the austral summer months (Thompson and Solomon, 2002; Marshall, 2003). This positive trend in the mode index is associated with a poleward migration and intensification of the southern hemisphere westerlies, and one may, provided with the discussion of residual-mean theory in section 2.2, hypothesize that this trend results in an increased Southern Ocean meridional overturning circulation through the Eulerian mean component. Such rationale was for example used by Le Quéré et al. (2007) to suggest that the observed weakening of the Southern Ocean as a net sink of atmospheric carbon dioxide is caused by an increased wind-driven upwelling of dissolved inorganic carbon to the ocean surface.

Coarse resolution general circulation model studies, such as Gent et al. (2001); Fyfe and Saenko (2006), do indeed find an increased Southern Ocean residual meridional overturning circulation when the zonal wind stress is increased. These models, in addition, also suggest that the baroclinic transport of the Antarctic Circumpolar Current increases through a meridional steepening of the isopycnals. The eddy effect in these models rely on the Gent-McWilliams parameterization, discussed in Section 2.3.1, typically with a constant value for the eddy transfer coefficient κ. The steeper isopycnals hence imply a compensation of the increased wind-driven overturning by the eddy-induced circulation, so-called *eddy compensation*. This phenomenon is also found in ocean models with explicit eddies (e.g. Viebahn and Eden, 2010). The sensitivity of the residual overturning circulation to the surface wind stress thus depends on the degree of eddy compensation present in the coarse resolution model, which in turn depends on the details of the implemented eddy parameterization.

Recent observations have highlighted that the Southern Ocean meridional density gradient appears insensitive to the trend in the Southern Annular Mode (Böning et al., 2008), which in contrast to the model simulations by Gent et al. (2001) and Fyfe and Saenko (2006) suggests an insensitive circumpolar transport to wind stress change. Hogg et al. (2015), using satellite altimetry, demonstrate a concurrent positive trend in the Southern Ocean surface eddy kinetic energy through the last couple of decades. These observations, in conjunction with several eddy-resolving model experiments that are discussed in the following subsection, have supported the idea that the Southern Ocean is in a state of *eddy saturation*, in which the circumpolar transport is independent from the surface wind stress.

If both eddy compensation, as a physical process, and eddy saturation, as a physical regime, applies to the real Southern Ocean, an apparent challenge to the modeling community is to represent both of these eddy effects simultaneously in coarse resolution models. From the construction of the Gent-McWilliams parameterization, eq. (2.83), it is evident that it is not possible to represent both processes by the parameterization with a constant transfer coefficient. That is, the isopycnal slope is required to increase to generate eddy compensation via a stronger eddy-induced circulation, but that results in a stronger baroclinic zonal time-mean transport which violates the possibility of an eddy saturation regime. This limitation of the parameterization indicates that the physical processes associated with mesoscale eddies are inadequately represented in coarse resolution models with constant κ, and also calls into question whether the sensitivity of the residual meridional overturning circulation to wind stress change is faithfully represented.

2.4.1 Eddy saturation

The concept of eddy saturation was first discussed by Straub (1993) and describes a marginally stable zonal current, which responds to a surface wind stress increase by a strengthened eddy field via baroclinic instability. In doing so it generates a stronger eddy form stress that transfers the excess momentum gain at the surface to the ocean bottom. Hence a stronger wind stress does not change the time-mean zonal transport or time-mean isopycnal slope of an eddy-saturated circumpolar current, but the variability about the mean state, a result of the presence of eddies, does increase. For an eddy-saturated current, the time-mean transport is instead determined by the rate at which the energy in the eddy field dissipates (Marshall et al., 2017). For a constant level of eddy energy determined by the wind stress strength, a stronger energy dissipation rate requires stronger baroclinic instability, which in turn requires a stronger vertical velocity shear and hence a stronger circumpolar transport.

Beside the few observation-based indications, the relevance of the concept of eddy saturation to the Southern Ocean has mainly been established by simple eddy-resolving quasi-geostrophic model experiments Hogg and Blundell (2006); Meredith and Hogg (2006); Hogg et al. (2008); Nadeau and Straub (2009); Morrow et al. (2010); Nadeau and Straub (2012) as well as through eddying primitive equation models with regional or idealized domain setups (Hallberg and Gnanadesikan, 2006; Morrison and Hogg, 2013; Munday et al., 2013). Notably, Meredith and Hogg (2006) attempt to explain the apparent lead-lag relation between observed wind stress variability, as measured by the Southern Annular Mode index, and observed surface eddy kinetic energy variability in the Southern Ocean through the use of eddy saturation arguments.

Both Hallberg and Gnanadesikan (2006) and Munday et al. (2013) compare the ability of general circulation models to represent the Southern Ocean circulation, and its sensitivity to momentum forcing, at coarse- and eddy-permitting horizontal grid resolution. These studies show that coarse resolution model setups with constant κ inadequately represent the insensitivity of the circumpolar transport to zonal wind stress change. In Munday et al. (2013), circumpolar transport in the coarse resolution model increases more or less linearly with wind stress magnitude whereas the eddy-permitting simulations suggest that Southern Ocean transport is eddy saturated, even for wind stress strengths below the present day magnitude. This result is also supported by the idealized eddying model simulations presented by Morrison and Hogg (2013), who find a weak (though finite) sensitivity for a relatively wide range of wind stress magnitudes.

The coarse resolution model deficiency has motivated research into a physically based formulation for κ; some of the proposed closures were discussed in Section 2.3.3. Farneti et al. (2015) compare a suite of coarse resolution ocean models, all forced with the same meteorological boundary conditions, which employ different choices for κ. None of the models are able to fully represent an eddy saturation regime, but those of the models which allow κ to vary in space and time favor a circumpolar transport less sensitive to the zonal wind stress. It was recently shown that formulating κ in terms of the eddy energy, κ_{MMB} given by eq. (2.96), allows for complete eddy saturation in a zonally-averaged channel model (Mak et al., 2017).

The consequence of implementing κ_{MMB} in a general circulation model however remains to be tested.

2.4.2 Eddy compensation

The water mass transformation involved in maintaining the meridional overturning circulation in the Southern Ocean necessitates the use of eddy-permitting or eddy-resolving primitive equation models in the study of eddy compensation. This restriction imposes limitations to any such study since the forward integration of these models are computationally demanding. A common compromise is to reduce the size of the model domain and simplify the basin geometry to allow for a desired number of equilibrated simulations (Viebahn and Eden, 2010; Munday et al., 2013; Morrison and Hogg, 2013). However, as touched upon in Chapter 1, the global ocean meridional overturning circulation is closed by a mixture of adiabatic upwelling in the Southern Ocean and diabatic upwelling in the Pacific and Indian basins (Talley, 2013). Hence a truncated model domain impacts the nature of the model's overturning circulation and may have an impact on the modeled eddy compensation (Jochum and Eden, 2015; Nielsen et al., 2018). Another common compromise is to retain a realistic model domain but reduce the simulation length (Hallberg and Gnanadesikan, 2006; Bishop et al., 2016). This choice allows for a realistic overturning circulation, but hinders a rigorous comparison of equilibrated model states and an exhaustive examination of the relevant parameter space.

The quantification of eddy compensation is not consistent in the scientific literature, mainly because of different definitions of the strength of the upper cell residual overturning circulation. Table 2.1 provides a list of studies conducted with eddying ocean models, both realistic and idealized, as well as the reported residual overturning response to a zonal wind stress perturbation. As indicated by the rightmost column in Table 2.1, different measures of the overturning response is at work and hence complicates a comparison of the degree of eddy compensation between models. There are, however, three commonalities which can be identified from the seven studies listed in Table 2.1. These are:

- ψ_{res} displays finite sensitivity to zonal wind stress in all models i.e. partial or no eddy compensation is present.
- ψ_{res} is sensitive to wind stress change while the zonal transport is eddy saturated.
- ψ_{res} in models which employ idealized basin geometry and no sea ice (highlighted with an asterisk in Table 2.1) appear less sensitive to the zonal wind stress.

The results from the idealized models, Viebahn and Eden (2010); Munday et al. (2013); Morrison and Hogg (2013), additionally suggest that full eddy compensation (i.e. no sensitivity of the overturning circulation to wind stress change) may emerge for sufficiently strong wind stress magnitude.

In the recent literature on the Southern Ocean, a much debated topic is whether coarse resolution ocean models with Gent-McWilliams parameterized eddies are able to simulate the correct sensitivity of ψ_{res} to zonal wind stress change. In particular, both Hallberg and Gnanadesikan (2006) and Munday et al. (2013) find that the residual meridional circulation is overly sensitive to wind stress change in coarse models with constant κ when compared

Table 2.1: A list of different studies on the response of the upper cell residual overturning circulation to a zonal wind stress perturbation using idealized and realistic eddying ocean models. The first column lists the specific study; an asterisk highlights those studies that use idealized model geometry. The second column lists the horizontal model resolution, the third column lists the percentage change of the zonal wind stress magnitude with respect to the control, the fourth column lists the relative increase of ψ_{res} in percent with respect to the control, and the fifth column lists details on how the ψ_{res} response is measured. The list is sorted with respect to horizontal model resolution.

Study	Resolution	τ^x increase	ψ_{res} response	Comment
Dufour et al. (2012)	1/4°	$\sim$ 100%	$\sim$ 210%	Average of ψ_{res} between 40°S and 55°S.
Munday et al. (2013)*	1/6°	100%	$\sim$ 15%	Max. ψ_{res} north of model equator.
Hallberg and Gnanadesikan (2006)	1/6°	20%	$\sim$ 25%	Max. ψ_{res} at 40°S.
Bishop et al. (2016)	1/10°	41%	39%	Max. ψ_{res} in the Southern Ocean domain.
Poulsen et al. (2018)	1/10°	-50%	-60%	Max. ψ_{res} in the Southern Ocean domain.
Morrison and Hogg (2013)*	1/16°	100%	$\sim$ 70%	Max. ψ_{res} at 30°S.
Viebahn and Eden (2010)*	5 km	100%	$\sim$ 30%	Max. ψ_{res} at 150 m depth.

to the same model at eddy-permitting horizontal resolution. Gent and Danabasoglu (2011) advocate that the implementation of a variable eddy transfer coefficient, such as the stratification dependent κ_{FMH}, eq. (2.95), results in appropriately parameterized eddy compensation. Farneti et al. (2015) compare a suite of coarse resolution ocean models, forced with the same meteorological boundary conditions which run from 1958 to 2007 (thus covering the positive Southern Annular Mode trend), and show that models which employ a spatiotemporal choice for κ systematically display a weaker sensitivity of the upper residual meridional overturning cell to wind stress increase. Model studies similar to Hallberg and Gnanadesikan (2006) and Munday et al. (2013), but which compare the parameterized sensitivity obtained with a dynamic κ to eddy-resolving model simulations, remains to be conducted.

Chapter 3

The Parallel Ocean Program

This thesis uses the Community Earth System Model (CESM, Gent et al., 2011) to address the scientific questions outlined in Chapter 1. The ocean module of CESM is the second version of the Parallel Ocean Program (POP), which is a hydrostatic z-level general circulation model. The model solves the Boussinesq-approximated primitive equations with no-normal flow and no-slip boundary conditions on a B-grid. The equations are discretized using the method of finite differences, and the reader is referred to Smith et al. (2010) for details on the actual discretization of the equations. By default in POP, vertical mixing is handled by the K-profile parameterization by Large et al. (1994).

3.1 Model setup

Two different configurations of the ocean model is considered. In the first configuration, the model is formulated on a horizontal grid of nominal $1°$ resolution, and this model setup is henceforth referred to as being of *coarse resolution*. In the second configuration, the model is formulated on a horizontal grid of nominal $0.1°$ resolution, and this setup is referred to as *eddy-resolving* in the following. The two different horizontal grid resolutions have implication for the resolved physics of the model and hence on the need for parameterization. This modeling aspect is discussed in the two following subsections.

3.1.1 Coarse resolution model

The coarse resolution model setup is discussed in detail in Danabasoglu et al. (2012). The vertical coordinate axis is discretized into 60 levels, and the distance between levels increases monotonically with depth and varies from 10 m at the surface to 250 m in the deeper part of the ocean. As outlined in Section 2.3, baroclinic mesoscale eddies are not resolved in this model setup and eddy fluxes require parameterization. The parameterization follows Gent and McWilliams (1990) as described in Section 2.3.1, and the specific implementation in the tracer equation is in accord with eq. (2.90) where baroclinic instability is introduced via skew-diffusion (Griffies, 1998) and eddy mixing via isopycnal down-gradient diffusion. In this model setup, the isopycnal diffusivity is set equal to κ,

$$\mu = \kappa. \tag{3.1}$$

κ is computed as proposed by Ferreira et al. (2005),

$$\kappa = \kappa_{\mathrm{FMH}} = \kappa_0 \frac{\mathcal{N}^2}{\mathcal{N}_{\mathrm{ref}}^2}, \tag{3.2}$$

which is the default expression for the eddy transfer coefficient in POP. Its implementation in the ocean model is described in Danabasoglu and Marshall (2007), and the specific choice of parameter values are provided by Danabasoglu et al. (2012). κ_0 is set to $3000\,\mathrm{m}^2/\mathrm{s}$ and $\mathcal{N}_{\mathrm{ref}}^2$ is the local vertical stability at the base of the surface boundary layer. Within the surface boundary layer, $\kappa = \kappa_0$ and the eddy-induced velocity is aligned with the ocean surface and has no vertical shear (Ferrari et al., 2008). Down-gradient horizontal diffusion is implemented in the surface boundary layer to account for diabatic eddy fluxes, and the horizontal diffusivity is set equal to the boundary layer value of the eddy transfer coefficient, κ_0. In a transition layer below the surface boundary layer, the horizontal diffusion transitions to interior ocean isopycnal diffusion and the horizontal eddy-induced velocity develops the vertical shear necessary to match the interior ocean circulation. In the ocean interior, the requirement of $\mathcal{N}^2/\mathcal{N}_{\mathrm{ref}}^2 \leq 1$ is implemented along with several other criteria on $\mathcal{N}^2$ to ensure well-behaved vertical variations in κ.

In addition to the mesoscale eddy parameterization, the model also includes a parameterization for submesoscale eddies in the mixed layer. For details on this parameterization, the reader is referred to Fox-Kemper et al. (2008) and Danabasoglu et al. (2012).

3.1.2 Eddy-resolving model

The eddy-resolving configuration of the ocean model is described in Small et al. (2014) and Bryan and Bachman (2015). The grid discretization in the vertical is identical to the coarse resolution model setup, but also features two additional levels at the bottom as a result of better resolved bottom topography and also includes a partial bottom cell representation. In this thesis, the term "eddy-resolving" refers to the fact that the model grid permits ocean eddies of spatial scale similar to the first baroclinic Rossby deformation radius. Chelton et al. (1998) provide spatial maps of the deformation radius based on observations, and show, in the zonal average, that this radius varies from $\sim 200\,\mathrm{km}$ at low latitudes to $\sim 10\,\mathrm{km}$ at $60°$ latitude. A typical grid box on the $0.1°$ grid has a characteristic size of $10\,\mathrm{km}$ at equator and $5\,\mathrm{km}$ at $60°\mathrm{S}$, and hence one may expect the model to only marginally resolve eddies of this spatial scale at high latitudes.

With the dominant part of the mesoscale eddy field explicitly resolved on most of the grid, the eddy-resolving model does not include the Gent-McWilliams eddy parameterization and nor does it include isopycnal Redi-diffusion. Lateral mixing of tracers due to unresolved subgrid-scale processes are parameterized with a biharmonic operator with diffusivity dependent on the local grid spacing (Bryan and Bachman, 2015). The submesoscale parameterization due to Fox-Kemper et al. (2008) is switched off as well.

3.1.3 Surface boundary conditions

The model, independent of its configuration, is forced with prescribed meteorological boundary conditions and freshwater input due to river run-off, and is coupled to the dynamically active sea ice model CICE which is documented in Hunke and Lipscomb (2010). The meteorological forcing fields are provided by Large and Yeager (2008) and originally derive from the data sets discussed in Large and Yeager (2004), which consist of a mixture of reanalysis products, satellite observations and in situ measurements. The data sets provide information on the near-surface atmospheric state from which the forcing fields, which cover the 23 year time period from 1984-2006, are computed. Specifically, the near-surface horizontal wind vector is used to compute the surface wind stress vector via a relation which depends on the square of the relative velocity between the near-surface atmospheric wind and the surface ocean current, as well as a drag coefficient. The estimated zonally-averaged climatological (the temporal mean over the 23 year time period) zonal wind stress compares well with other independent estimates, such as the ERA15 reanalysis product.

The forcing fields thus described were used in the second version of the Coordinated Ocean Research Experiments (CORE.v2), such as the experiment documented in Farneti et al. (2015), and are therefore referred to as the "CORE.v2" forcing fields. This thesis uses the so-called normal year forcing fields of CORE.v2, which consist of a repeat annual cycle of all meteorological fields with a temporal resolution of six hours. The "normal year" is not simply the climatology of CORE.v2 and is constructed in a fashion to retain weather, such as storm tracks (Large and Yeager, 2004). This specific type of forcing is henceforth referred to as CORE.v2.NYF.

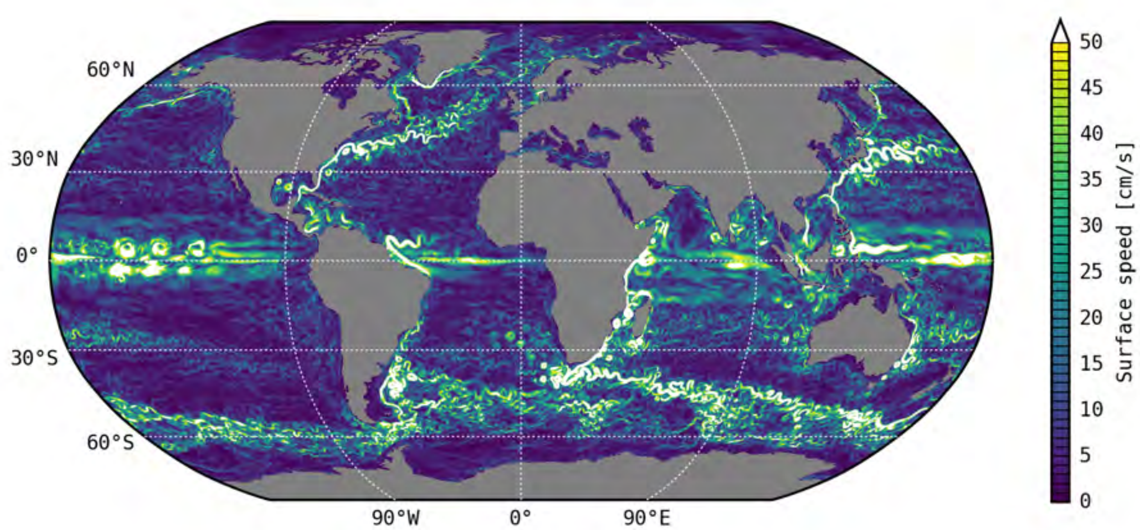

Figure 3.1: A random three-day time-mean snapshot of the surface ocean current speed from the eddy-resolving model. Units are in cm/s.

3.2 Simulations

Two control integrations and several Southern Ocean wind stress perturbation experiments were carried out using the two model setups. These simulations are described below.

3.2.1 Control integration

A control integration with default CORE.v2.NYF forcing fields was performed with both model configurations. The coarse resolution model was initialized from a state of rest on January 1st using the salt and temperature fields from the Polar Science Center Hydrographic Climatology (Steele et al., 2001), and the model was integrated forward for 400 model years. The eddy-resolving model was also initialized from a state of rest on January 1st, but with the property fields taken from the World Ocean Circulation Experiment Hydrographic Climatology (Gouretski and Koltermann, 2004). The first sixteen model years of the eddy-resolving model integration was performed at the National Center for Atmospheric Research (Bryan and Bachman, 2015). The simulation was subsequently extended at the Jülich Supercomputing Centre (located in Germany) with an additional 26 model years to obtain a total control simulation of 42 model year duration. A snapshot of the global ocean surface speed, simulated with the eddy-resolving model, is shown in Figure 3.1 and illustrates the turbulent nature of the ocean circulation. Several notable features stand out, such as western boundary currents, tropical instability waves, the complex frontal system in the Antarctic Circumpolar Current and rings shredding off the southern tip of Africa into the Atlantic Ocean.

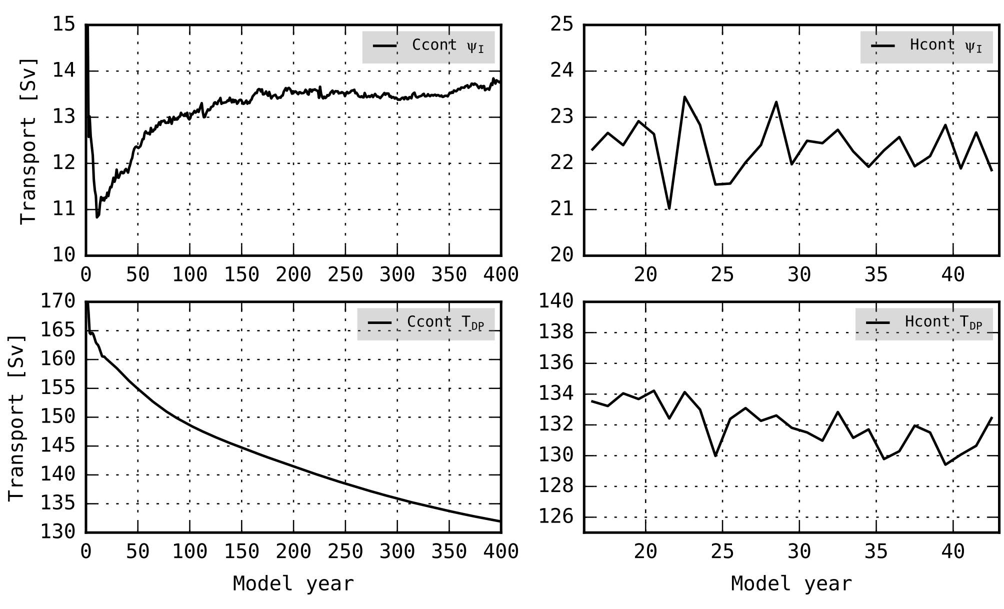

Figure 3.2: Annual mean residual meridional overturning strength in the Southern Ocean (upper panels) and annual mean Drake Passage transport (lower panels) for Ccont (left panes) and Hcont (right panels). The overturning strength is computed from the isopycnal streamfunction in accord with the caption text belonging to Figure 4.5. Note that the first 16 years of Hcont was conducted at the National Center for Atmospheric Research and are not available in this study.

The coarse and eddy-resolving control integrations are henceforth referred to as Ccont and Hcont, respectively, and the spin-up of the two simulations are shown in Figure 3.2. The residual overturning strength in the Southern Ocean of Ccont is seen to plateau around model year 200 about a transport value of 13-14 Sv (upper left panel). No trend is visible in the shorter Hcont time series (upper right panel), but the interannual variability and overturning strength is stronger in Hcont compared to Ccont. The Ccont Drake Passage transport, on the other hand, decreases throughout the 400 year integration period; during the last century of the integration, the transport decreases by approximately 4 Sv (lower left panel). Hcont displays an even stronger negative trend in the circumpolar transport of about 1 Sv/Decade and the time series is, as before, richer in interannual variability compared to Ccont (lower right panel). In Chapter 4 and 5, the focus is mainly on the physical response of the perturbed ocean circulation on decadal time scale. Therefore the first 300 years of Ccont and the first 16 years of Hcont is considered spin-up, and the drift in remaining part of Hcont and Ccont is deemed sufficiently small so that the last part of the two simulations can be taken to represent the experimental background.

The ability of both model configurations to reproduce the observed present-day climate on Earth is documented in Gent et al. (2011) and Small et al. (2014). To show that the two control integrations also are not radically different from one another when forced with CORE.v2.NYF, ten-year time mean fields of the barotropic streamfunction, potential temperature and salinity in the Southern Ocean from the two control simulations are compared in Figure 3.3. Both models display the same overall circulation pattern and a similar Drake Passage transport of 132 Sv and 136 Sv for Hcont and Ccont, respectively, which both compare well with observational estimates (e.g. Cunningham et al., 2003). In addition, the circulation in Hcont possesses more meanders and closed recirculation cells, such as the Zapiola anti-cyclone east of South America. The large-scale structure in temperature and salinity is also similar between the two models, but Hcont generally displays sharper horizontal gradients as well as higher salinity at polar latitudes. A relatively big salinity discrepancy between the models is also found in the eastern Pacific Ocean and at western boundaries in the mid-latitudes. A comparison of sea-ice distribution, surface boundary layer depth and Southern Ocean meridional overturning circulation between the two control integrations is discussed in detail in Chapter 4.

3.2.2 Wind stress perturbation experiments

Several zonal wind stress perturbation experiments were branched off from the control integrations. The spatial structure of the perturbation is zonally constant and follows

$$F(\theta) = \begin{cases} F_0, & \text{for } \theta \leq 35°\text{S} \\ \frac{a\pi}{180°}\theta + b, & \text{for } 35°\text{S} < \theta < 25°\text{S} \\ 1, & \text{otherwise,} \end{cases} \tag{3.3}$$

where θ is latitude and F_0 is the perturbation factor. a and b are implicitly determined by F_0 and are chosen such that the southward increase of the perturbation from 25°S to 35°S is continuous. The control zonal wind stress, τ_0^ϕ, computed from the CORE.v2.NYF near-surface

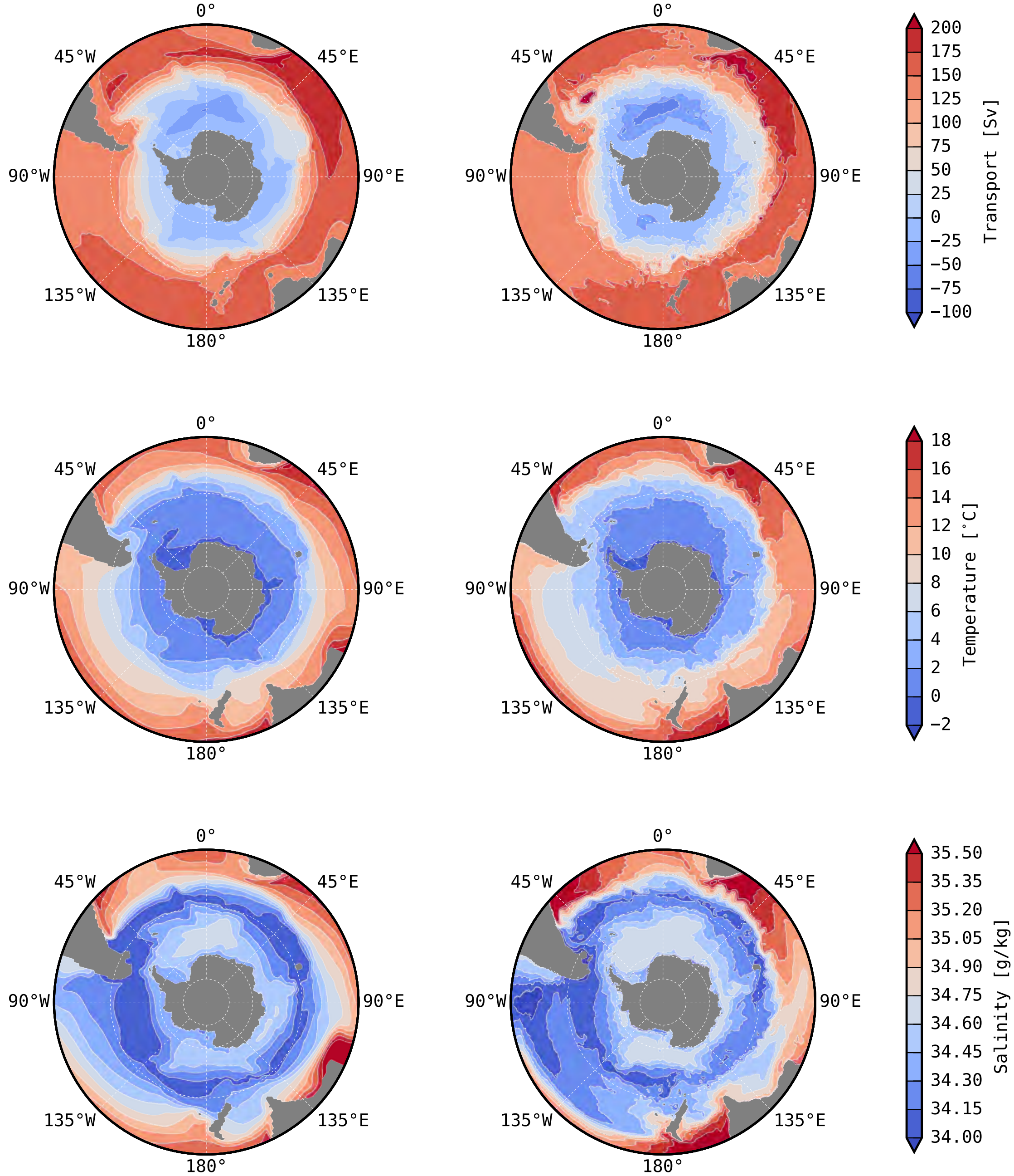

Figure 3.3: Ten-year time means of the barotropic streamfunction (upper panels), potential temperature at 200 m depth (middle panels) and salinity at 200 m depth (lower panels) for the coarse resolution model (left column) and the eddy-resolving model (right column). The time-mean of the coarse model covers the time period from model year 290 to 299. The time-mean of the eddy-resolving model covers the time period from model year 16 to 25.

wind velocity field, is perturbed according to

$$\tau^{\phi}(\phi, \theta, t) = \tau_0^{\phi}(\phi, \theta, t)F(\theta), \tag{3.4}$$

where ϕ is longitude and τ^{ϕ} is the perturbed zonal wind stress. The perturbation is implemented in the model coupler after the zonal wind stress has been computed, and hence the atmosphere does not experience the perturbation. Calculations of evaporation, sensible heat flux and latent heat flux are therefore unaffected in the wind stress change experiments.

The different perturbation factors, F_0, considered in this thesis are listed in Table 4.1. The perturbation is applied instantaneously on January 1st year 26 in the eddy-resolving model configuration and on January 1st year 300 in the case of the coarse resolution model. All perturbation experiments are integrated forward until they reach the final year of their respective control integration. That is, year 400 for the coarse model and year 42 for the eddy-resolving model. The annual-mean zonally-averaged zonal wind stress for the different experiments are shown in the upper left panel of Figure 4.1. The focus of Chapter 4 is on the local Southern Ocean response to the different perturbations, and further discussion is therefore deferred to that specific chapter.

3.2.3 A note on high performance computing, output frequency and data amounts

The high resolution of the eddy-resolving model grid requires that each of the model equations are solved on the order of 10^8 times for each time the model steps forward in time. The model time step is on the order of 1×10^3 s and the eddy-resolving model simulations considered in this thesis span several model decades. The forward integration of the model is thus computationally demanding and is a task for a high performance computer.

The model was run on 4096 cores of the IBM Blue Gene/Q supercomputer JUQUEEN at the Jülich Supercomputing Centre and produced approximately one model year in ten Earth days. In total the three simulations (control integration plus two perturbation experiments) consumed about 80 million core hours on the supercomputer and took a couple of years to complete. When commission began in 2012, JUQUEEN was theoretically capable of 5.9 PFlop/s and was among the fastest supercomputers in the world. In the spring of 2018, only six years later, it was decommissioned and replaced by its successor, JUWELS, with an estimated peak performance of 12 PFlops/s.

The eddy-resolving model was configured to output three-day time mean fields of all the model variables. This high output frequency was motivated by the characteristic time scale of mesoscale eddy variability, which is on the order of about a month and hence requires a high sampling rate to ensure reliable eddy statistics. Each three-day mean output file requires 86 GB of storage space and the total amount of raw model output considered in this thesis is about 800 TB. Local storage space was provided by the Electronic Research Data Archive which is installed and maintained by the e-science department at University of Copenhagen. Of course, only a small fraction of the output variables are of relevance to the two projects described in Chapter 4 and 5, and a considerable amount of time has been spent on reducing the data to an amount which is manageable on typical in-house computing facilities.

Chapter 4

Parameterized and resolved Southern Ocean eddy compensation

Preliminary notes

Section 4.1-4.6 of this chapter has been published in *Ocean Modelling*,

Poulsen, M. B., M. Jochum, and R. Nuterman, 2018: Parameterized and resolved southern ocean eddy compensation. *Ocean Modelling*, **124**, 1–15, doi:10.1016/j.ocemod.2018.01.008.

The study was mainly inspired by a recent debate in the scientific literature on the capability of the Gent-McWilliams eddy parameterization to faithfully represent the response of the Southern Ocean eddy field and circulation in coarse resolution ocean models to a zonal wind stress change when a dynamic eddy transfer coefficient is implemented (see e.g. Hallberg and Gnanadesikan, 2006; Böning et al., 2008; Gent and Danabasoglu, 2011; Munday et al., 2013; Bryan et al., 2014; Jochum and Eden, 2015). Specifically, this chapter examines the skill of

$$\kappa = \kappa_{\mathrm{FMH}} = \kappa_0 \frac{\mathcal{N}^2}{\mathcal{N}^2_{\mathrm{ref}}},$$

which was also discussed in Section 2.3.3 and used in the model study by Gent and Danabasoglu (2011).

The present study was also motivated by a desire to obtain a more rigorous estimate of the ocean response to zonal wind stress change in realistic settings, without the influence from effects related to the coupled atmosphere-ocean system. Previous efforts using realistic eddying ocean models, such as Bishop et al. (2016), implement wind stress perturbations similar to eq. (3.3) in coupled climate models. A wind stress perturbation, however, results in anomalous surface ocean Ekman currents which drive changes in e.g. sea surface temperatures. In a coupled model, such ocean surface changes feed back on the zonal wind stress since the meridional sea surface temperature gradient impacts the baroclinicity of the atmospheric circulation (Marshall and Connolley, 2006). As a consequence, the implemented perturbation does not stay fixed in time and space and hence introduces ambiguity in the interpretation of the model experiment: how much of the ocean response is related to indirect atmosphere-ocean feedback effects? A remedy to this problem is to consider forced ocean simulations, which is the choice in the manuscript presented in this chapter.

Note that this project was submitted for publication before the full extent of the eddy-resolving control integration was available. The difference in ocean state between the wind stress experiments and the control integration are therefore shifted in time and may in principle reflect change due to other effects than the wind stress perturbation alone, such as model drift. This caveat of the study is discussed in the manuscript. The model response has been re-evaluated after the full control integration has become available to the authors and the interpretation of the results, as anticipated, does not change. Also note that a typo in the text immediately below eq. (4.4) has been corrected.

Abstract

The ability to parameterize Southern Ocean eddy effects in a forced coarse resolution ocean general circulation model is assessed. The transient model response to a suite of different Southern Ocean wind stress forcing perturbations is presented and compared to identical experiments performed with the same model in 0.1° eddy-resolving resolution. With forcing of present-day wind stress magnitude and a thickness diffusivity formulated in terms of the local stratification, it is shown that the Southern Ocean residual meridional overturning circulation in the two models is different in structure and magnitude. It is found that the difference in the upper overturning cell is primarily explained by an overly strong subsurface flow in the parameterized eddy-induced circulation while the difference in the lower cell is mainly ascribed to the mean-flow overturning. With a zonally constant decrease of the zonal wind stress by 50% we show that the absolute decrease in the overturning circulation is insensitive to model resolution, and that the meridional isopycnal slope is relaxed in both models. The agreement between the models is not reproduced by a 50% wind stress increase, where the high resolution overturning decreases by 20%, but increases by 100% in the coarse resolution model. It is demonstrated that this difference is explained by changes in surface buoyancy forcing due to a reduced Antarctic sea ice cover, which strongly modulate the overturning response and ocean stratification. We conclude that the parameterized eddies are able to mimic the transient response to altered wind stress in the high resolution model, but partly misrepresent the unperturbed Southern Ocean meridional overturning circulation and associated heat transports.

4.1 Introduction

The outcropping isopycnals of the Southern Ocean provide an important adiabatic pathway for the meridional overturning circulation and hence aid the ventilation of the deep ocean (Marshall and Speer, 2012). Together with the zonally unblocked Antarctic Circumpolar Current, the Southern Ocean thus plays a central role in the modern view of the ocean general circulation (Gnanadesikan, 1999; Thompson et al., 2016), the global carbon cycle (Sigman and Boyle, 2000; Le Quéré et al., 2007; Bronselaer et al., 2016), ocean heat uptake (Marshall and Zanna, 2014) and the exchange of tracers between the major ocean basins (Thompson, 2008). The southern hemisphere westerlies are a key driving force of the circulation (e.g. Toggweiler and Samuels, 1995; Tansley and Marshall, 2001) and these have been subject to an intensification and poleward shift throughout the last several decades as a result of ozone depletion and anthropogenic emission of carbon dioxide (Thompson and Solomon, 2002; Marshall, 2003). A fundamental question is what implication the wind stress changes have on the global circulation and climate, and whether the relevant physics is faithfully represented in state-of-the-art climate models to allow for meaningful predictions of the response.

In this respect, the mesoscale eddy field in the Southern Ocean (e.g. Frenger et al., 2015) has proven to have a leading order influence on the local dynamics. Ocean models of varying complexity and basin geometry, but with an explicitly resolved eddy field, have demonstrated that a limit exists in which the time-mean transport of a circumpolar current becomes independent of the strength of the overlying zonal wind stress (Hogg and Blundell, 2006; Nadeau and Straub, 2009; Munday et al., 2013; Marshall et al., 2017). Beyond this limit additional momentum input to the surface ocean by the winds mainly fuel a stronger eddy field through baroclinic instability, which facilitates a vertical momentum transfer to the ocean floor and dissipation by form drag (Munk and Palmén, 1951; Johnson and Bryden, 1989), instead of accelerating the current. Recent observations from the Southern Ocean have shown that the isopycnal slope, and hence the baroclinic transport of the Antarctic Circumpolar Current, has indeed been insensitive to the wind stress changes (Böning et al., 2008) while the surface kinetic energy has increased (Hogg et al., 2015), supporting the model results and the notion that the Southern Ocean is in the so-called state of eddy saturation.

Contemporary residual-mean theory also emphasizes the role of mesoscale eddies in setting the strength of the upper cell of the meridional overturning in the Southern Ocean. Here they compensate the effect of a wind-driven northward Ekman flow anomaly through an oppositely directed flow akin to a Stokes drift (referred to as eddy compensation, see e.g. Marshall and Radko (2003)). The results from models with explicit eddies show that this is indeed the case (Hallberg and Gnanadesikan, 2006), but also that the sensitivity of the overturning circulation remains non-zero to a wind stress strength that is several times greater than the present day magnitude, unlike the behavior of the zonal transport (Munday et al., 2013). Using an idealized primitive equation model at various eddying resolutions, Morrison and Hogg (2013) likewise demonstrate the sensitivity difference between the zonal and meridional circulation to the zonal wind stress. They argue that the sensitivity difference arises because eddy compensation is a depth-dependent metric, whereas eddy saturation is depth-integrated and thus camouflages potentially higher local sensitivities in the vertical shear of the horizontal velocity field.

In a recent high-resolution coupled model experiment run for two model decades, Bishop et al. (2016) shows that the upper cell of the residual overturning increases in magnitude by 39% to a zonally constant 50% increase of the Southern Ocean zonal wind stress, and that the mean Drake Passage transport changes by 6% only. The degree of compensation and saturation that should be expected on a longer time scale is however still unclear as computational cost limits sufficiently long integrations of comprehensive high resolution ocean models. Moreover, the non-local response of the Atlantic meridional overturning circulation to a Southern Ocean wind stress change is continuously debated. For example, it has been suggested that models with idealized basin geometry do not capture the changes in diapycnal upwelling in the Pacific Ocean. Since this diabatic pathway is also able to provide the necessary closure for the meridional overturning circulation, these models potentially overestimate the role of the Southern Ocean winds (Jochum and Eden, 2015).

The results from eddy-resolving ocean models, despite their simplifications and shortcomings, have questioned the ability of coarse resolution ocean models to represent the eddy effect on the large-scale flow in a wind stress change scenario. Most climate models use the Gent-McWilliams parameterization (Gent and McWilliams, 1990; Gent et al., 1995) to model baroclinic instability and along-isopycnal eddy mixing in the interior ocean, and rely on the assumption that the strength of baroclinic instability is proportional to the isopycnal slope. Comparison studies have shown that when the proportionality parameter in the eddy down-gradient closure, the thickness diffusivity, is a constant, the zonal transport cannot possibly eddy saturate and the meridional circulation is too sensitive to wind stress changes (Hallberg and Gnanadesikan, 2006; Munday et al., 2013). When the eddy diffusivity is allowed to vary in space and time as function of the stratification (Ferreira et al., 2005; Danabasoglu and Marshall, 2007), the transport through Drake Passage shows a less sensitive relationship to the zonal wind stress (Gent and Danabasoglu, 2011). However, the change in the residual overturning still varies considerably among models subject to the same wind stress increase (Farneti et al., 2015), which complicates an assessment of the parameterized eddy effect.

Both Bitz and Polvani (2012) and Bryan et al. (2014) compare climate change experiments between a fully coupled coarse resolution model, using above parameterization, and an identical eddy-resolving model. The model solutions in the study by Bryan et al. (2014) show that the poleward eddy heat transport between 60°S and 50°S increases following an increase in the zonal wind stress in their low resolution model setup, whereas the high resolution model finds a response of opposite sign. Bitz and Polvani (2012) report similar model responses, where the resolved eddies contribute substantially less to the change in poleward heat transport compared to the parameterized eddies. While these results suggest that the parameterized eddies respond oppositely or overly strong to a wind stress change, ambiguity on the performance of the eddy parameterization still remains, because the modeled wind stress changes are dependent on the background climate. This is not necessarily the same at different model resolution, exemplified by Bryan et al. (2014), where differences in Antarctic sea ice thickness influence the modeled climate response. In addition, an increasing body of literature has shown that the strength of the Antarctic Circumpolar Current and the position of its fronts is sensitive to the spatial structure and strength of the wind stress field (Sallée et al., 2008; Morrow et al., 2010; Mazloff, 2012; Dufour et al., 2012; Zika et al., 2013; Langlais et al., 2015). The compilation of these results suggest a return to simpler general circulation model experimental setups with a complete control on the applied wind stress to elucidate the nature of the response.

In the present study we present simulations from the second version of the Parallel Ocean Program (POP) model configured at a horizontal resolution of 1° and 0.1°, the former employing a state-of-the-art eddy parameterization, forced with different prescribed Southern Ocean wind stress scenarios in an attempt to evaluate the performance of parameterized eddies. The results presented here indicate that the parameterized eddy-induced meridional circulation cancel the wind-driven overturning differently than the eddy-resolving model when forced with present day winds. Despite differences in the background ocean state we demonstrate that the two models respond similarly to wind stress perturbations, but note that the model comparison is not straightforward as changes in buoyancy forcing and sea ice cover are able to drive a complex model response. The latter point raises the question to what extent the current concept of eddy compensation is applicable to complex models.

4.2 Model description, experimental setup and spin-up assessment

We use the Community Earth System Model (CESM) with an active ocean and sea ice model on a global domain with realistic bottom topography with prescribed meteorological boundary conditions. The ocean and sea ice models share the same grid, and the solution of the governing equations is sought using two different horizontal grid resolutions; a tri-polar 0.1° grid, with the meridional grid spacing proportional to the cosine of latitude, and a dipole 1° grid that also has a meridional grid discretization that varies with latitude, with a latitudinal grid spacing of $\sim 0.5°$ in the Southern Ocean. The vertical axis that belongs to the first grid is resolved by 62 z-coordinate levels, with the distance of separation increasing monotonically with depth, and has a partial bottom cell representation in accord with the ETOPO2v2 bathymetry product. The coarse resolution grid holds 60 levels in the vertical and with no partial bottom cells. The dynamical core of the ocean model is the same for both grid resolutions and is documented in Smith et al. (2010), except for the treatment of motion on the mesoscale, which is outlined in the next paragraph. For further information on the grid layouts and aspects of the control integration of the fully coupled models, the reader is referred to Gent et al. (2011) and Small et al. (2014) with respect to the coarse and the fine resolution model, respectively. The prescribed atmosphere used in this study is given by the normal year forcing fields from the second version of the Coordinated Ocean Research Experiment (CORE.v2.NYF, Large and Yeager, 2008), compiled from atmospheric reanalysis and observations, and the fields have a temporal resolution of six hours and repeat themselves after one model year exactly.

Ideally the model solution that evolves on the 0.1° grid should be subject to motion on a characteristic length scale on the order of the first baroclinic Rossby radius (Chelton et al., 1998) and no mesoscale eddy parameterization is therefore enabled. The isopycnal tracer diffusion is likewise disabled, but a biharmonic operator is implemented to represent lateral mixing by subgrid-scale processes that remain unresolved (Bryan and Bachman, 2015). Ocean mesoscale eddies are not explicitly resolved on the 1° grid and are parameterized in the interior ocean using the Gent and McWilliams (1990) isopycnal mixing formulation with the spatiotemporal thickness diffusivity proposed by Ferreira et al. (2005). This choice of the eddy transfer coefficient ensures that it is surface intensified, in alignment with previous studies, and has shown to improve the model solution with respect to observations of the Southern Ocean density structure and leads to a greater cancellation between the wind-driven and eddy-induced Southern Ocean meridional cells (Danabasoglu and Marshall, 2007; Farneti et al., 2015). As default in POP, the parameterized ocean interior eddy fluxes are modified towards the surface boundary layer in accord with Ferrari et al. (2008), where diabatic eddy fluxes are aligned with the surface ocean. Of additional relevance to this study, convective instability is handled implicitly in both models; that is, the local vertical diffusivity is increased by several orders of magnitude when the water column is statically unstable. During statically stable conditions, the vertical mixing is parameterized as in Large et al. (1994).

The model on the 1° grid was initialized from a state of rest and the property fields from the Polar Science Center Hydrographic Climatology (Steele et al., 2001), and a control simulation (labeled Ccont) of 300 model years was integrated forward with the default wind stress, denoted by $\boldsymbol{\tau}_0 = (\tau_0^\phi, \tau_0^\theta)$. The control simulation with the 0.1° model (labeled Hcont), was also initialized from rest but the initial conditions to the salt and temperature fields were instead provided by the World Ocean Circulation Experiment Hydrographic Climatology (Gouretski and Koltermann, 2004). The first 16 years of Hcont were conducted at the National Center for Atmospheric Research and is described in detail in Bryan and Bachman (2015). The model run was hereafter adopted by the authors and integrated additionally ten years forward in time to reach a total Hcont length of 26 years.

Several wind stress change experiments were branched off from the last year of both Ccont and Hcont with the zonal wind stress in the Southern Ocean subject to

$$\tau^\phi(\phi, \theta, t) = \tau_0^\phi(\phi, \theta, t)F(\theta), \tag{4.1}$$

where τ^ϕ is the perturbed zonal wind stress. F is a time-invariant perturbation that has a zonally constant structure expressed by

$$F(\theta) = \begin{cases} F_0, & \text{for } \theta \leq 35°\text{S} \\ \frac{a\pi}{180°}\theta + b, & \text{for } 35°\text{S} < \theta < 25°\text{S} \\ 1, & \text{otherwise,} \end{cases} \tag{4.2}$$

and it is understood that θ increases northward. Here F_0 is the perturbation factor and a and b were chosen such that the linear decrease of the perturbation with latitude matches F_0 at $\theta = 35°$S and unity at 25°S. This is the same perturbation that was used in the coupled model studies by Gent and Danabasoglu (2011), Jochum and Eden (2015) and Bishop et al. (2016).

Table 4.1 summaries the suite of wind stress experiments presented in this paper, as well as their abbreviations, and provides the coefficients specific to the applied perturbations. A 50% wind stress increase and decrease experiment (blue and magenta line, upper left panel of Figure 4.1) were extended from the end of the high resolution control simulation (labeled Htau15 and Htau05, respectively), both of 16 years duration. The output from Htau15 and Htau05, as well as the last year from Hcont, was stored as three-day mean fields and subsequently reduced to monthly means to fit the purpose of this study. Identical perturbations to the wind stress

Table 4.1: List of experiments and their characteristics. The acronym for each of the different experiments is provided in the leftmost column. F_0, a and b are the coefficients that enter in the perturbation given by eq. 4.2.

Exp.	Resolution	F_0	a	b	Duration [years]
Hcont	0.1°	1.0	0.0	1.0	26
Htau05	0.1°	0.5	2.941	2.294	16
Htau15	0.1°	1.5	-2.941	-0.294	16
Ccont	1°	1.0	0.0	1.0	300
Ctau05	1°	0.5	2.941	2.294	100
Ctau15	1°	1.5	-2.941	-0.294	100
Ctau20	1°	2.0	-5.882	-1.588	100

field were conducted with the coarse resolution model, the experiments labeled Ctau05 and Ctau15, both of 100 model year duration. As will become evident later in the reading of the present study, the wind stress increase perturbation pushes the state of the marginal seas of the Southern Ocean towards a state that favors deep convection, which influences the overturning response in Htau15. To emphasize this point, a double wind stress increase experiment (green line, upper left panel of Figure 4.1) with the 1° model (labeled Ctau20) is performed, also of 100 year duration.

Throughout this study, and unless otherwise stated, the analysis of Ccont and Hcont is conducted on the ten years that lead up to the application of the wind stress perturbation. That is, year 16 to 25 for Hcont and year 290 to 299 for Ccont. The analysis of the high resolution wind stress experiments is focussed on the last ten years, the time span between year 33 and 42, and the corresponding time span for the coarse resolution experiments is between year 307 and 316. The time-mean of Ctau20 is taken between model year 313 to 322, shifted by six years relative to Ctau15, due to a difference in the timing of the onset of deep convection relative to Htau15.

The black curve in the upper left panel of Figure 4.1 shows the annual mean zonally-averaged zonal wind stress profile that arises from the unperturbed forcing field, and the peak wind stress is smaller by approximately 25% than what is found in the coupled model configuration (Gent and Danabasoglu, 2011; Bryan et al., 2014; Bishop et al., 2016). Comparing the time-mean Drake Passage transport profile from Hcont to the corresponding profile from Ccont, it is seen that there is an overall good agreement between the models in terms of the vertical velocity shear (upper right panel, Figure 4.1). The depth-integrated volume transport of Hcont and Ccont yields similar time-mean Drake Passage transports of 133 Sv and 136 Sv, respectively, and compares well with the 134 ± 27 Sv full-depth observational estimate reviewed by Cunningham et al. (2003). The more recent estimate of 141 ± 13 Sv by Koenig et al. (2014), based on satellite altimetry and mooring data, agrees with the presented model solutions as well, although the 173 ± 11 Sv estimate by Donohue et al. (2016), which additionally includes a barotropic contribution from resolved near-bottom currents, suggests that the modeled Drake Passage transport in both models is too low.

The winter-mean boundary layer depth simulated in the two models, defined in Large et al. (1994), is seen in the lower row of plots in Figure 4.1, as well as the 15% austral winter-mean

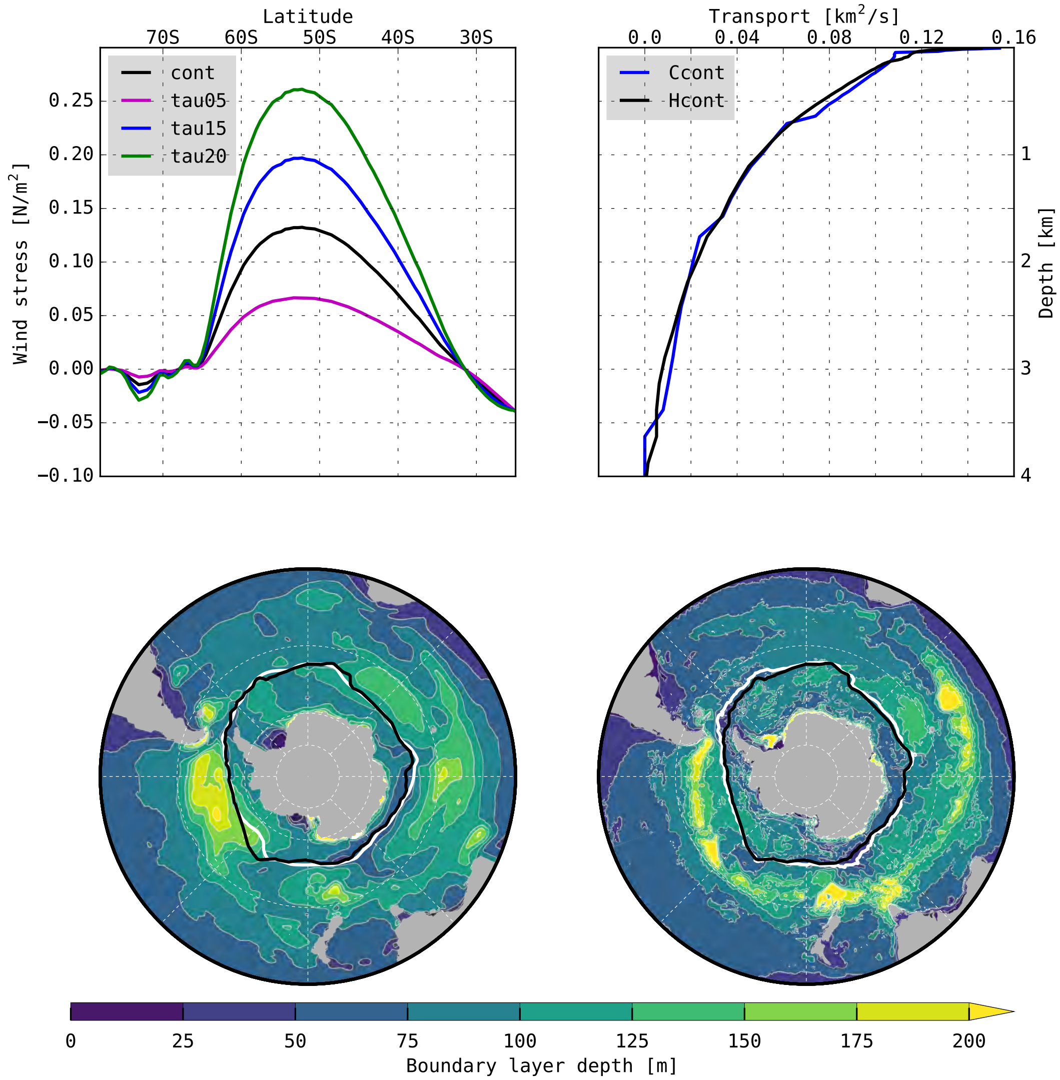

Figure 4.1: The upper left panel shows the zonal average of the annual mean zonal wind stress fields from the different experiments. The black, magenta, blue and green lines are from the control, 50% wind stress decrease, 50% increase and 100% increase, respectively. Units are in N/m^2. The upper right panel is the ten-year mean transport profiles from the Drake Passage. The blue line is from Ccont (year $290-299$) and the black line is from Hcont (year $16-25$). The units are in km^2/s. The lower left panel displays the ten-year mean winter (July-August-September) boundary layer depth from Ccont. The white and black solid lines are the 15% July-August-September sea ice concentration contour from the model and from observations, respectively. The lower right panel shows the same as the lower left panel, but for Hcont. Color interval is 25 m.

(July-August-September) sea ice concentration isoline from the model (white line) and from the Special Sensor Microwave Imager observations (black line, Comiso (2000)). The boundary layer depth of Ccont (left) in general agrees with Hcont (right) on the large scale, but Hcont also possesses several local maxima, of which some occur in proximity of topographic obstacles, and has a deeper boundary layer in the path of the Antarctic Circumpolar Current in the Indian Ocean sector. Hcont also displays a deeper boundary layer close to the coast of Antarctica, especially in the Weddell Sea, which is the signature of dense water formation. The observed extent of the winter sea ice cover in general compares well with the two model simulations, though with a misrepresentation in the Pacific sector in Ccont, and a too large extent in Hcont to the east of Drake Passage and south of Australia.

The computational costs of the 0.1° model made it difficult to integrate the high resolution simulations closer to their equilibrium solution given our resources. The total sum of 42 high resolution model years required more than a year to complete on 4096 cores of the BlueGene supercomputer located in Jülich, Germany, and exhausted our resources. Model drift therefore remains, and it is here examined in Hcont to identify the fraction of the model response presented in the results section which is due to model drift.

The upper left panel of Figure 4.2 displays the evolution of the horizontally averaged potential temperature field of the Southern Ocean in Hcont from model year 16 to 25. On decadal time-scale, as is the interest of the present study, significant drift is present between 1000 m and 400 m depth. The Southern Ocean warms at a rate about 0.2 °C/decade at 600 m depth, and is of the same magnitude and location as the warming trend presented by Small et al. (2014), who examine the model in its coupled configuration. The abyssal ocean also

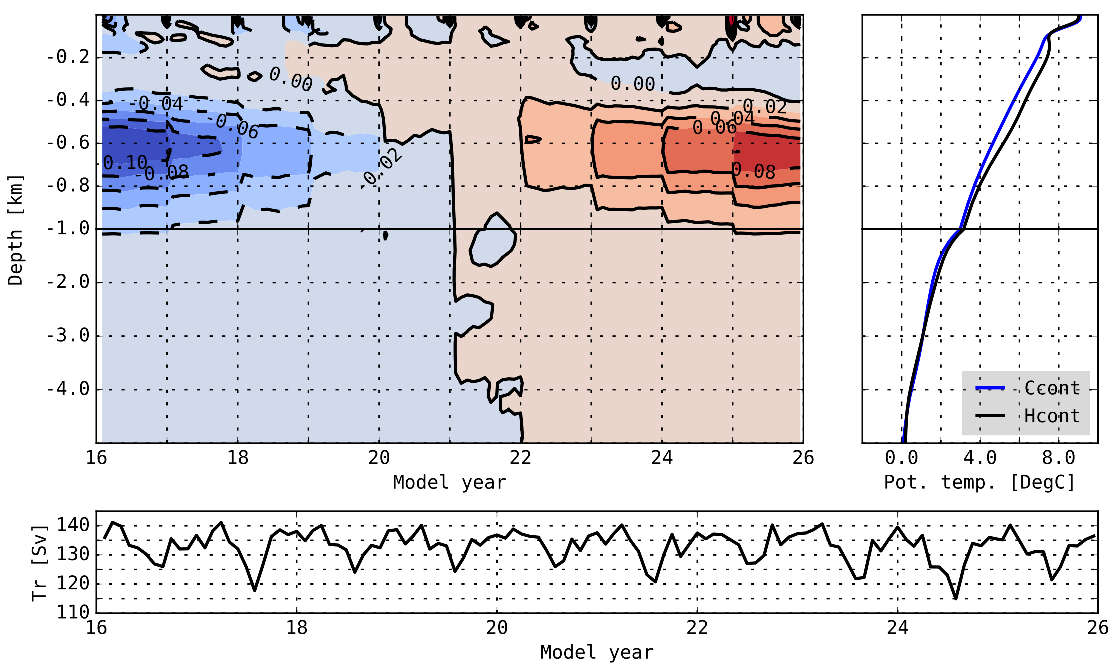

Figure 4.2: The upper left panel displays the temporal evolution of the horizontally-averaged potential temperature anomaly south of 30°S for Hcont between model year 16 and 25. The seasonal cycle has been removed. Dashed and solid contours are negative and positive, respectively, and the contour interval is 0.02 °C. The upper right panel shows the ten-year mean temperature profile for both Ccont (blue) and Hcont (black). The lower panel shows the Drake Passage transport time series from the last ten years of Hcont.

warms, but equilibrates the slowest and does not drift much on the decadal time-scale. For comparison, Ccont, which is integrated much further towards equilibrium, warms by approx. 0.003 °C/decade only at 600 m depth, evaluated between model year 290 and 299.

The ten-year mean temperature profiles of both Ccont (blue) and Hcont (black) are shown in the upper right panel. The profiles in the deep ocean match quite well, but Hcont is seen to be warmer by $\sim 1\,°\mathrm{C}$ than Ccont above 1 km depth, and the difference becomes bigger as time progress due to the model drift. However, the meridional density gradient across the Southern ocean does not appear to be affected by the difference in temperature stratification and the model drift, as is indirectly inferred from the time series of the Drake Passage transport in the lower panel of Figure 4.2. The strength of the Southern Ocean meridional overturning circulation also does not appear to drift, which is discussed in greater detail in Section 4.4, and shown in Figure 4.5. We thus consider a comparison between the high and coarse resolution model meaningful, but the shortness and drift of the high resolution model integrations is a caveat of the present study that should be kept in mind.

4.3 Decomposition of the meridional overturning circulation

To avoid the representation of artificial diapycnal flows in the Southern Ocean, the analysis of the meridional overturning circulation is here performed in density coordinates, in accord with previous related studies (e.g. Hallberg and Gnanadesikan, 2006; Munday et al., 2013; Bishop et al., 2016). When remapped to vertical coordinates, such overturning circulation is found to respect the adiabatic nature of the interior ocean, with streamlines approximately aligned with the isolines of the density field (Döös and Webb, 1994; Viebahn and Eden, 2012). The time-mean of the isopycnal stream function is given by

$$\overline{\psi_I}(\theta,\sigma) = \overline{\oint_0^{2\pi} \int_{\eta_B(\phi,\theta)}^{\eta(\phi,\theta,t)} v(\phi,\theta,z,t)\,\mathrm{d}z\,R\cos(\theta)\;\mathrm{d}\phi} \tag{4.3}$$

where ϕ, θ and z are the usual spherical coordinates, R is Earth's radius and σ is potential density. η_B is the depth of the ocean bottom and $\eta(\phi,\theta,t)$ is the depth of the surface of constant σ that varies in both space and time. $\overline{(\cdot)}$ denotes the averaging operator with respect to the time coordinate.

The overturning streamfunction is split into various components by decomposing the velocity and density fields into different terms that each are governed by distinct physics. The decomposition here consists of separating the velocity and density field into a time-mean and the deviation about it, $v(\phi,\theta,z,t) = \overline{v}(\phi,\theta,z) + v'(\phi,\theta,z,t)$, and likewise for σ. The isopycnal streamfunction that arises from the time-mean fields is here denoted Ψ_I and is given by

$$\Psi_I(\theta,\sigma) = \oint_0^{2\pi} \int_{\eta_B(\phi,\theta)}^{\overline{\eta}(\phi,\theta)} \overline{v}(\phi,\theta,z)\,\mathrm{d}z\,R\cos(\theta)\;\mathrm{d}\phi, \tag{4.4}$$

where $\overline{\eta}$ is the time-mean height of the density surface of constant σ. The difference between the time-mean of the isopycnal streamfunction and the streamfunction derived from the time-mean fields is the deviation from the time-mean,

$$\psi_I^* = \overline{\psi_I} - \Psi_I, \tag{4.5}$$

which captures the motion that varies on a temporal time scale shorter than the time span of the applied time-averaging operator. On a time scale less than a couple of months, the transient mesoscale eddy field is known to be a dominating contribution to ψ_I^* (Ballarotta et al., 2013), and its nature is to oppose the time-mean flow. The residual that arises from the cancellation between these two cells is thus given by the isopycnal streamfunction $\overline{\psi_I}$, which advects tracers and other physical properties.

The mesoscale eddy field is not resolved in the coarse resolution 1° model and is instead represented by the eddy-induced transport velocities given by the implemented eddy parameterization. The isopycnal overturning streamfunction is here calculated as

$$\begin{aligned}\overline{\psi_I} = &\overline{\oint_0^{2\pi} \int_{\eta_B}^{\eta} v \, \mathrm{d}z \, R \cos(\theta) \, \mathrm{d}\phi} \\ &+ \overline{\oint_0^{2\pi} \int_{\eta_B}^{\eta} v_{\mathrm{GM}} \, \mathrm{d}z \, R \cos(\theta) \, \mathrm{d}\phi}\end{aligned} \tag{4.6}$$

where v_{GM} is the meridional component of the eddy-induced velocity field. The first term on the right hand side of eq. (4.6) is the overturning streamfunction associated with the mean-flow and the second term is the time-mean eddy-induced overturning streamfunction, which in the analysis that follows are compared to the high-resolution overturning streamfunctions Ψ_I and ψ_I^*, respectively.

4.3.1 Choice of temporal resolution

As seen from satellite altimetry, Frenger et al. (2015) reports that the mean lifespan of a Southern Ocean eddy is about ten weeks. This is supported by the study by Ballarotta et al. (2013), who uses a 1/4° global ocean model to show that an estimate of the overturning streamfunction obtained with the use of monthly-mean output fields captures the majority of the eddy variability. However, the present study uses a model of 1/10° resolution which possesses more energy at the high frequencies and large wavenumbers. To assess the difference in the representation of the residual meridional overturning circulation in the 1/10° model at different temporal resolution, we compute $\overline{\psi_I}$ of Htau05 with both monthly-mean and three-day mean model output.

The left panel of Figure 4.3 shows the ten-year mean of ψ_I^* between model year 33 and 42, calculated using monthly-mean fields. The right panel shows the same as the left panel, but calculated using three-day mean output. The characteristics of the eddy-induced overturning is discussed in the succeeding section, and here we focus on its dependence on temporal resolution only. The structure of ψ_I^* is more or less independent from the temporal resolution of the output fields, but its magnitude does vary. The minimum in the heavier water masses changes from $-10\,\mathrm{Sv}$ to $-14\,\mathrm{Sv}$ when the temporal resolution is increased, but the second

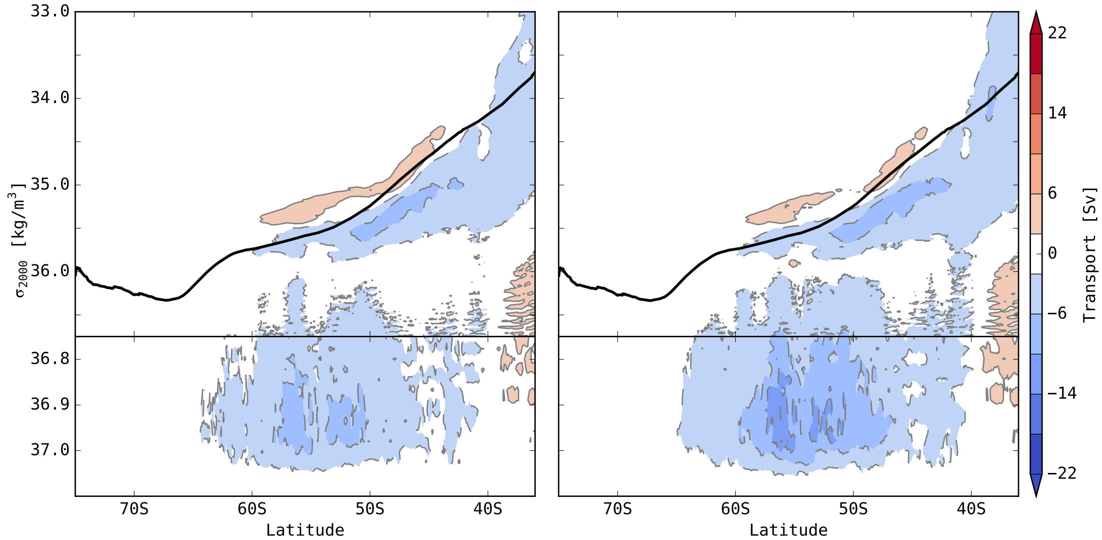

Figure 4.3: The left panel displays the ten-year mean eddy-induced overturning circulation ψ_I^* from the Htau05 experiment calculated with monthly-mean output fields. The right panel shows the same as the left panel, but calculated using three-day mean output. The time span is from model year 33 to 42. Units are in Sv, $1\,\mathrm{Sv} \equiv 1 \times 10^6\,\mathrm{m}^3/\mathrm{s}$, and color interval is 4 Sv. The black solid line is the zonal mean of the time-mean surface potential density field, and provides an approximate measure of the surface ocean. Note the non-linear y-axis.

minimum closer to the surface between 50°S and 40°S changes by less than 1 Sv. The latter minimum is associated with the overturning in the upper cell, which has been the primary focus in the discussion of eddy compensation in the Southern Ocean. Since this eddy motion appears to vary mostly on a time scale that exceeds a month, an appropriate estimate of the overturning metrics is possible to obtain by using monthly-mean fields. The minimum of the eddy overturning in the densest water is though underestimated by approximately 30% by this choice. The results presented in the subsequent section are all computed using monthly-mean fields since the main focus of this study is on the upper overturning cell.

4.4 Results

4.4.1 Background state overturning

Figure 4.4 presents the ten-year mean spatial structure of the meridional overturning circulation in the Southern Ocean from the two default simulations, as well as its decomposition, as function of potential density referenced to 2000 db. The decomposition of the overturning follows the procedure outlined in section 4.3 and the potential density axis was discretized into 200 equally-spaced levels between $1033.0\,\mathrm{kg/m^3}$ and $1037.5\,\mathrm{kg/m^3}$ for both model solutions. The black solid line in all panels is the zonal mean of the surface potential density field averaged over the same ten-year time span, and gives an approximate indication of the ocean surface.

The residual circulation (upper panels, Fig. 4.4) from both models in general show a quasi-adiabatic inflow of circumpolar deep water to the Southern Ocean in the density range

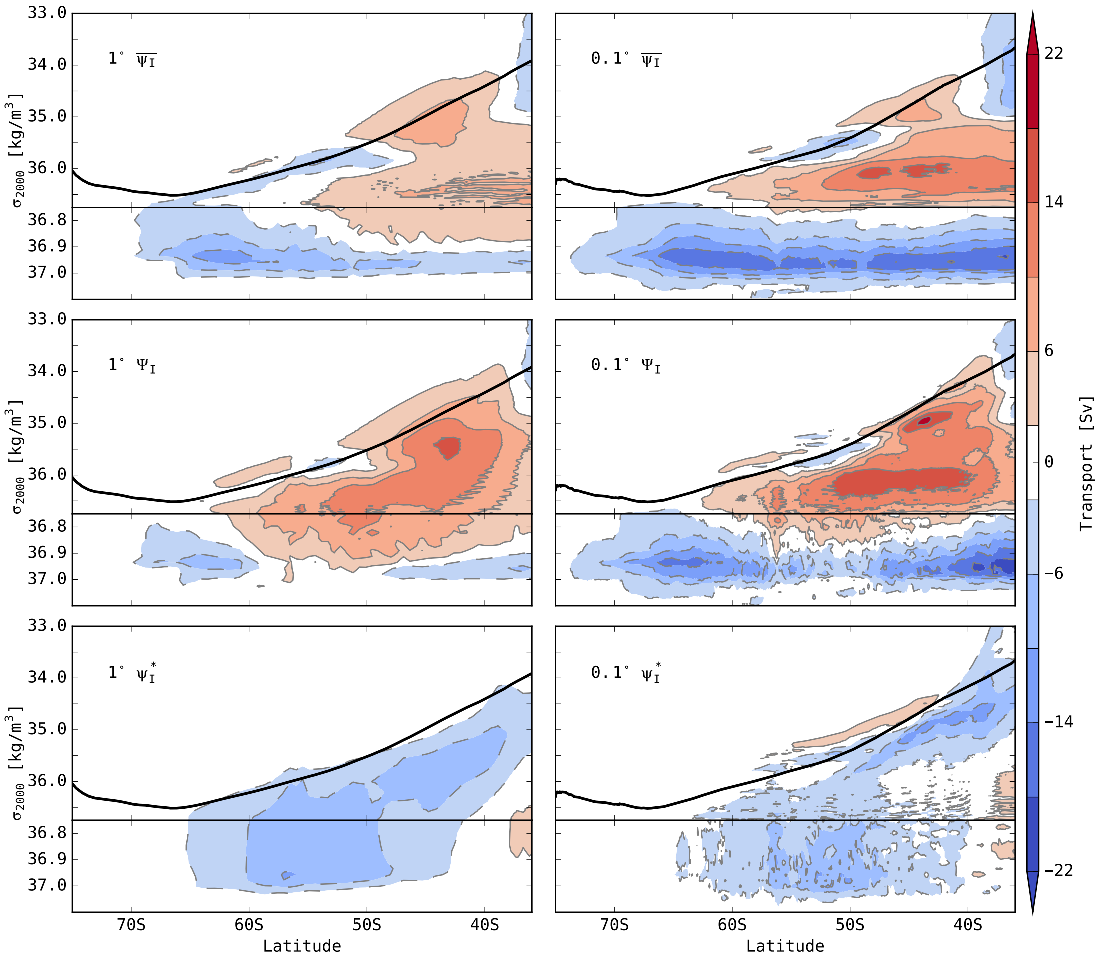

Figure 4.4: The Figure displays the residual overturning $\overline{\psi_I}$ (upper row), the overturning of the time-mean flow Ψ_I (middle row) and the bolus overturning ψ_I^* (lower row) for the control integration of the 1° model (left column) and the 0.1° model (right column). The overturning from the 1° model is the mean from year 290 to 299, whereas the overturning from the 0.1° model is based on a mean from year 16 to 25. The transient eddy overturning ψ_I^* is computed directly from the parameterized bolus velocities in the coarse resolution model. In the high resolution model, this overturning is obtained by subtracting Ψ_I from $\overline{\psi_I}$. Units are in Sv, $1\,\mathrm{Sv} \equiv 1 \times 10^6\,\mathrm{m^3/s}$, and color interval is 4 Sv. The black solid line is the zonal mean of the time-mean surface potential density field, and provides an approximate measure of the surface ocean. Note the non-linear y-axis.

$1036.5\,\mathrm{kg/m^3}$ - $1037.0\,\mathrm{kg/m^3}$ and a transformation and separation of water masses as the water upwells at higher southern latitudes. The water that upwells north of the separation point gains buoyancy at the surface and returns northward in the surface Ekman layer. This flow pattern is referred to as the upper cell (Farneti et al., 2015). Transformation of lower circumpolar deep water, the denser fraction of the water that enters the Southern Ocean, to bottom water between 65°S and 75°S is also seen in both model solutions, which replenish the bottom water masses that partly flows northward in the abyss and partly upwells due to mixing (Marshall and Speer, 2012). This circulation is referred to as the lower cell. Other cells, such as the anti-clockwise subtropical cell and anti-clockwise recirculation between 50°S and 55°S, are also seen at both model resolutions, but are not discussed further (see Farneti et al. (2015) for a thorough discussion on these cells).

The amount of dense water that flows into the Southern Ocean at 40°S, and subsequently upwells, is about 30 Sv in Hcont, but only ~ 12 Sv in Ccont. From the minimum and maximum of the lower- and upper cell, respectively, it is seen that the water that upwells to the surface divides approximately evenly between the two in Hcont, with an overturning of 15 Sv in the upper cell and 17 Sv in the lower cell. In Ccont, a substantial recirculation is seen in the lower cell, with a bottom water formation of 12 Sv between 70° and 60°S, but only 5 Sv leaves the domain to the north through the abyss. This is an expression of the weak formation of Antarctic Bottom Water in Ccont (Gent et al., 2011). The remaining 7 Sv that enters the Southern Ocean leaves through the upper cell. Similar residual overturning structures are also seen in the coupled model configuration of CESM, as well as the difference between the high and the low resolution runs, albeit with overall stronger amplitude due to overly strong modelled Southern Ocean winds (Gent and Danabasoglu, 2011; Bishop et al., 2016). In comparison to the multi-model study by Farneti et al. (2015), the upper cell strength of 7 Sv in Ccont is considerably weaker than the 12 to 18 Sv found in most state-of-the-art coarse resolution climate models forced with the CORE.v2 $1958 - 2007$ reanalysis product. This difference is at least partly explained by the fact that the Southern Ocean winds are subject to a $\sim 30\%$ intensification in this period.

The time series of the maximum and minimum of the upper and lower cell of the residual meridional overturning circulation from Hcont (upper right panel of Fig. 4.4) are shown by the black and green curve in Figure 4.5, respectively. Both time series show pronounced interannual variability that arises from the resolved eddy field, and an annual cycle is also visible. The maxima of the upper cell fall during the austral winter months where the zonal winds and the northward surface Ekman current are the strongest (See Yuan, 2004, for an observational estimate of the seasonality in the Southern Ocean winds). The minima of the bottom cell also occur during the winter months and is associated with the production of dense water due to an intense buoyancy loss to the atmosphere and brine rejection from sea ice formation. Also, neither time series possess any clear trend although the first two years of the lower cell appear to have a stronger (more negative) summer overturning. The same time series are also provided for Ccont (magenta and blue lines for the upper and lower cell, respectively) which are seen to share many features with Hcont, but with a more uniform annual cycle and a weaker circulation in general that was also reflected in the spatial structure of the residual overturning (upper panels, Figure 4.4).

Looking into the decomposition of the meridional flow, the overturning that arises from the time-mean velocity fields (middle panels, Figure 4.4) is overall stronger than the residual, and the subsurface maximum of the upper cell is also more comparable between the two models. This is not a surprise as the models are subject to identical surface boundary conditions and no cancellation from the transient eddies is present in this metric. A closed cell of clockwise circulation is also seen in both model solutions at the surface at about 1035 kg/m^3 and 45°S, again present in the coupled model solutions as well. It is also interesting to note that the

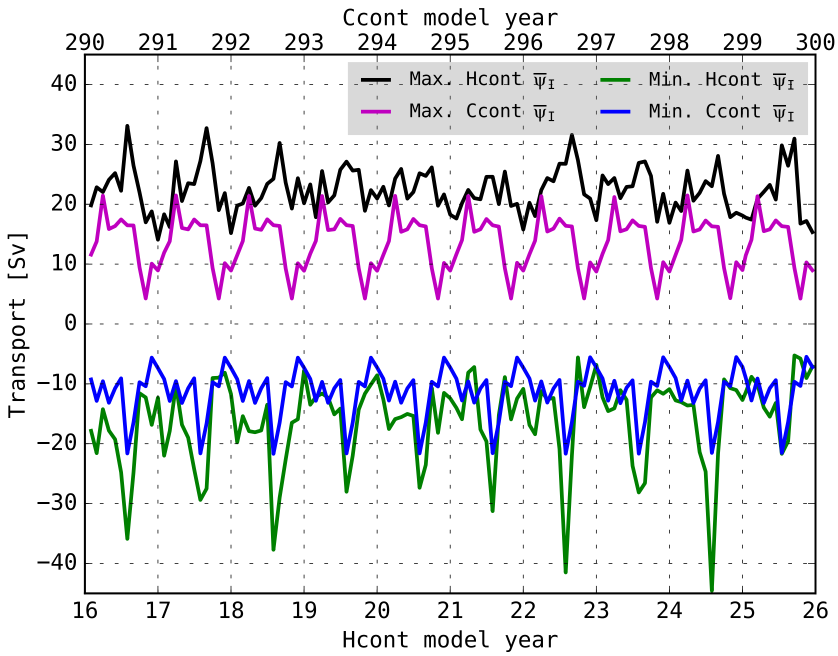

Figure 4.5: Time series of the Southern Ocean meridional overturning strength from the Ccont and Hcont experiments based on monthly means. The maximum streamfunction (black and magenta line for Hcont and Ccont respectively) reflects the subsurface strength of the upper cell and is extracted from south of 40°S. The minimum streamfunction (green and blue line for Hcont and Ccont respectively) is the strength of the lower cell at 60°S. All time series reflect circulation of water denser than 1035.7 kg/m^3. The upper and lower x-axis belong to the Ccont and Hcont time series, respectively. Units are in Sverdrups.

flow in the abyss between 60°S and 50°S is entirely eddy-induced in Ccont (left panel), but only partly at 0.1° resolution (right panel).

The flow driven by the transient eddies is different between the two models (lower panels, Figure 4.4). Whereas both models show that the eddy cell in general counteracts the time-mean flow and that the cells span the same latitude-density space, the minima of the eddy-driven overturning is differently located. The parameterized eddy field gives rise to a subsurface minimum in the densest waters between 50°S and 60°S and another subsurface minimum around 45°S and 1035.75 kg/m^3 (left panel). The explicit eddy field (right panel) also gives rise to the subsurface minimum in the densest water, but has a vanishing subsurface flow around 1036 kg/m^3 between 40°S and 50°S. This difference in spatial structure gives rise to different cancellations between the time-mean and the eddy-induced flow, resulting in the weaker residual overturning of the upper cell in the coarse resolution model.

4.4.2 Wind stress perturbation experiments

4.4.2.1 Circulation response

The model response that follows from the wind stress perturbations is reflected in the residual meridional overturning circulation, shown in Figure 4.6. The panels display the difference between the perturbation experiments and the control, in accord with the averaging intervals

Table 4.2: Drake Passage volume transport T_{DP} and effective thickness diffusivity κ. The thickness diffusivity metric is computed as in Jochum and Eden (2015), and consists of a vertical average between 200 m and 1000 m depth, a meridional average between 66°S and 38°S, and a complete zonal average. All measures are ten-year means, and are computed within the time spans outlined in Section 4.2. The Ccont value of κ is 521 m^2/s.

Exp.	κ [m^2/s]	T_{DP} [Sv]
Htau05	N/A	129
Htau15	N/A	180
Ctau05	521	124
Ctau15	561	147
Ctau20	690	196

mentioned in Section 4.2. The upper row of panels display the results from the high resolution model and the middle row of panels from the coarse resolution model. The left, middle and right column of panels is for the tau05, tau15, and tau20 experiment, respectively.

In terms of structure and absolute magnitude, Ctau05 and Htau05 show similar transient responses to the wind stress decrease. Both models show a weakening of similar magnitude of the upper overturning cell, and a smaller weakening of the lower overturning cell confined to high southern latitudes. The maximum of the upper overturning cell in Htau05 decreases from 15 Sv to 6 Sv, a 60% reduction, whereas the upper cell of Ctau05 collapses and finds a decrease of the upper cell maximum by 9 Sv, which corresponds to 130% relative decrease. The weakening of the lower cell corresponds to a northward retreat in both models, and the cell strength changes from 10 Sv to 6 Sv in Ctau05, and from 17 Sv to 10 Sv in Htau05, at 65°S. The ten-year mean Drake Passage transport decreases in Ctau05 and Htau05 by 12 and 4 Sv with respect to their control values, respectively (see Table 4.2), during the same time interval.

Shifting focus to the wind stress increase experiment, it is immediately seen that Ctau15 and Htau15 are subject to different transient model responses. Ctau15 finds a general increase of the upper cell and an increase, and displacement, of the maximum from 7 Sv to 14 Sv, as well as an increase in the zonal transport by 11 Sv. A greater value of the average thickness diffusivity, κ, is also seen (Table 4.2), but the change amounts to less than 10% compared to Ccont. Relatively small changes are seen in the lower cell between 70°S and 60°S, but a closer inspection also reveals that the positive changes seen in the densest waters between 60°S and the northern Southern Ocean reflects a weakening of the northward movement of bottom water. Surprisingly Htau15 shows a weakening of the upper cell and a relatively large increase in the Drake Passage transport by 47 Sv, opposite to the response seen in Ctau15 and different from the structure of the weakening seen in Htau05. The maximum of the upper cell decreases by about 3 Sv, but the lower cell increases in strength by several times the control value, fundamentally different to Ctau15. The inflow of water to the Southern Ocean increases in the 0.1° model, but the vast majority of the water enters the lower cell and leaves the domain through the abyss. The water that inflows in the 1° model increases as well, albeit weakly, but this water leaves the domain entirely through the upper cell.

The root cause of the different circulation responses to the stronger winds is at least partly due to the onset of deep convection in the Weddell Sea in Htau15. This response is similar

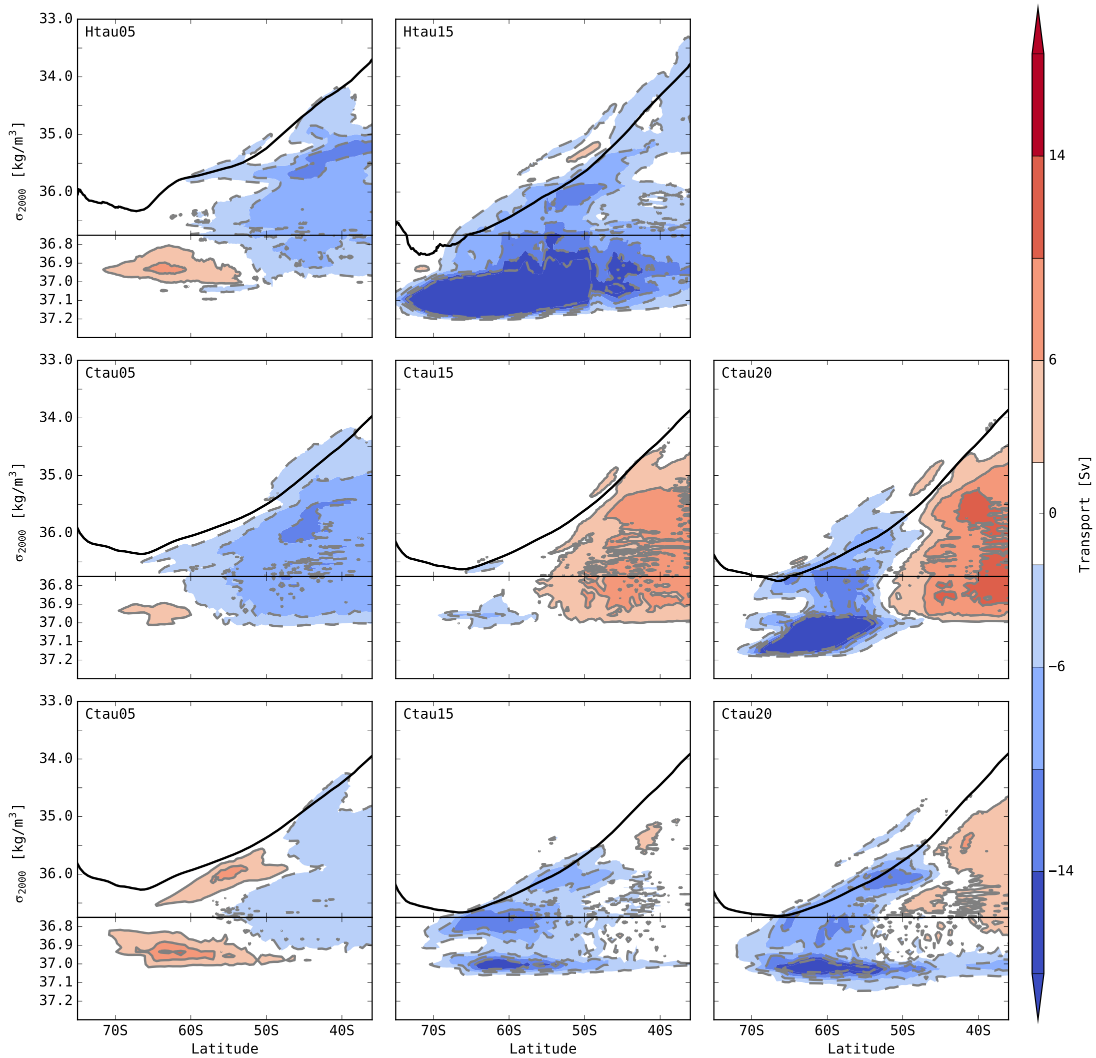

Figure 4.6: The figure shows the difference in ten-year mean estimates of $\overline{\psi_I}$ between the wind stress perturbation experiments and the control simulation. The left, middle and right column of panels show the difference for the tau05, tau15 and tau20 experiment. The upper and middle row of panels are with respect to the high resolution model and the coarse resolution model, respectively. The averaging intervals are outlined in Section 4.2. The lower row of panels is also from the coarse resolution model, but display the difference in $\overline{\psi_I}$ on centennial time scale (average is taken between model year 390 and 399). Note the non-linear y-axis.

to the model simulation presented in Cheon et al. (2014) in some aspects, and causes a sea ice retreat and an anomalous heat loss from the ocean to the atmosphere. A detailed account of the physical processes that lead to a destabilization of the water column is beyond the scope of the present study. It is though relevant to remark that minor differences in the Weddell Sea background stratification between Ccont and Hcont prevents deep convection in Ctau15 (the Weddell Sea hydrography is in general sensitive to model setup, see e.g. Kjellsson et al. (2015)). A stronger increase in the zonal wind stress in the coarse resolution model by

100% (Ctau20) does trigger Weddell Sea deep convection and enhances the lower overturning cell in a similar manner as seen in Htau15 (Figure 4.6, right middle panel), but the upper overturning cell appears less affected. Also, as seen from Table 4.2, both κ and the Drake Passage transport enhance by 32% and 44%, respectively, which indicate substantial changes in the ocean stratification.

The difference in involved physics in principle render a comparison of the eddy compensation between Ctau15 and Htau15 inappropriate, because the eddy-induced overturning component ψ_I^* of Htau15 is influenced by the transients of the bottom water formation. This difference in the behavior of the residual meridional overturning circulation in Ctau15, Htau15 and Ctau20 displays that the Southern Ocean model response is far from trivial when two overturning cells are present, as is the case in more comprehensive ocean models.

As previously emphasized in the literature (e.g. Munday et al., 2013), eddy compensation is a steady-state argument. The lower left and middle panel of Figure 4.6 display the difference in the ten-year mean residual overturning from Ctau05 and Ctau15 after 100 years worth of model integration and thus closer to model equilibrium. On centennial time-scale, both experiments unequivocally show that the initial response in the upper cell attenuates and that the transport anomaly in the lower cell grows. Ctau05 now features a more modest decrease in the upper cell maximum of 4 Sv, corresponding to a 43% reduction, and Ctau15 has regained its control value of approximately 7 Sv. Consistently, Ctau20 (lower right panel) also shows a weakening of the initial upper cell response with time. From the perspective of parameterized eddies, this comparison indicates that the adjustment time of the Southern Ocean overturning takes place on centennial time scale, possibly beyond, and that the bottom route as an outflow from the Southern Ocean appears to grow in importance as the overturning system equilibrates. This calls into question whether eddy compensation is meaningfully inferred from the residual meridional overturning as seen in complex model simulations, with a representation of both the upper and lower overturning cells and variable surface buoyancy forcing, that has not fully equilibrated.

Again comparing to the coupled model studies that similarly use CESM, Gent and Danabasoglu (2011) reports a 1.4 Sv increase of the upper cell 100 years subsequent to an increase of the zonal wind stress by 50%, and the recirculation in the lower cell is seen to increase as well (their Figure 3), but with a smaller outflow of the densest water. The present study similarly finds a weak response of the upper cell on a centennial time scale, though with a stronger outflow from the Southern Ocean in the abyss compared to Ccont. On decadal time scale, a comparison between the high resolution model responses is possible. With active deep convection Htau15 is different to its coupled model counterpart in Bishop et al. (2016) and finds a 20% weakening of the upper cell where they find a strengthening by 39%. However, both model finds a strengthening of the lower cell, which in their study is connected to a thinner austral winter sea ice cover in the Weddell Sea (see their Figure 13), much alike the physical response presented here.

4.4.2.2 Changes in the $1036.5\,\mathrm{kg/m^3}$ density surface

The change in the meridional slope of the Southern Ocean isopycnals is a salient measure pertinent to the discussion on the response of the circulation to a wind stress change due to the prevailing thermal wind balance. In addition, this metric should not be significantly influenced by the deep convection event in regions away from the Weddell Sea which allow us to indirectly infer the degree of compensation in Htau15. The upper panels of Figure 4.7 show the time-mean depth of the 1036.5 kg/m^3 potential density surface, henceforth denoted by $\sigma_{36.5}$, from Ccont (left) and Hcont (right). The remaining stereographic plots in the left column display the vertical displacement of the isopycnal between the wind stress perturbation experiments and the control integration for the coarse resolution model. The depth changes in the high resolution model is shown in the right column, and the lowermost plot shows the zonal mean difference in isopycnal depth for all experiments. The difference is taken between the ten-year means that are outlined in Section 4.2.

The choice to map the changes in $\sigma_{36.5}$ is motivated by Figure 4.4, which show that the upwelling in the Southern Ocean associated with the upper residual overturning cell is approximately along this density surface in both models. Both Ccont and Hcont finds that $\sigma_{36.5}$ sits at a depth that exceeds 1 km in the periphery of the Southern Ocean, and that it outcrops between 50°S and 60°S. This is in agreement with the residual meridional overturning circulation, which shows that water of density 1036.5 kg/m^3 is subject to upwelling and transformation in this latitude band.

Ctau05 and Htau05 both show a response that holds a zonal pattern; a deepening of the isopycnal at high southern latitudes and a rise in the mid-latitudes. This corresponds to a weakening of the meridional slope of $\sigma_{36.5}$ and a southward displacement of the outcrop line. Regional differences do exist between the two model responses, but the large-scale structure is similar. This is also seen from the lowermost panel, which shows that the peak zonally-averaged vertical depression of $\sigma_{36.5}$ (magenta lines) is about 50 m at high southern latitudes in both Ctau05 and Htau05.

True to both models, $\sigma_{36.5}$ rises at high southern latitudes, equivalent to a steepening, and is depressed farther to the north for the 50% wind stress increase. The rise of $\sigma_{36.5}$ in Ctau15 is rather modest and mirrors the response seen in Ctau05 to a high degree, which is also visible in the zonal mean (solid blue line). The high resolution model, on the other hand, has an increase of the isopycnal tilt of greater magnitude. The greater rise along the path of the Antarctic Circumpolar Current is expected to be the outcome of a complex interplay between the active deep convection in the Antarctic polar seas, the stronger winds and the transient eddy response. However, the deepening in the northern part of the domain takes place relatively far away from the deep convection zones and the response is therefore expected to follow the Ekman and eddy dynamics alone. Despite the two local maxima in the deepening in the Atlantic sector of Htau15, Ctau15 overall finds the strongest response in the northern part of the Southern Ocean. As seen from the zonal mean (blue lines), $\sigma_{36.5}$ displaces with $\sim$ 50 m in Ctau15 whereas Htau15 finds a zonally-averaged maximum deepening of about 25 m. This suggests a stronger parameterized sensitivity in Ctau15 to the zonal wind stress increase compared to Hcont15.

4.4.2.3 Northward heat transport response

To enable a direct comparison between Bitz and Polvani (2012), Bryan et al. (2014) and the present study, we investigate the total northward heat transport and its decomposition into

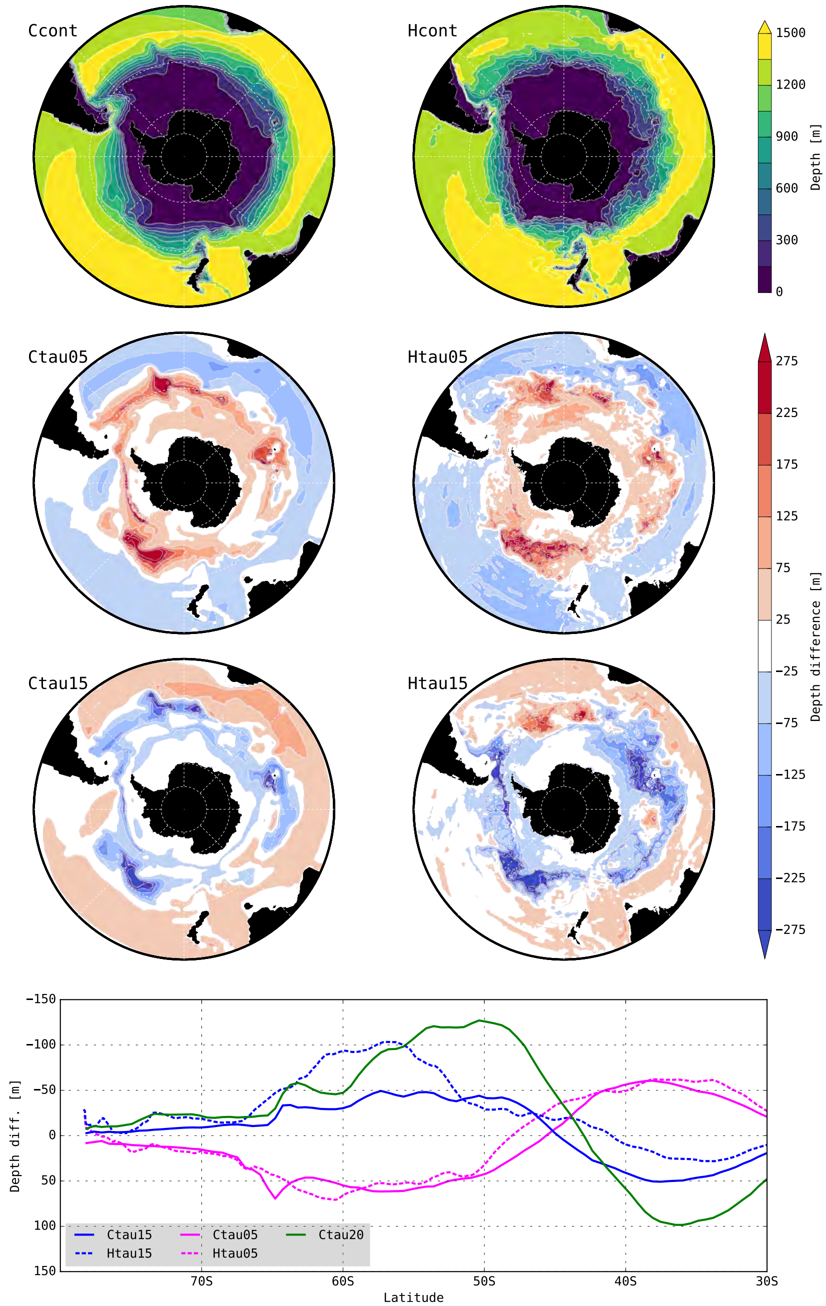

Figure 4.7: The panels display the depth and vertical displacement of the 1036.5 kg/m^3 isopycnal estimated from the time-mean potential density field referenced to 2000 db. The left and right column of plots is associated with the coarse and high resolution model, respectively. The upper row display the ten year mean depth of the isopycnal from Ccont and Hcont. The second and third row show the difference between the perturbation experiment and control for tau05 and tau15. The time-averaging intervals are stated in Section 4.2. The units are in meters. The lower panel displays the zonally-averaged depth difference as function of latitude.

contributions from the mean-flow and the eddy-induced circulation. The upper panel of Figure 4.8 shows the total northward heat transport, the middle panel the transport by the mean flow and the lower panel the eddy heat transport. The heat transport estimate from the coarse resolution model (solid lines) includes both the heat advection by the bolus velocities and isopycnal diffusion of heat, and the contribution from submesoscale eddies is not included. The total northward heat transport in the high resolution model (dashed lines) is obtained by integrating $\overline{v\theta}$ in the zonal and the vertical, and the eddy component is obtained by subtracting the product $\overline{v}\overline{\theta}$ from $\overline{v\theta}$ (here θ denotes potential temperature). Horizontal diffusion of heat due to the biharmonic operator is orders of magnitude smaller than the advective terms and is therefore not included.

The total heat transport of Ccont and Hcont (solid and dashed black lines, upper panel) both show that it is directed southward everywhere in the Southern Ocean, and that the two models deviate the greatest between 60°S and 50°S with about 0.1 PW. The estimates are in agreement with those modeled by (Bryan et al., 2014, their Fig. 2), but with a less strong discrepancy north of 40°S. The decomposition shows that the northward heat transport by the mean flow (middle panel) is overall weaker in Hcont. The eddy contribution (lower panel) is southward at all latitudes in both models, but the parameterized eddies suggest a greater southward eddy heat transport than Hcont, as was also the case in Bryan et al. (2014).

Ctau05 and Htau05 (magenta lines) agree that the northward heat transport decreases north of 55°S when the wind stress is reduced. This is primarily due to the changes in the mean flow, which follow from the reduced northward surface Ekman drift, as was also seen in the residual overturning response shown in Figure 4.6. This change is partly balanced by a reduced southward heat transport by the eddies. Ctau05 suggests a stronger weakening in the total northward heat transport, which is a result of a greater change in the mean flow heat transport compared to Htau05, in concert with a weaker parameterized eddy response.

As was already seen from the response in the residual overturning circulation and the density structure, Ctau15 and Htau15 (blue lines) respond differently to the 50% wind stress increase. Ctau15 shows a response that is opposite to that seen in Ctau05 in the total heat transport and its two components. Htau15, on the other hand, shows that the total heat transport becomes increasingly southward everywhere, with a peak southward transport beyond 1 PW around 60°S. Recalling that the eddy transport also encompasses the transient response from the convection in the Weddell Sea, the decomposition shows that both the mean flow and the eddy transport contributes to the increased southward heat transport. As was evident from Figure 4.6, the Htau15 circulation intensifies as function of the stronger winds, but the majority of the water densifies upon upwelling and enters the lower overturning cell. Figure 4.8 shows that this enhanced poleward flow also increases the amount of heat that is transported southward. A similar response is also seen in Ctau20 (green lines) where the southward heat transport is increased south of 50°S, mainly due to the changes in the mean-flow. The heat transport in the northern part of the Southern Ocean does not appear to be affected the same way as Htau15 by the convection in the polar seas. This is in line with the residual overturning response, seen in the middle right panel of Figure 4.6, where both the upper and lower cell strength of Ctau20 increases as function of the stronger wind stress.

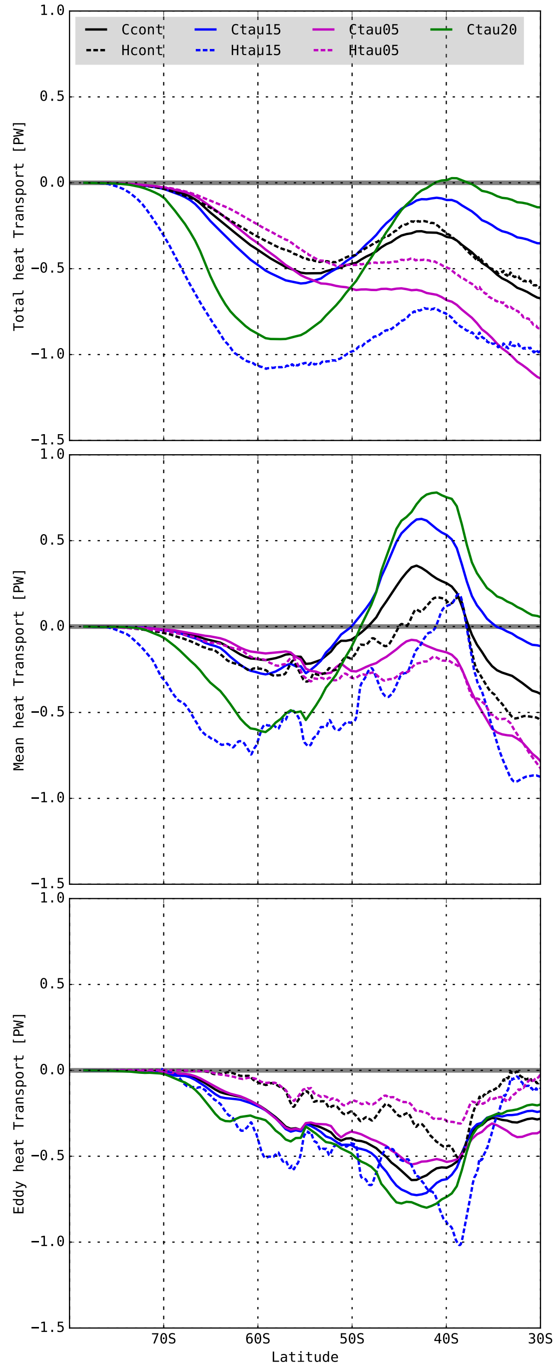

Figure 4.8: The upper panel displays the total northward heat transport for tau05 (magenta), cont (black), tau15 (blue) and tau20 (green). The middle and lower panel show the heat transport contributions from the mean-flow and from the eddy-induced flow, respectively. The results from the coarse resolution model are shown in solid lines and the high resolution model with dashed lines.

4.4.2.4 Buoyancy forcing response

An increase in the residual meridional overturning circulation must be accompanied with an increase in the transformation of water masses in the ocean mixed layer. We therefore examine the surface buoyancy forcing changes to the wind stress perturbations to understand the thermodynamical response associated with the changes in $\overline{\psi_I}$. We adopt the same approach as in Bishop et al. (2016) and compute the ocean surface buoyancy forcing as function of the surface heat fluxes, atmospheric fresh water contributions from precipitation and evaporation, prescribed river run-off and contributions from interactions with the active sea ice model. The upper panels of Figure 4.9 show the Ccont (left) and Hcont (right) ten-year mean surface buoyancy forcing fields. A positive buoyancy forcing indicates that the ocean surface became fresher and/or warmer. It is seen that the forcing field of Ccont and Hcont holds a similar structure; in the long term mean, the ocean surface losses buoyancy along the coast of Antarctica due to brine rejection, gains buoyancy below the sea ice due to ice melt (Abernathey et al., 2016), and warm western boundary currents release heat to the relatively colder atmosphere above. The largest difference between Ccont and Hcont is seen in the Indian sector, where a strong meridional gradient associated with the Antarctic Circumpolar Current is present in Hcont, but not in Ccont.

The zonally-averaged difference in surface buoyancy forcing between the wind stress change experiments and the control simulations is seen in the lower panel of Figure 4.9. Changes in

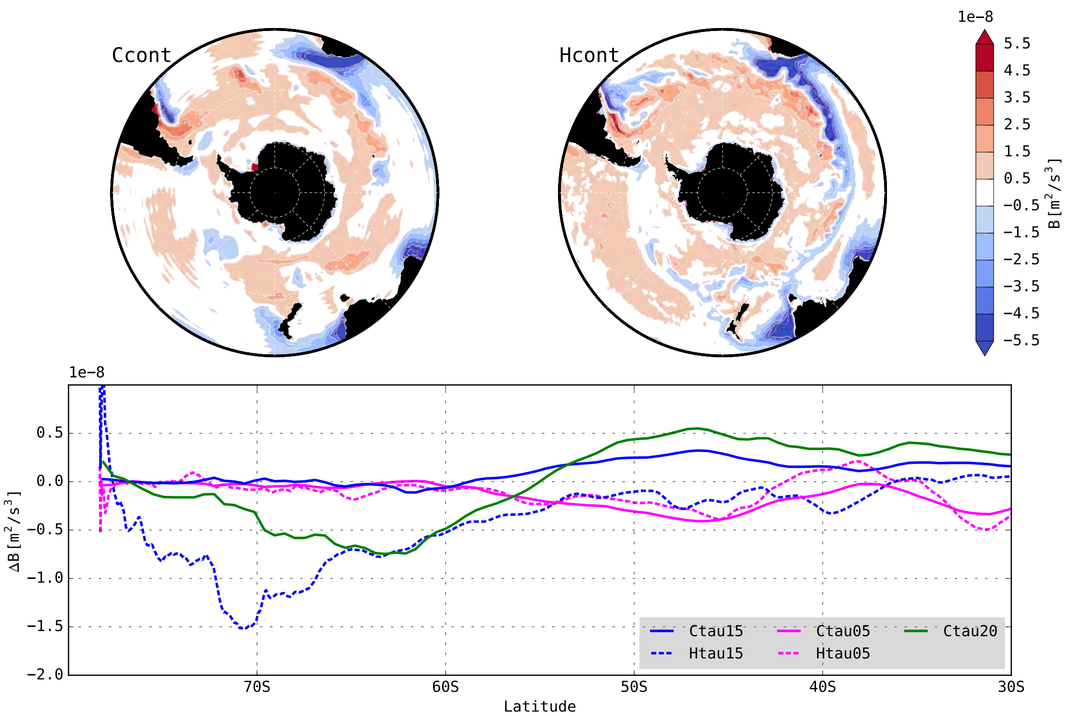

Figure 4.9: The upper left and upper right panel shows the ten-year mean buoyancy forcing in Ccont (left) and Hcont (right). The color interval is 1×10^{-8} m^2/s^3. A positive buoyancy forcing implies that the ocean surface became fresher and/or warmer. The lower panel shows the zonally-averaged difference in ten-year mean buoyancy forcing between the wind stress perturbation experiments and the control integrations.

the buoyancy forcing reflect changes in ocean surface properties and sea ice cover since the meteorological forcing fields are prescribed. The coarse resolution model response to the 50% wind stress increase and decrease is approximately linear, as was also the case in the changes of $\overline{\psi_I}$ and $\sigma_{36.5}$, and the modeled response is confined to north of 60°S. This latitude coincides approximately with the austral winter sea ice edge (Fig. 4.1). Ctau15 (blue solid line) gains more buoyancy in the region where water upwells, consistent with an equatorward displacement of the $\sigma_{36.5}$ outcrop latitude (Fig. 4.7), and an increased residual overturning circulation in the upper cell (Fig. 4.6). Vice versa, Ctau05 (solid magenta line) finds a decrease in the buoyancy forcing in accord with a relaxation of the isopycnal slope and decrease in the upper cell strength. The Htau05 buoyancy forcing response (dashed magenta line) is in many ways similar to Ctau05, although it suggests a buoyancy gain about 40°S relative to Hcont.

The changes in the buoyancy forcing in the model simulations that involve enhanced deep convection, Htau15 and Ctau20, behaves differently compared to Ctau15. Htau15 (blue dashed line) finds a zonally-averaged buoyancy loss throughout the Southern Ocean, most notably at 70°S where the response peaks at $-1.5 \times 10^{-8}\,\mathrm{m}^2/\mathrm{s}^3$. This is the expression of a strong heat loss to the atmosphere due to a reduced sea ice cover in this model simulation. This is also the region where bottom waters are formed in Hcont (Fig. 4.4), and explains the much stronger lower cell seen in Figure 4.6. Accordingly, Ctau20 (green solid line) also finds a strong heat loss at high southern latitudes and a stronger lower cell. The upper cell does not strengthen in Htau15 despite the stronger winds, and the buoyancy forcing response suggests that the reason is a thermodynamical constraint on the water mass transformation. This constraint is not present in Ctau20, where the mid-latitudes gains more buoyancy than in Ccont, why the upper residual overturning cell increases as function of the stronger winds.

4.5 Discussion

The decomposition of the residual meridional overturning circulation seen in Figure 4.4 shows that the lower cell in the control simulations is weaker in Ccont compared to Hcont. This is largely explained by differences in the mean-flow circulation (middle panels, Figure 4.4). In addition to the fact that it is overall weaker, it is also more or less absent between 60°S and 50°S and does not extend as far southward as seen in Hcont. This mismatch between the two simulations is most likely a function of the inability of the coarse resolution model to produce dense bottom waters, which is a common shortcoming of most CMIP5 models (Heuzé et al., 2013). In support of this conclusion, the buoyancy forcing fields from Ccont and Hcont (Figure 4.9) also shows that the Antarctic coastal buoyancy loss is greater in Hcont and therefore allows for a greater dense water formation.

The upper mean-flow overturning cell has a closer resemblance between the two models and the dissimilarity in the residual of the upper cell is primarily a function of the eddy-induced flow, which in the lower panels of Figure 4.4 is shown to have a different structure in latitude-density space. Specifically, the flow of water between 50°S and 40°S with densities about $1036\,\mathrm{kg/m}^3$ is poorly represented in Ccont as Hcont suggests a more surface-intensified eddy-driven circulation. More promising is the parameterized eddy-flow in the most dense water between 60°S and 50°S which compares better to Hcont. As seen from Figure 4.3, this part of the eddy circulation in Hcont is however underestimated in ψ_I^* by our choice of using monthly-mean output in the computation of $\overline{\psi_I}$. This is not the case with respect to the discrepancy in the upper cell, which is not an artifact of a misrepresentation of ψ_I^*, but rather originates in the limitations of the Gent-McWilliams parameterization. Differences in the surface buoyancy forcing are able to contribute to the difference in the residual overturning circulation as well. This effect is though ascribed a minor contribution given that the Ccont and Hcont forcing fields are similar in both structure and magnitude, as seen from Figure 4.9.

A similar result was found in the inter-model comparison study by Farneti et al. (2015). They estimated the eddy-induced overturning circulations that arise explicitly in the GFDL and Kiel ocean models of $1/4°$ horizontal resolution and compared it to the circulation from the coarse resolution version of the same models. Admittedly not able to resolve the full eddy field, especially not at high southern latitudes, the eddy permitting models do indicate that the parameterization either do not represent or significantly underestimates the eddy-induced flow in the lighter water masses close to the surface to the north of 50°S (see their Figure 18), which is the case in the present study as well. That a discrepancy between the resolved and parameterized eddy-induced overturning circulation exists is perhaps not unexpected. For example, it has previously been shown that a down-gradient closure for eddy fluxes of isopycnal thickness is of limited skill (Roberts and Marshall, 2000), and that ambiguity remains to the optimal choice of the thickness diffusivity (Eden et al., 2009).

The parameterized sensitivity of the circulation to the Southern Ocean zonal wind stress compares well to that of an eddy-resolving model for a wind stress reduction. On decadal time scale, Ctau05 and Htau05 find a reduction of the upper residual overturning cell of comparable magnitude and spatial structure (Fig. 4.6). This contrasts with Hallberg and Gnanadesikan (2006) that also investigate the overturning response on a 20 year time scale, but use a constant thickness diffusivity. In addition, both model simulations suggest a reduction of the meridional slope of $\sigma_{36.5}$, which is seen as a depression at high southern latitudes and a lift in the mid-latitudes of about 50 m in the zonal mean (Fig. 4.7). The same comparison for a 50% wind stress increase is made less straightforward by the complex model response of the Htau15 experiment. As noted in the results section, it might be reasonable to assume that the changes in $\sigma_{36.5}$ in the northern part of the Southern Ocean is unaffected by the deep convection in the polar marginal seas. Here Ctau15 shows a stronger response than Htau15 (Fig. 4.7), which might imply that the sensitivity is higher in the coarse resolution model than in the eddy-resolving model with respect to a wind stress increase. This inference is though complicated by the fact that the buoyancy forcing change is different between Ctau15 and Htau15 as well (Fig. 4.9).

Comparing the modeled heat transport responses to preceding model studies (Fig. 4.8), Bryan et al. (2014) finds that the parameterized eddy heat transport becomes increasingly southward between 60°S and 50°S due to stronger winds in a coupled model experiment. Moreover, they find that an eddy-resolving model obtains an eddy response of opposite sign in an identical forcing scenario. In the wind stress reduction experiments analyzed in this study, the parameterized and resolved eddy field both result in a consistent weakening of the southward heat transport, and the largest response is found between 40°S and 50°S. Also, where Bitz and Polvani (2012) show that the parameterized response is stronger than the response by the explicit eddies in an ozone forcing experiment, we here demonstrate the opposite case with prescribed atmospheric forcing. This latter point is also true for the 50% wind stress increase experiments, where the explicit eddies respond strongest, even in the northern part of the domain away from the Antarctic convective zones. This inconsistency with past studies is likely the result of differences in experimental setup and the presence of ocean-atmosphere feedbacks in the coupled simulations.

The disparate transient overturning responses simulated in the Ctau15 and Htau15 experiments, displayed in the middle column of panels in Figure 4.6, also deserve more attention. Despite ambiguity in terms of adjustment time and amplitude, the response seen in the Ctau15 experiment in general aligns itself with previous coarse resolution eddy-parameterizing general circulation model studies that show that the upper residual cell increases in strength as function of stronger zonal wind stress (Gent and Danabasoglu, 2011; Farneti et al., 2015). The message from high resolution model studies has been that a similar, though attenuated response is found when the eddies are explicitly resolved (Hallberg and Gnanadesikan, 2006; Munday et al., 2013). The weakening of the upper cell as seen from the Htau15 experiment contrasts with these studies, and appears to be controlled by the active deep convection in the Weddell Sea to some extent. The sea ice retreat that follows allows for an efficient loss of buoyancy that drives an enhanced formation of bottom water and an amplification of the lower cell (Fig. 4.9), much alike the results from the buoyancy forcing experiments presented in Jansen and Nadeau (2016).

A recent study by Hogg et al. (2017) finds a similar decrease of the upper residual cell strength in a global $1/4^{\circ}$ resolution general circulation model in an experiment where the Southern Ocean winds are subject to a poleward shift and intensification. In accord with the present study, their overturning response is concurrent with deep convection in the Weddell Sea. Evidently compensation of the wind-driven Southern Ocean upwelling is not only possible to achieve through increased eddy activity, but also through high-latitude deep convection, which complicates an assessment of the eddy-effect in isolation from non-equilibrated model runs. Whether this result has implications for past wind stress change experiments with relatively short adjustment time and changes in surface buoyancy fluxes is not clear. The literature on Southern Ocean wind stress change experiments however shows that it is not uncommon to invoke perturbations of similar magnitude as those tested in the present study (e.g. Gent and Danabasoglu, 2011; Dufour et al., 2012; Munday et al., 2013; Jochum and Eden, 2015; Bishop et al., 2016).

Lastly we note that observations have shown that the isopycnals have subsided throughout the Southern Ocean over the last several decades as a function of stronger westerlies, but with minimal changes to the isopycnal slope (Böning et al., 2008, their Figure 4a). Though not directly comparable to the model responses investigated here due to the simplicity of the applied wind stress perturbations and the integration length of the experiments, it is possible to compare the nature of the modeled response seen in Ctau15 and Htau15 to the observations. The observations show that the modeled adjustment of the $1036.5\,\mathrm{kg/m^3}$ density surface is of correct sign and is within the correct order of magnitude in the northern part of the domain, regardless of model resolution. However, neither of the models capture the deepening of $\sigma_{36.5}$ at the higher southern latitudes, and instead find an increase of the isopycnal slope and the

Drake Passage transport (Table 4.2). The high resolution wind stress reduction experiment, Htau05, which does not experience a reduced sea ice extent, also provides evidence for a finite sensitivity of the isopycnal slope to the zonal wind stress.

Appropriate to the discussion of the results presented here is also the short spin-up of the high resolution model, and the void of a control integration through the 50% wind stress change experiments, which are obvious drawbacks to the analysis of Hcont, Htau05 and Htau15. Figure 4.2 shows that the horizontally-averaged Southern Ocean temperature field drifts, and that Hcont is warmer than Ccont in the upper 1 km. The time series of the overturning strength of the upper and lower cell shown in Figure 4.5, as well as the Drake Passage transport time series seen in the bottom panel of Figure 4.2, do provide some comfort in that the metrics under investigation do not drift prior to the initiation of the perturbation experiments. A weakening of the lower cell with time is visible (green line, Fig. 4.5), a result that most likely stems from an insufficient spin-up of the deep ocean, and enters the results section as an overestimation of the strength of the lower cell. The drift in Hcont also influences the results from the wind stress change experiments as the ten year means obtained from the control and the perturbation experiments are shifted in time due to the absence of a sufficiently long control integration. However, given the short integration times involved in this study and the negligible drift in the Hcont overturning strength, we do not expect remaining drift to change the results significantly.

4.6 Summary

We compare forced ocean general circulation model simulations of 1° and 0.1° horizontal resolution to assess the ability of the eddy mixing parameterization as formulated in Danabasoglu and Marshall (2007) to mimic resolved eddy effects. A comparison of the Southern Ocean isopycnal streamfunction from the two models shows that the coarse resolution model has a weaker transport in both overturning cells with present-day wind stress magnitude. From a decomposition of the residual overturning streamfunction into a mean-flow and an eddy-induced component, it is evident that a different distribution of the eddy circulation across water masses is responsible for a substantial part of the dissimilarity seen in the upper cell of the residual overturning. Differences in the mean-flow overturning circulation also exist, but the implication of this discrepancy is most important for the lower overturning cell. For example, the deep flow in the coarse resolution model appears to be entirely eddy-driven between 60°S and 50°S, but this is not the case in the high-resolution model. In addition, the decomposition of the meridional heat transport reveals that the parameterized poleward eddy heat flux is overly strong in the Southern Ocean.

A zonally constant decrease of the Southern Ocean zonal wind stress south of 25°S results in a decrease of similar magnitude in the upper residual overturning cell in both models. Concurrently, the meridional isopycnal slope reduces and the northward meridional heat transport decreases, regardless of model resolution. An increase of the wind stress by 50%, on the other hand, is found to drive a complex model response in the 0.1° resolution model, but not in the coarse resolution model. On decadal time-scale, the transient response from the high-resolution model shows a weakening of the upper residual overturning cell by approx. 20%

and a strengthening of the lower cell driven by enhanced bottom water formation in the Weddell Sea. This follows from a retreat of the austral winter sea ice edge that allows for a strong loss of heat to the prescribed atmosphere. In contrast, the residual meridional overturning in the coarse resolution model finds a 100% increase of the upper cell on the same time-scale, and with no discernible change in the lower cell. A 100% wind stress increase experiment with the coarse resolution model also features a reduction in Antarctic sea ice and stronger residual overturning in the bottom cell, demonstrating that the complex model response is not limited to the high resolution model.

The main conclusion from the presented suite of experiments is that the parameterized eddies are able to mimic the nature of the resolved eddy field during wind stress change, but are less skillful in representing the residual meridional overturning circulation and the heat transport for present day wind stress. In addition we also emphasize that the dynamics of eddy compensation are probably more involved than what is found in simple models (e.g. Marshall and Radko, 2003). As exemplified by the high resolution model experiment with stronger wind stress, the interaction between the sea ice and the ocean results in buoyancy forcing changes that overwhelm the eddy response. It appears that the challenge for future general circulation model studies is to design clever experimental setups that clearly isolate the effect from the eddies yet preserve the complexity of the problem.

Acknowledgements

The research leading to these results has received funding from the European Research Council under the European Community's Seventh Framework Programme (FP7/2007-2013) / ERC grant agreement 610055 as part of the ice2ice project. The authors gratefully acknowledge the Gauss Centre for Supercomputing (GCS) for providing computing time through the John von Neumann Institute for Computing (NIC) on the GCS share of the supercomputer JUQUEEN at Jülich Supercomputing Centre (JSC). The authors are also grateful for computing resources provided by the Danish Center for Climate Computing, a facility build with support of the Danish e-Infrastructure Corporation and the Niels Bohr Institute, as well as for Alison Baker (NCAR) for her help setting up CESM on JUQUEEN, and ERDA developers and maintainers Jonas Bardino and Klaus Birkelund Jensen for providing the computational infrastructure to analyze the model output. The authors also thank Carsten Eden and Laure Zanna for constructive discussions, as well as the editor and two anonymous reviewers, whose comments greatly improved the manuscript.

4.7 Supplementary results

This section deals with three additional aspects of the simulations described in Poulsen et al. (2018), which were either briefly or not touched upon in the manuscript itself, but deserve more attention in the present dissertation.

The first aspect concerns the appearance and development of an open-ocean polynya in the Weddell Sea in the high-resolution 50% wind stress increase experiment, Htau15. A discussion of the polynya itself was intentionally left out of the original manuscript to maintain a clear focus throughout the text, but its effect on the Antarctic sea ice extent and the buoyancy forcing of the high-latitude Southern Ocean was included. For completeness, the mechanism that causes the polynya is discussed below, as well as the associated hydrographic changes.

The second aspect has to do with seasonality in the meteorological forcing fields and the decomposition of the isopycnal streamfunction. Figure 4.5 shows that a seasonal cycle is visible in the strength of both overturning cells, and hence meridional circulation related to the seasonal cycle may enter the isopycnal streamfunction decomposition as an additional contribution to the transient overturning circulation, ψ^*, and may lead to wrong interpretations of the eddy-driven circulation. A decomposition of the isopycnal streamfunction, taking the seasonal cycle into account, is therefore discussed below.

The third aspect is related to the time scale of the response in Southern Ocean overturning circulation to wind stress change. In Figure 4.6 it was shown that the circulation response in the coarse model attenuates with time and that the response on centennial time scale is substantially different from that seen on decadal time scale. To support this result, the temporal evolution of the overturning circulation is detailed in Section 4.7.3.

4.7.1 Weddell Sea polynya

In the model years which immediately follow the onset of the wind stress increase in Htau15, a polynya emerges and develops in the Antarctic sea ice in the Weddell Sea region during austral winter (Figure 4.10). The polynya is associated with ocean ventilation through deep convection, revealed by a deepening of the mixed-layer in the region of the polynya (red contour, Fig. 4.10). This process brings relatively warm and saline water to the surface due to the characteristics of the hydrography at high southern latitudes (Figure 4.11). The warm surface water keeps the polynya open during austral winter, and this in turn maintains deep convection through a loss of heat to the cold atmosphere above and a densification of the surface ocean. The fixed atmosphere, by construction, is not able to respond to the additional heat gained by the ocean and hence does not attenuate the heat exchange. As a consequence, deep convection does not cease before the subsurface heat reservoir is emptied and the evolution of the polynya is therefore quite unrealistic. Two questions, however, merit further investigation; 1) what large-scale circulation changes are associated with the polynya and 2) which process, caused by the increase of zonal wind stress, is responsible for the onset of deep convection?

4.7.1.1 Circulation changes associated with deep convection

Enhanced production of dense water at high southern latitudes, as function of the heat loss to the atmosphere within the polynya, results in a stronger meridional density gradient across the Southern Ocean. This in turn increases the baroclinic transport of the Antarctic Circumpolar Current in the model (Table 4.2), a well-known response documented in several past studies, e.g. Hirabara et al. (2012); Cheon et al. (2014); Martin et al. (2015); Pedro et al. (2016); Behrens et al. (2016); Hogg et al. (2017). The stronger production of dense water is also seen in the isopycnal streamfunction where the bottom cell strengthens following the opening of the polynya (upper middle panel, Fig. 4.6). Perhaps the most important effect, although more subtle to explain, is the influence of the polynya on the upper overturning cell, which in

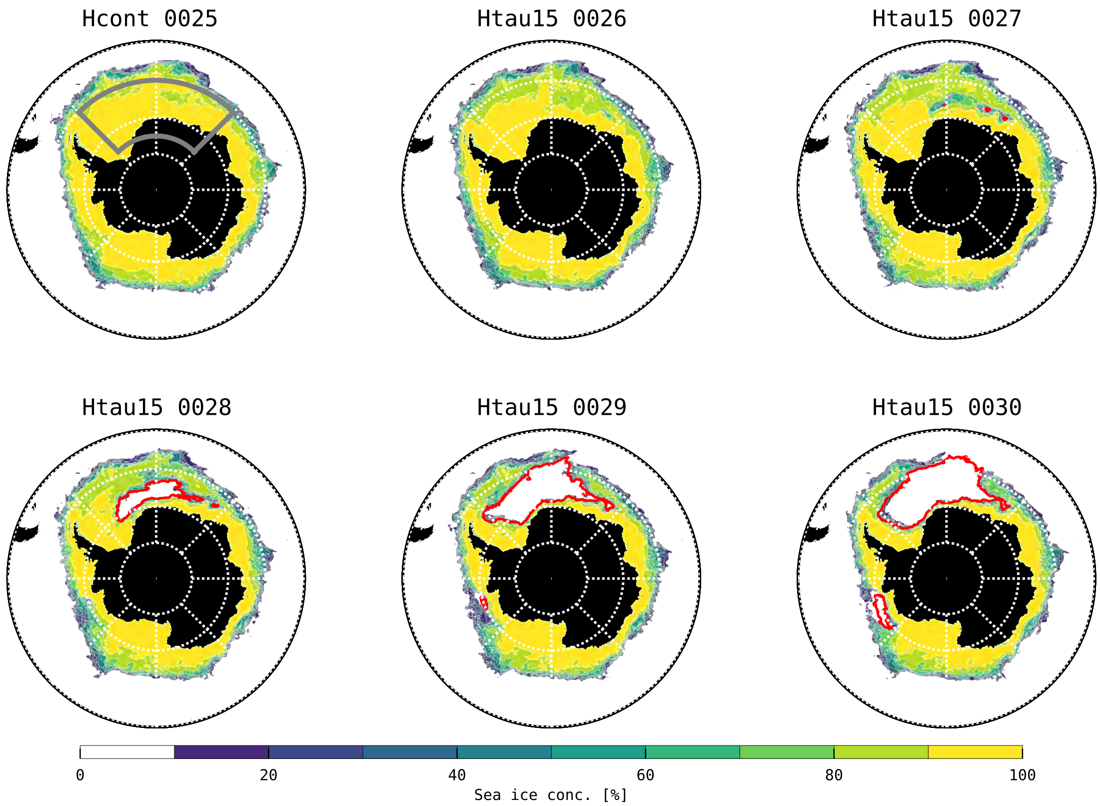

Figure 4.10: Consecutive austral winter-mean (July-August-September) Antarctic sea ice concentration maps following the onset of the 50% wind stress increase in the 0.1° model (Htau15) January 1st model year 0026. The upper left panel displays the winter-mean sea ice concentration from the last year of the control integration before the perturbation is applied. The red contour is the 1 km depth contour of the austral winter mixed-layer depth. The gray contour in the upper left panel displays the study area for the hydrographic sections presented in Figure 4.11, 4.13 and 4.14.

Htau15 is seen to weaken despite a stronger northward Ekman current. Figure 4.9 shows that the buoyancy gain decreases in Htau15 compared to Hcont throughout the Southern Ocean in the zonal average. Since an increased overturning circulation in the upper cell requires an enhanced buoyancy gain to transform water to a lighter density class at an increased rate, the buoyancy forcing response suggests that the explanation for the weaker upper cell is rooted in thermodynamics.

As seen in Figure 4.12, the spatial pattern in buoyancy forcing change is mainly controlled by changes in sea surface temperature, an expected result since the meteorological forcing fields are prescribed. It is seen that there is a systematic buoyancy loss in the region where sea ice is no longer present during austral winter. This buoyancy loss is an expression of at least two effects; firstly, the insulating effect from the sea ice is lost and exposes the ocean surface to the cold winter atmosphere, and secondly, relatively warm water reaches the surface via deep convection in the region and increases the temperature contrast at the atmosphere-ocean interface. Northward movement of the isopycnal outcrop position, implied by the lower right

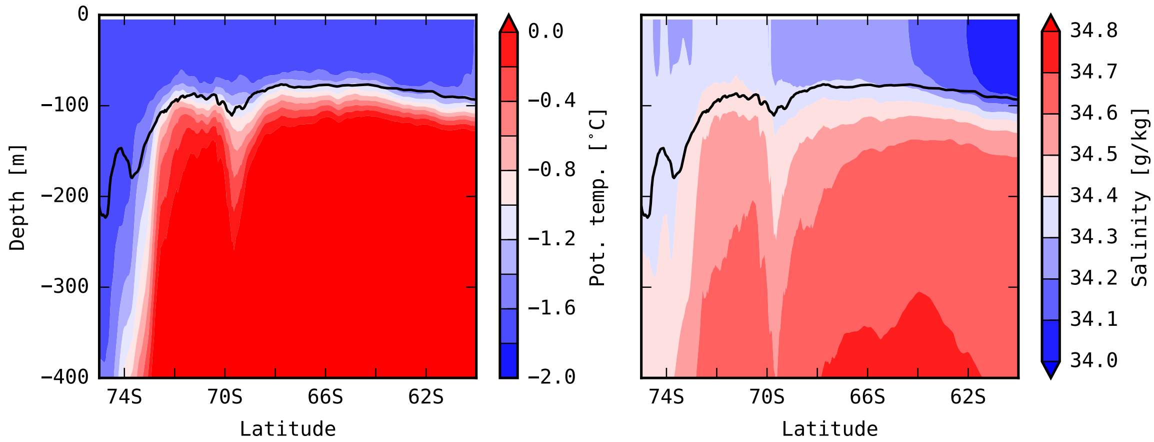

Figure 4.11: Zonally-averaged potential temperature (left) and salinity (right), within the box drawn in gray in Figure 4.10, for the winter-mean (June-July-August) of year 25 of Hcont. This is the austral winter before the onset of the wind stress increase January 1st year 26. The black contour is the zonally-averaged winter-mean mixed-layer depth. The dip in temperature and salinity about 70°S is a result of zonal averaging along the coastline of Antarctica where coastal polynyas are present, which are associated with sea ice production and brine rejection.

panel in Figure 4.7, results in negative sea surface temperature anomalies in the Pacific and Indian Ocean sectors between 40°S and 60°S, and are associated with ocean buoyancy gain. However, a large area of positive sea surface temperature anomalies in the Atlantic Ocean sector, related to a relative buoyancy loss, is also present and ultimately gives rise to the negative buoyancy forcing change seen in the zonal average (Fig. 4.9). A contribution to this pattern may stem from horizontal advection by the subpolar gyre of the relatively warm water which emerges at the surface through deep convection at high southern latitudes in the Atlantic sector (streamlines, Fig. 4.12). Another contribution appears to be the result of southeastward horizontal advection of warm water from the east coast of South America via the Antarctic Circumpolar Current. On an assumption that this region of decreased buoyancy gain is important for the water mass transformation associated with the upper overturning cell, these advective processes appear as a possible explanation for the weakened upper cell overturning despite the stronger northward Ekman transport.

4.7.1.2 What causes the onset of deep convection?

Polynyas, and associated deep convection, in the Antarctic sea ice is a common phenomenon in freely running coupled coarse resolution earth system models with preindustrial forcing and atmospheric carbon dioxide concentration level (Lavergne et al., 2014). Southern Ocean deep convection is in fact the most common process by which coarse models produce bottom water masses, in contrast to reality where deep convection rarely occurs and Antarctic Bottom Water mainly forms on the continental shelf, which spills off into the abyss along the continental slope (Heuzé et al., 2013). Although the majority of coarse ocean models are able to simulate a production of dense shelf water, this newly formed water mass is mixed with surrounding water on its descend towards greater depth due to numerical entrainment and horizontal diffusion.

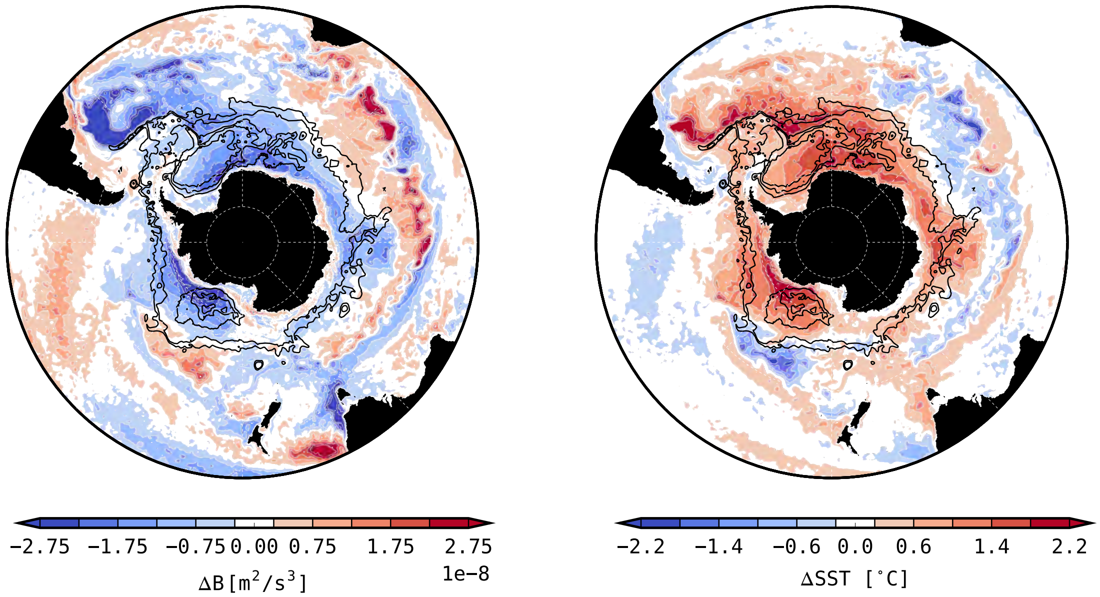

Figure 4.12: Difference in surface buoyancy forcing (left) and sea surface temperature (right) between Htau15 and Hcont for the ten-year mean between model year 33 and 42. Black contours are selected streamlines from the barotropic streamfunction of Htau15.

This erroneous introduction of relatively dense water at shallow depth weakens the vertical stratification in the polar marginal seas and is a likely explanation for why coarse models feature deep convection more frequent than observed (Heuzé et al., 2013; Kjellsson et al., 2015). That is, the polar water column stability in coarse resolution coupled models is more sensitive to the model's internal variability.

Dufour et al. (2017) show that an ocean model of increased horizontal resolution (e.g. 0.1°) better preserves the properties of the overflow waters along the continental slope, which results in a stronger and more realistic polar ocean stratification. One would therefore expect the water column stability in Ccont to be more sensitive to a surface hydrographic anomaly, for example introduced through a change in forcing, than in Hcont. The opposite scenario is however found to be the case in the wind stress increase experiment; Ctau15 stays stable whereas Htau15 features a multi-year deep convection event. Looking into the austral winter stratification in the region where the polynya emerges (Fig. 4.13), it is seen that Hcont is weaker stratified than Ccont, mainly because the salinity stratification in Hcont is weaker. This difference in stratification is attributed to the different initial conditions used for the two models, as well as different model spin-up length.

Both Cheon et al. (2014) and Hogg et al. (2017) show that it is possible to force the opening of a Weddell Sea polynya through an increase or meridional shift in the southern hemisphere westerlies, and Hirabara et al. (2012) also find that local wind stress curl anomalies may play a role. The study by Cheon et al. (2014), which implement a perturbation of similar type to the one introduced in Htau15, find that increased surface Ekman current divergence mechanically lifts the polar ocean water column and hence allows the warm subsurface water to reach and

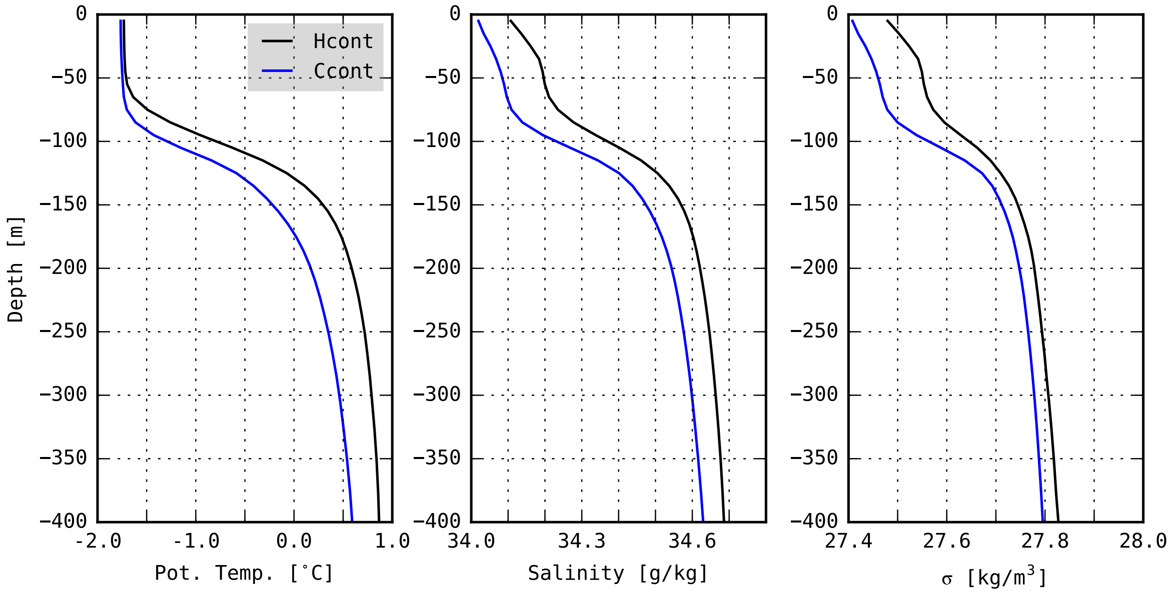

Figure 4.13: Austral winter-mean (June-July-August) potential temperature (left), salinity (middle) and potential density (right) profiles, horizontally averaged within the gray box shown in the left panel of Fig. 4.10. The black lines are from Hcont year 25 and the blue lines are from Ccont year 299, the model years prior to the wind stress perturbation.

melt the sea ice during austral winter. A polynya eventually forms and a loss of heat to the atmosphere during the winter months results in the onset of deep convection and a reoccurring polynya in the subsequent years.

To verify whether this hypothesis holds for Htau15 as well, Figure 4.14 shows the evolution of zonally-averaged austral winter hydrography for the region where the polynya emerges (gray box, left panel in Figure 4.10). The austral winter of year 26, the first winter following the increased wind stress, shows a cooling and freshening of the water immediately below the base of the mixed-layer (indicated by the green and black line), and an increased salinity and higher temperatures in the mixed-layer itself. These hydrographic anomalies are more clear in the subsequent year, and the mixed-layer is seen to deepen at 65°S as well. The presence of deep convection is unequivocal from year 28 and onwards; the mixed-layer deepens below 400 m depth, the water column homogenizes and the polynya appears in the sea ice (Fig. 4.10).

Since both temperature and salinity increases with depth in Hcont (Fig. 4.11), the change seen in year 26 and 27 is not immediately indicative of a lift of the water column as suggested by Cheon et al. (2014). Also, a northward shift of the water column would be able to explain the changes seen in the mixed-layer, but not the changes seen below it. The slightly deeper winter mixed-layer during model year 26 and 27 in Htau15 compared to Hcont rather suggests that wind-driven mixing reaches to a greater depth and entrains warm saline water into the fresh and cold mixed-layer, a natural consequence of increased wind stress. Another likely contributor to the saltier surface polar ocean is strengthened upwelling of saline North Atlantic Deep Water due to the stronger winds, which according to Figure 4.4 takes place mainly between 50°S and 60°S. Since salinity mainly controls the density of sea water in polar conditions, the

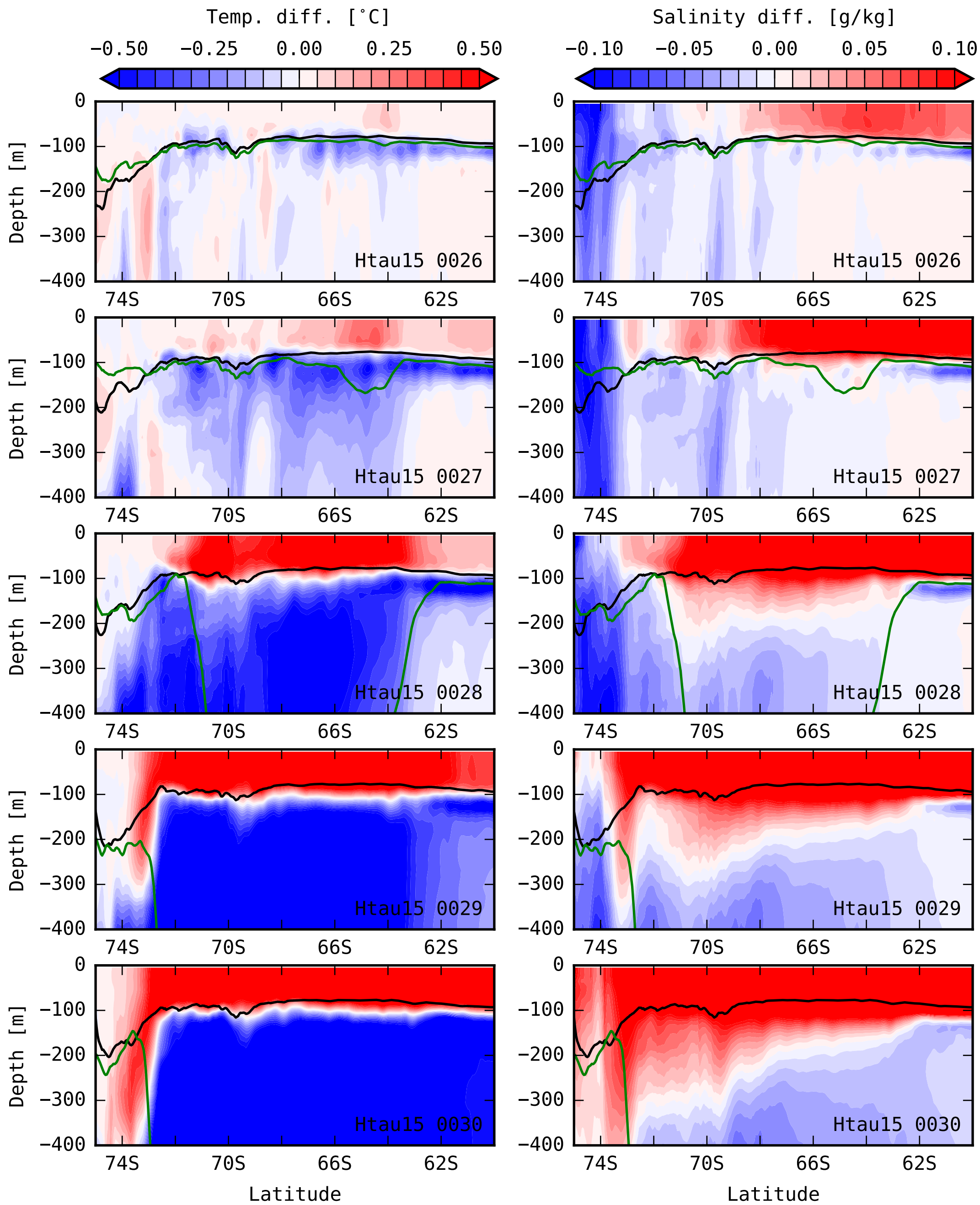

Figure 4.14: Difference in zonally-averaged potential temperature (left) and salinity (right) between Htau15 and Hcont for five consecutive austral winters (June-July-August) following the wind stress increase. Year 26 (upper panels) is the first austral winter after the application of the wind stress perturbation. The zonal averaging is within the gray box shown in Figure 4.10. The black and green line are the zonally-averaged winter-mean mixed-layer depth for Hcont and Htau15, respectively.

anomalously saline surface layer results in an unstable water column and deep convection.

It is interesting to note that both Bryan et al. (2014) and Bishop et al. (2016), who use the same high-resolution ocean model as in the present study, find increased polynya activity, or reduced sea ice cover, with stronger zonal wind stress in the Southern Ocean. Notably, Bishop et al. (2016) find a thinning of the austral winter sea ice in the Weddell Sea, associated with an intensified heat loss from high southern latitudes and a stronger overturning in the lower cell, when the zonal wind stress is increased by 50% in a coupled model configuration. The results presented here suggests that this sea ice response follows from increased salinity in the surface Southern Ocean which weakens the polar water column stability.

4.7.2 The influence of the seasonal cycle on the isopycnal streamfunction

Figure 4.15 shows the Hcont isopycnal streamfunction decomposition for the ten-year time span between year 33 and 42 using monthly-mean output. The left column of panels follow the same decomposition as shown in Figure 4.4 and hence the two decompositions are nearly identical (they only differ by the time interval in consideration). For the decomposition shown in the right column of Figure 4.15, the ten year time span has been divided into the four seasons and an isopycnal streamfunction decomposition was carried out for each season. A time-mean across the four seasons was subsequently applied. This approach reduces the sampling of correlations between isopycnal height and meridional velocity due to low frequency variability of characteristic time scale beyond a couple of months, such as the seasonal cycle. The greatest effect of this modified decomposition is seen in the lighter water masses close to the surface where the eddy-induced streamfunction is generally reduced.

From a water mass perspective, relatively dense water at the surface is transported southward when winter ends and the isopycnals move southward. Oppositely, relatively warm water is transported northward when summer ends and the isopycnals move northward. In density space, this transport associated with the seasonal cycle should appear as a positive overturning cell (clockwise circulation). Indeed, the weak positive overturning cell at the surface centered about 50°S disappears from the eddy-induced overturning cell when the effect from the seasonal cycle is reduced. The counter-clockwise cell further to the north, however, also reduces when the seasonal cycle is removed but the overturning direction does not have the signature of seasonal cycle transport thus described. This reduction may be linked to seasonality in the Agulhas retroflection region which is situated at these latitudes.

4.7.3 The time scale of eddy compensation

Figure 4.16 shows the temporal evolution of the strength of the upper and lower overturning cells in the Southern Ocean for the different model simulations considered in this chapter. First focusing on the upper cell, it is seen that both the coarse (solid lines) and high (dashed lines) resolution model experience an instantaneous Ekman response when the zonal wind stress is changed, followed by a more gradual return towards the unperturbed state. For Ctau05 and Ctau15, the gradual adjustment takes place on centennial time scale and still progresses in the last decade of the simulations (marked with the rightmost gray band). The shortness of the Htau05 experiment makes it difficult to understand whether the high resolution model obeys a

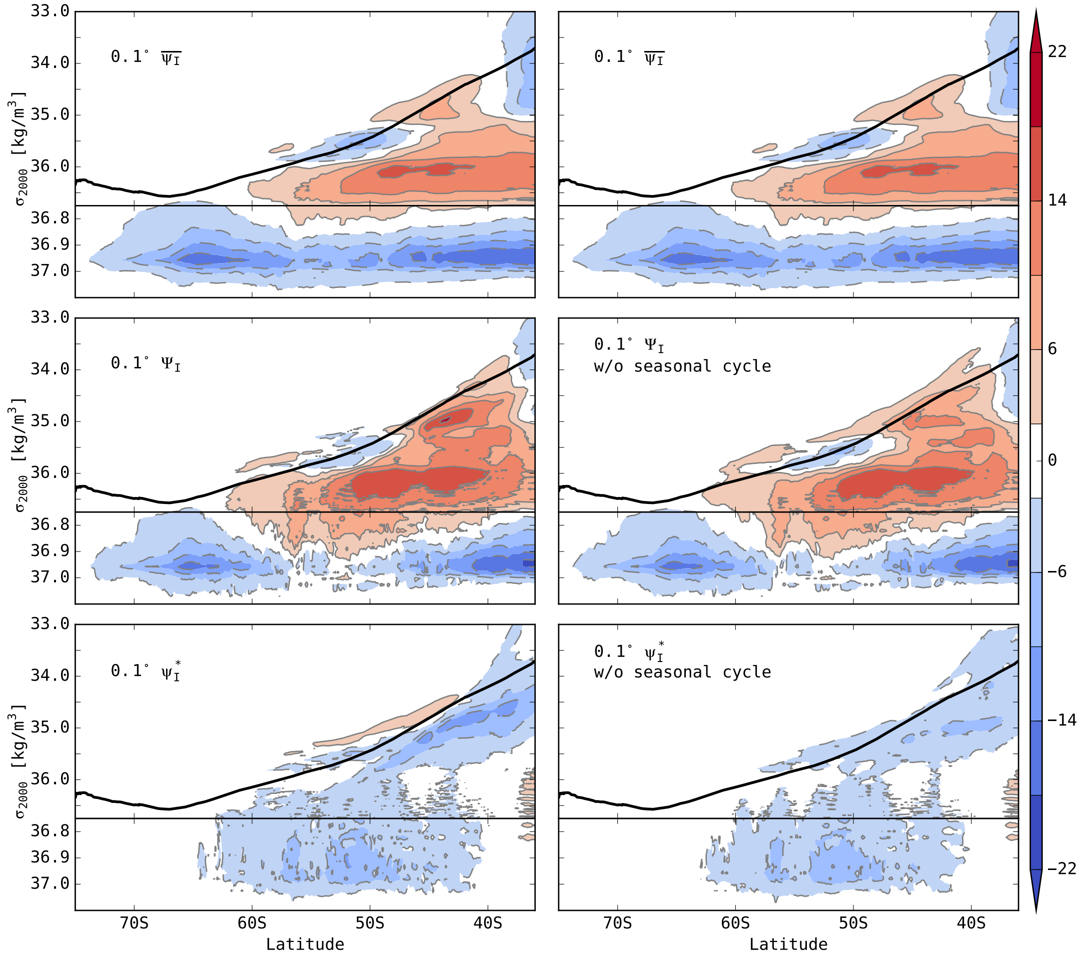

Figure 4.15: Decomposition of the Southern Ocean residual meridional overturning circulation with and without removing the seasonal cycle. The top row of panels is the residual streamfunction, the middle row is the circulation associated with the time-mean fields and the lower row is the eddy-induced circulation. The left column of panels is computed in the same manner as Figure 4.4, but for the time span between model year 33 and 42, and does not attempt to remove the seasonal cycle. The right column of panels shows the streamfunction decomposition where the seasonal cycle is taken into account.

similar adjustment time scale, but a similar trend in the overturning strength is though visible during the first ~ 20 years. Both Ctau20 and Htau15 adjust relatively faster following the wind stress change, but these overturning responses are complicated by the enhanced bottom water formation at high southern latitudes, evident in the lower panel of Figure 4.16. Furthermore, Ctau20 indicates that the overturning recovers with time.

A possible explanation for the gradual overturning adjustment is a slow response in the eddy-induced overturning, which in the coarse resolution model is parameterized solely in terms of the ocean stratification. In accord with simple Gnanadesikan (1999)-type models, a wind stress increase leads to a deepening of the oceanic pycnocline in the basins to the north and hence a steeper isopycnal slope in the Southern Ocean and a stronger eddy-induced circulation.

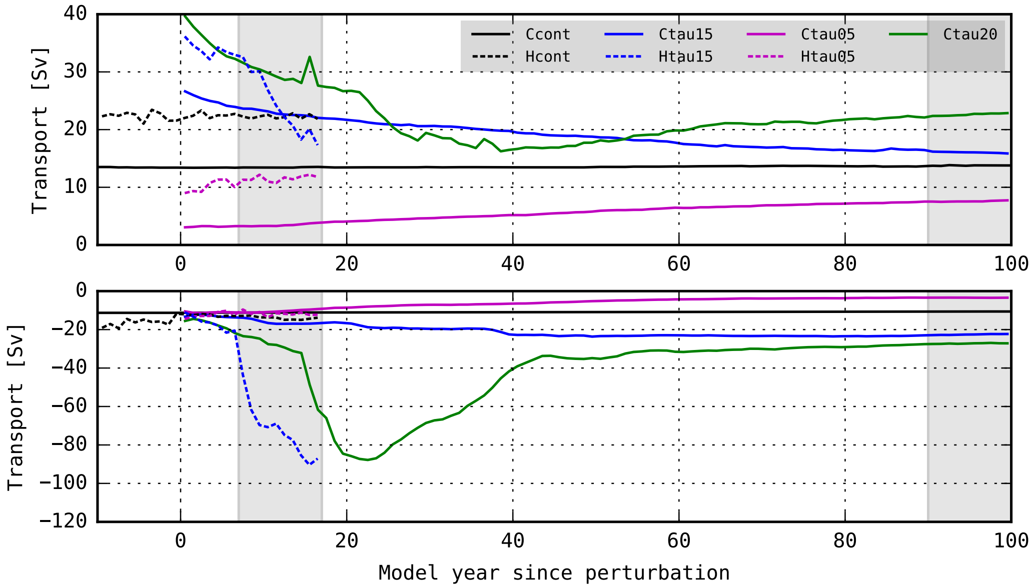

Figure 4.16: Time series of annual mean Southern Ocean meridional overturning circulation strength for the upper cell (upper panel) and for the lower cell (lower panel). The strength of the overturning cells is computed in accord with the method described in the caption of Figure 4.5. The gray bands indicate the time spans used for the analysis of the residual overturning circulation in Figure 4.6.

Figure 4.6 discusses the spatial structure of the overturning response within the time spans outlined by the gray bands in Figure 4.16, and it is visible that examining the response within the leftmost band will not reveal the full response. If the eddy-induced circulation is the origin behind the equilibration time scale, the eddy compensation effect requires centuries to fully develop.

Chapter 5

A geometric interpretation of Southern Ocean eddy form stress

Preliminary notes

Section 5.1-5.7 of the present chapter have been submitted to *Journal of Physical Oceanography*,

Poulsen, M. B., M. Jochum, J. R. Maddison, D. P. Marshall, and R. Nuterman, Submitted: A geometric interpretation of southern ocean eddy form stress. *Journal of Physical Oceanography*,

and the idea behind this work was conceived during a three-month exchange to University of Oxford, which was hosted by prof. David Marshall. In the framework presented in Marshall et al. (2012) and discussed in Section 2.2.5, eddy fluxes of momentum and buoyancy are reformulated in terms of the eddy energy and a set of parameters related to the geometry of the mesoscale eddy field. Specifically, the reformulation of the horizontal eddy buoyancy flux can be used to express the eddy transfer coefficient appropriate to the Gent-McWilliams parameterization as

$$\kappa = \kappa_{\mathrm{MMB}} = \alpha E \frac{\mathcal{N}_0}{\mathcal{M}^2},$$

which was also briefly discussed in Section 2.3.3. This expression for κ has been shown in Mak et al. (2017, 2018) to support an eddy saturation regime in idealized ocean models, in contrast to previous model studies with a constant value for κ. Moreover, Bachman et al. (2017) have shown that the skill of this specific eddy transfer coefficient in predicting κ inferred from a channel model of a baroclinically unstable current is higher than any of the other proposed closures (e.g. Visbeck et al., 1997; Eden and Greatbatch, 2008).

Motivated by the attractive properties of κ_{MMB}, this work explores the interpretation of the eddy geometry described by α as well as the spatial structure of α as seen from the control simulation of the eddy-resolving model outlined in Chapter 3. This work is useful because α generally varies in space and ultimately requires parameterization for use in coarse resolution ocean models. In particular, the hope is that the work presented in this chapter is sufficient to guide a future parameterization for α.

Abstract

This study exploits the geometric properties of the Eliassen-Palm flux tensor to formulate the eddy interfacial form stress in terms of the eddy energy and three geometric parameters. It is shown that the geometry describes an ellipse, whose size, shape and orientation with respect to the mean-flow determine the strength and direction of vertical momentum transfers. As recently proposed in Marshall et al. (2012), this framework is used to form a Gent-McWilliams eddy transfer coefficient which depends on the eddy energy and a non-dimensional geometric parameter α, bounded in magnitude by unity. Given the available eddy energy, α expresses the efficiency by which eddies flux buoyancy horizontally down the mean buoyancy gradient, an eddy flux equivalent to an eddy form stress along mean buoyancy contours. An eddy-resolving ocean general circulation model is used to estimate the spatial structure of α in the Southern Ocean and assess its robustness to external forcing change. In the limiting case where the horizontal eddy buoyancy flux is down-gradient, α averages to 0.13 and is characterized by a uniform vertical structure. Furthermore, a reduction of the zonal wind stress by 50% results in less than 5% change in α, but a $\sim 20\%$ decrease in eddy form stress magnitude. Upper ocean horizontal eddy buoyancy fluxes, however, mainly align with contours of mean buoyancy, a behavior which persists when rotational fluxes are removed, and results in a reduced α of 0.02. Conversely, horizontal eddy fluxes are predominantly down-gradient at greater depth where α is several times larger. Possible strategies to parameterize α are discussed.

5.1 Introduction

The Antarctic Circumpolar Current is embedded in a rich mesoscale eddy field, as readily seen from both satellite altimetry and realistic eddy-resolving model simulations (Storch et al., 2012; Roullet et al., 2014; Frenger et al., 2015; Stewart et al., 2015). The vertical structure of the eddy field is associated with undulated interior ocean neutral surfaces which enable a vertical transfer of horizontal momentum through eddy form stress (Johnson and Bryden, 1989; Wolff et al., 1991; Ivchenko et al., 1996; Olbers, 1998). This process is fundamental to the Southern Ocean as it causes a net downward momentum transfer and hence permits a governing momentum balance between surface wind stress and topographic form drag across shallow ridges and continents (Munk and Palmén, 1951; Masich et al., 2015). For adiabatic and geostrophic eddies the zonal interfacial stress additionally induces a meridional circulation which compensates Southern Ocean wind-driven overturning (Danabasoglu et al., 1994; Marshall, 1997; Marshall and Radko, 2003; Viebahn and Eden, 2010), with implication for the strength and structure of the residual circulation.

Recent studies have highlighted that eddy interfacial form stress is predominantly localized in several standing meanders within the circumpolar current (Thompson and Garabato, 2014; Masich et al., 2018). This zonal heterogeneity has also been reported in the upwelling associated with the residual overturning circulation (Tamsitt et al., 2017). The meanders form when large-scale flow navigates submarine topographic obstacles and are associated with elevated deep-reaching eddy kinetic energy (Hallberg and Gnanadesikan, 2001; Bischoff and Thompson, 2014; Barthel et al., 2017). In addition both eddy-resolving models and observations show that the strength of the Antarctic Circumpolar Current is remarkably insensitive to an intensification of the zonal wind stress (Hallberg and Gnanadesikan, 2006; Meredith and Hogg, 2006; Böning et al., 2008; Munday et al., 2013; Morrison and Hogg, 2013; Marshall et al., 2017; Poulsen et al., 2018). This is thought to be a consequence of concurrent strengthening of the eddy form stress which is able to balance the additional momentum input, a phenomenon known as eddy saturation (Straub, 1993).

The horizontal grid resolution of ocean general circulation models typically employed to study processes on centennial or millennial timescales does not permit explicit eddy form stress to develop. Instead the effects caused by the stress need to be introduced through parameterization, and the ability to represent Southern Ocean eddy form stress constitutes a key measure to assess the quality of any proposed closure. Presently the most common approach is to use a skew-diffusive flux scheme with the diffusivity taken proportional to the isopycnal slope (Gent and McWilliams, 1990; Griffies, 1998). This choice ensures a removal of available potential energy from the large-scale flow, a fundamental property of baroclinic instability. The implementation of this scheme, however, requires a specification of an eddy transfer coefficient κ. Previous attempts to estimate κ based on inferred divergent eddy buoyancy fluxes find that it is a function of both time and space, and locally may be of negative sign (e.g. Roberts and Marshall, 2000; Eden et al., 2007b). Different closures for the transfer coefficient as function of ocean stratification (Visbeck et al., 1997; Ferreira et al., 2005) or local eddy kinetic energy (Eden and Greatbatch, 2008) have been proposed, yet none of these has emerged as superior or able to support an eddy saturation regime (Eden et al., 2009; Farneti et al., 2015; Jochum and Eden, 2015).

Marshall et al. (2012), in a quasi-geostrophic context, introduces a framework in which to parameterize eddy fluxes based on the inherent geometric properties of the Eliassen-Palm flux tensor. This framework revolves around a reformulation of the Reynolds and interfacial form stresses in terms of the total eddy energy and five bounded dimensionless parameters, related to the geometry of the eddy field. Provided with a prognostic equation for the eddy energy, the main hypothesis is that the bounds on the involved parameters render the eddy parameterization problem more tractable. A corollary that follows from their conceptual framework is a new expression for κ in terms of the eddy energy E, oceanic stratification and a dimensionless parameter α,

$$\kappa = \alpha E \frac{\mathcal{N}_0}{\mathcal{M}^2}, \tag{5.1}$$

where $\mathcal{N}_0$ and $\mathcal{M}$ refer to the local vertical and horizontal stratification, respectively. α, henceforth referred to as an eddy efficiency, carries information on the geometry of horizontal eddy buoyancy fluxes and is bounded by unity in magnitude. Results from implementation and analysis of eq. (5.1) in idealized model setups, using a constant value for α, have shown promising representations of inferred tracer fluxes (Bachman et al., 2017) and eddy saturation (Mak et al., 2017, 2018).

Formally the eddy geometry described in Marshall et al. (2012) is associated with two distinct ellipses; one in the horizontal plane associated with Reynolds stress, and one oriented in the vertical plane that relates to eddy interfacial form stress. The strength and anisotropy of the eddy fluxes are expressed through the size and eccentricity of the ellipses, respectively, and their orientation with respect to the background velocity shear determines the stability of the mean-flow. The Reynolds stress ellipse has been used in several past studies to diagnose eddy-mean flow interactions in various barotropic systems. Hoskins et al. (1983) studied eddy feedbacks in the atmospheric mid-latitude westerlies, Morrow et al. (1994) investigated Southern Ocean jet stability from satellite altimetry, and Waterman et al. (2011); Waterman and Lilly (2015) examined the jet stability in a western boundary current extension region using an idealized model. These studies, together with the attractive properties that emerge from the geometrically-informed transfer coefficient, eq. (5.1), suggest that a geometric perspective is useful to understand and parameterize eddy-mean flow interactions.

While the application of this approach to Reynolds stresses is well documented in the literature, little attention has been dedicated to the eddy interfacial form stress geometry which is encapsulated in α. Marshall et al. (2012) examined the spatial structure of α in a quasi-geostrophic model of a wind-driven gyre, demonstrating that its features relate to the large-scale circulation, but the structure of α in more complex settings is unknown. The most recent estimate for α is a spatially uniform value of 0.2, extracted from a highly idealized model of a baroclinically unstable current (Bachman et al., 2017).

The aim of the present study is twofold: firstly, to clarify the connection between the Eliassen-Palm flux tensor and its geometric interpretation in terms of two ellipses, and secondly, to diagnose the eddy form stress geometry in a global eddy-resolving general circulation. The latter objective is motivated by the desire to construct a parameterization for α for use in complex ocean models. The analysis presented in this study is focussed on the Southern Ocean where the vertical structure of the eddy field is of primary importance to the momentum balance. The present work can be seen as complimentary to the study by Stewart et al.

(2015) who examined the Reynolds stress anisotropy from both satellite altimetry and model output. Taken together these studies are intended to provide guidance towards the long-term goal of a unified parameterization of eddy stresses via the Eliassen-Palm flux tensor.

The plan of the paper is the following. Section 5.2 reviews the decomposition by Marshall et al. (2012) and outlines its geometric representation through two distinct ellipses. Based on the geometry, the eddy efficiency, α, is defined. As explained in e.g. Marshall and Shutts (1981) it is only the divergence of contributions to the eddy buoyancy flux which is dynamically active; a discussion on diagnosing divergent fluxes is therefore provided in Section 5.3. Section 5.4 describes the model setup and simulations carried out, as well as the computation of eddy statistics relevant to the geometric decomposition. Section 5.5 presents the geometric decomposition as seen from the numerical model and highlights noteworthy characteristics of α, with and without horizontal rotational fluxes. Discussion and summary then follows in Section 5.6 and 5.7, respectively.

5.2 Geometric framework

5.2.1 Eddy stress tensor

The eddy forcing of the time-mean quasi-geostrophic potential vorticity equation, F_q, is expressed through the divergence of the horizontal eddy potential vorticity flux. This forcing is in turn related to the eddy stress tensor E,

$$F_q = \nabla_h \cdot [\mathbf{k} \times (\nabla \cdot \mathsf{E})] \,, \tag{5.2}$$

where $-\nabla \cdot \mathsf{E}$ is the eddy forcing of the associated horizontal momentum equation. Here ∇ and ∇_h are the three-dimensional and horizontal divergence operator, respectively, and $\mathbf{k}$ is the vertical unit vector. Equation (5.2) involves two applications of the divergence operator, hence certain gauge freedom is permitted in the specification of E. As shown in Maddison and Marshall (2013) several natural choices for E exist. The eddy stress tensor of interest in the present study is

$$\mathsf{E} = \begin{bmatrix} -M+K & N & 0 \\ N & M+K & 0 \\ -S & R & 0 \end{bmatrix}, \tag{5.3}$$

which is on the same residual-mean form as the forcing tensor derived by Cronin (1996). Here M and N are the eddy Reynolds stresses,

$$M = \frac{\overline{v_g' v_g'} - \overline{u_g' u_g'}}{2}, \quad N = \overline{u_g' v_g'}, \tag{5.4}$$

R and S are the eddy interfacial form stresses,

$$R = \frac{f_0}{\mathcal{N}_0^2} \overline{b' u_g'}, \quad S = \frac{f_0}{\mathcal{N}_0^2} \overline{b' v_g'}, \tag{5.5}$$

and K is the eddy kinetic energy,

$$K = \frac{\overline{u_g' u_g'} + \overline{v_g' v_g'}}{2}. \tag{5.6}$$

u_g' and v_g' are the horizontal geostrophic eddy velocities, b' denotes the buoyancy deviation, f_0 is the Coriolis parameter and $\mathcal{N}_0$ is the buoyancy frequency. The overline denotes an appropriate time-mean.

Marshall et al. (2012) derive energetic bounds for the magnitude of the eddy Reynolds stress, $M^2 + N^2$, and the eddy form stress, $R^2 + S^2$. These bounds allow for an expression of the eddy stresses in terms of the eddy energy and five bounded dimensionless parameters related to the statistics of the eddy field. Following the discussion in Maddison and Marshall (2013), the decomposition of the constituents of E is

$$\mathbf{M} = (M, N) = \gamma_m L \cos^2(\lambda^*)\, \mathbf{r}_m \tag{5.7a}$$

$$\mathbf{R} = (R, S) = \gamma_b L \sin(2\lambda^*)\, \mathbf{r}_b, \tag{5.7b}$$

where

$$\mathbf{r}_m = [-\cos(2\phi_m), \sin(2\phi_m)] \tag{5.8a}$$

$$\mathbf{r}_b = [\cos(\phi_b), \sin(\phi_b)]. \tag{5.8b}$$

L is the weighted sum of the eddy kinetic and potential energies,

$$L = K + \frac{f_0^2}{\mathcal{N}_0^2} P, \tag{5.9}$$

where P is the quasi-geostrophic eddy potential energy,

$$P = \frac{\overline{b'b'}}{2\mathcal{N}_0^2}. \tag{5.10}$$

The angle λ^* expresses the partitioning of L between potential and kinetic energy,

$$\frac{f_0^2}{\mathcal{N}_0^2}\frac{P}{L} = \sin^2(\lambda^*), \quad \frac{K}{L} = \cos^2(\lambda^*), \tag{5.11}$$

and is bounded between 0 and $\pi/2$. The goal of the following subsections is to clarify the meaning of the geometric parameters ϕ_m, γ_m, ϕ_b and γ_b.

5.2.2 Reynolds stress ellipse

As shown in Waterman and Lilly (2015); Tamarin et al. (2016), the Reynolds stress geometry describes an ellipse. The geometry follows from an eigendecomposition of $\mathbf{E}_\mathrm{m}$,

$$\mathbf{E}_\mathrm{m} = \begin{bmatrix} -M+K & N & 0 \\ N & M+K & 0 \\ 0 & 0 & 0 \end{bmatrix}, \tag{5.12}$$

which is the horizontal velocity covariance matrix and is equivalent to the eddy stress tensor $\mathbf{E}$ in the absence of buoyancy fluxes, $R = S = 0$. The two non-zero eigenvalues of $\mathbf{E}_\mathrm{m}$ are,

$$\Lambda_\pm = K\left(1 \pm \gamma_m\right) \tag{5.13}$$

where

$$\gamma_m = \frac{\Lambda_+ - \Lambda_-}{\Lambda_+ + \Lambda_-} = \frac{\sqrt{M^2+N^2}}{K} \tag{5.14}$$

is the eddy momentum anisotropy, which in Marshall et al. (2012) is shown to be bounded as $0 \leq \gamma_m \leq 1$. Hence the eddy momentum flux tensor $\mathbf{E}_\mathrm{m}$ is positive semidefinite and describes a horizontal ellipse in the u'_g-v'_g plane with semi-major and semi-minor axis lengths given by the square root of the largest and smallest eigenvalue, respectively (see panel A of Figure 5.1). The anisotropy γ_m then describes the eccentricity of the ellipse and K determines its size. The eigenvector associated with the largest eigenvalue is directed along the semi-major axis, and its angle ϕ_m with respect to the zonal,

$$\tan\left(2\phi_m\right) = -\frac{N}{M}, \tag{5.15}$$

defines direction. The Reynolds stress decomposition, eq. (5.7a), readily follows by combining eq. (5.11), (5.14) and (5.15).

In accord with linear stability analysis (Pedlosky, 1987), the orientation of the ellipse with respect to the mean-flow determines the horizontal shear stability. In the idealized case of a meridionally-sheared zonal mean-flow as depicted in panel C of Figure 5.1, the mean-flow is stable when the ellipse leans with the shear and unstable when the ellipse leans into the shear, resembling the eddy-mean flow interaction implied by the "banana-shaped" eddy presented in Wardle and Marshall (2000). Note that the eddy-mean flow interaction is a result of the anisotropic part of $\mathbf{E}_\mathrm{m}$ since the isotropic contribution is associated with a purely divergent eddy momentum flux, which does not directly influence the dynamics (Waterman and Lilly, 2015). Accordingly, in the case of a purely isotropic eddy momentum flux, $\gamma_m = 0$, $\mathbf{E}_\mathrm{m}$ describes a circle and the interaction between the mean-flow and the eddy momentum flux vanishes, consistent with eq. (5.7a).

5.2.3 Eddy form stress ellipse

The geometry related to the eddy form stress additionally includes the fluctuation in buoyancy, b', and hence requires an additional spatial dimension for a complete description. The goal is therefore to deduce a 3×3 symmetric tensor with an eigendecomposition which results in eq. (5.7b), and which is associated with some geometry to be determined. Since $\mathbf{E}_\mathrm{m}$ is fundamentally a covariance tensor, consider the averaged outer product of

$$\left[-v_g', \quad u_g', \quad f_0 b'/\mathcal{N}_0^2\right]^T \tag{5.16}$$

with itself,

$$\mathbf{C} = \begin{bmatrix} M+K & -N & -S \\ -N & -M+K & R \\ -S & R & 2\frac{f_0^2}{\mathcal{N}_0^2}P \end{bmatrix}. \tag{5.17}$$

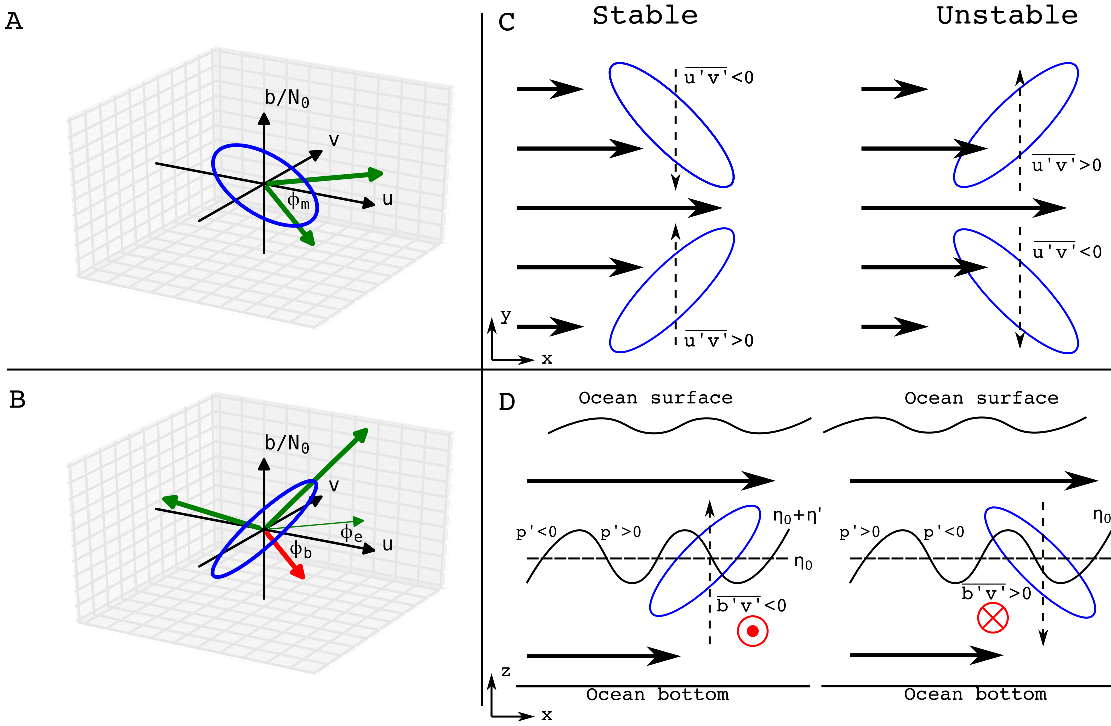

Figure 5.1: A) Ellipse (blue) in the horizontal plane with $\gamma_m = 0.8$, $K = 0.5$ and $\phi_m = -\pi/4$. The green vectors are the principal components which are aligned with the major and minor axes of the ellipse. ϕ_m is defined with respect to the ellipse major axis. B) Same as for A, but for the vertical ellipse with $\gamma_t = 0.9$, $E = 0.5$, $\phi_b = -\pi/4$ and $\phi_t = 5\pi/16$. The thin green vector is the projection of the largest principal component to the horizontal plane, here shown to provide sense to the direction of the ellipse. The vertical angle ϕ_t is not indicated, but is defined with respect to the ellipse major axis and the horizontal plane. The red vector has components $(R, S, 0)$ and is perpendicular to the ellipse and hence the two eigenvectors. C) Stability analysis of an idealized horizontally-sheared mean-flow with the use of the Reynolds stress ellipse. The shear sharpens when the ellipse leans with the shear and weakens when the ellipse leans into the shear. The dashed black arrows show the direction of the zonal momentum transfer. D) Stability analysis of an idealized vertically-sheared zonal mean-flow on the northern hemisphere with the use of the interfacial form stress ellipse. When $\overline{\eta' p_x'} > 0$, $\overline{b'v'} < 0$ and $S < 0$. Thus the ellipse leans with the shear, the lower layer exerts an eastward force on the upper layer, the momentum transfer is upwards (dashed black arrow) and the shear strengthens. The opposite is true for $\overline{\eta' p_x'} < 0$. Note that this interpretation also holds for the southern hemisphere because S changes sign when f_0 changes sign.

In combination with E_m it is possible to define

$$\mathsf{E}_\mathrm{b} = \mathsf{C} + \mathsf{E}_\mathrm{m} = 2\begin{bmatrix} K & 0 & -\frac{1}{2}S \\ 0 & K & \frac{1}{2}R \\ -\frac{1}{2}S & \frac{1}{2}R & \frac{f_0^2}{\mathcal{N}_0^2}P \end{bmatrix}, \tag{5.18}$$

which in the following is referred to as the eddy form stress tensor. The quadratic surface described by E_b is given by $\mathbf{x}^T\mathsf{E}_\mathrm{b}\mathbf{x} = \text{const.}$ (Riley et al., 2006), where $\mathbf{x}$ defines a displacement vector. Since, for any anti-symmetric tensor A, $\mathbf{x}^T\mathsf{A}\mathbf{x} = 0$, E_b and $\mathsf{E}_\mathrm{b} + \mathsf{A}$ define the same geometry for any such A. A particular choice for A results in

$$\mathsf{E}_\mathrm{b} + \mathsf{A} = 2\begin{bmatrix} K & 0 & 0 \\ 0 & K & 0 \\ -S & R & \frac{f_0^2}{\mathcal{N}_0^2}P \end{bmatrix}, \tag{5.19}$$

which shows that E_b relates to the eddy stress tensor E in the limit where $M = N = 0$, but deviates by the tensor entry associated with the scaled potential energy. Hence E_b does not result in the dynamically correct eddy form stress forcing, but it nonetheless provides a consistent interpretation of the geometry involved in eq. (5.7b), as will be shown in the following.

The E_b tensor given by eq. (5.18) has eigenvalues $2K$ and

$$\Lambda_\pm = L\left(1 \pm \gamma_t\right) \tag{5.20}$$

where

$$\gamma_t = \frac{\Lambda_+ - \Lambda_-}{\Lambda_+ + \Lambda_-} = \sqrt{\cos^2\left(2\lambda^*\right) + \sin^2\left(2\lambda^*\right)\gamma_b^2} \tag{5.21}$$

and

$$\gamma_b = \frac{\mathcal{N}_0}{2f_0}\sqrt{\frac{R^2+S^2}{KP}}. \tag{5.22}$$

γ_b constitutes an energetic bound on the eddy form stress magnitude and is equivalent to a characteristic measure of the anisotropy of the eddy buoyancy flux. Marshall et al. (2012) show that γ_b is bounded between zero and unity, which implies that $0 \leq \gamma_t \leq 1$ as well. Hence E_b is positive semidefinite and describes an ellipsoid, the three-dimensional generalization of the ellipse. As the case for E_m, the length of the principal axes of the ellipsoid are given by the square root of the eigenvalues. The horizontal orientation of the ellipsoid major axis, equivalent to the orientation of the eigenvector associated with the largest eigenvalue, Λ_+, is given by the angle ϕ_e,

$$\cos\left(\phi_e\right) = \mp\frac{S}{\sqrt{R^2+S^2}}, \quad \sin\left(\phi_e\right) = \pm\frac{R}{\sqrt{R^2+S^2}}, \tag{5.23}$$

which is defined with respect to the zonal direction. Since the horizontal orientation of the eddy buoyancy flux vector is defined by

$$\cos(\phi_b) = \frac{R}{\sqrt{R^2+S^2}}, \quad \sin(\phi_b) = \frac{S}{\sqrt{R^2+S^2}}, \tag{5.24}$$

it is seen that $\phi_e = \phi_b \pm \pi/2$ i.e. the major axis of the ellipsoid leads/lags the eddy buoyancy flux vector with $\pi/2$ in the horizontal.

Let T denote the 2×3 transformation matrix which rotates the ellipsoid about the vertical coordinate axis through an angle $-\phi_e$ and subsequently selects the points on the ellipsoid surface in the vertical u_g'-b' plane. Transforming E_b using T results in

$$\mathsf{E}_\mathrm{b}^\dagger = \mathsf{T}\mathsf{E}_\mathrm{b}\mathsf{T}^T = 2\begin{bmatrix} K & \frac{1}{2}\sqrt{R^2+S^2} \\ \frac{1}{2}\sqrt{R^2+S^2} & \frac{f_0^2}{\mathcal{N}_0^2}P \end{bmatrix}, \tag{5.25}$$

which describes the vertical ellipse at the intersection between the ellipsoid and the vertical plane aligned with its major axis (panel B in Figure 5.1). $\mathsf{E}_\mathrm{b}^\dagger$ has eigenvalues given by eq. (5.20), which implies that the ellipse has eccentricity γ_t and size proportional to $\sqrt{L}$, and its horizontal orientation, described by eq. (5.23), is perpendicular to the horizontal eddy buoyancy flux.

The vertical orientation of the ellipse is defined by the angle between its major axis eigenvector and the horizontal plane, ϕ_t, with $0 \leq \phi_t \leq \pi/2$ when the eigenvector is defined with a positive vertical component. Through the use of trigonometric identities, one finds that

$$\tan(2\phi_t) = \pm\frac{\sqrt{R^2+S^2}}{K - \frac{f_0^2}{\mathcal{N}_0^2}P} = \pm\gamma_b \tan(2\lambda^*), \tag{5.26}$$

where it is understood that the sign varies in accord with the sign in the expression for the horizontal orientation, eq. (5.23). In combination with eq. (5.21), the relation for the vertical tilt provides an alternative expression for the ellipse eccentricity,

$$\gamma_t = \frac{\cos(2\lambda^*)}{\cos(2\phi_t)}. \tag{5.27}$$

Then, combining eq. (5.11), (5.22) and (5.24), it is possible to arrive at the decomposition for R and S given by eq. (5.7b). Alternatively, one may write this decomposition in terms of the vertical ellipse geometry via eq. (5.26) and (5.27),

$$\mathbf{R} = \gamma_t L \sin(2\phi_t)\, \mathbf{r}_b, \tag{5.28}$$

where $\mathbf{r}_b = [\pm\sin(\phi_e), \mp\cos(\phi_e)] = [\cos(\phi_b), \sin(\phi_b)]$. Hence the vertical ellipse described by $\mathsf{E}_\mathrm{b}^\dagger$, together with the horizontal orientation of the eddy buoyancy flux, eq. (5.24), provides an interpretation of the geometry involved in decomposition (5.7b).

Marshall et al. (2012) consider a related decomposition,

$$\mathbf{R} = \gamma_b \frac{f_0}{\mathcal{N}_0} E \sin(2\lambda)\, \mathbf{r}_b, \tag{5.29}$$

where $E = K + P$ is the eddy energy and λ is the eddy energy partitioning angle,

$$\frac{P}{E} = \sin^2(\lambda), \quad \frac{K}{E} = \cos^2(\lambda), \tag{5.30}$$

bounded between 0 and $\pi/2$. This decomposition follows from a scaled version of E_b (see Maddison and Marshall, 2013), which similarly describes a vertical ellipse with horizontal orientation determined by ϕ_b, but with size, eccentricity and vertical tilt determined by E and λ instead of L and λ^*. Since E is a more familiar invariant compared to L, and the geometric interpretation is the same, the decomposition (5.29) is considered in what follows.

The geometry of the vertical ellipse determines whether the eddy form stress gives rise to an upward or downward momentum transfer in the water column, and how strongly the eddy field and the mean-flow interact. This in turn decides whether the vertical shear in the background horizontal velocity field strengthens or weakens. To see this, first note that the $f_0/\mathcal{N}_0^2$-scaled eddy buoyancy flux is related to the eddy form stress, $\boldsymbol{\tau}_i$, according to

$$\mathbf{R} = \frac{f_0}{\mathcal{N}_0^2}\overline{b'\mathbf{u}'_g} = -\frac{1}{\rho_0}\mathbf{k} \times \overline{\eta' \nabla_h p'} = \frac{\mathbf{k} \times \boldsymbol{\tau}_i}{\rho_0}, \tag{5.31}$$

a relationship pointed out by Johnson and Bryden (1989). Here ρ_0 is the reference density and p' is the pressure deviation. The property that the large-scale turbulence is in geostrophic balance, as well as the quasi-geostrophic assumption $\eta' = -b'/\mathcal{N}_0^2$, η' being the interface height displacement, have been used. Hence eq. (5.29) and (5.31) in combination tell us that the largest interfacial form stress is found in regions of high equally-partitioned ($\lambda = \pi/4$) eddy energy and high eddy buoyancy anisotropy γ_b, or, in terms of the ellipse geometry, when its vertical angle is $\pi/4$ and its eccentricity $\gamma_t = \gamma_b \to 1$. The horizontal orientation of the ellipse, ϕ_e, determines the direction of the stress and hence the nature of the vertical momentum transfer. As in Marshall et al. (2012), this interpretation of the ellipse geometry is shown for an idealized vertically-sheared zonal mean-flow in panel D of Figure 5.1 in the case where $\mathbf{R}$ is perpendicular to the mean-flow. In accord with linear stability analysis (such as the Eady model) the vertical shear weakens when the ellipse leans into the shear, corresponding to the case where the energy conversion is from the mean-flow to the eddies.

5.2.4 Eddy efficiency

As a practical application of the geometric decomposition we now follow Marshall et al. (2012) and construct an expression for the transfer coefficient κ appropriate to the Gent and McWilliams (1990) eddy closure. The down-gradient closure for the horizontal eddy buoyancy flux results in

$$\kappa = -\frac{\nabla_h \bar{b} \cdot \overline{b'\mathbf{u}'_g}}{\mathcal{M}^4} = -\frac{\mathbf{n} \cdot \overline{b'\mathbf{u}'_g}}{\mathcal{M}^2}, \tag{5.32}$$

where $\mathcal{M}^2 = |\nabla_h \bar{b}|$ and $\mathbf{n} = \mathcal{M}^{-2}\nabla_h \bar{b}$ is the buoyancy gradient unit vector. Using eq. (5.29) one finds

$$\kappa = \alpha E \frac{\mathcal{N}_0}{\mathcal{M}^2}, \tag{5.33}$$

which is the transfer coefficient used in Mak et al. (2017); Bachman et al. (2017); Mak et al. (2018). Here

$$\alpha = -\gamma_b \sin(2\lambda)\, \mathbf{n} \cdot \mathbf{r}_b \tag{5.34}$$

is the eddy efficiency, a combination of geometric parameters, and is bounded by unity in magnitude, $|\alpha| \leq 1$. For vertically-sheared mean-flow along $\overline{b}$ contours, the ellipse leans into the shear when $\alpha > 0$ i.e. the momentum transfer is downwards.

In the limit where the eddy buoyancy flux is purely down-gradient, the large-scale buoyancy gradient and eddy buoyancy flux are strictly anti-parallel, $\mathbf{n} \cdot \mathbf{r}_b = -1$, and α reduces to

$$\alpha_{\|} = \gamma_b \sin(2\lambda)\,. \tag{5.35}$$

This results in $\alpha = -\alpha_{\|}\mathbf{n} \cdot \mathbf{r}_b$ and $|\alpha| \leq |\alpha_{\|}| \leq 1$. The central focus of the remaining part of the paper is to obtain appropriate estimates of α and $\alpha_{\|}$, which necessitates a discussion on rotational eddy buoyancy fluxes.

5.3 Rotational eddy buoyancy fluxes

In an appropriate topology, any horizontal vector field, such as $\overline{b'\mathbf{u}'_g}$, has an associated horizontal Helmholtz decomposition,

$$\overline{b'\mathbf{u}'_g} = \nabla_h \chi_{\text{div}} + \mathbf{k} \times \nabla_h \chi_{\text{rot}}, \tag{5.36}$$

where the vector field is expressed through two scalar potentials, χ_{div} and χ_{rot}. These potentials are related to purely divergent and rotational contributions to $\overline{b'\mathbf{u}'_g}$, respectively. The eddy forcing of the mean-flow is given by the horizontal divergence of the eddy potential vorticity flux, eq. (5.2), and hence it is only divergent contributions to $\overline{b'\mathbf{u}'_g}$ which are dynamically active. A rotational eddy buoyancy flux may however be a substantial contribution to the full flux and potentially complicates an assessment of eddy-mean flow interaction. For example, the wavenumber spectra presented in Griesel et al. (2009) show that the magnitude of the eddy heat flux curl overwhelms the flux divergence at all relevant length scales in the Southern Ocean. Although ambiguous with respect to the size of the rotational eddy heat flux itself, this result indicates that the presence of rotational fluxes cannot be disregarded. Therefore, since this study aims to describe and interpret the dynamically relevant eddy efficiency, α, a method to remove the influence from rotational fluxes is implemented in the analysis.

A number of approaches to diagnose the rotational flux contribution exist. One option is to solve for the two potentials in eq. (5.36) simultaneously, which is the approach taken in, for example, Roberts and Marshall (2000). Given appropriate boundary conditions for the divergent and rotational flux potentials, this method yields a complete separation of the flux contributions. Generally, however, these boundary conditions are unknown and the freedom of choice renders the decomposition non-unique (Fox-Kemper et al., 2003). In quasi-geostrophy it is possible to relate the momentum tendency to a force function, a scalar potential akin to a streamfunction in interpretation (Marshall and Pillar, 2011), because the geostrophic flow is non-divergent. It has been shown that this force function, dynamically constrained by the no-normal flow boundary condition, can be used to define a unique divergent eddy potential vorticity flux (Maddison et al., 2015). Since $\overline{q'\mathbf{u}'_g} = -\mathbf{k} \times (\nabla \cdot \mathbf{E})$, this force function may in principle be used to extract unique divergent eddy buoyancy fluxes through vertical integration.

A second option, which is pursued in this study, is to approximate the potential χ_{rot} through physical insight into the dynamics of the rotational eddy fluxes. If the eddy motion is geostrophically balanced and along contours of the perturbation buoyancy b', one expects the eddy buoyancy fluxes to follow contours of eddy variance $\overline{\Phi}$ (where $\overline{\Phi} = \overline{b'b'}/2$). Provided closed contours of Φ, such rotational fluxes are associated with eddy variance flux by the geostrophic mean-flow in the idealized case where the mean-flow exactly follows contours of $\overline{b}$ (Marshall and Shutts, 1981). A consequence of this assumption is that down-gradient eddy buoyancy fluxes are directly related to baroclinic instability in steady adiabatic conditions (see Eden et al., 2007b, for a detailed discussion).

Eden et al. (2007a) provide a generalization of the ideas presented above, without making assumptions on the mean-flow, and derive an exact expression for the rotational potential. This potential consists of an infinite sum of moments of b' of increasing order. A truncation of the sum after second order moments captures most of the rotational flux (see their Figure 5) and the potential reduces to

$$\tilde{\chi}_{\text{rot}} = |\nabla_h \overline{b}|^{-2} \overline{\mathbf{u}_g \Phi} \cdot \left(\mathbf{k} \times \nabla_h \overline{b}\right), \tag{5.37}$$

which is also obtained in the theory of Medvedev and Greatbatch (2004). As in Marshall and Shutts (1981) the rotational flux is associated with the part of the eddy variance flux which is along mean buoyancy contours, but now including the eddy contribution $\overline{\mathbf{u}'_g \Phi}$ which in the Southern Ocean might be substantial. Note that eq. (5.37) is only an approximation to a χ_{rot} and is therefore not expected to be able to capture the entire rotational eddy flux field. In the present study we use $\tilde{\chi}_{\text{rot}}$ to obtain the approximate divergent eddy buoyancy flux,

$$\overline{b'\mathbf{u}'_g}_{\text{div}} = \nabla_h \chi_{\text{div}} \approx \overline{b'\mathbf{u}'_g} - \mathbf{k} \times \nabla_h \tilde{\chi}_{\text{rot}}. \tag{5.38}$$

This allow us to estimate an eddy efficiency based on the orientation of the divergent fluxes,

$$\alpha_{\text{div}} = -\gamma_b \sin(2\lambda)\, \mathbf{n} \cdot \mathbf{r}_{\text{div}}, \tag{5.39}$$

where $\mathbf{r}_{\text{div}} = [\cos(\phi_{b,\text{div}}), \sin(\phi_{b,\text{div}})]$ and $\phi_{b,\text{div}}$ is the horizontal angle of the divergent eddy buoyancy flux. The fraction of the eddy energy associated with the divergent flux contribution thus defined, and its partitioning between K and P, is unknown and inhibits an estimate of the divergent flux anisotropy. Moreover, it is not obvious that the approximated divergent flux satisfies the local energetic bound, $0 \leq \gamma_b \leq 1$, and hence the geometric interpretation in terms of a vertical ellipse may no longer hold in general. The full flux anisotropy is therefore used in the expression for α_{div}.

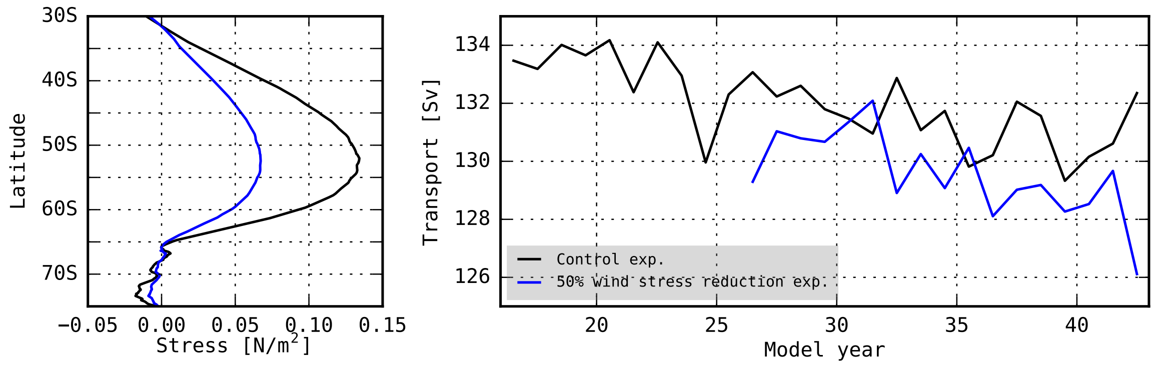

Figure 5.2: The left panel displays the zonally-averaged annual-mean zonal wind stress from the control (black) and wind stress decrease (blue) simulation. The right panel shows the time series of annual mean Drake Passage transport in the two simulations. The wind stress perturbation is applied January 1st in year 26.

5.4 Model setup and output post-processing

We use the z-coordinate Parallel Ocean Program version 2 (POP2), configured at an eddying horizontal resolution of $1/10^{\circ}$ on a global domain, to diagnose the eddy geometry in the Southern Ocean. We refer to Small et al. (2014) and Poulsen et al. (2018) and references therein for a detailed account of the model setup and its comparison to the same model at 1° nominal resolution. Here we discuss aspects of the model relevant to this study only.

The model is formulated on a B-grid and the vertical is discretized into 62 levels which separation increases monotonically with depth (Smith et al., 2010). The setup includes an active sea ice model and the meteorological boundary conditions are prescribed by the CORE.v2 normal year forcing fields (Large and Yeager, 2008). The forcing fields, compiled from reanalysis and observations, are updated every 6th model hour and repeat themselves after one model year. The ocean model is initiated from the World Ocean Circulation Experiment Hydrographic Climatology (Gouretski and Koltermann, 2004). The model was run for 42 model years, the first 16 years at the National Center for Atmospheric Research and documented in Bryan and Bachman (2015). The model solution drifts due to the relatively short spin-up, as for example seen in the horizontally-averaged temperature field which is subject to a 0.2°C/decade warming trend at 600 m depth in the Southern Ocean. Nevertheless, both the annual mean Drake Passage transport and strength of the residual overturning circulation in the Southern Ocean are stable with time (see right panel, Fig. 5.2, and Poulsen et al. (2018)).

To assess the robustness of the eddy geometry to an external forcing change, an experiment with a 50% reduced Southern Ocean zonal wind stress field is included in the analysis. The spatial structure of the perturbation consists of a zonally constant decrease of the wind stress south of 35°S in combination with a linear attenuation of the perturbation between 35°S and 25°S to ensure a continuous forcing field (see left panel of Figure 5.2). The wind stress reduction is applied instantaneously January 1st year 26 and the simulation is run for 17 years to match the length of the control integration.

The eddy statistics involved in the geometric framework are computed offline based on the years 34-42 where three-day time-mean fields, evaluated on constant depth-levels, are available from both simulations. This timespan is divided into the four seasons to account for the seasonal cycle present in the meteorological forcing fields. Eddy statistics are computed within each of the four seasons and the statistics used in this study is provided by the mean. The eddy variance flux, necessary for the rotational buoyancy flux estimate, eq. (5.37), is computed as

$$\overline{\mathbf{u}_g \Phi} = \frac{1}{2}\overline{\mathbf{u}_g b' b'} = \frac{1}{2}\left(\overline{\mathbf{u}_g b b} - \overline{\mathbf{u}_g}\,\bar{b}\,\bar{b} - 2\bar{b}\,\overline{b' \mathbf{u}_g'}\right). \tag{5.40}$$

Eddy statistics are horizontally coarse-grained, with one grid cell on the coarse grid consisting of 10×10 grid boxes on the original fine grid. This effectively reduces the horizontal grid resolution to about $1^\circ \times 1^\circ$ and results in smoother horizontal structures.

5.5 Results

5.5.1 Geometric decomposition

Although this study solely focuses on eddy form stress geometry, we begin by comparing the momentum and buoyancy anisotropy, γ_m and γ_b, to examine whether mutual characteristics are present (Panel A and B, Figure 5.3). At 500 m depth, below the austral winter mixed layer in which $\mathcal{N}_0$ is ill-defined, the horizontal structure of these fields have at least three properties in common; 1) both are subject to considerable structure on the mesoscale in the interior ocean away from topographic obstacles, 2) both fields show elevated anisotropies in western boundary current regions and in proximity to larger bathymetric objects, such as the Kerguelen Plateau, and 3) neither of the fields display a clear signature of the circumpolar current system. A pronounced difference, on the other hand, is that γ_m approaches unity on the periphery of topography which γ_b does not. This property of γ_m follows from the no-normal flow boundary condition (see Marshall et al., 2012). We also note that the estimate of γ_m is in qualitative agreement with γ_m presented by Stewart et al. (2015), who use both satellite altimetry and model output, indicating that the highlighted features are not model specific.

Vertical sections along the path of the Antarctic Circumpolar Current expose the same properties of the anisotropies as was shown in Figure 5.3 but additionally reveals a coherent vertical structure (Panel A and B, Figure 5.4). In contrast to the persistent mesoscale variations in the horizontal, γ_m shows a consistent vertical amplification with depth above rough topography and γ_b a nearly uniform vertical structure. The former property was shown in Stewart et al. (2015) to be a result of steep gradients in f/H, H being the depth of the water column, which constrains the directionality of the eddy motion. Similar reasoning does not appear to apply in the case of γ_b which suggests approximate isotropic eddy buoyancy fluxes in the immediate grid cells above bottom topography.

The eddy energy partitioning angle, λ, is shown in Panel C of Figure 5.3 and exhibits smoother spatial variations compared to γ_b. Eddy potential energy exceeds eddy kinetic energy at this particular depth, especially in the polar marginal seas and along the coast of Antarctica. Geostrophic scaling of the governing equations suggests $K/P \sim L_d^2/L^2$, where L_d is the baroclinic deformation radius and L is the characteristic length scale of the motion. In terms of the Eady model the most unstable wave evolves on a length scale of $3.9L_d$ (Eady,

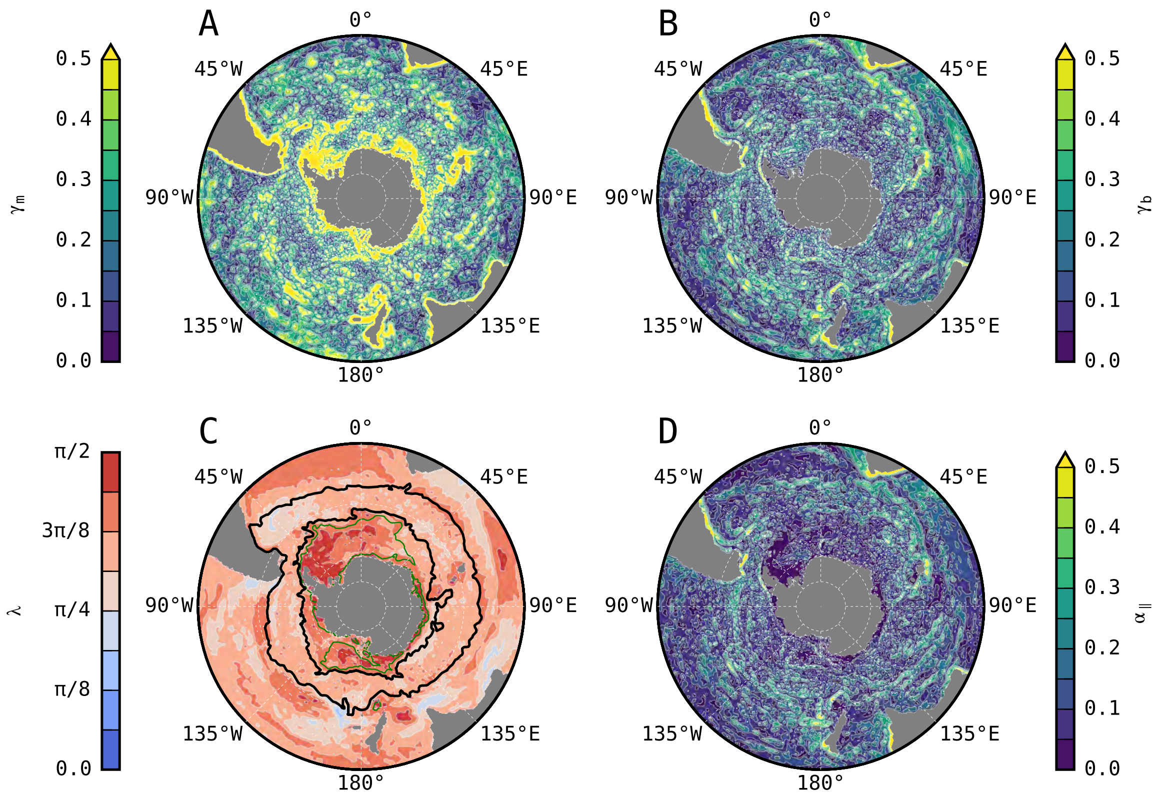

Figure 5.3: Constituents of the eddy geometry at 500 m depth. Panel A through D display the momentum anisotropy γ_m (A), buoyancy anisotropy γ_b (B), eddy energy partitioning angle λ (C) and combined geometric parameter $\alpha_\parallel = \gamma_b \sin(2\lambda)$ (D). The green line in panel C is the $\mathcal{N}_0^2 = 1 \times 10^{-6}\,\mathrm{s}^{-2}$ contour. The two black lines are the 5 and 125 Sv contours of the barotropic streamfunction, which define the circumpolar current envelope used in the following analysis.

1949; Vallis, 2006), corresponding to a partitioning angle $\lambda \approx 7\pi/16$. This is consistent with $K/P < 1$ as seen in the realistic eddy-resolving model, although the Eady model suggests an overly large fraction of eddy potential energy. Also, since $L_d = \mathcal{N}_0 H/f_0$, one may expect to find a larger fraction of eddy potential energy in weakly stratified waters. This is seen to be the case in the high southern latitudes where regions of $P > K$ coincide with $\mathcal{N}_0 < 1 \times 10^{-3}\,\mathrm{s}^{-1}$ (green thin line in panel C, Fig. 5.3).

Within the current envelope the eddy energy is closer to equi-partitioning ($\lambda = \pi/4$), the optimal configuration for large eddy stresses, but the associated vertical section (Panel C, Fig. 5.4) shows that this structure is subject to considerable along-stream variation. This is especially visible in flat-bottomed regions where $K > P$ at greater depth, an indication that large fluctuations in buoyancy relate to large variation in bottom topography. The buoyancy anisotropy combines with the eddy partitioning angle to form $\alpha_\parallel$, eq. (5.35), the eddy efficiency appropriate in the limit where eddy buoyancy fluxes are down the mean buoyancy gradient. The horizontal distribution of $\alpha_\parallel$ is shown in panel D of Figure 5.3. Since $\alpha_\parallel = \gamma_b$ for equi-

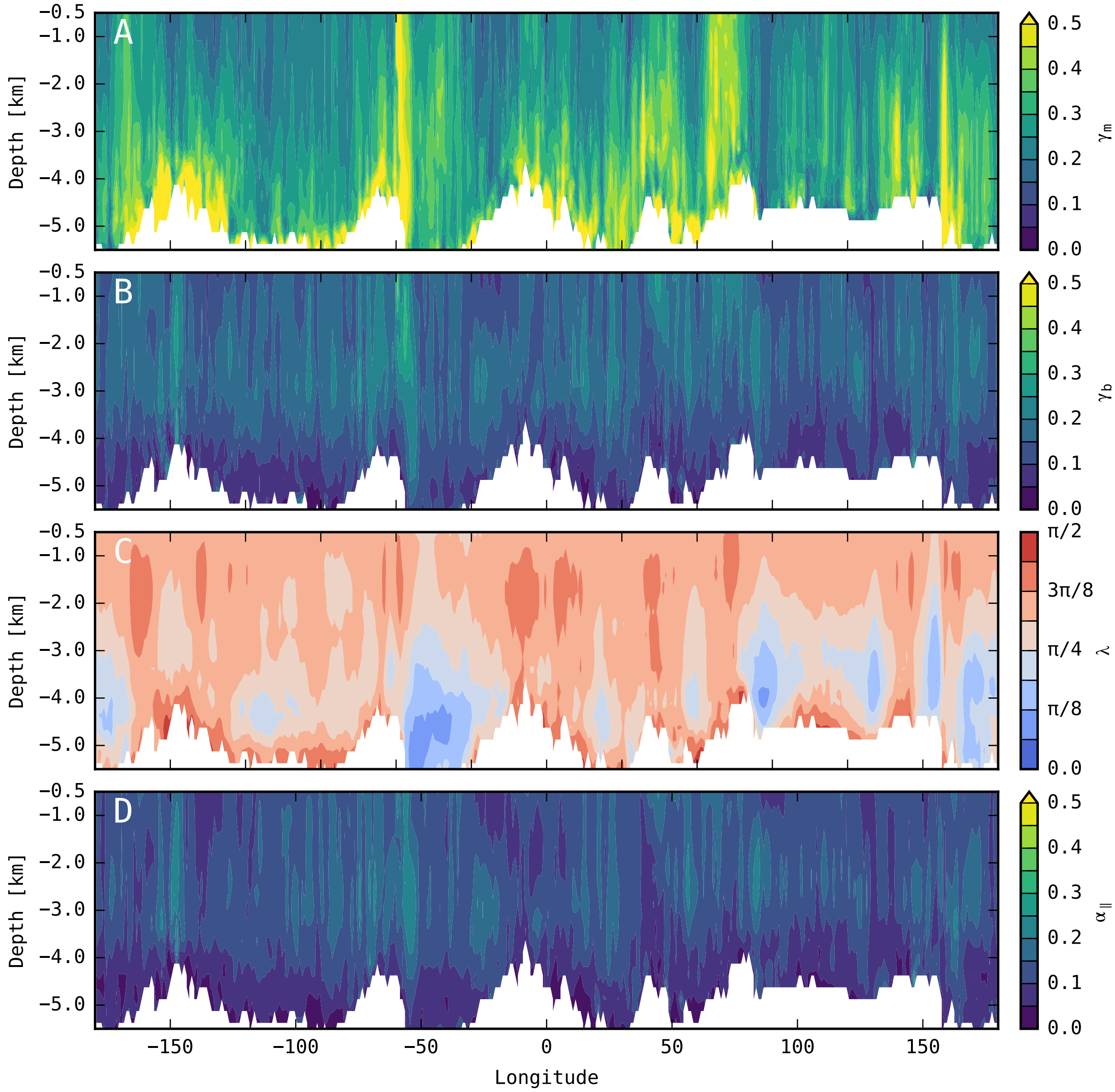

Figure 5.4: Meridionally-averaged sections of the eddy geometry within the circumpolar current envelope, shown by the two black streamlines in panel C of Figure 5.3. From top to bottom: momentum anisotropy γ_m (A), buoyancy anisotropy γ_b (B), eddy energy partitioning angle λ (C) and the combined geometric parameter $\alpha_\parallel = \gamma_b \sin(2\lambda)$ (D).

partitioned eddy energy, the largest variations between $\alpha_\parallel$ and γ_b is found at high southern latitudes. Most notable are the anisotropic boundary currents which also appear in $\alpha_\parallel$.

The vertical section of $\alpha_\parallel$ (panel D, Figure 5.4) possesses the weak vertical structure which is also visible in γ_b. Given the decomposition (5.29), this implies that it is primarily the eddy energy and the stratification in the geometric decomposition which sets the structure in the eddy interfacial form stress magnitude, $|\mathbf{R}|$. That this is the case is visible in Figure 5.5, which shows the vertical section of eddy form stress magnitude, $|\mathbf{R}|$ (panel A), and the eddy energy scaled by the Prandtl ratio, $f_0 E/\mathcal{N}_0$ (panel B). The stress is vertically sustained in several locations in the along-stream direction and suggests that vertical transfer of horizontal momentum due to transient eddies is concentrated in the standing meanders along the path of the current, corroborating the same finding presented in Thompson and Garabato (2014) and Masich et al. (2018). A similar structure is seen in $f_0 E/\mathcal{N}_0$ and suggests that $\alpha_\parallel$ only plays a secondary role in setting the interfacial stress magnitude. This is promising in the context of a geometrically-informed eddy closure, as it suggests that one can effectively reduce $\alpha_\parallel$ to a two-dimensional problem.

Motivated by this result we now ask to what extent one can assume a linear relationship between the form stress magnitude and the scaled eddy energy using a constant value for $\alpha_\parallel$. The left panel of Figure 5.6 shows the joint probability distribution of the eddy stress and eddy energy within the current envelope between 0.5 and 3.0 km depth, as well as the minimum mean square error fit (black solid line). A linear model with $\alpha_\parallel = 0.13$ is able to account for 62% of the variance in the eddy stress magnitude. The probability density function for $\alpha_\parallel$ itself is shown by the green line in the right panel of Figure 5.6. It is narrowly distributed and with a long tail towards the anisotropic regime. This supports the linear model with a constant value for $\alpha_\parallel$ but also shows that it comes at a cost of underestimated stresses in e.g. boundary currents. Lastly we note that the momentum anisotropy, γ_m (black line), displays a wider distribution and a greater mean value than the buoyancy anisotropy, γ_b (blue line), hence Reynolds stresses are on average more anisotropic than form stresses, at least in this particular model.

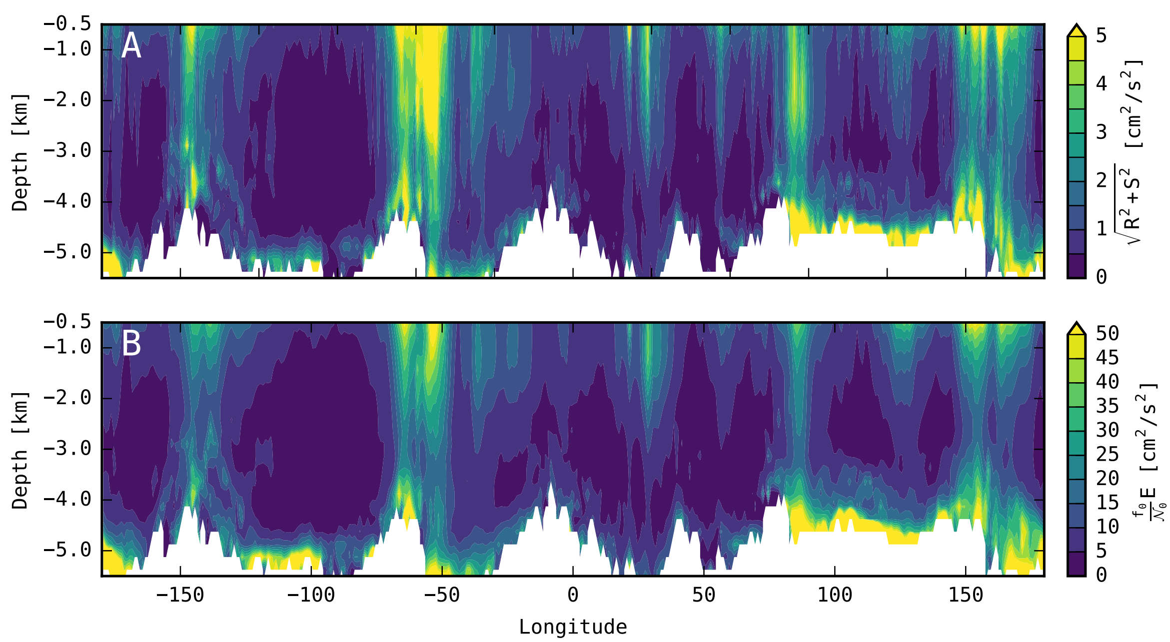

Figure 5.5: The upper and lower panels display the meridionally-averaged eddy interfacial form stress magnitude, $\sqrt{R^2 + S^2}$, and scaled eddy energy, $f_0/\mathcal{N}_0 E$, respectively, within the circumpolar current envelope (see streamlines in panel C of Figure 5.3).

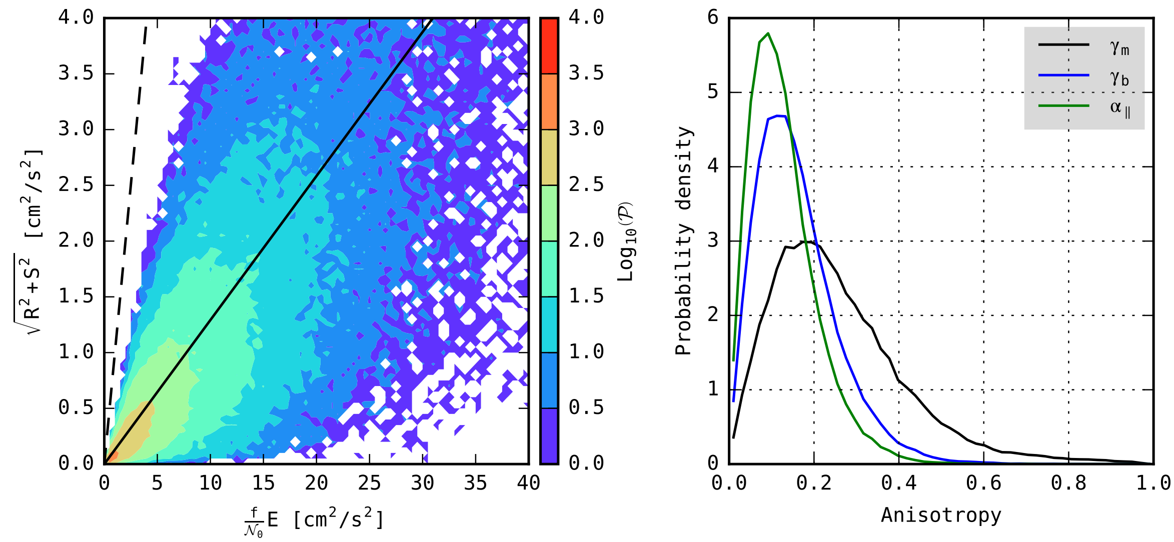

Figure 5.6: The left panel is the joint probability density functions for the scaled eddy energy, $f_0 E/\mathcal{N}_0$, and eddy interfacial form stress magnitude, $\sqrt{R^2 + S^2}$, within the Antarctic Circumpolar Current envelope between 0.5 and 3.0 km depth. The color scale is logarithmic. The solid black line is the minimum mean square error fit to the realizations, with model parameter $\alpha_\parallel$ value of 0.13. The dashed line is $\alpha_\parallel = 1$, the theoretical upper bound on $\alpha_\parallel$. The right panel shows the probability density functions for the anisotropies, γ_m and γ_b, and $\alpha_\parallel$ within the current envelope below 0.5 km and above 3.0 km depth.

5.5.2 Eddy efficiency α

We now turn toward the general expression for the eddy efficiency,

$$\alpha = -\alpha_\parallel \mathbf{n} \cdot \mathbf{r}_b,$$

which takes the orientation of the eddy buoyancy flux with respect to the mean buoyancy gradient into account. Here horizontal rotational eddy buoyancy fluxes play a role and may influence the interpretation of the eddy efficiency. Therefore we first examine the rotational flux before we describe the eddy efficiency estimates based on the full and divergent eddy fluxes.

The left panel of Figure 5.7 shows the eddy variance flux along mean buoyancy contours, $|\nabla_h \bar{b}|^{-1} \overline{\mathbf{u}_g \Phi} \cdot \left(\mathbf{k} \times \nabla_h \bar{b}\right)$, in the Southern Ocean at 500 m depth. This field sets the rotational fluxes according to eq. (5.37). It is mainly negative and is large in regions of strong mean-flow, especially downstream from the Agulhas retroflection region. Within the current envelope the greatest flux is found in proximity of the northern streamline and in regions where the flow navigates major topographic obstacles. For comparison the panel on the right hand side shows the eddy variance flux across mean buoyancy contours, $|\nabla_h \bar{b}|^{-1} \overline{\mathbf{u}_g \Phi} \cdot \nabla_h \bar{b}$, also at 500 m depth. This field is less sign definite and weaker compared to the flux along $\bar{b}$ contours. On average within the current, the eddy variance flux makes an angle of 75° at 500 m depth with respect to the mean buoyancy gradient, hence the majority of the eddy variance flux is indeed along $\bar{b}$ contours as suggested by Marshall and Shutts (1981).

The left panel of Figure 5.8 shows the probability density function of the angle between the large-scale buoyancy gradient unit vector, $\mathbf{n}$, and the eddy form stress unit vector, $\mathbf{r}_b$ (which is anti-parallel to the eddy buoyancy flux in the southern hemisphere), at two different depth intervals within the Antarctic Circumpolar Current. In the shallow depth interval, 0.5-1.0 km, the most probable orientation of the full eddy buoyancy flux is $\pm\pi/2$ with respect to $\nabla_h \bar{b}$ (black solid line). At greater depth (2.0 km-3.0 km), however, the probability distribution peaks in vicinity of zero, in favor of a down-gradient eddy buoyancy flux (dashed black line). The effect of removing rotational eddy buoyancy fluxes mainly plays a role in the upper part of the water column. The angle distribution for the divergent flux in the 0.5-1.0 km depth interval is more symmetric about zero (blue solid line) and with an increased probability in the interval between $-\pi/2$ and $\pi/2$, but the maxima at $\pm\pi/2$, however, are still present. A minor shift in the probability density distribution is visible at greater depth (blue dashed line), but the most likely orientation of the eddy flux remains down the mean gradient.

The implication for the eddy efficiency of removing the rotational flux contribution is therefore modest. Panel A and B of Figure 5.9 display the horizontal distribution of α, based on the full eddy buoyancy flux, at 500 m and 3000 m depth, respectively. At the shallow depth level the eddy efficiency is relatively weak and of mixed sign within the current envelope, and averages to about 0.01. This is a substantial reduction with respect to $\alpha_\parallel = 0.13$ and follows from $\mathbf{n} \cdot \mathbf{r}_b \approx 0$ on average. In the deep Southern Ocean where the eddy fluxes are more down-gradient, α is mainly positive and with a greater average of 0.08. α_{div}, the eddy efficiency based on the divergent flux, is shown for the same two depth levels in panel C and D. Some regions of negative α are subject to a sign change at 500 m depth, and here α_{div} averages to 0.02. α_{div} is weaker compared to α at 3 km depth, but the horizontal structure

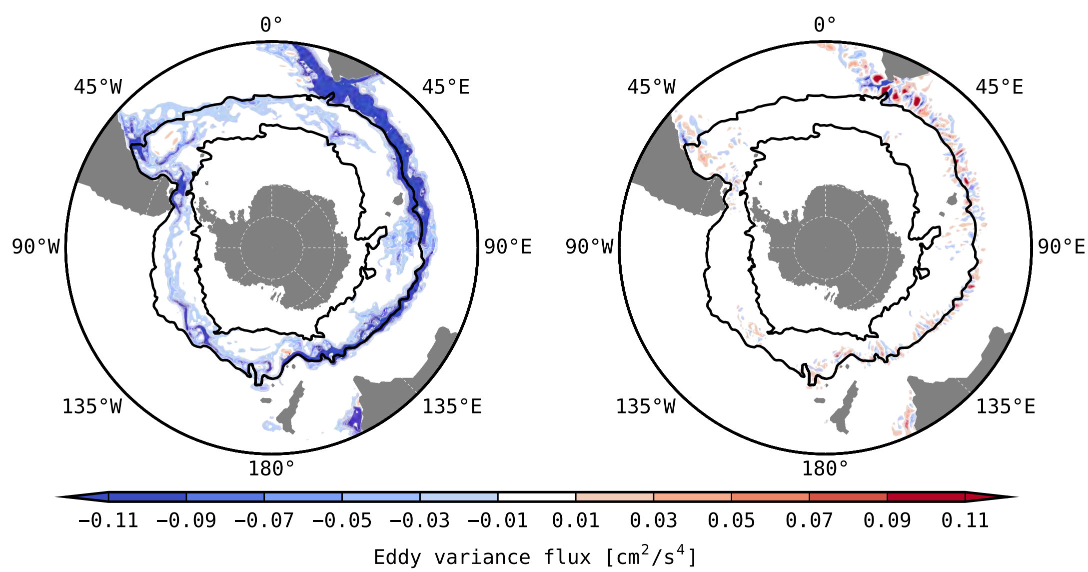

Figure 5.7: Eddy variance flux along mean buoyancy contours, $|\nabla_h \bar{b}|^{-1} \overline{\mathbf{u}_g \Phi} \cdot \left(\mathbf{k} \times \nabla_h \bar{b}\right)$ (left panel), and across mean buoyancy contours, $|\nabla_h \bar{b}|^{-1} \overline{\mathbf{u}_g \Phi} \cdot \nabla_h \bar{b}$ (right panel), at 500 m depth. The two black circumpolar lines are the 5 Sv and 125 Sv contours from the barotropic streamfunction.

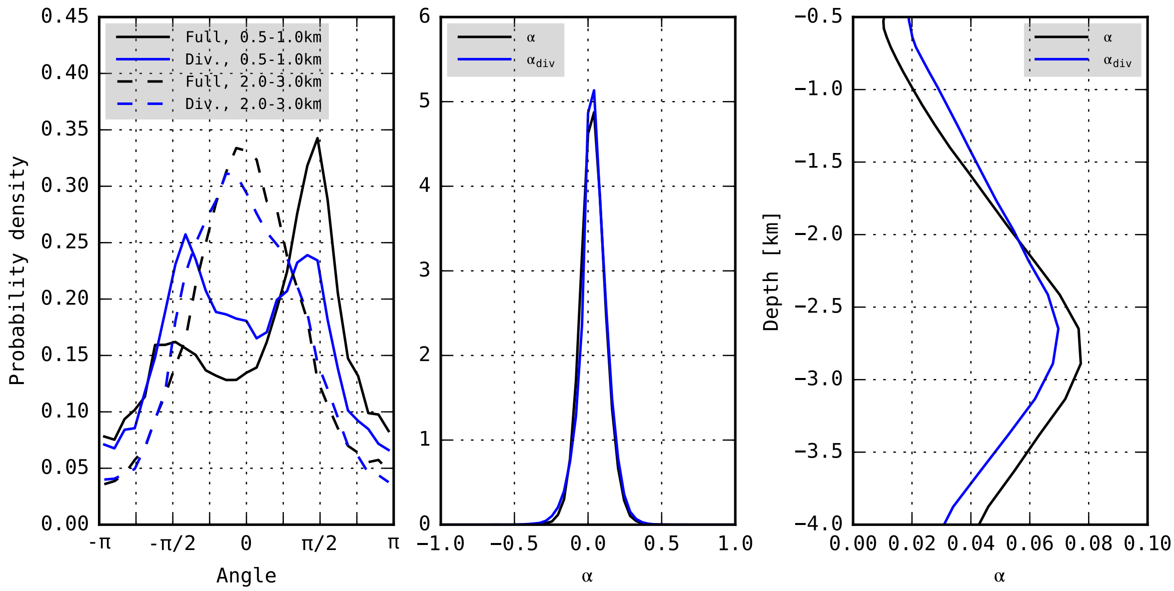

Figure 5.8: The left panel shows the probability density functions of the angle between $\nabla\bar{b}$ and $\mathbf{R} = (R, S)$ in the depth intervals 0.5 km-1.0 km (solid lines) and 2.0 km-3.0 km (dashed lines) using the full (black) and divergent (blue) eddy buoyancy flux. The angle measures the amount by which $\nabla_h\bar{b}$ must rotate anti-clockwise to reach $\mathbf{R}$. Hence a negative angle occur when $\nabla_h\bar{b}$ leads $\mathbf{R}$ and a positive angle when $\mathbf{R}$ leads $\nabla_h\bar{b}$. The middle panel shows the full-depth probability density functions for α and α_{div}. The right panel displays the horizontally-averaged profile of α and α_{div}. All panels consider the part of the Southern Ocean within the circumpolar current envelope shown by the black lines in panel C of Figure 5.3.

does not change. The horizontally-averaged profiles of the two eddy efficiency estimates (right panel, Fig. 5.8) show that both α and α_{div} increase with depth, the latter relatively less, and both are subject to a maximum at 2.5-3.0 km depth. Considering the full water column below 500 m depth and within the current envelope, the probability density distribution of α and α_{div} are similar and centered about mean values of 0.046 and 0.043, respectively (middle panel, Fig. 5.8).

5.5.3 Response to change in wind stress forcing

Finally we examine the response of eddy form stress, eddy energy and $\alpha_{\parallel}$ to the zonally constant Southern Ocean zonal wind stress decrease by 50%. The annual-mean zonally-averaged wind stress profiles from the control and perturbation experiments are shown in the left panel of Figure 5.2 and the associated Drake Passage transport time series in the right panel. Though not fully equilibrated, the time series display the characteristic insensitivity of the transport to surface wind stress, in agreement with past studies (e.g. Hallberg and Gnanadesikan, 2006). The difference in mean transport from the last five years of the two simulations is 3 Sv, a 2% decrease.

Figure 5.10 shows the horizontally-averaged profiles of the variables of interest for the two experiments (upper panels), as well as the relative change with respect to the control simulation (lower panels). The meridional component of the interfacial form stress vector $\mathbf{R}$ is generally larger than the zonal component (panel A), and it is positive throughout the water column, consistent with a net downward momentum transfer on average. The scaled eddy energy, $\frac{f_0}{N_0}E$, is largest at the surface and exhibits a minimum at about 3 km depth (panel C). The horizontally-averaged $\alpha_{\parallel}$ profile (panel E) is nearly constant in the upper three kilometers of the water column, as was also visible in Figure 5.4, and weakens toward the ocean bottom.

The meridional component of the interfacial stress weakens by 20-30% when the wind stress decreases (Panel A and B), and an even larger relative change is seen in the zonal component. The resultant reduction in stress magnitude is approximately 15-20% (green lines). Hence less horizontal momentum is transferred to a depth where a balance with topographic form drag is possible, in alignment with the insensitive circumpolar transport (Figure 5.2). We note that the relative change in stress magnitude does not match the 50% reduced wind stress, but emphasize that the simulation, and hence the eddy field, has not fully equilibrated to the adjusted forcing. The interfacial stress change is accompanied with a vertically-uniform decrease of the eddy energy by 15% (Panel C and D). $\alpha_{\parallel}$, on the other hand, displays a mixed

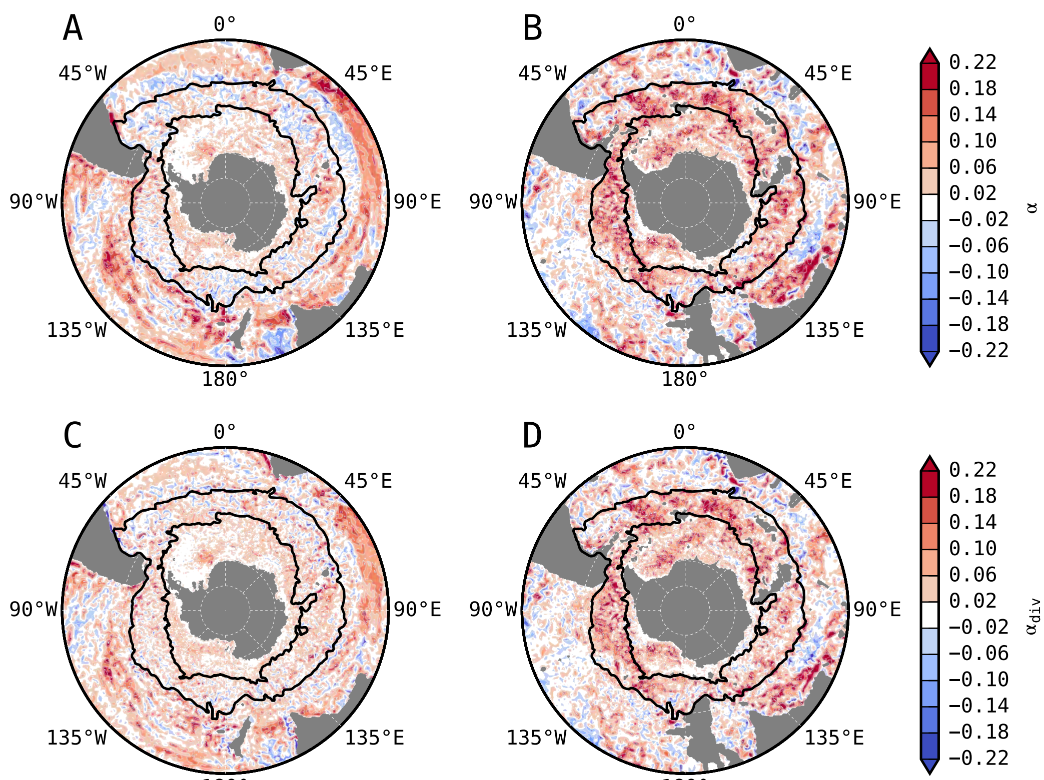

Figure 5.9: Eddy efficiency α, defined by eq. (5.34), at 0.5 km depth (left panels) and 3.0 km depth (right panels) using full (upper panels) and divergent (lower panels) eddy buoyancy fluxes. Black lines are the 5 and 125 Sv streamlines from the barotropic streamfunction. Rotational fluxes are estimated and removed using the rotational flux potential given by eq. (5.37).

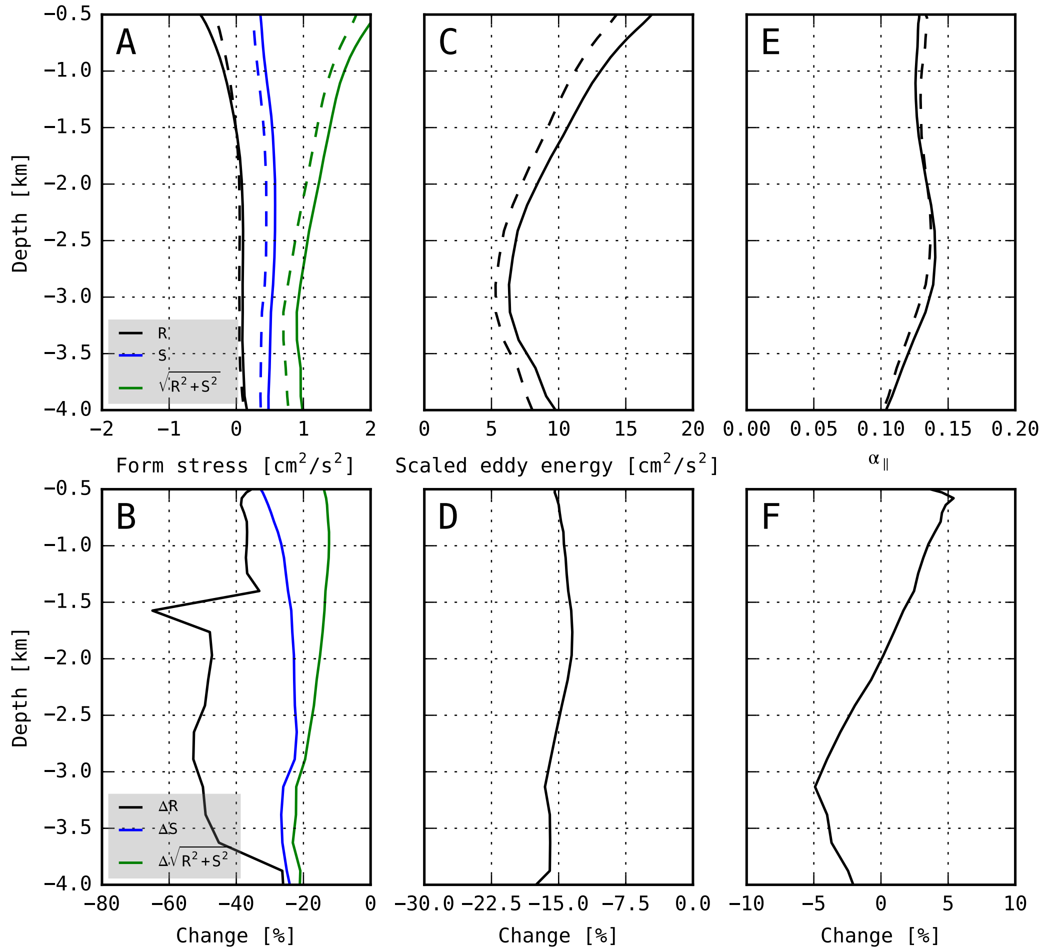

Figure 5.10: Horizontally-averaged profiles of interfacial form stress (panel A and B), eddy energy scaled by $f_0/\mathcal{N}_0$ (panel C and D) and $\alpha_\parallel$ (panel E and F) within the circumpolar current envelope (see streamlines in panel C of Figure 5.3). The upper panels show the profiles from the control (solid lines) and wind stress decrease (dashed line) experiments. The black and blue line in panel A and B are the zonal and meridional components of the interfacial form stress vector, $\mathbf{R} = (R, S)$, and the green line is the horizontally-averaged stress magnitude, $\sqrt{R^2 + S^2}$. The lower panel shows the relative change with respect to the control simulation.

response, with an increase in the upper part of the water column and a weakening below 2 km depth (Panel E and F). The relative change amounts to no more than 5% and demonstrates that the eddy geometry is robust to surface wind stress change.

5.6 Discussion

Despite the complex horizontal structure seen in the buoyancy anisotropy, the probability density function of γ_b shows that the Southern Ocean eddy field mainly sits in a weakly anisotropic regime (Right panel, Fig. 5.6). Topography appears to control the anisotropy to some extent, especially in regions where flow is guided by continental boundaries and larger bathymetric features, such as Drake Passage (Panel B, Fig. 5.3). Most importantly the analysis presented here suggests that γ_b varies weakly in the vertical (Panel B, Fig. 5.4). Since the anisotropy largely sets the structure in $\alpha_{\|}$, the eddy efficiency valid for a purely down-gradient flux, one may exploit this property and assume $\alpha_{\|} \approx \alpha_{\|}(x, y, t)$. In simpler model domains, where the absence of topography likely decreases spatial variations in the eddy anisotropy, it may even be appropriate to reduce $\alpha_{\|}$ to a function of time only (Bachman et al., 2017). Lastly, the 50% wind stress reduction experiment also suggests that $\alpha_{\|}$ is insensitive to the external forces which act on the ocean, an intriguing result since the eddy field is subject to large changes during the wind stress decrease (Figure 5.10).

The more general eddy efficiency, α, on the other hand, which is bounded in magnitude by $\alpha_{\|}$, is subject to a pronounced vertical structure within the Antarctic Circumpolar Current. $\alpha \approx 0.01$ at 500 m depth but is almost an order of magnitude larger at ~ 3 km depth where $\alpha = 0.08$ (Fig. 5.8 and 5.9). This intensification with depth is a consequence of the horizontal eddy buoyancy flux orientation with respect to the large scale buoyancy gradient. Eddy buoyancy fluxes mainly align with $\bar{b}$ contours in the upper part of the circumpolar current whereas the fluxes are predominantly down the mean buoyancy gradient at greater depth. Removing dynamically inert rotational fluxes reduces the variation of α with depth yet substantial vertical structure remains.

Thus, in the context of a future parameterization for α, a challenge is to understand what sets the horizontal orientation of the eddy buoyancy flux. The common assumption is that the horizontal divergent eddy buoyancy flux is directed down the large-scale gradient and is related to baroclinic instability through $\overline{w'b'}$ (Marshall and Shutts, 1981). This relationship has been intensively studied in the past (e.g. Roberts and Marshall, 2000; Eden et al., 2007b,a; Griesel et al., 2010). Taken together, these works show that the down-gradient assumption may provide accurate divergent eddy flux estimates regionally but cannot be expected to hold globally. Notably, Eden et al. (2007b) demonstrate that a substantial component of the eddy buoyancy flux is perpendicular to $\nabla\bar{b}$ in a model of the North Atlantic Current region, even when a rotational flux component is removed. In the quasi-geostrophic mean buoyancy budget, the along-contour part of the eddy buoyancy flux can be interpreted as a horizontal eddy-induced advection of mean buoyancy, which may be as large as the mean-flow advection in certain regions (Eden et al., 2007b). Hence divergence of the along-contour eddy flux component affects the mean buoyancy budget, with implications for the stratification and large-scale circulation, but is commonly not accounted for in ocean models without explicit eddy fluxes. Moreover, Jochum and Murtugudde (2006); Jochum et al. (2007) also find that horizontal eddy heat flux along mean isotherms in the equatorial mixed-layer, generated by tropical instability waves, is important to the mixed-layer heat budget.

Recent implementations of the geometrically-informed eddy transfer coefficient, eq. (5.1), in idealized channel models have treated α as a constant. The zonally-averaged model study by Mak et al. (2017) demonstrates that eddy saturation is a robust feature independent of the numerical value of α, whereas the zonal transport is inversely proportional to the eddy efficiency. In Mak et al. (2018), using the MITgcm together with a parameterization of the vertically-integrated eddy energy, $\alpha = 0.04$ is deemed appropriate as it results in a channel transport for present day wind stress magnitude which matches that of an identical simulation at eddy-permitting grid resolution. This value is in agreement with the estimated average of $\alpha_{\text{div}} = 0.043$, appropriate to the Antarctic Circumpolar Current, documented in the present study (Fig. 5.8). Bachman et al. (2017), on the other hand, suggests $\alpha \approx 0.2$ for fully-developed turbulence in a channel model of the non-linear Eady problem, and Marshall et al. (2012) show that $\alpha = 0.62$ for the most unstable mode in the linear Eady model. The eddy efficiency thus appear to decrease with increasing model complexity, such as the presence of β-effects, but a complete account of this behavior remains an open question.

The implementation of the parameterization framework in an ocean model also requires an evolution equation for the eddy energy E. One approach is to assume equi-partitioning of the energy ($\lambda = \pi/4$), such that $E = 2K$, in accord with quasi-geostrophic scaling, i.e. $K/P \sim 1$. If the validity of the assumption holds in a primitive equation model it constitutes a significant simplification since a parameterization for the eddy kinetic energy already exists (Eden and Greatbatch, 2008). Figure 5.3 and 5.4 show that λ varies between $\pi/4 \pm \pi/8$ within the Antarctic Circumpolar Current, representing as much as a factor of six between K and P. Thus a parameterization for E based on the eddy kinetic energy alone may be prone to large errors unless a structure function for λ is implemented as well. The variations in λ are to some extent related to topographic variations, most notable in the vertical section (panel C in Figure 5.4) when the large-scale flow passes over flat-bottomed regions. Indeed, in simpler model domain setups without bottom topography, the assumption of $\lambda \approx \pi/4$ has been shown to be more appropriate (Bachman et al., 2017). For use in realistic models, the suggested approach is to let two separate models for K and P evolve simultaneously.

5.7 Summary

This study has exploited the geometric properties of the Eliassen-Palm flux tensor to reformulate the horizontal eddy buoyancy flux in terms of the eddy energy and a set of bounded geometric parameters related to the eddy field. One goal of the present study has been to show that the eddy geometry describes an ellipse in the vertical plane and its orientation, shape and size in combination serves as a diagnostic tool to determine vertical momentum transfer and stability of baroclinic mean-flow. A particular focus has been the eddy efficiency α, a combination of the geometric ellipse parameters, bounded by unity in magnitude. α appears in the eddy transfer coefficient appropriate to the Gent-McWilliams closure for mesoscale eddies when the geometric decomposition is used to close for the eddy buoyancy flux. Provided that it is possible to parameterize α and the eddy energy, this geometrically-informed transfer coefficient can be used to close for eddy fluxes in coarse resolution ocean models in an energetically consistent way. The present study has taken initial steps toward the parameterization of α.

The geometry of the Southern Ocean eddy field has been diagnosed in a $1/10^{\circ}$ eddy-resolving general circulation model and the following aspects of α has been identified:

- In the limit where the horizontal eddy buoyancy flux is purely down-gradient, the eddy efficiency averages to 0.13 within the Antarctic Circumpolar Current and is subject to a uniform vertical structure. This structure changes by less than 5% to a 50% zonal wind stress reduction which suggests that α is insensitive to changes in external forcing.

- Horizontal eddy buoyancy fluxes aligned with $\bar{b}$ contours prevail in the upper Southern Ocean and suggests a reduced eddy efficiency of $\alpha = 0.01$. This contrasts to $\alpha \approx 0.1$ at $2-3$ km depth where the fluxes are mostly down-gradient.

- Removing rotational eddy buoyancy fluxes, using the method proposed in Eden et al. (2007a), only explains a minor contribution to the vertical variations in α.

- The average eddy efficiency within the Antarctic Circumpolar Current is $\alpha = 0.043$, a relative low efficiency given that $|\alpha| \leq 1$. This is mainly a result of weakly anisotropic eddies and that a substantial component of the horizontal eddy buoyancy flux aligns with $\bar{b}$ contours.

Acknowledgements

The research leading to these results has received funding from the European Research Council under the European Community's Seventh Framework Programme (FP7/2007-2013) / ERC grant agreement 610055 as part of the ice2ice project. JRM and DPM acknowledge support from the UK Natural Environment Research Council, NE/R000999/1. The authors gratefully acknowledge the Gauss Centre for Supercomputing (GCS) for providing computing time through the John von Neumann Institute for Computing (NIC) on the GCS share of the supercomputer JUQUEEN at Jülich Supercomputing Centre (JSC). The authors are also grateful for computing resources provided by the Danish Center for Climate Computing, a facility build with support of the Danish e-Infrastructure Corporation and the Niels Bohr Institute, as well as for Alison Baker (NCAR) for her help setting up CESM on JUQUEEN, and ERDA developers and maintainers Jonas Bardino and Klaus Birkelund Jensen for providing the computational infrastructure to analyze the model output. MBP and MJ would also like to thank Carsten Eden for constructive discussions.

5.8 Supplementary results

5.8.1 Eddy transfer coefficient estimates

The present chapter is part of an ongoing effort to parameterize α and the eddy energy in coarse resolution ocean general circulation models in order to arrive at an energetically consistent parameterization for the eddy transfer coefficient via eq. (5.1). The success of any proposed theory for κ should ideally be measured by the ocean model's ability to reproduce the observed hydrography and circulation of the world's ocean, as well as phenomena associated with mesoscale eddy activity, such as eddy saturation. However, since κ and the ocean stratification are tightly coupled, an indirect measure of success is to check whether the implemented parameterization for κ is able to mimic the features seen in κ diagnosed from eddy-resolving models.

Figure 5.11 shows the eddy transfer coefficient diagnosed from the high-resolution model at 500 m (left) and 3000 m (right) depth using the full (panel A and B) and divergent (panel C and D) eddy buoyancy flux. These have been estimated in accord with eq. (2.101), setting χ_{rot} equal to zero and eq. 5.37, respectively. Despite the high eddy energy in the Antarctic Circumpolar Current, the largest values for κ at 500 m depth, using the full flux (panel A), are found outside the current envelope (black lines) in western boundary currents, the Zapiola anti-cyclone and the Agulhas return current. The values are of mixed sign and in excess of $5000\,\mathrm{m}^2/\mathrm{s}$ in many regions, in broad agreement with past studies on the same subject (e.g. Eden, 2006; Eden et al., 2007b). Largest eddy transfers inside the current envelope appear in regions where the large-scale flow interacts with topography, such as downstream from Kerguelen Plateau and in Drake Passage. As was also the case for the estimates of α, shown in Figure 5.9, some regions of negative κ changes to positive when the divergent flux is considered (panel C), especially the relatively small values within the current system. That is, the divergent flux has a stronger tendency to have a down-gradient component compared to the full eddy flux. At 3000 m depth (panel B and D), where the eddy energy is less, it is interesting to note that regions of enhanced κ are those within the current envelope which also emerged at 500 m depth, namely regions of flow-topography interaction. These regions of vertically-sustained κ have been highlighted as dynamically important in previous studies of eddy-mean flow interaction in the Southern Ocean (Thompson and Garabato, 2014; Masich et al., 2018).

The zonal average of the two eddy transfer coefficient estimates are shown in the two leftmost panels in Figure 5.12. These mainly consist of positive values less than $500\,\mathrm{m}^2/\mathrm{s}$, considerably weaker than the values seen in Figure 5.11 because of partial cancellation between negative and positive values along the zonal integration path. The estimate based on the divergent flux (middle panel) suggests larger values for κ in the upper part of the Southern Ocean compared to the estimate based on the full flux (left panel). This is an expression of the fact that divergent fluxes, on average, are directed more down the mean buoyancy gradient relative to raw eddy buoyancy fluxes in the upper part of the Southern Ocean. Consequently, the eddy transfer coefficient based on the divergent eddy flux appears less dependent on depth.

Using the diagnosed eddy energy from the high-resolution model, it is possible to parameterize κ using the simplest possible parameterization for α, namely a spatially and temporally constant value of 0.043. In Section 5.5, this is the spatially-averaged value found to be appropriate to the Antarctic Circumpolar Current. The effect of using eq. (5.1) together with a constant value for α in a coarse resolution model setup has already been considered in Mak et al. (2017); Bachman et al. (2017); Mak et al. (2018). The horizontal structure of the parameterized κ is shown in panel E and F in Figure 5.11, and the zonally-averaged structure in the right panel of Figure 5.12. Although unable to mimic the regions of negative κ seen in panel C, the parameterized eddy transfer coefficient captures the overall spatial pattern at 500 m depth (panel E). The parameterized κ also captures some of the structure at 3000 m depth, but with an insufficient magnitude because the estimated α increases with depth (right

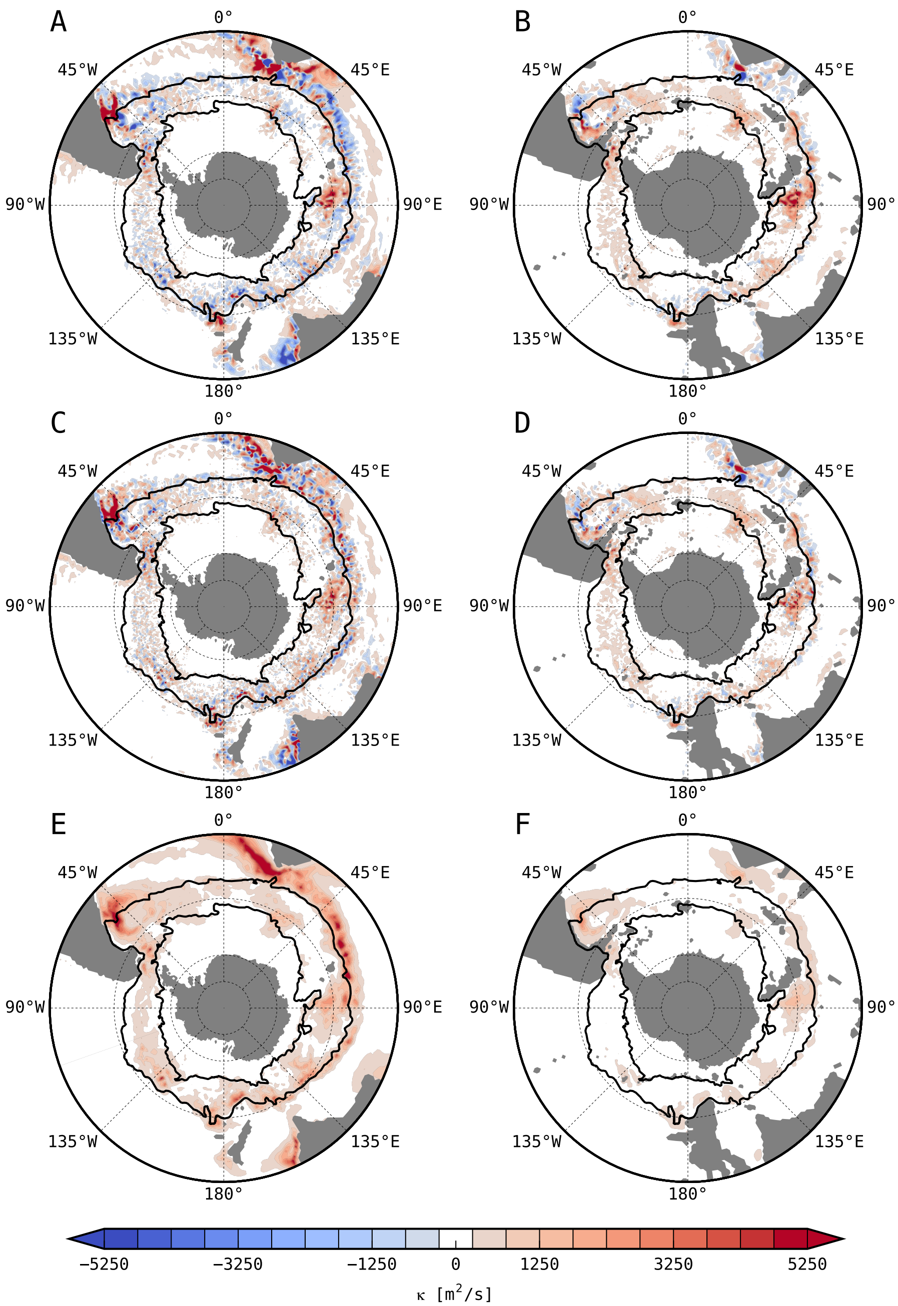

Figure 5.11: Estimates of the eddy transfer coefficient, κ, for 500 m (left) and 3000 m (right) depth using the full (A,B) and divergent (C,D) horizontal eddy buoyancy flux. Panel E and F shows κ based on eq. (5.1) using $\alpha = 0.043$ and the estimated eddy energy from the high-resolution model. All estimates are computed using the coarse-grained eddy statistics described in Section 5.4. The black lines are the 5 and 125 Sv streamlines from the barotropic streamfunction. Note that a lower bound on the length of the horizontal buoyancy gradient, $\mathcal{M}^2$, have been imposed to avoid unrealistically large values of κ. This choice is justified by the fact that weak buoyancy gradients are associated with weak vertical velocity shear and weak baroclinic instability and hence a small value for κ.

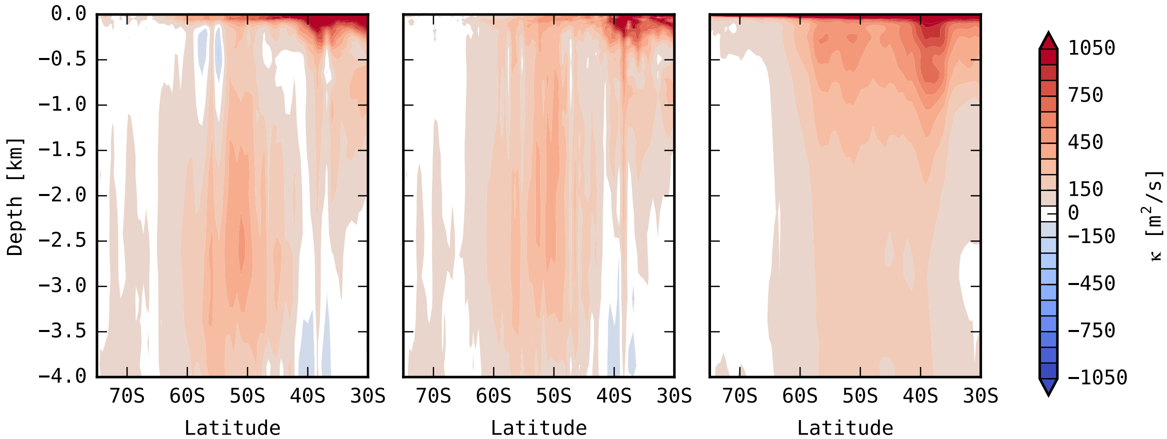

Figure 5.12: Zonal average of the eddy transfer coefficient, κ, using the full (left panel) and divergent (middle panel) eddy buoyancy flux. The right panel shows the zonally-averaged κ based on eq. (5.1) using $\alpha = 0.043$ and the estimated eddy energy from the high-resolution model. Note that a lower bound on the length of the horizontal buoyancy gradient, $\mathcal{M}^2$, have been imposed to avoid unrealistically large values of κ. This choice is justified by the fact that weak buoyancy gradients are associated with weak vertical velocity shear and weak baroclinic instability and hence a small value for κ.

panel, Fig. 5.8). This is also visible in the zonal average (right panel, Figure 5.12) where a clear depth-dependence in κ is visible, in contrast to the diagnosed κ (middle panel) from the eddying model.

It is also interesting to compare the estimates of κ, shown in Figure 5.11 and 5.12, to those presented in Farneti et al. (2015). These authors examine a suite of state-of-the-art coarse resolution ocean general circulation models, all forced with the CORE.v2 dataset published in Large and Yeager (2008) and discussed in Chapter 3. The suite of models employ different choices for κ, and hence, as seen from Figure 20 in Farneti et al. (2015), the spatial structure varies considerably. Panel C in Figure 5.11 suggests that the eddy transfer coefficient should be elevated in the proximity or downstream of complex bottom topography within the Antarctic Circumpolar Current, and this also appears to be the case in most of the coarse models. Many models, however, also suggest enhanced κ in regions where the eddy-resolving model does not. For example, the AWI and NCAR models, which both employ the $\mathcal{N}^2$-dependent transfer coefficient (Ferreira et al., 2005), show high values of κ upstream from the Drake Passage, a rather quiescent part of the circumpolar current in terms of eddy energy. This feature is also reproduced in the coarse resolution model of this study (which is the NCAR model) and is shown in Figure 5.13. Another example is the Bergen model, which uses a variant of the Eden and Greatbatch (2008) κ formulation, eq. (2.97), and also suggests overly large values north of the circumpolar current. Figure 21 of Farneti et al. (2015), which shows the zonally-averaged κ for four different models, is directly comparable to Figure 5.12 in the present dissertation. Common to the four selected models in Farneti et al. (2015) is that they all show an attenuation of κ with depth, in contrast to κ diagnosed from the divergent eddy buoyancy fluxes from the eddy-resolving model (middle panel, Fig. 5.12) which is more independent with depth.

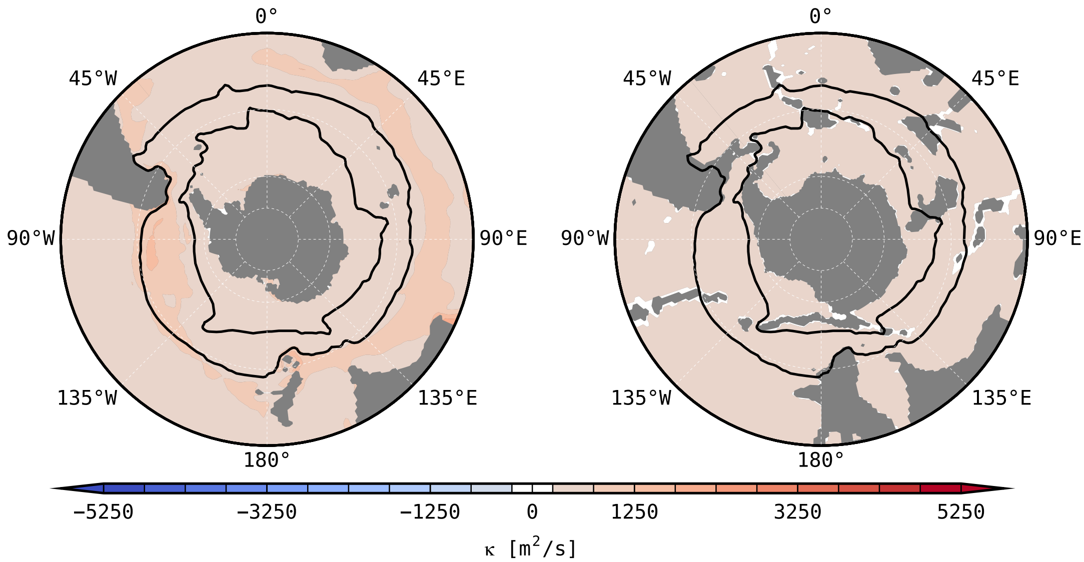

Figure 5.13: Ten-year mean eddy transfer coefficient at 500 m (left) and 3000 m (right) depth in the coarse resolution control integration between year 290 and 299. The model employs the stratification-dependent eddy transfer coefficient by Ferreira et al. (2005), discussed in Section 2.3.3. The colorbar is identical to Figure 5.11 to facilitate comparison. Black lines are the 5 and 125 Sv streamlines from the barotropic streamfunction.

Chapter 6

Acquired insight and outlook

This thesis has addressed the problem of parameterizing eddy-induced velocities in coarse resolution ocean models. On an assumption that the present modeling approach via a skew-diffusive tracer flux is appropriate, this parameterization problem primarily pivots around the specification of an eddy transfer coefficient, κ. The properties of two notable closures for κ have been examined. The first is the stratification-dependent closure by Ferreira et al. (2005), which presently forms the default choice for κ in the ocean model POP. The second is the geometrically-informed closure by Marshall et al. (2012), which is yet to be implemented in an Earth system model but has demonstrated promising properties, such as the possibility for an eddy saturation regime, in idealized model setups. The two expressions for κ have been examined in two independent but related studies. In Chapter 4, the skill of the former closure is assessed with respect to past claims that a dynamic κ is able to provide the correct overturning circulation sensitivity to zonal wind stress in coarse models of the Southern Ocean. This is evaluated with the use of a set of wind stress experiments conducted with POP in both coarse and eddy-resolving resolution. In Chapter 5, the latter closure for κ is examined on a more theoretical basis to understand the meaning of the involved parameters with respect to mean-flow stability. In addition, the parameters are examined and interpreted using output from the aforementioned eddy-resolving ocean model to guide its future implementation in complex models. Conclusions from the two studies follow below and Section 6.2 briefly discusses four possible future studies based upon open questions that arose during the preparation of the thesis work.

6.1 Conclusions from this thesis work

The work presented in Chapter 4 and 5 reduces to the following five main conclusions:

1. Chapter 4 shows that, despite implementation of the eddy transfer coefficient proposed by Ferreira et al. (2005), there is room for improvement in the representation of eddy-induced circulation and northward eddy heat transport in the coarse resolution version of the ocean model POP. Both Southern Ocean residual overturning cells are weaker in the coarse resolution model than in the same model of eddy-resolving resolution, and a streamfunction decomposition reveals that this discrepancy is a function of differences

in both the time-averaged and eddy-induced circulations (Fig. 4.4). The parameterized eddy-induced circulation in the coarse resolution model is distributed across a range of densities, including those water masses which upwell to the surface Southern Ocean, which the explicit eddy-induced overturning in the eddy-resolving model does not support. The total northward heat transport, on the other hand, compares well between the two models, but the decomposition into contributions from the Eulerian-mean and eddy-induced circulation shows that parameterized eddies provide an overly strong southward heat transport, especially between 40°S and 50°S (Fig. 4.8). This latitude span coincides with the biggest discrepancy between the streamfunctions of the parameterized and explicit eddy-induced circulation.

2. In contrast to the first conclusion, Chapter 4 also shows that the parameterized response and sensitivity to Southern Ocean zonal wind stress change compares well with the eddy-resolving model on decadal time scale. This conclusion is based on a 50% wind stress reduction experiment in which the residual overturning, vertical isopycnal displacement and northward heat transport respond with the same sign and magnitude regardless of model resolution (Fig. 4.6,4.7,4.8). This indicates that the implementation of κ proposed by Ferreira et al. (2005) is able to alleviate coarse resolution models from the overly strong sensitivity to zonal wind stress change previously reported when constant transfer coefficients were used (e.g. Hallberg and Gnanadesikan, 2006). This result also supports a similar finding in the multi-model comparison study by Farneti et al. (2015), which demonstrates a reduced sensitivity of the residual circulation to wind stress change when κ is allowed to vary in space and time. Finally, the finite and similar Southern Ocean vertical isopycnal displacement of the two model setups conflicts with the observation-based study by Böning et al. (2008), in which the Southern Ocean isopycnal slope is found insensitive to the zonal wind stress.

3. The suite of wind stress experiments with the coarse resolution model, discussed in Chapter 4, indicates that the adjustment timescale of the Southern Ocean is at least centennial. In particular, the response of the upper cell of the residual meridional overturning circulation to wind stress perturbations is weaker when the streamfunction difference is evaluated a century after the application of the wind stress change compared to the decadal response discussed in the preceding paragraph (Fig. 4.6, 4.16). Since the Ekman response to a change in wind stress is instantaneous, it is suggested that the long adjustment timescale is explained by the parameterized eddy-induced circulation which depends on the local ocean stratification, and which itself depends on the adjustment of the stratification in the basins to the north of the Southern Ocean. If this characteristic timescale also applies to an eddying model, one may question whether the time is ripe to diagnose the degree of Southern Ocean eddy compensation with realistic eddy-resolving models on global domains, simply because it is not currently feasible to run such computationally demanding models for centuries. Moreover, the 50% wind stress increase experiment with the eddy-resolving model also demonstrates that additional physical processes, such as those related to a reduction in the Antarctic sea ice, is able to influence the residual overturning response and thereby blur the relation to zonal wind

stress. Future model experiments which address the problem of eddy compensation must incorporate these two aspects into the experimental design.

4. On the path towards an energetically consistent expression for κ, Chapter 5 shows that there exists a one-to-one relationship between eddy fluxes of buoyancy and variance ellipse geometry. A similar result has been derived and explored for eddy momentum fluxes in the past (e.g. Waterman and Lilly, 2015), and Chapter 5 extends the framework to also incorporate eddy buoyancy fluxes. The ellipse geometry associated with eddy buoyancy fluxes is shown to offer a concise interpretation of stability of vertically-sheared horizontal mean-flow and vertical transfers of horizontal momentum (Fig. 5.1). As shown in Marshall et al. (2012), it is possible to decompose the eddy buoyancy flux into the variance ellipse geometry and the eddy energy. This decomposition can be used to formulate a new expression for the eddy transfer coefficient in terms of the eddy energy and a combined geometric parameter, α, which is bounded in magnitude by unity. Notably, recent model studies have shown that such an expression for κ supports an eddy saturation regime in idealized model configurations with a constant value for α (Mak et al., 2017, 2018).

5. In this thesis, α is coined an "eddy efficiency" and its structure is examined in the Southern Ocean of the eddy-resolving model (Fig. 5.9). Chapter 5 shows that the volume averaged eddy efficiency is 0.043 in the Antarctic Circumpolar Current, in close alignment with the constant value of 0.042 deemed optimal in the channel model configuration of Mak et al. (2018). Provided with the theoretical bound, $|\alpha| \leq 1$, the average eddy efficiency of 0.043 is low but positive, in alignment with an overall release of available potential energy in the current. The low eddy efficiency is found to be a product of weakly anisotropic baroclinic mesoscale eddies, equivalent to a weak polarization of horizontal eddy buoyancy fluxes, and that horizontal eddy buoyancy fluxes tend to have a strong vectorial component along time-mean buoyancy contours instead of across. The latter conclusion holds even when a dynamically inert rotational contribution to the horizontal eddy buoyancy flux is removed via the method outlined in Eden et al. (2007a). It is also found that the eddy efficiency increases with depth in the horizontal average within the circumpolar current and has a subsurface maximum at about 2.5 km depth (Fig. 5.8). It is hypothesized that this property of the eddy efficiency becomes important in future implementations of the geometrically-informed κ in complex models since it influences the vertical structure on which the horizontal eddy-induced velocity depends (Fig. 5.12).

6.2 Looking ahead

Provided with the conclusions from this thesis work, this section attempts to motivate four potential future studies which build upon the work presented in Chapter 4 and 5.

6.2.1 A divergent eddy buoyancy flux along mean buoyancy contours

In Chapter 5 it was found that the horizontal eddy buoyancy flux in the upper Southern Ocean is partially composed of a vector component along time-mean buoyancy contours, even when dynamically inert rotational vector contributions were removed. A similar result was also obtained by Eden (2006) and Eden et al. (2007b) in two regional eddy-resolving ocean models of the Southern Ocean and North Atlantic, respectively. This property of the horizontal eddy buoyancy flux is concisely visualized by computing the parameter ν,

$$\nu = -|\nabla_h \bar{b}|^{-2} \mathbf{F}_{\text{div}} \cdot \left(\mathbf{k} \times \nabla_h \bar{b} \right), \tag{6.1}$$

described in detail in Section 2.3.4, where $\mathbf{F}_{\text{div}}$ is the divergent contribution to the horizontal eddy buoyancy flux. ν relates to the part of the divergent eddy buoyancy flux vector which is along time-mean buoyancy contours and, according to eq. (2.100), can be interpreted as a streamfunction (see also Eden et al., 2007b). The ν parameter extracted from the control simulation of the eddy-resolving model used in this thesis, computed from the nine-year time interval also used in Chapter 5, is shown in Figure 6.1 for 500 m depth using both raw and divergent eddy buoyancy fluxes. The ν field does not weaken when rotational fluxes are removed (right panel) and both fields are subject to a zonally-banded structure, mostly visible along the northern edge of the Antarctic Circumpolar Current. Given the streamfunction property of ν, this gross horizontal structure implies zonal advection of mean buoyancy. This advective contribution is not accounted for by the Gent-McWilliams eddy parameterization and may be indicative of missing physics in coarse resolution models, with possible implication for model dynamics. But what is the physical process which gives rise to the horizontal eddy advection described by ν?

One possible hypothesis is that zonal advection associated with ν relates to Stokes drift due to Rossby waves. Like surface gravity waves impinging upon the beach induce a net mass transport towards the beach, Marshall et al. (2013) show that a westward mass transport of similar character is induced by propagating long Rossby waves. In a zonally-bounded basin, a net westward mass transport by Rossby waves requires a compensating eastward mass transport in the long-term mean (coined Rossby rip currents). Such compensation is not needed in the Southern Ocean which is absent of meridional boundaries and hence allows for a net zonal mass transport. Testing this hypothesis, and understanding the dynamical implication of the westward Stokes drift for the Southern Ocean, appears as a natural extension to Chapter 5.

6.2.2 Eddy forcing of the residual circulation

Recent model studies, such as Thompson and Garabato (2014) and Masich et al. (2018), have suggested that the eddy force due to vertical convergence in eddy form stress is elevated in standing meanders in the Antarctic Circumpolar Current (see also review by Rintoul, 2018). Thus, a possible extension to the model comparison study in Chapter 4 is to evaluate the eddy force which acts on the mean-flow in both the coarse resolution and eddy-resolving model to understand whether the parameterization is able to reproduce this characteristic feature of the circulation. Figure 5.5 in Chapter 5 shows that the eddy form stress magnitude in the eddy-resolving model is indeed stronger throughout the water column within the standing meanders, and one could compute the vertical derivative of the stress, as in Thompson and Garabato (2014), to understanding the structure of the eddy forcing. The influence from

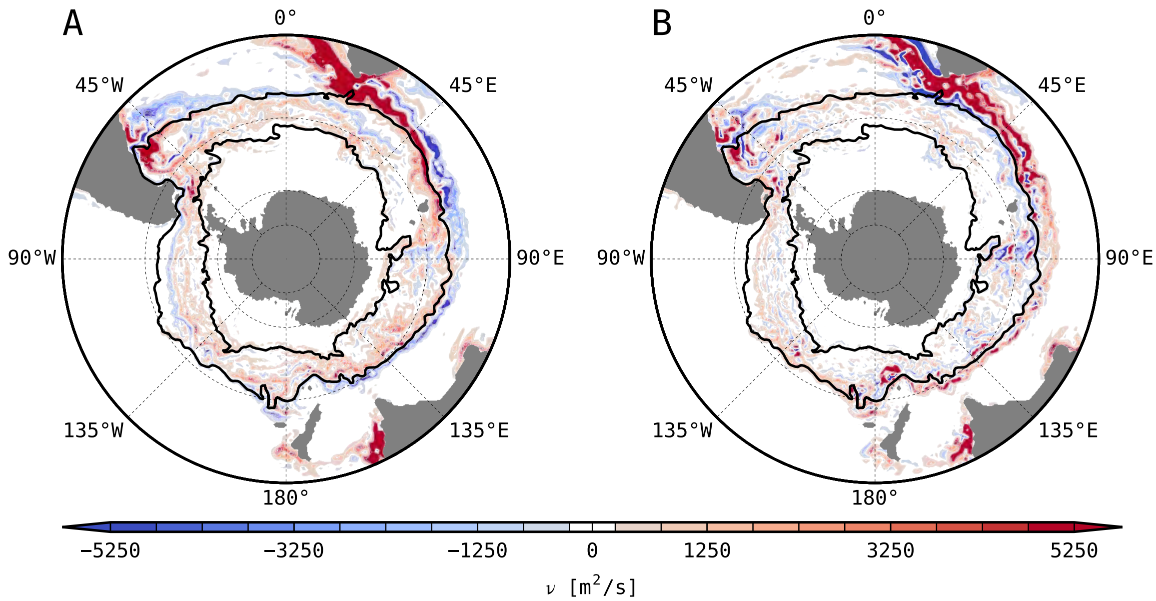

Figure 6.1: The parameter ν, defined in eq. (2.102), which relates to the magnitude of the horizontal eddy buoyancy flux along contours of $\bar{b}$, and is complimentary to κ which relates to fluxes across $\bar{b}$ contours. The left and right panel show ν using raw and divergent fluxes, respectively, the latter obtained using the rotational flux potential given by eq. (5.37). Both fields are for 500 m depth and the black contours are the 5 and 125 Sv streamlines from the barotropic streamfunction. Following Eden (2006); Eden et al. (2007b), the ν scalar field can be interpreted as a streamfunction which advects mean buoyancy in the horizontal.

rotational eddy buoyancy fluxes and noise related to spatial derivatives however pose two disadvantages of this approach, and one may therefore seek alternatives. One such alternative is to consider so-called force functions, a concept defined in Marshall and Pillar (2011), which are scalar potentials expressing the local horizontal momentum tendency due to individual forces applied to the fluid. That is,

$$\mathbf{F} = \rho_0 \mathbf{k} \times \nabla\psi, \tag{6.2}$$

where $\mathbf{F}$ is the non-divergent part of the horizontal force which projects directly onto the local acceleration, and ψ is the force function. This approach is attractive because 1) the force functions are interpreted like streamfunctions and hence constitute an intuitive way of interpreting the forcing, and 2) the force functions are subject to less noise because they are the scalar potentials (i.e. an integrated measure) of the force.

An example of the usefulness of the force functions is provided by Maddison et al. (2015) in a quasi-geostrophic context. Here the non-divergent property of the horizontal geostrophic velocity field, $\nabla \cdot \overline{\mathbf{u}_g} = 0$, is used to express the different terms in the horizontal residual-mean momentum equation in terms of force functions, such as the eddy form stress convergence. In a closed domain, the force functions are obtained by solving Poisson's equation subject to Dirichlet boundary conditions. In a more realistic domain, such as found in a general circulation model, the same type of boundary condition applies to all land boundaries but the

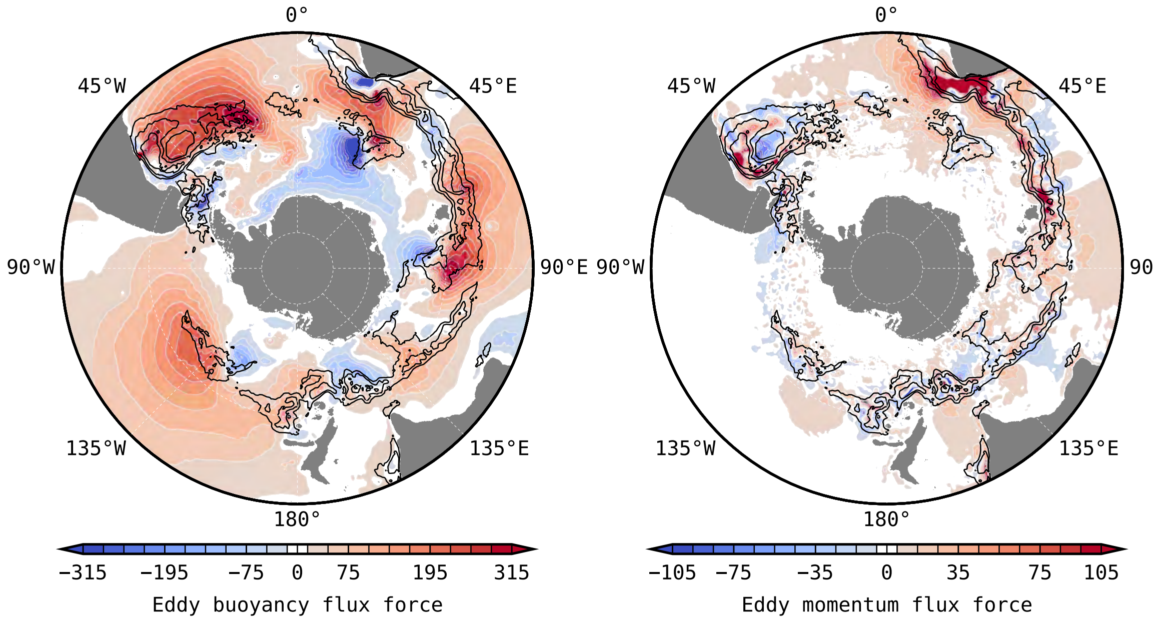

Figure 6.2: Force functions (Marshall and Pillar, 2011) due to eddy interfacial form stress (left) and eddy Reynolds stress (right) obtained from the control integration of the eddy-resolving model using the method described in Maddison et al. (2015). Units are in $\mathrm{cm}^2/\mathrm{s}^2$. The force function is interpreted like a streamfunction, with the horizontal force along lines of constant force function. Red cells denote clockwise forcing and opposite for blue cells. It is emphasized that the solutions for the force function are obtained with a constant value of zero at all land boundaries, despite the fact that the boundaries are not connected; tackling this boundary value problem is a possible future project. Computation of eddy fluxes is in accord with the description in Chapter 5. Black lines are contours of eddy kinetic energy at the same depth level.

constant value on the different boundaries may in general be different. Following Maddison et al. (2015), Figure 6.2 shows the force functions for the eddy form stress (left) and eddy Reynolds stress (right) at 1 km depth in the eddy-resolving model, but with the same constant value for the force function applied to all land boundaries. In this estimate, the force due to eddy form stress convergence retards the time-mean circulation at all the major standing meanders (the dipole structures), but forcing also appears in unexpected quiescent regions and is likely due to a wrong boundary value choice. Finding correct boundary values, and subsequently compare to the force function obtained from the coarse resolution model, is a task for the future.

6.2.3 The Vertical structure in eddy energy

A puzzling result which emerged during the preparation of Chapter 5 is the apparent bottom intensification of eddy kinetic energy in the Southern Ocean of the eddy-resolving model. This is readily seen in the left panel of Figure 6.3, which shows the horizontally-averaged energy profiles from south of 30°S. As seen from the vertical profiles, both eddy kinetic and potential energy are surface intensified, consistent with observations (Roullet et al., 2014), but a bottom intensification below $\sim$ 4 km depth is also visible in eddy kinetic energy. It is common to describe the vertical structure of the interior ocean in terms of Rossby wave modes, upon which temporal variability associated with the ocean mesoscale projects. These modes originate from the linearized quasi-geostrophic potential vorticity equation when one seeks wave-like solutions to the equation. As shown in Pedlosky (1987), the set of modes consist of a bottom-trapped wave mode plus a set of surface intensified modes when the bottom boundary condition is a topographic slope of a certain magnitude. LaCasce (2017) argues that the bottom slope in most parts of the world's ocean is more than sufficient to favor such a set of modes, and one may hypothesize that the eddy kinetic energy profile shown in Figure 6.3 is indicative of a Southern Ocean vertical structure dominated by the gravest surface intensified wave mode and a bottom-trapped wave.

Eddy kinetic energy in the Southern Ocean is generally concentrated in the standing meanders of the circumpolar current (Bischoff and Thompson, 2014; Barthel et al., 2017; Masich et al., 2018), which arise when the mean-flow navigates major topographic obstacles. Thompson and Garabato (2014) examined the vertical structure of individual standing meanders and found that eddy kinetic energy is surface intensified, but deep reaching, and is elevated near the bottom as well. The latter point is also supported by the eddy-resolving model used in this thesis, which shows that high bottom eddy kinetic energy is indeed found in the location of the standing meanders (right panel, Fig. 6.3). Thompson and Garabato (2014) relates the variability in the standing meanders to Rossby waves arrested in the strong eastward mean-flow of the circumpolar current. Thus, provided with the fact that standing meanders are a product of flow-topography interaction, is the vertical structure of the eddy kinetic energy an indication of the presence of arrested Rossby waves with a vertical structure dictated by the first surface mode and the bottom-trapped wave mode? The answer to this question is interesting as the vertical structure in the standing meanders is important to the momentum

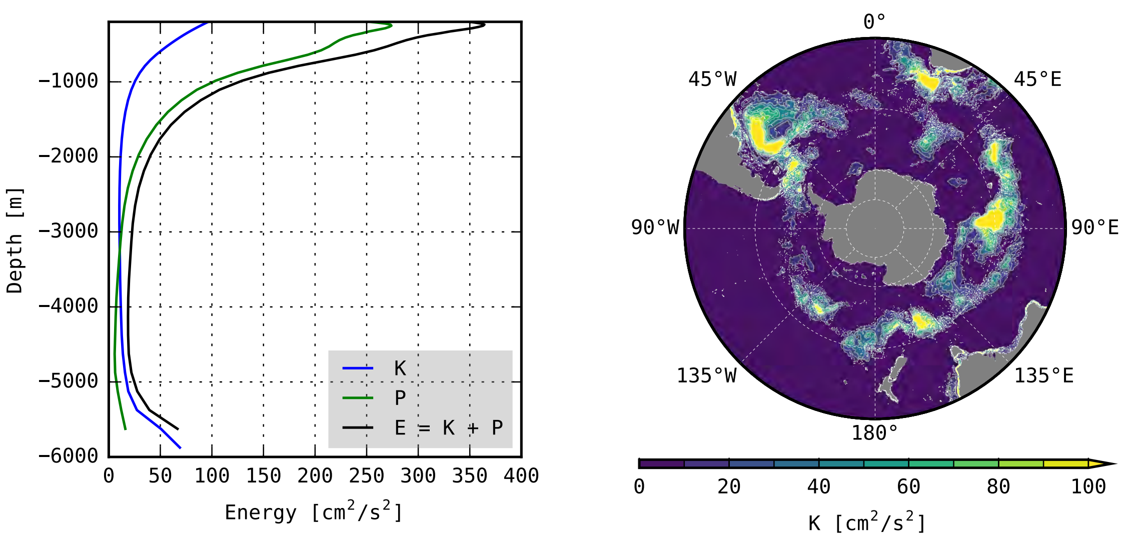

Figure 6.3: The left panel shows horizontally-averaged eddy kinetic and potential energy, as well as their sum, for the region south of 30°S from the eddy-resolving model. The right panel shows the eddy kinetic energy in the penultimate grid cell above bottom topography in the eddy-resolving control simulation. The eddy energy, and its partitioning into kinetic and potential contributions, is computed in accord with Chapter 5.

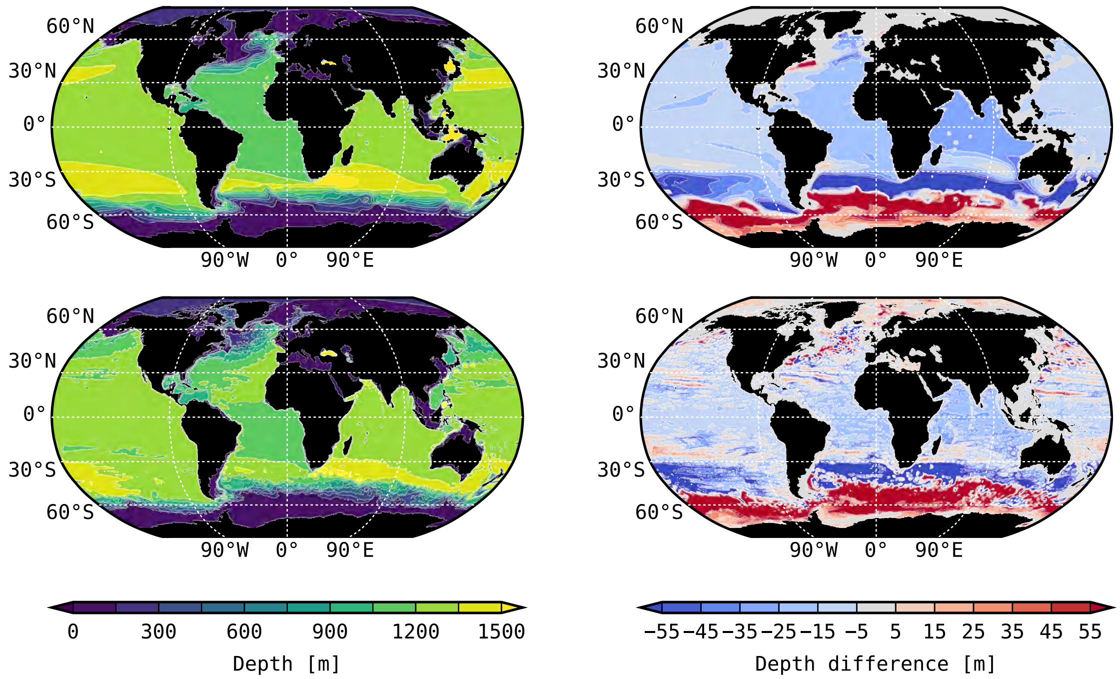

Figure 6.4: Annual-mean global depth of the $\sigma_2 = 36.5\,\mathrm{kg/m^3}$ density surface at year 316 (upper left) and 42 (lower left) in the control simulations of the 1° and 0.1° resolution model, respectively. The right panels show the annual-mean depth difference of the density surface between the 50% wind stress reduction experiment and the control integration, 16 years after the application of the perturbation. This density surface is the same as examined in Figure 4.7. The colorbar for the panels on the right hand side is saturated in the Southern Ocean sector in order to highlight the non-local response to the wind stress change. Units are in meters and negative depth difference indicates an isopycnal lift.

balance of the circumpolar current, as already discussed in the preceding section.

6.2.4 Non-local response to Southern Ocean wind stress change

As an extension to the discussion in Chapter 4 on the local vertical displacement of the isopycnals in the Southern Ocean following the wind stress change, one may as well look into the global response in the two models to investigate whether information on changed surface boundary conditions spreads throughout the ocean similarly despite the difference in model resolution. This comparison is important as the isopycnal displacement both affects the ocean pressure field, and hence the circulation, as well as ocean-atmosphere exchanges of heat. Figure 6.4 shows the global annual-mean depth of the σ_2 density surface $36.5\,\mathrm{kg/m^3}$, the same density surface in focus in Figure 4.7, as well as the change in annual-mean depth 16 years after the application of the 50% wind stress reduction in the Southern Ocean. Besides the difference due to mesoscale eddy variability present in the eddy-resolving model in e.g. western boundary current regions, both models show a general lift of this specific isopycnal surface away from the Southern ocean, in combination with a band of isopycnal depression around 25°S.

In this respect, a question of particular interest is the instability of Rossby waves and its influence on the isopycnal adjustment process. Long baroclinic Rossby waves propagate westward from the eastern boundary and influence the interior ocean density field, but LaCasce and Pedlosky (2004) show that such waves are prone to baroclinic instability and may break up into mesoscale eddies before their traverse across the ocean basin is complete. According to their theory, this effect is especially pronounced at mid- and high latitudes where the phase speed of long Rossby waves is relatively low and baroclinic instability strong, and hence may prevent an isopycnal adjustment in the western part of the major ocean basins. On an assumption that this wave instability is not present in a coarse resolution model, one may hypothesize that the isopycnal displacement in the mid latitudes would be stronger in the 1° model than in the 0.1° model. A vague indication of this effect may be seen in Figure 6.4, but an unequivocal conclusion cannot be drawn because of the presence of pronounced eddy activity (which itself may be the effect of unstable Rossby waves). To answer the question ultimately requires eddy-resolving model integrations closer to equilibrium and longer time-averages, or alternatively ensemble-averages, to reduce temporal variability in the western part of the basins. The high resolution model runs in focus in this thesis are presently being extended and may facilitate such a study in the near future.

Abbreviations

This thesis has been written with the philosophy that abbreviations compromise the readability of scientific literature and therefore should be avoided. The few exceptions are listed below.

Abbreviations

CESM Community Earth System Model

CMIP5 Coupled Model Intercomparison Project 5

CORE.v2 Coordinated Ocean Research Experiment version 2

CORE.v2.NYF Coordinated Ocean Research Experiment version 2 - Normal Year Forcing

POP Parallel Ocean Program

Bibliography

Abernathey, R., J. Marshall, and M. Mazloff, 2010: Enhancement of mesoscale eddy stirring at steering levels in the southern ocean. *Journal of Physical Oceanography*, **40**, 170–184, doi:10.1175/2009JPO4201.1.

Abernathey, R. P., I. Cerovecki, P. R. Holland, E. Newsom, M. Mazloff, and L. D. Talley, 2016: Water-mass transformation by sea ice in the upper branch of the southern ocean overturning. *Nature geoscience*, **9**, 596–603, doi:10.1038/NGEO2749.

Andrews, D. G., and M. E. McIntyre, 1976: Planetary waves in horizontal and vertical shear: the generalized eliassen-palm relation and the mean zonal acceleration. *Geophysical Research Letters*, **33**, L11 606, doi:10.1029/2006GL026157.

Arbic, B. K., J. G. Richman, J. F. Shriver, P. G. Timko, E. J. Metzger, and A. J. Wallcraft, 2012: Global modeling of internal tides with an eddying ocean general circulation model. *Oceanography*, **25(2)**, 20–29, doi:10.5670/oceanog.2012.38.

Bachman, S. D., B. Fox-Kemper, and F. O. Bryan, 2015: A tracer-based inversion method for diagnosing eddy-induced diffusivity and advection. *Ocean Modelling*, **86**, 1–14, doi:10.1016/j.ocemod.2014.11.006.

Bachman, S. D., J. P. Marshall, J. R. Maddison, and J. Mak, 2017: Evaluation of scalar eddy transport coefficient based on geometric constraints. *Ocean Modelling*, **109**, 44–54, doi:10.1016/j.ocemod.2016.12.004.

Ballarotta, M., S. Drijfhout, T. Kuhlbrodt, and K. Döös, 2013: The residual circulation of the southern ocean: Which spatio-temporal scales are needed? *Ocean Modelling*, **64**, 46–55, doi:10.1016/j.ocemod.2013.01.005.

Barthel, A., A. M. Hogg, S. Waterman, and S. Keating, 2017: Jet-topography interactions affect energy pathways to the deep southern ocean. *Journal of Physical Oceanography*, **47**, 1799–1816, doi:10.1175/JPO-D-16-0220.1.

Behrens, E., G. Rickard, O. Morgenstern, T. Martin, A. Osprey, and M. Joshi, 2016: Southern ocean deep convection in global climate models: A driver for variability of subpolar gyres and drake passage transport on decadal timescales. *Journal of Geophysical Research: Oceans*, **121**, 3905–3925, doi:10.1002/2015JC011286.

Bischoff, T., and A. F. Thompson, 2014: Configuration of a southern ocean storm track. *Journal of Physical Oceanography*, **44**, 3072–3078, doi:10.1175/JPO-D-14-0062.1.

Bishop, S. P., P. Gent, F. O. Bryan, A. F. Thompson, M. C. Long, and R. Abernathey, 2016: Southern ocean overturning compensation in an eddy-resolving climate simulation. *Journal of Physical Oceanography*, **46**, 1575–1592, doi:10.1175/JPO-D-15-0177.1.

Bitz, C. M., and L. M. Polvani, 2012: Antarctic climate response to stratospheric ozone depletion in a fine resolution ocean climate model. *Geophysical Research Letters*, **39**, L20 705, doi:10.1029/2012GL053393.

Böning, C. W., A. Dispert, M. Visbeck, S. R. Rintoul, and F. U. Schwarzkopf, 2008: The response of the antarctic circumpolar current to recent climate change. *Nature Geoscience*, **1**, 864–869, doi:10.1038/ngeo362.

Bronselaer, B., L. Zanna, D. R. M. Munday, and J. Lowe, 2016: The influence of southern ocean winds on the north atlantic carbon sink. *Global Biogeochemical Cycles*, **30**, 844–858, doi:10.1002/2015GB005364.

Bryan, F. O., and S. Bachman, 2015: Isohaline salinity budget of the north atlantic salinity maximum. *Journal of Physical Oceanography*, **45**, 724–736, doi:10.1175/JPO-D-14-0172.1.

Bryan, F. O., P. R. Gent, and R. Tomas, 2014: Can southern ocean eddy effects be parameterized in climate models? *Journal of Climate*, **27**, 411–425, doi:10.1175/JCLI-D-12-00759.1.

Chelton, D. B., R. A. DeSzoeke, M. G. Schlax, K. E. Naggar, and N. Siwertz, 1998: Geographical variability of the first baroclinic rossby radius of deformation. *Journal of Physical Oceanography*, **28**, 433–460, doi:10.1175/1520-0485(1998)028<0433:GVOTFB>2.0.CO;2.

Cheon, W. G., Y. Park, J. R. Toggweiler, and S. Lee, 2014: The relationship of weddell polynya and open-ocean deep convection to the southern hemisphere westerlies. *Journal of Physical Oceanography*, **44**, 694–713, doi:10.1175/JPO-D-13-0112.1.

Comiso, J. C., 2000: Bootstrap sea ice concentrations from nimbus-7 smmr and dmsp ssm/i-ssmis, version 2., doi:10.5067/J6JQLS9EJ5HU, boulder, Colorado USA. NASA National Snow and Ice Data Center Distributed Active Archive Center.

Cronin, M., 1996: Eddy-mean flow interaction in the gulf stream at 68°W. part ii: Eddy forcing on the time-mean flow. *Journal of Physical Oceanography*, **26**, 2132–2151, doi:10.1175/1520-0485(1996)026<2132:EMFIIT>2.0.CO;2.

Cunningham, S. A., S. G. Alderson, B. A. King, and M. A. Brandon, 2003: Transport and variability of the antarctic circumpolar current in drake passage. *Journal of Geophysical Research*, **108 (C5)**, 8084, doi:10.1029/2001JC001147.

Danabasoglu, G., S. C. Bates, B. P. Briegleb, M. Jochum, W. G. Large, S. Peacock, and S. G. Yeager, 2012: The CCSM4 ocean component. *Journal of Climate*, **25**, 1361–1389, doi:10.1175/JCLI-D-11-00091.1.

Danabasoglu, G., and J. Marshall, 2007: Effects of vertical variations of thickness diffusivity in an ocean general circulation model. *Ocean Modelling*, **18**, 122–141, doi:10.1016/j.ocemod.2007.03.006.

Danabasoglu, G., J. C. McWilliams, and P. R. Gent, 1994: The role of mesoscale tracer transports in the global ocean circulation. *Science*, **264**, 1123–1126, doi:10.1126/science.264.5162.1123.

Dansgaard, W., and Coauthors, 1993: Evidence for general instability of past climate from a 250-kyr ice-core record. *Nature*, **364**, 218–220, doi:10.1038/364218a0.

Dokken, T. M., K. H. Nisancioglu, C. Li, D. S. Battisti, and C. Kissel, 2013: Dansgaard-oeschger cycles: Interactions between ocean and sea ice intrinsic to the nordic seas. *Paleoceanography*, **28**, 491–502, doi:10.1002/palo.20042.

Donohue, K. A., K. L. Tracey, D. R. Watts, M. P. Chidichimo, and T. K. Chereskin, 2016: Mean antarctic circumpolar current transport measured in drake passage. *Geophysical Research Letters*, **43**, 11 760–11 767, doi:10.1002/2016GL070319.

Döös, K., and D. J. Webb, 1994: The deacon cell and the other meridional cells of the southern ocean. *Journal of Physical Oceanography*, **24**, 429–442, doi:10.1175/1520-0485(1994)024<0429:TDCATO>2.0.CO;2.

Dufour, C. O., J. Le Sommer, J. D. Zika, M. Gehlen, J. C. Orr, P. Mathiot, and B. Barnier, 2012: Standing and transient eddies in the response of the southern ocean meridional overturning to the southern annular mode. *Journal of Climate*, **25**, 6958–6974, doi:10.1175/JCLI-D-11-00309.1.

Dufour, C. O., A. K. Morrison, S. M. Griffies, I. Frenger, H. Zanowski, and M. Winton, 2017: Preconditioning of the weddell sea polynya by the ocean mesoscale and dense water overflows. *Journal of Climate*, **30**, 7719–7737, doi:10.1175/JCLI-D-16-0586.1.

Eady, E. T., 1949: Long waves and cyclone waves. *Tellus*, **1**, 33–52, doi:10.1111/j.2153-3490.1949.tb01265.x.

Eden, C., 2006: Thickness diffusivity in the southern ocean. *Geophysical Research Letters*, **33**, L11 606, doi:10.1029/2006GL026157.

Eden, C., and R. J. Greatbatch, 2008: Towards a mesoscale eddy closure. *Ocean Modelling*, **20**, 223–239, doi:10.1016/j.ocemod.2007.09.002.

Eden, C., R. J. Greatbatch, and D. Olbers, 2007a: Interpreting eddy fluxes. *Journal of Physical Oceanography*, **37**, 1282–1296, doi:10.1175/JPO3050.1.

Eden, C., R. J. Greatbatch, and J. Willebrand, 2007b: A diagnosis of thickness fluxes in an eddy-resolving model. *Journal of Physical Oceanography*, **37**, 727–742, doi:10.1175/JPO2987.1.

Eden, C., M. Jochum, and G. Danabasoglu, 2009: Effects of different closures for thickness diffusivity. *Ocean Modelling*, **26**, 47–59, doi:10.1016/j.ocemod.2008.08.004.

EPICA Community Members, 2006: One-to-one coupling of glacial climate variability in greenland and antarctica. *Nature*, **444**, 195–198, doi:10.1038/nature05301.

Farneti, R., and Coauthors, 2015: An assessment of antarctic circumpolar current and southern ocean meridional overturning circulation during 1958-2007 in a suite of interannual CORE-II simulations. *Ocean Modelling*, **93**, 84–120, doi:10.1016/j.ocemod.2015.07.009.

Ferrari, R., J. C. McWilliams, V. M. Canuto, and M. Dubovikov, 2008: Parameterization of eddy fluxes near oceanic boundaries. *Journal of Climate*, **21**, 2770–2789, doi:10.1175/2007JCLI1510.1.

Ferreira, D., J. Marshall, C. M. Bitz, S. Solomon, and A. Plumb, 2015: Antarctic ocean and sea ice response to ozone depletion: A two-time-scale problem. *Journal of Climate*, **28**, 1206–1226, doi:10.1175/JCLI-D-14-00313.1.

Ferreira, D., J. Marshall, and P. Heimbach, 2005: Estimating eddy stresses by fitting dynamics to observations using a residual-mean ocean circulation model and its adjoint. *Journal of Physical Oceanography*, **35**, 1891–1910, doi:10.1175/JPO2785.1.

Flato, G., and Coauthors, 2013: Evaluation of climate models. *Climate Change 2013: The Physical Science Basis. Contribution of Working Group I to the Fifth Assessment Report of the Intergovernmental Panel on Climate Change*, Cambridge University Press, Cambridge, United Kingdom and New York, NY, USA, chap. 9.

Fox-Kemper, B., R. Ferrari, and R. Hallberg, 2008: Parameterization of mixed layer eddies. part i: theory and diagnosis. *Journal of Physical Oceanography*, **38**, 1145–1165, doi:10.1175/2007JPO3792.1.

Fox-Kemper, B., R. Ferrari, and J. Pedlosky, 2003: On the indeterminacy of rotational and divergent eddy fluxes. *Journal of Physical Oceanography*, **33**, 478–483, doi:10.1175/1520-0485(2003)033<0478:OTIORA>2.0.CO;2.

Frenger, I., M. Münnich, N. Gruber, and R. Knutti, 2015: Southern ocean eddy phenomenology. *Journal of Geophysical Research: Oceans*, **120**, 7413–7449, doi:10.1002/2015JC011047.

Frölicher, T. L., J. L. Sarmiento, D. J. Paynter, J. P. Dunne, and M. Krasting, J. P. Winton, 2015: Dominance of the southern ocean in anthropogenic carbon and heat uptake in cmip5 models. *Journal of Climate*, **28**, 862–886, doi:10.1175/JCLI-D-14-00117.1.

Fyfe, J. C., and O. A. Saenko, 2006: Simulated changes in the extratropical southern hemisphere winds and currents. *Geophysical Research Letters*, **33**, L06 701, doi:10.1029/2005GL025332.

Gent, P. R., and G. Danabasoglu, 2011: Response to increasing southern hemisphere winds in CCSM4. *Journal of Climate*, **24**, 4992–4998, doi:10.1175/JCLI-D-10-05011.1.

Gent, P. R., and J. C. McWilliams, 1990: Isopycnal mixing in ocean circulation models. *Journal of Physical Oceanography*, **20**, 150–155, doi:10.1175/1520-0485(1990)020<0150:IMIOCM>2.0.CO;2.

Gent, P. R., J. Willebrand, T. J. McDougall, and J. C. McWilliams, 1995: Parameterizing eddy-induced tracer transports in ocean circulation models. *Journal of Physical Oceanography*, **25**, 463–474, doi:10.1175/1520-0485(1995)025<0463:PEITTI>2.0.CO;2.

Gent, P. R., G. L. William, and F. O. Bryan, 2001: What sets the mean transport through drake passage? *Journal of Geophysical Research*, **106**, 2693–2712, doi:10.1029/2000JC900036.

Gent, P. R., and Coauthors, 2011: The community climate system model version 4. *Journal of Climate*, **24**, 4973–4991, doi:10.1175/2011JCLI4083.1.

Gille, S., 2003: Float observations of the southern ocean. part ii: Eddy fluxes. *Journal of Physical Oceanography*, **33**, 1182–1196, doi:10.1175/1520-0485(2003)033<1182:FOOTSO>2.0.CO;2.

Gille, S. T., 1994: Mean sea surface height of the antarctic circumpolar current from geosat data: Method and application. *Journal of Geophysical Research*, **99**, 18 225–18 273, doi:10.1029/94JC01172.

Gille, S. T., 2002: Warming of the southern ocean since the 1950s. *Science*, **295**, 1275–1277, doi:10.1126/science.1065863.

Gnanadesikan, A., 1999: A simple predictive model for the structure of the oceanic pycnocline. *Science*, **283**, 2077–2079, doi:10.1126/science.283.5410.2077.

Goodman, P. J., 2001: Thermohaline adjustment and advection in an ogcm. *Journal of Physical Oceanography*, **31**, 1477–1497, doi:10.1175/1520-0485(2001)031<1477:TAAAIA>2.0.CO;2.

Gouretski, V. V., and K. P. Koltermann, 2004: Woce global hydrographic climatology: A technical report. *Bundesamt für seeschifffahrt und hydrographie*, **35**, 9pp.

Greatbatch, R. J., and K. G. Lamb, 1990: On parameterizing vertical mixing of momentum in non-eddy resolving ocean models. *Journal of Physical Oceanography*, **20**, 1634–1637, doi:10.1175/1520-0485(1990)020<1634:OPVMOM>2.0.CO;2.

Griesel, A., C. Eden, N. Koopmann, and E. Yulaeva, 2015: Comparing isopycnal diffusivities in the southern ocean with predictions from linear theory. *Ocean Modelling*, **94**, 33–45, doi:10.1016/j.ocemod.2015.08.001.

Griesel, A., S. T. Gille, J. Sprintall, J. L. McClean, J. H. LaCasce, and M. E. Maltrud, 2010: Isopycnal diffusivities in the antarctic circumpolar current inferred from lagrangian floats in an eddying model. *Journal of Geophysical Research*, **115**, C06 006, doi:10.1029/2009JC005821.

Griesel, A., S. T. Gille, J. Sprintall, J. L. McClean, and M. E. Maltrud, 2009: Assessing eddy heat flux and its parameterization: A wavenumber perspective from a $1/10^\circ$ ocean simulation. *Ocean Modelling*, **29**, 248–260, doi:10.1016/j.ocemod.2009.05.004.

Griffies, S. M., 1998: The gent-mcwilliams skew flux. *Journal of Physical Oceanography*, **28**, 831–841, doi:10.1175/1520-0485(1998)028<0831:TGMSF>2.0.CO;2.

Grootes, P. M., M. Stulver, J. W. C. White, S. Johnsen, and J. Jouzel, 1993: Comparison of oxygen isotope records from the gisp2 and grip greenland ice cores. *Nature*, **366**, 552–554, doi:10.1038/366552a0.

Hallberg, R., and A. Gnanadesikan, 2001: An exploration of the role of transient eddies in determining the transport of a zonally reentrant channel. *Journal of Physical Oceanography*, **31**, 3312–3330, doi:10.1175/1520-0485(2001)031<3312:AEOTRO>2.0.CO;2.

Hallberg, R., and A. Gnanadesikan, 2006: The role of eddies in determining the structure and response of the wind-driven southern hemisphere overturning: Results from the modeling eddies in the southern ocean (meso) project. *Journal of Physical Oceanography*, **36**, 2232–2252, doi:10.1175/JPO2980.1.

Heuzé, C., K. J. Heywood, and J. K. Stevens, D. P. Ridley, 2013: Southern ocean water mass characteristics in cmip5 models. *Geophysical Research Letters*, **40**, 1409–1414, doi:10.1002/grl.50287.

Hirabara, M., H. Tsujino, H. Nakano, and G. Yamanaka, 2012: Formation mechanism of the weddell sea polynya and the impact on the global abyssal ocean. *Journal of Oceanography*, **68**, 771–796, doi:10.1007/s10872-012-0139-3.

Hirst, A. C., and T. J. McDougall, 1998: Meridional overturning and dianeutral transport in a z-coordinate ocean model including eddy-induced advection. *Journal of Physical Oceanography*, **28**, 1205–1223, doi:10.1175/1520-0485(1998)028<1205:MOADTI>2.0.CO;2.

Hogg, A., M. P. Meredith, D. P. Chambers, E. P. Abrahamsen, C. W. Hughes, and A. K. Morrison, 2015: Recent trends in the southern ocean eddy field. *Journal of Geophysical Research*, **120**, 257–267, doi:10.1002/2014JC010470.

Hogg, A. M., and J. R. Blundell, 2006: Interdecadal variability of the southern ocean. *Journal of Physical Oceanography*, **36**, 1626–1645, doi:10.1175/JPO2934.1.

Hogg, A. M., J. R. Blundell, M. P. Meredith, and C. Wilson, 2008: Eddy heat flux in the southern ocean: Response to variable wind forcing. *Journal of Climate*, **21**, 608–620, doi:10.1175/2007JCLI1925.1.

Hogg, A. M., P. Spence, O. A. Saenko, and S. M. Downes, 2017: The energetics of southern ocean upwelling. *Journal of Physical Oceanography*, **47**, 135–153, doi:10.1175/JPO-D-16-0176.1.

Hoskins, B. J., I. N. James, and G. H. White, 1983: The shape, propagation and mean-flow interaction of large-scale weather systems. *Journal of the Atmospheric Sciences*, **40**, 1595–1612, doi:10.1175/1520-0469(1983)040<1595:TSPAMF>2.0.CO;2.

Howard, E., A. M. Hogg, S. Waterman, and D. P. Marshall, 2014: The injection og zonal momentum by buoyancy forcing in a southern ocean model. *Journal of Physical Oceanography*, **45**, 259–271, doi:10.1175/JPO-D-14-0098.1.

Hunke, E. C., and W. H. Lipscomb, 2010: CICE: the los alamos sea ice model documentation and software user's manual version 4.1. Tech. Rep. LA-CC-06-012, Los Alamos National Laboratory.

Ivchenko, V. O., K. J. Richards, and D. P. Stevens, 1996: The dynamics of the antarctic circumpolar current. *Journal of Physical Oceanography*, **26**, 753–774, doi:10.1175/1520-0485(1996)026<0753:TDOTAC>2.0.CO;2.

Jansen, M. F., and L. P. Nadeau, 2016: The effect of southern ocean surface buoyancy loss on the deep-ocean circulation and stratification. *Journal of Physical Oceanography*, **46**, 3455–3470, doi:10.1175/JPO-D-16-0084.1.

Jochum, M., M. F. Cronin, W. S. Kessler, and D. Shea, 2007: Observed horizontal temperature advection by tropical instability waves. *Geophysical research letters*, **34**, L09 604, doi:10.1029/2007GL029416.

Jochum, M., and C. Eden, 2015: The connection between southern ocean winds, atlantic meridional overturning circulation and indo-pacific upwelling. *Journal of Climate*, **28**, 9250–9256, doi:10.1175/JCLI-D-15-0263.1.

Jochum, M., A. Jahn, S. Peacock, D. A. Bailey, J. T. Fasullo, J. Kay, S. Levis, and B. Otto-Bliesner, 2012: True to milankovitch: Glacial inception in the new community climate system model. *Journal of Climate*, **25**, 2226–2239, doi:10.1175/JCLI-D-11-00044.1.

Jochum, M., and R. Murtugudde, 2006: Temperature advection by tropical instability waves. *Journal of Physical Oceanography*, **36**, 592–605, doi:10.1175/JPO2870.1.

Johnsen, S. J., and Coauthors, 1992: Irregular glacial interstadials recorded in a new greenland ice core. *Nature*, **359**, 311–313, doi:10.1038/359311a0.

Johnson, G. C., and L. H. Bryden, 1989: On the size of the antarctic circumpolar current. *Deep-sea Research*, **36**, 39–55, doi:10.1016/0198-0149(89)90017-4.

Kawase, M., 1987: Establishment of deep ocean circulation driven by deep-water production. *Journal of Physical Oceanography*, **17**, 2294–2317, doi:10.1175/1520-0485(1987)017<2294:EODOCD>2.0.CO;2.

Kjellsson, J., and Coauthors, 2015: Model sensitivity of the weddell and ross seas, antarctica, to vertical mixing and freshwater forcing. *Ocean Modelling*, **94**, 141–152, doi:10.1016/j.ocemod.2015.08.003.

Kleppin, H., M. Jochum, B. Otto-Bliesner, C. A. Shields, and S. Yeager, 2015: Stochastic atmospheric forcing as a cause of greenland climate transitions. *Journal of Climate*, **28**, 7741–7763, doi:10.1175/JCLI-D-14-00728.1.

Koenig, Z., C. Provost, R. Ferrari, N. Sennéchael, and M.-H. Rio, 2014: Volume transport of the antarctic circumpolar current: Production and validation of a 20 year long time series obtained from in situ and satellite observations. *Journal of Geophysical Research: Oceans*, **119**, 5407–5433, doi:10.1002/2014JC009966.

Kuhlbrodt, T., A. Griesel, M. Montoya, A. Levermann, M. Hofmann, and S. Rahmstorf, 2007: On the driving processes of the atlantic meridional overturning circulation. *Reviews of Geophysics*, **45**, RG2001, doi:10.1029/2004RG000166.

LaCasce, J. H., 2017: The prevalence of oceanic surface modes. *Geophysical Research Letters*, **44**, 11 097–11 105, doi:10.1002/2017GL075430.

LaCasce, J. H., and J. Pedlosky, 2004: The instability of rossby basin modes on the oceanic eddy field. *Journal of Physical Oceanography*, **34**, 2027–2041, doi:10.1175/1520-0485(2004)034<2027:TIORBM>2.0.CO;2.

Langlais, C. E., S. R. Rintoul, and J. D. Zika, 2015: Sensitivity of antarctic circumpolar current transport and eddy activity to wind patterns in the southern ocean. *Journal of Physical Oceanography*, **45**, 1051–1067, doi:10.1175/JPO-D-14-0053.1.

Large, W. G., J. C. McWilliams, and S. C. Doney, 1994: Oceanic vertical mixing: A review and a model with nonlocal boundary layer parameterization. *Reviews of Geophysics*, **32**, 363–403, doi:10.1029/94RG01872.

Large, W. G., and S. G. Yeager, 2004: Diurnal to decadal global forcing for ocean and sea-ice models: The data sets and flux climatologies. Tech. Rep. NCAR/TN-460+STR, National Center for Atmospheric Research, Boulder, Colorado, 105 pp. doi:10.5065/D6KK98Q6.

Large, W. G., and S. G. Yeager, 2008: The global climatology of an interannually varying air-sea flux data set. *Climate Dynamics*, **33**, 341–364, doi:10.1007/s00382-008-0441-3.

Lavergne, C. d., J. B. G. E. D. Palter, R. Bernardello, and I. Marinov, 2014: Cessation of deep convection in the open southern ocean under anthropogenic climate change. *Nature Climate Change*, **4**, 278–282, doi:10.1038/nclimate2132.

Le Quéré, C., and Coauthors, 2007: Saturation of the southern ocean CO_2 sink due to recent climate change. *Science*, **316**, 1735–1737, doi:10.1126/science.1136188.

Lorenz, E. N., 1955: Available potential energy and the maintenance of the general circulation. *Tellus*, **2**, 157–167, doi:10.1111/j.2153-3490.1955.tb01148.x.

Lovenduski, N. S., N. Gruber, S. C. Doney, and I. D. Lima, 2007: Enhanced CO_2 outgassing in the southern ocean from a positive phase of the southern annular mode. *Global Biochemical Cycles*, **21**, GB2026, doi:10.1029/2006GB002900.

Maddison, J., and D. Marshall, 2013: The eliassen-palm flux tensor. *Journal of Fluid Mechanics*, **729**, 69–102, doi:10.1017/jfm.2013.259.

Maddison, J. R., D. P. Marshall, and J. Shipton, 2015: On the dynamical influence of ocean eddy potential vorticity fluxes. *Ocean Modelling*, **92**, 169–182, doi:10.1016/j.ocemod.2015.06.003.

Mak, J., J. R. Maddison, D. P. Marshall, and D. R. Munday, 2018: Implementation of a geometrically and energetically constrained mesoscale eddy parameterization in an ocean circulation model. *Journal of Physical Oceanography*, **48**, 2363–2382, doi:10.1175/JPO-D-18-0017.1.

Mak, J., D. P. Marshall, J. R. Maddison, and S. D. Bachman, 2017: Emergent eddy saturation from an energy constrained eddy parameterization. *Ocean Modelling*, **112**, 125–138, doi:10.1016/j.ocemod.2017.02.007.

Marshall, D. P., 1997: Subduction of water masses in an eddying ocean. *Journal of marine research*, **55**, 201–222, doi:10.1357/0022240973224373.

Marshall, D. P., M. H. P. Ambaum, J. R. Maddison, D. R. Munday, and L. Novak, 2017: Eddy saturation and frictional control of the antarctic circumpolar current. *Geophysical Research Letters*, **44**, 2016GL071 702, doi:10.1002/2016GL071702.

Marshall, D. P., and H. L. Johnson, 2013: Propagation of meridional circulation anomalies along western and eastern boundaries. *Journal of Physical Oceanography*, **43**, 2699–2717, doi:10.1175/JPO-D-13-0134.1.

Marshall, D. P., J. R. Maddison, and P. S. Berloff, 2012: A framework for parameterizing eddy potential vorticity fluxes. *Journal of Physical Oceanography*, **42**, 539–557, doi:10.1175/JPO-D-11-048.1.

Marshall, D. P., and H. R. Pillar, 2011: Momentum balance of the wind-driven and meridional overturning circulation. *Journal of Physical Oceanography*, **41**, 960–978, doi:10.1175/2011JPO4528.1.

Marshall, D. P., B. Vogel, and X. Zhai, 2013: Rossby rip currents. *Geophysical Research Letters*, **40**, 4333–4337, doi:10.1002/grl.50842.

Marshall, D. P., and L. Zanna, 2014: A conceptual model of ocean heat uptake under climate change. *Journal of Climate*, **27**, 8444–8465, doi:10.1175/JCLI-D-13-00344.1.

Marshall, G. J., 2003: Trends in the southern annular mode from observations and reanalyses. *Journal of Climate*, **1**, 4134–4143, doi:10.1175/1520-0442(2003)016<4134:TITSAM>2.0.CO;2.

Marshall, G. J., and W. M. Connolley, 2006: Effect of changing southern hemisphere winter sea surface temperatures on the southern annular mode strength. *Geophysical Research Letters*, **33**, L17 717, doi:10.1029/2006GL026627.

Marshall, J., and T. Radko, 2003: Residual-mean solutions for the antarctic circumpolar current and its associated overturning circulation. *Journal of Physical Oceanography*, **33**, 2341–2354, doi:10.1175/1520-0485(2003)033<2341:RSFTAC>2.0.CO;2.

Marshall, J., and G. Shutts, 1981: A note on rotational and divergent eddy fluxes. *Journal of Physical Oceanography*, **11**, 1677–1680, doi:10.1175/1520-0485(1981)011<1677:ANORAD>2.0.CO;2.

Marshall, J., and K. Speer, 2012: Closure of the meridional overturning circulation through southern ocean upwelling. *Nature Geoscience*, **5**, 171–180, doi:10.1038/NGEO1391.

Martin, T., W. Park, and M. Latif, 2015: Southern ocean forcing of the north atlantic at multi-centennial time scale in the kiel climate model. *Deep-sea research II*, **114**, 39–48, doi:10.1016/j.dsr2.2014.01.018.

Masich, J., T. K. Chereskin, and M. R. Mazloff, 2015: Topographic form stress in the southern ocean state estimate. *Journal of Geophysical Research: Oceans*, **120**, 7919–7933, doi:10.1002/2015JC011143.

Masich, J., M. R. Mazloff, and T. K. Chereskin, 2018: Interfacial form stress in the southern ocean state estimate. *Journal of Geophysical Research: Oceans*, **123**, doi:10.1029/2018JC013844.

Mazloff, M. R., 2012: On the sensitivity of the drake passage transport to air-sea momentum flux. *Journal of Climate*, **25**, 2279–2290, doi:10.1175/JCLI-D-11-00030.1.

Mazloff, M. R., P. Heimbach, and C. Wunsch, 2010: An eddy-permitting southern ocean state estimate. *Journal of Physical Oceanography*, **40**, 880–899, doi:10.1175/2009JPO4236.1.

McDougall, T. J., P. R. Gent, and S. Drijfhout, 2007: Comments on "dynamical model of mesoscales in z-coordinates" and "the effect of mesoscales on the tracer equation in z-coordinates ogcms" by v. m. canuto and m. s. dubovikov. *Ocean Modelling*, **17**, 163–171, doi:10.1016/j.ocemod.2006.11.004.

McDougall, T. J., and P. C. McIntosh, 1996: The temporal-residual-mean velocity. part i: derivation and the scalar conservation equations. *Journal of Physical Oceanography*, **26**, 2653–2665, doi:10.1175/1520-0485(1996)026<2653:TTRMVP>2.0.CO;2.

McDougall, T. J., and P. C. McIntosh, 2001: The temporal-residual-mean velocity. part ii: isopycnal interpretation and the tracer and momentum equations. *Journal of Physical Oceanography*, **31**, 1222–1246, doi:10.1175/1520-0485(2001)031<1222:TTRMVP>2.0.CO;2.

McIntosh, P. C., and T. J. McDougall, 1996: Isopycnal averaging and the residual mean circulation. *Journal of Physical Oceanography*, **26**, 1655–1660, doi:10.1175/1520-0485(1996)026<1655:IAATRM>2.0.CO;2.

Medvedev, A. S., and R. J. Greatbatch, 2004: On advection and diffusion in the mesosphere and lower thermosphere: the role of rotational fluxes. *Journal of Geophysical Research*, **109**, D07 104, doi:10.1029/2003JD003931.

Meredith, M. P., and A. M. Hogg, 2006: Circumpolar response of southern ocean eddy activity to a change in the southern annular mode. *Geophysical Research Letters*, **33**, L16 608, doi:10.1029/2006GL026499.

Morrison, A. K., and A. M. Hogg, 2013: On the relationship between southern ocean overturning and acc transport. *Journal of Physical Oceanography*, **43**, 140–148, doi:10.1175/JPO-D-12-057.1.

Morrow, R., R. Coleman, J. Church, and D. Chelton, 1994: Surface eddy momentum flux and velocity variances in the southern ocean from geosat altimetry. *Journal of Physical Oceanography*, **24**, 2050–2071, doi:10.1175/1520-0485(1994)024<2050:SEMFAV>2.0.CO;2.

Morrow, R., M. L. Ward, A. Hogg, and S. Pasquet, 2010: Eddy response to southern ocean climate modes. *Journal of Geophysical Research*, **115**, C10 030, doi:10.1029/2009JC005894.

Munday, D. R., H. L. Johnson, and D. P. Marshall, 2013: Eddy saturation of equilibrated circumpolar currents. *Journal of Physical Oceanography*, **43**, 507–532, doi:10.1175/JPO-D-12-095.1.

Munk, W. H., 1966: Abyssal recipes. *Deep-Sea Research*, **13**, 707–730, doi:10.1016/0011-7471(66)90602-4.

Munk, W. H., and E. Palmén, 1951: Note on the dynamics of the antarctic circumpolar current. *Tellus*, **3**, 53–55, doi:10.1111/j.2153-3490.1951.tb00776.x.

Nadeau, L., and D. N. Straub, 2009: Basin and channel contributions to a model antarctic circumpolar current. *Journal of Physical Oceanography*, **39**, 986–1002, doi:10.1175/2008JPO4023.1.

Nadeau, L., and D. N. Straub, 2012: Influence of wind stress, wind stress curl, and bottom friction on the transport of a model antarctic circumpolar current. *Journal of Physical Oceanography*, **42**, 207–222, doi:10.1175/JPO-D-11-058.1.

Nielsen, S. B., M. Jochum, C. Eden, and R. Nuterman, 2018: An energetically consistent vertical mixing parameterization in CCSM4. *Ocean Modelling*, **127**, 46–54, doi:10.1016/j.ocemod.2018.03.002.

Olbers, D., 1998: Comments on "On the obscurantist physics of 'Form Drag' in theorizing about the circumpolar current". *Journal of Physical Oceanography*, **28**, 1647–1654, doi:10.1175/1520-0485(1998)028<1647:COOTOP>2.0.CO;2.

Olbers, D., and M. Visbeck, 2005: A model of the zonally averaged stratification and overturning in the southern ocean. *Journal of Physical Oceanography*, **35**, 1190–1205, doi:10.1175/JPO2750.1.

Orsi, A. H., T. Whitworth, and W. D. Nowlin, 1995: On the meridional extent and fronts of the antarctic circumpolar current. *Deep-sea Research*, **42**, 641–673, doi:10.1016/0967-0637(95)00021-W.

Pedlosky, J., 1987: *Geophysical Fluid Dynamics*. 2nd ed., Springer, 710 pp.

Pedro, J. B., M. Jochum, C. Buizert, F. He, S. Barker, and S. O. Rasmussen, 2018: Beyond the bipolar seesaw: Toward a process understanding of interhemispheric coupling. *Quaternary Science Reviews*, **192**, 27–46, doi:10.1016/j.quascirev.2018.05.005.

Pedro, J. B., T. Martin, E. J. Steig, M. Jochum, W. Park, and S. O. Rasmussen, 2016: Southern ocean deep convection as a driver of antarctic warming events. *Geophysical Research Letters*, **43**, 2192–2199, doi:10.1002/2016GL067861.

Peltier, W. R., and G. Vettoretti, 2014: Dansgaard-oeschger oscillations predicted in a comprehensive model of glacial climate: A "kicked" salt oscillator in the atlantic. *Geophysical Research Letters*, **41**, 7306–7313, doi:10.1002/2014GL061413.

Plumb, R. A., 1986: Three-dimensional propagation of transient quasi-geostrophic eddies and its relationship with the eddy forcing of the time-mean flow. *Journal of the Atmospheric Sciences*, **43**, 1657–1678, doi:10.1175/1520-0469(1986)043<1657:TDPOTQ>2.0.CO;2.

Poulsen, M. B., M. Jochum, J. R. Maddison, D. P. Marshall, and R. Nuterman, Submitted: A geometric interpretation of southern ocean eddy form stress. *Journal of Physical Oceanography*.

Poulsen, M. B., M. Jochum, and R. Nuterman, 2018: Parameterized and resolved southern ocean eddy compensation. *Ocean Modelling*, **124**, 1–15, doi:10.1016/j.ocemod.2018.01.008.

Prandtl, L., 1925: Bericht über untersuchungen zur ausgebildeten turbulenz. *Z. Angew. Math. Mech.*, **5**, 136–139.

Rasmussen, S. O., and Coauthors, 2014: A stratigraphic framework for abrupt climatic changes during the last glacial period based on three synchronized greenland ice-core records: refining and extending the intimate event stratigraphy. *Quaternary Science Reviews*, **106**, 14–28, doi:10.1016/j.quascirev.2014.09.007.

Redi, M. H., 1982: Ocean isopycnal mixing by coordinate rotation. *Journal of Physical Oceanography*, **12**, 1154–1158, doi:10.1175/1520-0485(1982)012<1154:OIMBCR>2.0.CO;2.

Riley, K. F., M. P. Hobson, and S. J. Bence, 2006: *Mathematical Methods for Physics and Engineering*. 3rd ed., Cambridge University Press, 1333 pp.

Ringler, T., and P. Gent, 2011: An eddy closure for potential vorticity. *Ocean Modelling*, **39**, 125–134, doi:10.1016/j.ocemod.2011.02.003.

Rintoul, S. R., 2018: The global influence of localized dynamics in the southern ocean. *Nature*, **558**, 209–218, doi:10.1038/s41586-018-0182-3.

Rintoul, S. R., and A. C. N. Garabato, 2013: Dynamics of the southern ocean circulation. *Ocean Circulation and Climate - A 21st Century Perspective*, Vol. 103, 2nd ed., Academic Press, chap. 18, 471–492.

Roberts, M. J., and D. P. Marshall, 2000: On the validity of downgradient eddy closures in ocean models. *Journal of Geophysical Research*, **105**, 28 613–28 627, doi:10.1029/1999JC000041.

Roullet, G., X. Capet, and G. Maze, 2014: Global interior eddy available potential energy diagnosed from argo floats. *Geophysical Research Letters*, **41**, 1651–1656, doi:10.1002/2013GL059004.

Sallée, J. B., K. Speer, and R. Morrow, 2008: Response of the antarctic circumpolar current to atmospheric variability. *Journal of Climate*, **21**, 3020–3039, doi:10.1175/2007JCLI1702.1.

Sigman, D. M., and E. A. Boyle, 2000: Glacial/interglacial variations in atmospheric carbon dioxide. *Nature*, **407**, 859–869, doi:10.1038/35038000.

Small, R. J., and Coauthors, 2014: A new synoptic scale resolving global climate simulation using the community earth system model. *Journal of Advances in Modeling Earth Systems*, **6**, 1065–1094, doi:10.1002/2014MS000363.

Smith, R. D., and Coauthors, 2010: The parallel ocean program (POP) reference manual, ocean component of the community climate system model (CCSM). Tech. rep., Los Alamos National Laboratory. URL http://n2t.net/ark:/85065/d70g3j4h.

Spence, P., O. A. Saenko, M. Eby, and A. J. Weaver, 2009: The southern ocean overturning: parameterized versus permitted eddies. *Journal of Physical Oceanography*, **39**, 1634–1651, doi:10.1175/2009JPO4120.1.

Steele, M., R. Morley, and W. Ermold, 2001: Phc: A global ocean hydrography with a high-quality arctic ocean. *Journal of Climate*, **14**, 2079–2087, doi:10.1175/1520-0442(2001)014<2079:PAGOHW>2.0.CO;2.

Steffensen, J. P., and Coauthors, 2008: High-resolution greenland ice core data show abrupt climate change happens in few years. *Science*, **321**, 680–684, doi:10.1126/science.1157707.

Stewart, K. D., P. Spence, S. Waterman, J. Le Sommer, J.-M. Molines, J. M. Lilly, and M. H. England, 2015: Anisotropy of eddy variability in the global ocean. *Ocean Modelling*, **95**, 53–65, doi:10.1016/j.ocemod.2015.09.005.

Stocker, T. F., and S. J. Johnson, 2003: A minimum thermodynamic model for the bipolar seesaw. *Paleoceanography*, **18(4)**, 1087, doi:10.1029/2003PA000920.

Stommel, H., and A. B. Arons, 1959: On the abyssal circulation of the world ocean - i. stationary planetary flow patterns on a sphere. *Deep Sea Research*, **6**, 140–154, doi:10.1016/0146-6313(59)90065-6.

Storch, J. V., C. Eden, I. Fast, H. Haak, D. Hernández-Decker, E. Maier-Reimer, J. Marotzke, and D. Stammer, 2012: An estimate of the lorenz energy cycle for the world ocean based on the 1/10° storm/ncep simulation. *Journal of Physical Oceanography*, **42**, 2185–2205, doi:10.1175/JPO-D-12-079.1.

Straub, D. N., 1993: On the transport and angular momentum balance of channel models of the antarctic circumpolar current. *Journal of Physical Oceanography*, **23**, 776–782, doi:10.1175/1520-0485(1993)023<0776:OTTAAM>2.0.CO;2.

Talley, L. D., 2013: Closure of the global overturning circulation through the indian, pacific and southern oceans: Schematics and transports. *Oceanography*, **26(1)**, 80–97, doi:10.5670/oceanog.2013.07.

Tamarin, T., J. R. Maddison, E. Heifetz, and D. P. Marshall, 2016: Geometric interpretation of eddy reynolds stresses in barotropic ocean jets. *Journal of Physical Oceanography*, **46**, 2285–2307, doi:10.1175/JPO-D-15-0139.1.

Tamsitt, V., and Coauthors, 2017: Spiraling pathways of the global deep waters to the surface of the southern ocean. *Nature Communications*, **8**, 172, doi:10.1038/s41467-017-00197-0.

Tansley, C. E., and D. P. Marshall, 2001: On the dynamics of a wind-driven circumpolar current. *Journal of Physical Oceanography*, **31**, 3258–3273, doi:10.1175/1520-0485(2001)031<3258:OTDOWD>2.0.CO;2.

Thompson, A. F., 2008: The atmospheric ocean: Eddies and jets in the antarctic circumpolar current. *Philosophical Transactions of the Royal Society*, **366**, 4529–4541, doi:10.1098/rsta.2008.0196.

Thompson, A. F., and A. C. N. Garabato, 2014: Equilibration of the antarctic circumpolar current by standing meanders. *Journal of Physical Oceanography*, **44**, 1811–1828, doi:10.1175/JPO-D-13-0163.1.

Thompson, A. F., A. L. Stewart, and T. Bischoff, 2016: A multi-basin residual-mean model for the global overturning circulation. *Journal of Physical Oceanography*, **46**, 2583–2604, doi:10.1175/JPO-D-15-0204.1.

Thompson, D. W. J., and S. Solomon, 2002: Interpretation of recent southern hemisphere climate change. *Science*, **296**, 895–899, doi:10.1126/science.1069270.

Thompson, D. W. J., and J. M. Wallace, 2000: Annular modes in the extratropical circulation. part i: Month-to-month variability. *Journal of Climate*, **13**, 1000–1016, doi:10.1175/1520-0442(2000)013<1000:AMITEC>2.0.CO;2.

Toggweiler, J. R., and B. Samuels, 1995: Effect of drake passage on the global thermohaline circulation. *Deep-Sea Research*, **42**, 477–500, doi:10.1016/0967-0637(95)00012-U.

Toggweiler, J. R., and B. Samuels, 1998: On the ocean's large-scale circulation near the limit of no vertical mixing. *Journal of Physical Oceanography*, **28**, 1832–1852, doi:10.1175/1520-0485(1998)028<1832:OTOSLS>2.0.CO;2.

Treguier, A. M., I. M. Held, and V. D. Larichev, 1997: Parameterization of quasigeostrophic eddies in primitive equation ocean models. *Journal of Physical Oceanography*, **27**, 567–580, doi:10.1175/1520-0485(1997)027<0567:POQEIP>2.0.CO;2.

Treguier, A. M., J. Le Sommer, J. M. Molines, and B. De Cuevas, 2010: Response of the southern ocean to the southern annular mode: Interannual variability and multidecadal trend. *Journal of Physical Oceanography*, **40**, 1659–1668, doi:10.1175/2010JPO4364.1.

Vallis, G. K., 2006: *Atmospheric and Oceanic Fluid Dynamics*. 1st ed., Cambridge University press, 745 pp.

Viebahn, J., and C. Eden, 2010: Towards the impact of eddies on the response of the southern ocean to climate change. *Ocean Modelling*, **34**, 150–165, doi:10.1016/j.ocemod.2010.05.005.

Viebahn, J., and C. Eden, 2012: Standing eddies in the meridional overturning circulation. *Journal of Physical Oceanography*, **42**, 1486–1508, doi:10.1175/JPO-D-11-087.1.

Visbeck, M., J. Marshall, T. Haine, and M. Spall, 1997: Specification of eddy transfer coefficients in coarse-resolution ocean circulation models. *Journal of Physical Oceanography*, **27**, 381–402, doi:10.1175/1520-0485(1997)027<0381:SOETCI>2.0.CO;2.

WAIS Divide Project Members, 2015: Precise interpolar phasing of abrupt climate change during the last ice age. *Nature*, **520**, 661–665, doi:10.1038/nature14401.

Wardle, R., and J. Marshall, 2000: Representation of eddies in primitive equation models by a pv flux. *Journal of Physical Oceanography*, **30**, 2481–2503, doi:10.1175/1520-0485(2000)030<2481:ROEIPE>2.0.CO;2.

Waterman, S., N. G. Hogg, and S. R. Jayne, 2011: Eddy-mean flow interaction in the kuroshio extension region. *Journal of Physical Oceanography*, **41**, 1182–1208, doi:10.1175/2010JPO4564.1.

Waterman, S., and J. M. Lilly, 2015: Geometric decomposition of eddy feedbacks in barotropic systems. *Journal of Physical Oceanography*, **45**, 1009–1024, doi:10.1175/JPO-D-14-0177.1.

Wolff, J.-O., E. Maier-Reimer, and D. J. Olbers, 1991: Wind-driven flow over topography in a zonal β-plane channel: A quasi-geostrophic model of the antarctic circumpolar current. *Journal of Physical Oceanography*, **21**, 236–264, doi:10.1175/1520-0485(1991)021<0236:WDFOTI>2.0.CO;2.

Wunsch, C., 1998: The work done by the wind on the oceanic general circulation. *Journal of Physical Oceanography*, **28**, 2332–2340, doi:10.1175/1520-0485(1998)028<2332:TWDBTW>2.0.CO;2.

Wunsch, C., and R. Ferrari, 2004: Vertical mixing, energy and the general circulation of the oceans. *Annual Reviews of Fluid Mechanics*, **36**, 281–314, doi:10.1146/annurev.fluid.36.050802.122121.

Young, W. R., 2012: An exact thickness-weighted average formulation of the boussinesq equations. *Journal of Physical Oceanography*, **42**, 692–707, doi:10.1175/JPO-D-11-0102.1.

Yuan, X., 2004: High-wind-speed evaluation in the southern ocean. *Journal of Geophysical Research*, **109**, D13 101, doi:10.1029/2003JD004179.

Zika, J. D., J. L. Sommer, C. O. Dufour, A. N. Garabato, and A. Blaker, 2013: Acceleration of the antarctic circumpolar current by wind stress along the coast of antarctica. *Journal of Physical Oceanography*, **43**, 2772–2784, doi:10.1175/JPO-D-13-091.1.